Dynamics in filled elastomers and consequences

Aurélie Papon

THESE DE DOCTORAT DE L'UNIVERSITE PIERRE ET MARIE CURIE

Spécialité

Chimie et Physico-Chimie des Polymères
(Ecole doctorale 397, Physique et Chimie des Matériaux)

Présentée par

Mlle Aurélie PAPON

Pour obtenir le grade de

DOCTEUR DE L'UNIVERSITE PIERRE ET MARIE CURIE

Sujet de la thèse :

Dynamique dans les élastomères renforcés et conséquences

Soutenue le 16 septembre 2011 devant le jury composé de :

M. Ralph COLBY	Professeur, Pennsylviana State University	Rapporteur
M. Jean-François JOANNY	Professeur, UPMC-Institut Curie	Président
M. Pierre LEVITZ	Directeur de recherche, Ecole Polytechnique	Rapporteur
M. Cédric LORTHIOIR	Chargé de recherche, Université Paris-Est	Examinateur
M. François LEQUEUX	Directeur de recherche, ESPCI ParisTech	Directeur de thèse
Mme Hélène MONTES	Maître de conférences, ESPCI ParisTech	Directrice de thèse

Invités :

M. Laurent GUY	Rhodia Opérations
M. Didier LONG	Directeur de recherche CNRS
M. Julian OBERDISSE	Directeur de recherche, Université Montpellier 2
M. Kay SAALWÄCHTER	Professeur, Martin-Luther-Universität Halle-Wittenberg

Université Pierre & Marie Curie - Paris 6
Bureau d'accueil, inscription des doctorants et base de données
Esc G, 2ème étage
15 rue de l'école de médecine
75270-PARIS CEDEX 06

Tél. Secrétariat : 01 42 34 68 35
Fax : 01 42 34 68 40
Tél. pour les étudiants de A à EL : 01 42 34 69 54
Tél. pour les étudiants de EM à MON : 01 42 34 68 41
Tél. pour les étudiants de MOO à Z : 01 42 34 68 51
E-mail : scolarite.doctorat@upmc.fr

Remerciements

Voilà ces trois années de thèse qui s'achèvent (déjà !) et je tiens à remercier tous ceux qui ont contribué à leur excellent déroulement.

Pour commencer, je veux remercier Rhodia pour avoir financé cette thèse et Christian Frétigny, directeur du laboratoire PPMD-SIMM, de m'avoir accueillie et fourni tous les moyens nécessaires à ce travail, ainsi que pour toutes les discussions scientifiques que nous avons eues.

Ensuite, je tiens à remercier mes encadrants au laboratoire, Hélène et François, qui ont formé une équipe de choc pour diriger ces recherches. Merci pour votre disponibilité malgré vos nombreuses occupations, merci pour votre encadrement et vos conseils toujours pertinents et merci pour votre bonne humeur à toute épreuve. Nos réunions étaient toujours l'occasion d'un travail fructueux mais aussi de très joyeux moments !

Je veux également remercier Laurent qui a suivi mon travail très régulièrement tout au long de ma thèse. Son regard plus proche de l'application industrielle nous a beaucoup apporté.

J'adresse tous mes remerciements aux membres du jury pour l'intérêt qu'ils ont porté à ce travail et en particulier à Ralph Colby et Pierre Levitz qui m'ont fait l'honneur d'en être les rapporteurs et à Jean-François Joanny pour avoir présidé ce jury.

Cette thèse s'est déroulée en collaboration avec plusieurs équipes.

Merci à Kay Saalwächter de m'avoir accueillie dans son groupe de RMN du solide à l'Université Martin-Luther Halle-Wittenberg en Allemagne. Vielen Danke Kay ! In addition to spin relaxation, I have discovered Halle, Leipzig and Berlin. Thanks also to everyone in the group to have welcomed me there, in particular Kerstin and Henriette.

D'autres mesures RMN se sont déroulées au LPMA à Lyon grâce à la précieuse aide de Paul Sotta et de Roberto Perez-Aparicio. Un grand merci à tous les deux et à tout le LPMA pour votre accueil. Je garderai en particulier un souvenir impérissable de "Rubber", un film sur un pneu tueur...

Egalement un grand merci à Julian Oberdisse qui m'a initiée aux simulations Monte-Carlo inverses à Montpellier. Ce fut un séjour rapide mais efficace pour me mettre au Fortran !

Enfin merci à Samy Merabia au LPMCN à Lyon et Didier Long au LPMA qui nous ont notamment permis de comparer nos résultats expérimentaux aux simulations qu'ils ont obtenues avec leur modèle de renforcement.

Au laboratoire, je tiens à remercier toutes les personnes qui ont contribué scientifiquement à cette étude : Freddy pour la synthèse des silices, Ludovic pour la création de pièces sur-mesure pour diverses machines, Bruno et Maxime pour l'utilisation de la RMN, Mohamed pour la DSC et Guylaine pour la rhéologie. Merci également à Annie, Gilles, Flore et Armand pour leur aide au jour le jour pour des problèmes moins scientifiques mais tout aussi importants.

Et puis évidemment je remercie toutes les personnes qui ont fait que je garderai de ces trois années au laboratoire un excellent souvenir : Astrid, Juliette et Elise pour les pauses goûter, Freddy pour les séances de mots-croisés, Chau-Jean, Piero, Laetitia et Jennifer qui ont partagé mon bureau, Séverine, Clémence, Etienne, François, David et Anne-Charlotte pour nos déjeuners animés, les dégustations de Petits écoliers®, l'organisation de la via-ferrata et bien plus encore, Julien, Maxime, Céline et leur réserve de fraises Tagada®, M&M's® ou chocolats, toujours réconfortants, et je n'oublie pas Marie-Charlotte, Toan, Basile, Peiluo, Elodie, Guillaume, Eloïse, Sandrine, Solenn, Lucie, Jordan, Dongmei, Wei, Nisita et tous ceux avec qui j'ai partagé de très bons moments autour d'un verre le vendredi soir.

J'adresse enfin mes plus sincères remerciements à ma famille pour m'avoir encouragée et supportée tout au long de mes études et à Eric pour son soutien sans faille pendant ses trois années et depuis bien plus longtemps encore.

Sommaire

Introduction générale

Les élastomères sont connus pour leur grande élasticité, mais c'est en leur incorporant de fines particules solides que leurs propriétés deviennent plus intéressantes pour les applications industrielles telles que les pneumatiques, les semelles ou encore les joints. En effet, l'ajout de charges - généralement noir de carbone ou silice - permet d'augmenter significativement leur résistance à l'abrasion ainsi que leur capacité d'amortissement. Dans les années 90, Rhodia a notamment développé une silice ayant une bien meilleure capacité à se disperser dans l'élastomère ce qui a permis de créer un pneu "vert" présentant de meilleures propriétés de résistance au roulement et d'adhérence, sans diminution de la résistance à l'usure. Un des principaux challenges actuels de l'industrie du pneumatique est ainsi de continuer dans cette optique de diminution de la résistance au roulement et donc de la consommation de carburant des véhicules.

Pour cela, il est indispensable de mieux comprendre les mécanismes physiques et chimiques mis en jeu lors du renforcement par des charges solides. Deux paramètres clés sont alors à prendre en compte : l'état de dispersion des charges et leur affinité avec l'élastomère. Cependant, ce sont des paramètres interdépendants, difficilement séparables dans l'étude de systèmes classiques obtenus par malaxage de l'élastomère avec les charges. Pour permettre une étude plus aisée de ces systèmes, Julien Berriot [1] et Thomas Chaussée [2] ont mis au point lors de leur thèse des élastomères renforcés modèles. Ces systèmes ont des compositions plus simples que des systèmes industriels ainsi qu'un meilleur contrôle de la dispersion des particules, même dans le cas d'une affinité faible entre la silice et le polymère. L'étude de ces systèmes a déjà permis d'identifier l'éxistence d'une couche de polymère rigide autour des charges pouvant être responsable des principales propriétés des élastomères renforcés telles que leur important renforcement et leurs propriétés en déformation.

Cette thèse poursuit l'étude de ces systèmes selon trois axes principaux.

- D'abord, des mesures de Résonance Magnétique Nucléaire (RMN) en collaboration avec K. Saalwächter à Halle (Allemagne) permettent une analyse plus fine de la dynamique du polymère, tant du point de vue du ralentissement des chaînes proches des particules que du point de vue des contraintes topologiques du réseau (Chapitre 2). Ces résultats nous amènent ensuite à la première interprétation directe de résultats de RMN par un gradient de température de transition vitreuse autour des charges (Chapitre 3).

- Ensuite, l'analyse en rhéologie des propriétés mécaniques en cisaillement sinusoïdal nous

permet d'observer deux phénomènes en régime non linéaire : non seulement l'effet Payne étudié classiquement, mais aussi l'apparition de signaux non sinusoïdaux caractérisés par un raidissement et une rhéofluidification lorsque les systèmes sont soumis à de fortes déformations. Nous verrons que ces observations sont en bon accord qualitatif avec les simulations obtenues avec le modèle de renforcement par ponts vitreux développé par S. Merabia (maintenant au LPMCN), P. Sotta et D. Long au LPMA à Lyon (Chapitre 4).

- Enfin, des simulations Monte-Carlo inverses mises au point avec J. Oberdisse au LCVN à Montpellier permettent de déterminer l'arrangement des particules de silice dans chaque échantillon. Combiné aux chapitres 2 et 3, cela nous permet de discuter les mesures de dynamique du polymère et de les traduire en termes d'épaisseur de polymère immobilisé autour des charges. Nous pouvons ensuite faire le lien entre la composition des systèmes (état de dispersion des charges et épaisseur de polymère immobilisé) et leur propriétés mécaniques (Chapitre 5).

General introduction

Elastomers are known for their high elasticity, but it is the introduction of small solid particles that makes their properties more attractive for industrial applications such as tires. The addition of fillers - usually carbon black or silica - significantly increases their wear resistance as well as their damping capacity. In the 90s, Rhodia developed a silica particle with a much better ability to be dispersed in the elastomer. This allowed the creation of a "green" tire with improved rolling resistance and wet grip without reducing the wear resistance. One of the main challenges of today's tire industry is to continue reducing the rolling resistance, and thus the fuel consumption of vehicles.

To do this, it is essential to understand the physical and chemical mechanisms involved in the reinforcement induced by the addition of solid fillers. Two key parameters to take into account are the dispersion state of the fillers and their affinity with the elastomer. However, these parameters are interdependent, and are thus difficult to separate in the study of classical systems obtained by mixing the elastomer with the fillers. To provide insight into such systems, Julien Berriot [1] and Thomas Chaussée [2] have developed model reinforced elastomers. These systems have a simpler composition than industrial systems and a better control of the particles dispersion, even in the case of systems with low affinity between silica and polymer. The study of these model systems revealed a rigid polymer layer around the fillers that is attributed to the main properties of filled rubbers such as their large reinforcement and non linear properties.

This PhD work continues the study of these model systems along three main directions.

- Firstly, Nuclear Magnetic Resonance (NMR) measurements, done in collaboration with K. Saalwächter in Halle (Germany), allow a more detailed analysis of the polymer dynamics, including both the mobility of the polymer chains in the vicinity of the particles and the topological constraints in the network (Chapter 2). These results lead us to the first direct interpretation of NMR results in terms of *gradient* of glass transition temperature around the fillers (Chapter 3).

- Secondly, the analysis of the mechanical properties in oscillatory shear gives us the opportunity to observe two phenomena in the non linear regime : the Payne effect which is classically studied in filled rubbers, and also the apparition of non sinusoidal signals exhibiting strain-stiffening and shear-thinning effects inside each cycle of solicitation. We find that these observations are in good qualitative agreement with the simulations obtained

by the glassy bridge reinforcement model developed by S. Merabia (now in LPMCN), P. Sotta and D. Long at the LPMA in Lyon (Chapter 4).

- Thirdly, reverse Monte Carlo simulations developed with J. Oberdisse at the LCVN in Montpellier enable the description of particles arrangement in each sample. Combined with Chapters 2 and 3's results, it opens a discussion on the polymer dynamics measurements and allows to translate these results in terms of glassy and immobilized polymer thicknesses around the fillers. We can then make the connection between the composition of the model systems (dispersion state of fillers and immobilized polymer thickness) and their mechanical properties (Chapter 5).

Chapitre 1

Bibliographie

Ce chapitre aborde tout d'abord la littérature générale ayant trait aux élastomères renforcés puis présente les principaux résultats obtenus lors des deux thèses précédentes sur ce sujet au laboratoire. A partir de cet état de l'art, la problématique de ce travail de thèse est développée.

Sommaire

1.1 Bibliographie générale sur les élastomères renforcés

Les élastomères sont des réseaux tridimensionnels de chaînes de polymère attachées entre elles par des points de réticulation. Ce sont des systèmes capables d'une grande élasticité mais qui résistent assez mal à la fracture et à l'abrasion. Pour améliorer leurs propriétés, on peut les renforcer en leur incorporant des charges solides, généralement des particules de noir de carbone ou de silice. Cela permet d'améliorer largement leur propriétés mécaniques et d'en faire de très bons candidats pour des applications d'amortissement. Ce sont des systèmes qui sont ainsi largement utilisés dans l'industrie, notamment du pneumatique, et la compréhension du mécanisme de renforcement de ces systèmes est donc un enjeu très important.

Dans cette partie, nous allons d'abord présenter les différents constituants des élastomères renforcés ainsi que leur structure. Ensuite nous aborderons leur comportement mécanique aux faibles et aux grandes déformations ainsi que les différents modèles qui sont proposés dans la littérature pour les expliquer. Enfin, nous nous intéresserons aux deux thèses qui ont été faites précédemment au laboratoire sur ce sujet et à leurs principales conclusions avant d'extraire la problématique qui sera abordée lors de cette thèse.

1.1.1 Les élastomères renforcés

Les élastomères renforcés sont composés d'une matrice élastomère dans laquelle des charges solides, de taille inférieure au micron, ont été dispersées. Nous allons ici décrire les différents composants de ces systèmes ainsi que la façon dont ils sont mis en œuvre puis nous verrons quel type de microstructure ils présentent.

• **Les élastomères**

Les élastomères sont constitués de chaînes de polymère liées entre elles de façon permanente par des points de réticulation. Cette réticulation est généralement obtenue par réaction chimique au niveau des insaturations de la chaîne et s'appelle la vulcanisation.

Élasticité Le réseau ainsi formé possède des propriétés élastiques très importantes. Il peut être étiré de plusieurs fois sa taille et revenir dans sa configuration initiale lorsque la contrainte est relâchée, grâce aux points de réticulation permanents. Cette élasticité est d'origine entropique.

Transition vitreuse Ce comportement élastique se produit à haute température, mais lorsque que la température est diminuée, le réseau subit un ralentissement progressif et son temps de relaxation devient supérieur au temps d'observation de l'expérience. Le système est alors dans un état solide *désordonné* et *hors équilibre* appelé état vitreux. Ce ralentissement a généralement lieu à basse température et s'appelle la transition vitreuse. En dessous de la température de transition vitreuse T_g, les chaînes ont perdu la majeure partie de leur mobilité et le réseau présente de grandes hétérogénéités dynamiques : les temps de relaxation peuvent varier de quatre ordres de grandeur sur des échelles de longueur caractéristiques de quelques nanomètres. La température de transition T_g dépend principalement de la structure chimique du polymère et de la présence de solvant.

Superposition temps-température Lorsque l'on considère le comportement mécanique des élastomères, il est équivalent d'augmenter la fréquence ou de diminuer la température. Cette superposition temps-température est bien décrite par la loi WLF qui donne le facteur à appliquer à la fréquence pour obtenir le module élastique à une température T lorsqu'on connait le module à la température T_{ref}.

$$G(T_{ref}, \omega) = G(T, a_{T/T_{ref}}\omega) \tag{1.1}$$

$$\log a_{T/T_{ref}} = -\frac{C_1(T - T_{ref})}{C_2 + T - T_{ref}} \tag{1.2}$$

où C_1 et C_2 sont des paramètres dépendant de la structure du polymère considéré et de la température de référence choisie T_{ref}. Cette propriétés est très utile pour la construction des courbes maîtresses : à partir de balayages en fréquence effectués à différentes températures, on peut superposer les courbes afin de reconstruire le comportement de l'échantillon sur une plus grande gamme de fréquence.

• **Les charges**

Afin d'améliorer les propriétés de résistance à la fracture et à l'abrasion des élastomères, on incorpore dans la matrice élastomère des charges solides qui peuvent être de différentes natures : il s'agit en général de noir de carbone ou de silice mais d'autres systèmes sont étudiés comme par exemple les argiles ou les nanotubes de carbone. Deux paramètres vont être importants lors de l'incorporation de ces charges dans une matrice élastomère : la géométrie des particules et leurs caractéristiques physico-chimiques de surface.

Structure Les charges incorporées dans les élastomères se présentent généralement sous la forme d'agrégats insécables de particules élémentaires nanométriques. Ces agrégats peuvent interagir et former des agglomérats, mais ces derniers peuvent être détruits lorsqu'ils sont soumis à des sollicitations. Une caractéristique importante de ces charges est leur surface spécifique, c'est-à-dire l'aire de contact qu'elles offrent à l'élastomère après malaxage. Plus elle sera grande et plus le renforcement potentiel de l'élastomère pourra être important. La surface spécifique va notamment dépendre de la compacité des agrégats et se trouve habituellement autour de 100 m^2/g.

Physico-chimie de surface De l'état de surface des charges dépendent les interactions charge-charge et charge-polymère et donc la qualité de la dispersion des renforts dans la matrice. Ces interactions peuvent être de type liaisons hydrogène, liaisons covalentes ou bien liaisons de Van der Waals. La physico-chimie de surface des charges peut être modifiée par différents traitements (plasma, ozone, greffage) et ainsi les interactions entre les charges et avec la matrice peuvent être modulées. Pour les silices, c'est généralement le greffage de molécules à la surface qui est utilisé. Les greffons employés sont des silanes qui sont liés de façon covalente aux silices et permettent soit la limitation des interactions (agent de recouvrement), soit la création de liaisons covalentes avec la matrice polymère (agent de couplage). Dans cette thèse, nous utiliserons ces deux types de greffons.

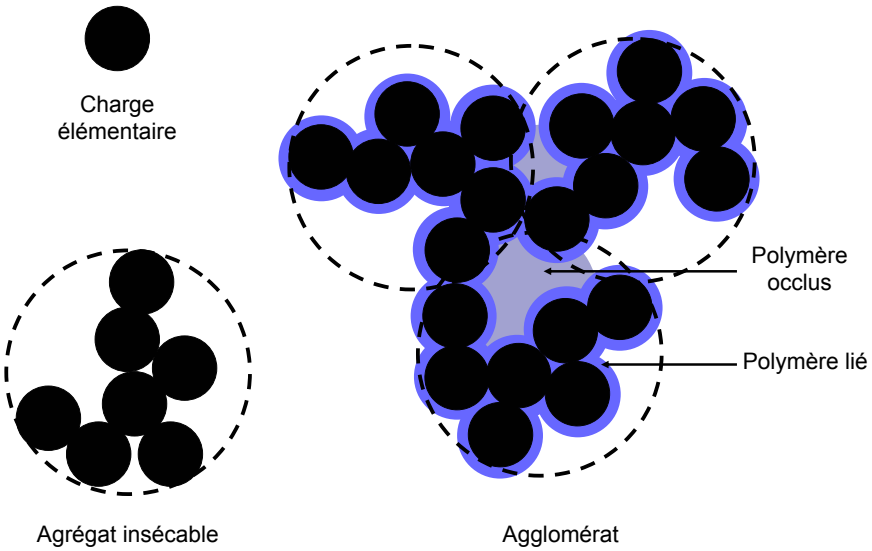

FIGURE 1.1 – Représentation schématique de la structure d'un élastomère renforcé.

• **La mise en œuvre**

Industriellement, l'incorporation des charges dans la matrice polymère se fait par malaxage. C'est une étape très importante puisqu'elle va déterminer l'état de dispersion des charges dans le système, ce qui aura une grande influence sur le comportement mécanique des systèmes. Les malaxeurs appliquent donc de très forts taux de cisaillement afin de briser les agglomérats mais également d'incorporer les autres ingrédients du système (huiles, greffons, etc). Dans ce travail, nous utiliserons des échantillons modèles synthétisés au laboratoire. La polymérisation de l'élastomère sera faite en masse, autour de particles de silice sphériques et monodisperses. Cela permettra de beaucoup mieux contrôler l'état de dispersion des charges et d'éviter la présence d'agrégats.

• **La microstructure des élastomères renforcés**

La microstructure des élastomères renforcés est schématisée en Figure 1.1

Agrégats et réseau de charges Une fois dispersées dans la matrice élastomère, les charges se trouvent généralement encore sous la forme d'agrégats. Si la fraction volumique de charges est assez importante, ces agrégats peuvent former à travers l'échantillon un réseau continu de charges. Il y a alors percolation du réseau de charges et les propriétés mécaniques du système changent de façon significative. Le seuil de percolation peut être mis en évidence par des mesures mécaniques ou électriques si les charges sont conductrices.

Polymère occlus La présence d'agrégats et d'agglomérats laisse entrevoir qu'une partie du polymère peut être piégée à l'intérieur de ces structures. Ce polymère occlus n'est donc pas

sollicité lors des déformations subies par le système et peut donc augmenter la fraction apparente de renfort dans le système. Cette notion est couramment utilisée pour expliquer le très fort renforcement mesuré dans les élastomères chargés. Nous ne l'utiliserons pas ici, d'une part à cause du bon état de dispersion obtenu dans nos systèmes qui limite la quantité de polymère occlus, et d'autre part car nous privilégierons le rôle joué par le polymère lié.

Polymère lié En effet, lorsque des élastomères renforcés (non réticulés) sont dissous dans un solvant, une partie du polymère ne peut être extraite. Ces chaînes sont donc liées aux charges, soit par interaction chimique (liaisons covalentes) soit par interaction physique (liaisons hydrogène ou de Van der Waals). Par ailleurs, des mesures RMN montrent qu'une partie du polymère a une dynamique très ralentie par rapport à des chaînes libres. Cependant, le lien entre polymère lié et polymère ralenti n'est pas clairement établi. La présence de ces chaînes liées va avoir une influence sur les propriétés mécaniques des élastomères renforcés. Notamment, le réseau de charges précédemment évoqué peut ainsi se faire soit par interaction directe des charges entre elles, soit par l'intermédiaire du polymère lié. Nous verrons dans le paragraphe suivant d'autres conséquences que peuvent avoir ces chaînes liées sur le comportement mécanique des systèmes.

1.1.2 Propriétés mécaniques en cisaillement

Nous allons maintenant discuter des propriétés mécaniques des élastomères renforcés. Nous allons principalement considérer les propriétés mécaniques mesurées en cisaillement sinusoïdal. En effet, nous nous intéressons à l'application des élastomères renforcés dans le domaine des pneumatiques, où ils sont sollicités de façon cyclique.

Les élastomères renforcés présentent un comportement viscoélastique. Lorsque la déformation appliquée est de la forme

$$\gamma(t) = \gamma_0 sin(\omega t) \tag{1.3}$$

la contrainte mesurée est une sinusoïde déphasée que l'on peut décomposer en deux termes :

$$\begin{aligned} \sigma(t) &= \sigma_0 sin(\omega t + \delta) && (1.4)\\ &= \sigma_0 sin(\omega t) cos\delta + \sigma_0 cos(\omega t) sin\delta && (1.5)\\ &= \frac{\sigma_0 cos\delta}{\gamma_0}\gamma(t) + \frac{\sigma_0 sin\delta}{\gamma_0}\frac{\dot{\gamma}(t)}{\omega} && (1.6) \end{aligned}$$

La partie de la contrainte en phase avec la déformation est ainsi la partie élastique et l'on note $G' = \frac{\sigma_0 cos\delta}{\gamma_0}$ le module élastique, tandis que la partie en quadrature avec la déformation est la partie visqueuse et l'on note $G'' = \frac{\sigma_0 sin\delta}{\gamma_0}$ le module visqueux. Le ratio entre ces deux modules correspond au facteur d'amortissement $\tan\delta = G''/G'$, ce qui correspond au ratio entre l'énergie dissipée et l'énergie stockée.

Nous allons voir comment évoluent ces paramètres lorsque des charges sont incorporées à un élastomère. Pour cela, nous allons successivement aborder le comportement des élastomères renforcés dans le régime linéaire, domaine de déformation où G' et G'' sont indépendants de l'amplitude de déformation imposée, puis dans le régime non linéaire.

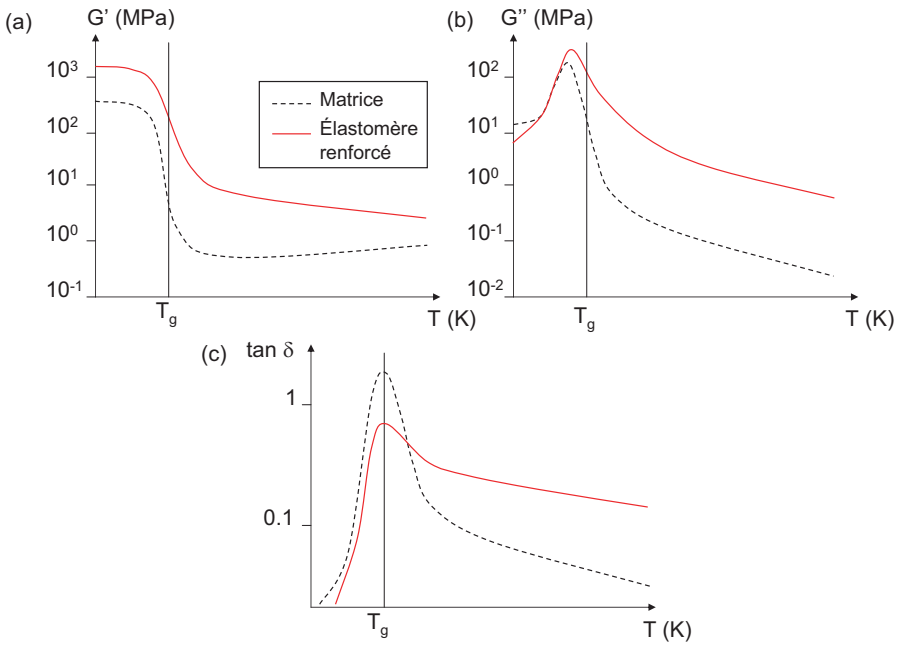

FIGURE 1.2 – Évolution des modules élastique (a) et visqueux (b) et du facteur d'amortissement (c) avec la température pour un élastomère pur et un élastomère renforcé.

• **Effet du renforcement sur les propriétés en température dans le régime linéaire**

Le régime linéaire est le domaine où les modules élastiques et visqueux ne dépendent pas de l'amplitude de la déformation imposée.

Si l'on regarde le comportement en température d'un élastomère pur, on observe une forte augmentation du module élastique lorsque la température diminue : c'est la transition vitreuse. Cette transition correspond à un maximum de G'' et de $\tan\delta$. A basse température, le système est dans un état rigide désordonné avec un module élastique $G' \simeq 10^9$ Pa et à haute température c'est un élastomère avec $G' \simeq 10^6$ Pa. Dans le domaine élastomère, le module élastique augmente linéairement avec la température à cause de l'origine entropique de l'élasticité.

Etalement de la transition vitreuse Lorsque des charges sont incorporées, la transition vitreuse se fait sur un domaine de température plus étendu : la diminution du module élastique s'étale aux hautes températures (Figure 1.2).

Renforcement Quelle que soit la température, l'ajout de charges solides induit une augmentation très significative du module élastique de l'échantillon, ainsi qu'une augmentation de son module visqueux. Pour ce qui est du facteur d'amortissement $\tan\delta$, il est diminué à basse température mais augmenté à plus haute température. A haute température l'élastomère chargé dissipe donc plus d'énergie que l'élastomère. Remarquons également que le renforcement est plus important dans le domaine élastomère que dans le domaine vitreux. De plus, à $T > T_g$, le module élastique de l'élastomère chargé décroît avec la température, contrairement à l'élastomère pur. On voit ainsi que l'élasticité du matériau n'est plus uniquement d'origine entropique.

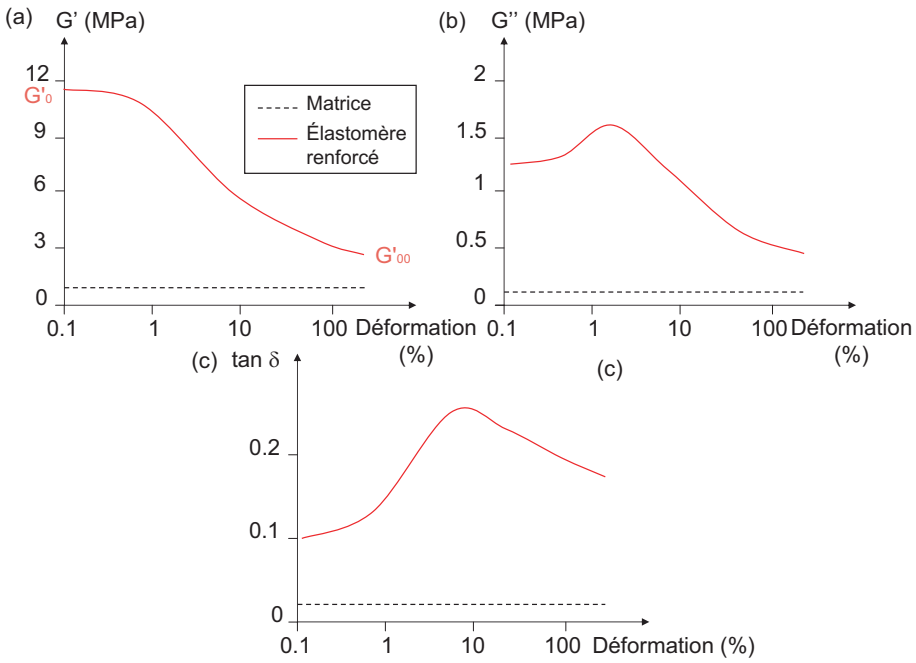

FIGURE 1.3 – Évolution des modules élastique (a) et visqueux (b) et du facteur d'amortissement (c) avec l'amplitude de la déformation pour un élastomère pur et un élastomère renforcé.

Influence des caractéristiques des échantillons L'amplitude du renforcement observé dépend des caractéristiques des échantillons considérés. Plus la fraction volumique de renfort augmente et plus les effets décrits précédemment sont marqués : le renforcement est plus important et l'étalement de la transition vitreuse est plus significatif. Un autre paramètre important est l'état de dispersion des charges : plus la dispersion est de bonne qualité et plus les propriétés des élastomères chargés se rapprochent de celles de l'élastomère pur. Les interactions charge-charge et charge-polymère vont également avoir une influence, principalement car elles vont déterminer l'état de dispersion du système. Si les interactions charge-polymère sont plus importantes que celles entre les charges, les particules auront tendance à être mieux dispersées et donc les propriétés mécaniques se rapprocheront de celles de l'élastomère pur.

- **Effet du renforcement sur les propriétés en déformation**

Regardons à présent l'influence des charges sur les propriétés mécaniques des élastomères renforcés lorsque l'on augmente l'amplitude des déformations imposées. Les propriétés mécaniques d'un élastomère pur ne dépendent pas de l'amplitude de la déformation imposée jusqu'à une centaine de pour-cent de déformation. En revanche, pour un élastomère renforcé, les propriétés peuvent varier très fortement à partir d'amplitudes de déformation inférieures au pour cent, c'est le régime non linéaire.

Description de l'effet Payne L'évolution des modules dynamiques avec l'amplitude de déformation est décrite en Figure 1.3. On constate que le module élastique décroît très fortement avec l'amplitude de déformation. A faible déformation, le module présente un plateau à G'_0 qui correspond au module dans le domaine élastomère discuté dans la section précédente. A plus

haute déformation, le module diminue jusqu'à se stabiliser à une valeur G'_∞. Ce phénomène est appelé effet Payne et est observé dans de nombreux matériaux divisés. Simultanément, le module visqueux passe par un maximum, ce qui traduit une dissipation d'énergie lors de ce processus. Un comportement similaire est observé pour le facteur d'amortissement.

On peut se demander si la forme de décroissance du module élastique avec l'amplitude de déformation est universelle. Payne a montré que les courbes obtenues pour différents systèmes (différentes charges, polymères, fractions de renfort) pouvaient être superposées en traçant le module réduit [3]

$$G'_r(\gamma_0) = \frac{G'_r(\gamma_0) - G'_\infty}{G'_0 - G'_\infty} \tag{1.7}$$

Il est aussi important de noter que même si les modules mesurés dépendent de l'amplitude de la déformation appliquée, les signaux de contrainte mesurés sont toujours quasi-sinusoïdaux [4]. Ceci peut paraître surprenant puisque le module dépend de la déformation, ce qui laisserait penser que la réponse du système pourrait être non linéaire à l'intérieur de chaque cycle de déformation. Dans ce sens, on peut dire que le comportement du système est linéaire pour chaque amplitude de déformation.

Influence des conditions expérimentales L'effet Payne est sensible à la température et à la fréquence de sollicitation, principalement par l'intermédiaire de la valeur du module aux faibles déformations G'_0, tandis que G'_∞ varie peu. Lorsque la température augmente, nous avons vu que G'_0 diminuait, ce qui fait diminuer l'amplitude de l'effet Payne. La température modifie également l'amplitude de la déformation à partir de laquelle le module élastique commence à décroître. L'effet de la fréquence se fait également sentir sur la valeur de G'_0. La valeur de G'_0 augmente avec la fréquence et donc l'amplitude de l'effet Payne également [3, 4].

L'histoire mécanique subie par l'échantillon est également importante dans la description de l'effet Payne, notamment les amplitudes de déformation subies précédemment. En effet, les courbes de modules obtenues après un premier balayage en déformation ne sont pas reproductibles par un deuxième balayage. En revanche les deuxième, troisième balayages et les suivants sont superposables à condition d'attendre assez longtemps entre chaque.

Influence des caractéristiques des échantillons Comme précédemment, la structure des élastomères renforcés va avoir une influence sur le comportement des échantillons dans le régime non linéaire. La structure va principalement agir sur la valeur de G'_0 et aura peu d'influence sur G'_∞. L'augmentation de la fraction volumique de renfort ou de sa surface spécifique fait augmenter G'_0 et donc l'amplitude de l'effet Payne. La force des interactions particule-particule et particule-polymère vont influer sur G'_0 principalement par l'intermédiaire de l'état de dispersion. Plus la dispersion est bonne, plus G'_0 est faible et donc moins l'effet Payne est important.

1.1.3 Interprétations : interactions particule-particule vs particule-polymère

Plusieurs modèles ont été proposés pour expliquer ces observations. Les premiers sont des modèles hydrodynamiques se basant simplement sur l'effet géométrique de l'ajout d'une fraction solide dans une matrice molle. D'autres modèles mettent l'accent sur l'importance des interactions particule-particule et expliquent ces phénomènes par la formation d'un réseau de charges. Enfin

un troisième groupe de modèles met plutôt l'accent sur le rôle du polymère adsorbé à la surface des charges et son éventuelle immobilisation.

• Modèles hydrodynamiques

Ces modèles trouvent leur origine dans la formule proposée par Einstein pour modéliser la viscosité d'une suspension de particules rigides sphériques dans un milieu de viscosité η_0 [5]

$$\eta = \eta_0(1 + 2.5\phi) \tag{1.8}$$

avec ϕ la fraction volumique de particules. Cette formule a ensuite été étendue aux modules d'Young par Smallwood [6], puis Guth et Gold [7] ont introduit un terme du second ordre dans cette expression pour pouvoir l'appliquer à des suspensions plus concentrées. Enfin, Guth [8] a proposé l'ajout d'un facteur de forme f pour tenir compte de l'éventuelle anisotropie des charges :

$$E = E_0(1 + 0.67f\phi + 1.62f^2\phi^2) \tag{1.9}$$

Mais cette expression sous-estime largement les valeurs de renforcement si l'on ne tient compte que de la fraction de charges solides introduites. De plus, cette formule ne peut expliquer la décroissance du module des élastomères renforcés avec la température quand celui des élastomères purs croît de façon linéaire.

• Rôle du réseau de charges

L'interprétation proposée par Payne pour expliquer le comportement des élastomères renforcés se base sur les interactions particule-particule [3]. Lorsque ces interactions sont fortes, elles permettent la création d'un réseau de charges percolant qui est responsable du très important renforcement observé. Par ailleurs, à fortes déformations, ce réseau se casse ce qui peut expliquer la diminution du module élastique. Ce modèle de désagglomération du réseau implique une dissipation d'énergie qui peut expliquer le maximum de G''.

Ce raisonnement basé sur le rôle du réseau de charges a été formalisé par Kraus [9] qui a modélisé le taux d'agglomération - désagglomération d'un réseau de particules de noir de carbone liées entre elles par des interactions de Van der Waals. C'est un modèle phénoménologique basé sur la cinétique de création et rupture des contacts entre les charges. Il rend bien compte de la diminution du module avec l'amplitude de déformation par la diminution du nombre moyen de contacts. Par contre la dissipation d'énergie est moins bien décrite.

Ce modèle a ensuite été dérivé sous diverses formes qui tiennent compte du caractère fractal du réseau de charges formé par l'association d'agrégats [10, 11]. Ils permettent ainsi d'apporter un caractère plus physique au modèle de Kraus. C'est notamment le cas de Huber et Vilgis [12] qui mettent en avant le fait que la taille moyenne des agglomérats diminue avec l'amplitude de la déformation.

De plus, la structure formée par le réseau crée une fraction de polymère occlus qui n'est pas sollicitée lors des déformations. Medalia prend en compte cette fraction dans la fraction effective de charge pour expliquer le renforcement [13]. Wang utilise également ce concept pour expliquer l'effet Payne par les effets superposés de la destruction du réseau de charge à grande déformation

et de la libération de la gomme occluse qui ne participerait ainsi plus au renforcement [14].

Néanmoins ces modèles phénoménologiques n'expliquent pas les variations de module avec la température et la fréquence. Par ailleurs, Funt a montré par des mesures de conductivité que la présence d'un réseau percolant de charges n'était pas nécessaire à l'observation de l'effet Payne [15]. Il met ainsi en valeur le rôle que peut jouer le polymère adsorbé à la surface des charges.

• Rôle du polymère adsorbé / lié

Ainsi, plutôt que d'insister sur l'importance des interactions particule-particule, d'autres modèles se focalisent plutôt sur les interactions particule-charge et le rôle du polymère adsorbé à la surface des particules. Ce rôle peut être envisagé sous trois angles principaux.

D'abord, le polymère lié peut expliquer le renforcement des échantillons par l'intermédiaire de l'augmentation de la réticulation effective. En effet, l'ancrage des chaînes de polymère sur les charges (par adsorption, liaison hydrogène ou liaison covalente), fait que les charges peuvent être considérées comme des points de réticulation multifonctionnels. Maier et Göritz [16] proposent un modèle se basant sur cette considération pour expliquer l'effet Payne. La diminution du module avec l'amplitude de déformation serait due à un phénomène d'adsorption-désorption des chaînes à l'interface. Plusieurs types de jonctions sont considérées dans ce modèles : les jonctions permanentes (points de réticulation chimique), les jonctions fortes (chaînes de polymère ayant plusieurs points d'ancrage sur les charges) et jonctions faibles (chaînes ayant peu de points d'adsorption). La densité de liens atteint alors un équilibre pour chaque amplitude de déformation qui diminue lorsque l'amplitude augmente. La dissipation d'énergie au cours de chaque cycle est, quant à elle, attribuée au glissement des chaînes à la surface des charges. Par ailleurs la diminution du module avec la température en régime linéaire s'explique également par une diminution du nombre de liens avec l'agitation thermique. Dans un autre modèle, Funt explique le renforcement par l'enchevêtrement du polymère lié avec le polymère libre, ce qui aurait également pour effet l'augmentation de la densité de réticulation effective [15]. L'effet Payne, quant à lui, s'expliquerait par leur désenchevêtrement. Néanmoins, ces interprétations négligent le rôle pourtant important du réseau de charges et de l'agglomération.

Il est donc intéressant de combiner les deux aspects vus précédemment pour tenir compte à la fois du phénomène d'agglomération-désagglomération du réseau de charges et de l'adsorption - désorption des chaînes à la surface des particules. Le polymère adsorbé peut ainsi être considéré comme une phase intermédiaire permettant la formation du réseau de charges. Il contribue alors à la formation d'un réseau percolant et les mécanismes d'agglomération-désagglomération évoqués dans la section précédente restent valables. Chabert montre en effet que le renforcement peut s'expliquer par un réseau de charges formé par l'intermédiaire du polymère confiné entre les charges [17], et Klüppel propose une expression du module élastique tenant compte de la couche de polymère lié aux charges [18]. Heinrich et Klüppel mettent également en avant le fait que la dissipation d'énergie ne peut être expliquée uniquement par le changement de conformation du réseau et qu'il faut tenir compte du glissement des chaînes de polymère lié à la surface avec les charges [19].

Enfin, on peut se demander quelle est la nature exacte de ce polymère "lié", dans quel état physique il est. S'il est immobilisé, voire dans un état vitreux, il pourrait contribuer au renforcement au même titre que les charges. C'est ce que nous allons étudier dans la section suivante.

1.1.4 Existence de polymère vitreux à l'interface ?

La difficulté à obtenir un consensus sur les précédentes interprétations provient de l'interdépendance des deux types d'interactions considérées : la modification des charges va à la fois modifier les interactions particule-particule et particule-matrice. Par ailleurs, si ces modèles phénoménologiques décrivent bien la diminution du module élastique avec l'augmentation de la déformation ainsi que l'effet du taux de charges, ils ne parviennent pas à décrire l'influence de la température ou de la fréquence. Pour résoudre ce problème, il faut prendre en compte la modification du comportement des chaînes de polymère à proximité des charges.

• Nature du polymère à la surface des particules

Comme nous l'avons vu précédemment, les chaînes à proximité des charges ont une dynamique plus lente que des chaînes libres. Une des questions posées concerne la nature vitreuse ou non de ces chaînes.

Des chaînes ralenties Des mesures RMN sur les élastomères renforcés ont pu montrer l'existence de chaînes de polymère ayant une mobilité moins importante que celle de l'élastomère pur [20–25]. Kaufman a, en particulier, pu identifier trois régions avec des mobilités différentes : une région mobile loin des particules, une coquille extérieure avec une mobilité moins importante et une coquille interne avec une mobilité très faible. La couche de polymère lié se divise donc en deux parties : une partie fortement liée (proche de la surface) et une partie faiblement liée plus externe qui serait composée de chaînes en partie prise dans la zone fortement liée. Des mesures calorimétriques sur des nanocomposites ont également confirmé l'existence de polymère immobilisé. Ruggerone *et al.* [26] constatent une diminution de la hauteur du saut de chaleur spécifique (ΔC_p) à la transition vitreuse avec l'augmentation de la quantité de charges. Cette observation est interprétée en termes de couche de polymère immobilisé à la surface des charges.

La diminution de mobilité des chaînes à la surface des charges peut être interprétée de différentes manières. Comme nous l'avons vu précédemment, on peut considérer que les points d'ancrage des chaînes sur les charges constituent des points de réticulation supplémentaires, ainsi la diminution de mobilité peut être attribuée à l'augmentation de la densité de réticulation effective autour des charges. Mais d'autres auteurs considèrent que c'est en fait la dynamique même des chaînes qui est ralentie, et que l'immobilisation des chaînes ne correspond pas à une surréticulation mais à un état vitreux. Cette hypothèse est supportée par plusieurs types de mesures.

Mesures thermo-mécaniques et vieillissement physique C'est tout d'abord Struik qui a formulé cette hypothèse à partir de mesures de vieillissement physique [27]. Pour un élastomère pur, un phénomène de vieillissement n'est observé que lorsque la température est inférieure à la température de transition vitreuse T_g. Struik a mis en évidence un vieillissement des élastomères renforcés au-dessus de T_g, montrant ainsi la présence de polymère vitreux dans ces systèmes, même au dessus de T_g.

Mesures mécaniques D'autres auteurs ont montré la présence d'une couche de polymère immobilisé autour des charges en étudiant les propriétés mécaniques de ces systèmes renforcés. Tsagaropoulos et Eisenberg [28] ont montré la présence de deux pics de tanδ en fonction de la température pour les systèmes chargés. Selon leur interprétation, un de ces pics correspond à celui observé dans l'élastomère pur mais avec une amplitude plus faible - signifiant qu'une partie des chaînes ne participe pas à la transition vitreuse - et l'autre apparaît à une température plus élevée et est attribué à la transition vitreuse de chaînes ayant une mobilité réduite.

Étude des films minces de polymère Pour vérifier cette hypothèse et connaitre l'influence de la proximité d'une surface solide sur des chaînes de polymère, il est intéressant d'étudier le comportement de films minces de polymères déposés sur des substrats [29, 30]. Fryer *et al.* ont ainsi pu montrer que la T_g de films minces de PMMA dépend de l'épaisseur du film et des interactions avec le substrat. Dans le cas d'interactions fortes, T_g augmente quand l'épaisseur du film diminue. Pour des interactions faibles, T_g va au contraire avoir tendance à diminuer. Cette augmentation de T_g à la proximité de la surface solide pourrait ainsi expliquer la présence de polymère vitreux autour des charges.

• Interprétation du comportement des élastomères renforcés par la présence de polymère vitreux

L'existence de polymère vitreux autour des particules peut expliquer les principaux aspects du comportement des élastomères renforcés, comme cela est envisagé par Wang [14]. Cette couche de polymère étant rigide, elle augmente la fraction effective de renfort et peut donc expliquer le renforcement dans le cadre d'un modèle hydrodynamique. Un autre paramètre important dans l'explication du renforcement est le recouvrement des couches de polymère vitreux de charges voisines. En effet, ces couplages mécaniques peuvent expliquer un sur-renforcement (Figure 1.4). Par ailleurs, la fraction de polymère vitreux étant dépendante de la température et de la fréquence, on s'attend bien à des comportements différents en fonction de ces deux paramètres. Lorsque la température augmente, la quantité de polymère vitreux diminue, ce qui peut expliquer la diminution du module élastique. De même lorsque la fréquence augmente, le module du polymère vitreux ou proche de la transition augmente, ce qui peut provoquer une augmentation du module élastique du nanocomposite.

Wang explique néanmoins l'effet Payne par un effet classique de rupture de réseau de charges (liées entre elles directement ou par l'intermédiaire du polymère vitreux). Il n'envisage pas les effets de l'application de fortes déformations sur le polymère à l'état vitreux. Cette idée sera soulevée lors de deux thèses précédemment effectuées au laboratoire, que nous verrons plus en

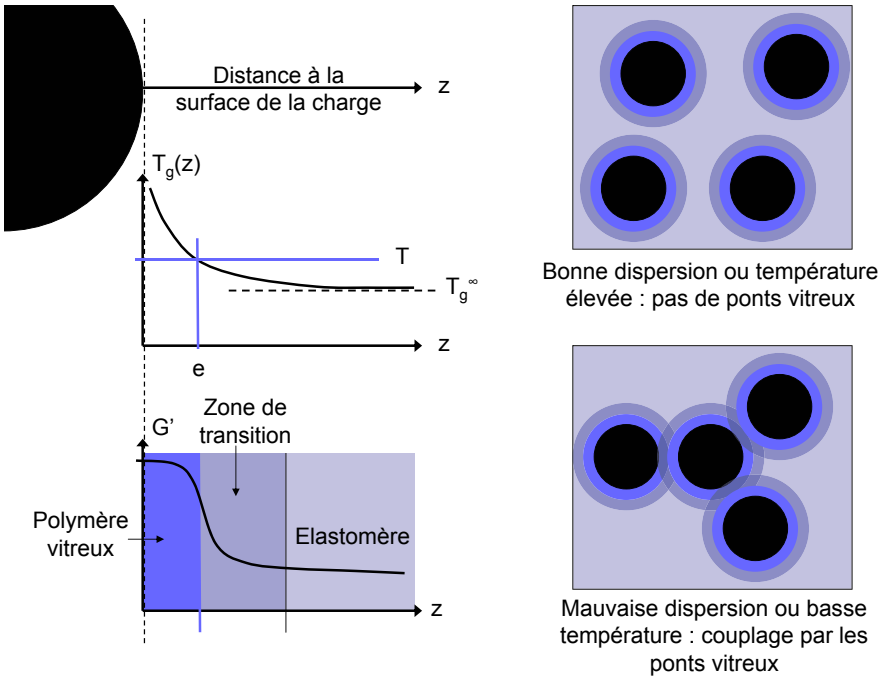

FIGURE 1.4 – Représentation schématique d'un gradient de température de transition vitreuse autour des charges.

détails dans la section suivante [1, 2]. Dans ces études, la quantité de polymère immobilisé est déterminée par RMN et un modèle de gradient de T_g basé sur les résultats obtenus par Fryer *et al.* [30] sur les films minces de polymère est utilisé [31]. Dans ce modèle, la température de transition vitreuse à une distance z d'une surface solide s'écrit :

$$T_g(z) = T_g^\infty \left(1 + \left(\frac{\delta}{z}\right)^\nu\right) \tag{1.10}$$

avec T_g^∞ la température de transition vitreuse du polymère en masse, δ la distance caractéristique du gradient (de l'ordre du nm) et ν un exposant proche de l'unité (0.88), que nous prendrons égal à 1 dans la suite. L'épaisseur de polymère vitreux attendue est donc e telle que $T_g(e) = T$, soit

$$e = \delta \frac{T_g^\infty}{T - T_g^\infty} \tag{1.11}$$

Lors de ces études, il a été montré qu'une courbe maîtresse était obtenue lorsque le renforcement était tracé en fonction de $\frac{T_g^\infty}{T-T_g^\infty}$ pour $T > T_g + 50K$ [32]. Ainsi le renforcement à haute température ne semble dépendre que de l'épaisseur de polymère vitreux. L'effet Payne, quant à lui, peut s'expliquer par la plastification des ponts vitreux [33]. En effet, si des ponts vitreux lient les particules entre elles, il y a formation d'un squelette rigide au travers de l'échantillon qui concentre toutes les contraintes subies. Les contraintes maximales sont obtenues entre les particules et si elles dépassent une contrainte seuil, une plastification peut s'opérer et ainsi conduire à la diminution du module élastique de l'échantillon. Dans cette hypothèse l'état de dispersion est important puisqu'il détermine la présence ou non de ponts vitreux entre les particules. La comparaison de systèmes ayant les mêmes caractéristiques physico-chimiques mais des état de

dispersion très différents vient appuyer cette interprétation (voir en ennexe la référence [34]). Dans le cas de systèmes mal dispersés, les distances entre particules voisines sont faibles et conduisent à la création de ponts vitreux. Sur ces systèmes, un effet Payne très important est observé. En revanche, dans le cas de systèmes bien dispersés, la distance entre particules voisines est trop grande par rapport à l'épaisseur de polymère vitreux et il n'y pas de formation de ponts vitreux. Dans ce cas, l'amplitude de l'effet Payne observé est très faible. Néanmoins, il est important de remarquer que ce modèle n'utilise finalement pas directement la notion de *gradient* de T_g. Il s'agit en fait d'une approximation cœur-coquille de ce gradient, valable uniquement à haute température quand le gradient est très abrupt.

• Une interprétation contestée

L'interprétation du comportement des élastomères renforcés par l'existence de polymère vitreux n'est pas consensuelle. Tout d'abord, sur les films minces de polymère, Kremer *et al.* prétendent qu'il n'y a pas de variation significative de T_g avec l'épaisseur des films minces déposés [35–38]. Ils attribuent les précédentes variations mesurées à une contrainte résiduelle lors de la préparation des échantillons. Dans leur étude, cette contrainte est supprimée par une étape de recuit à haute température. Une discussion de ces résultats et plus généralement de l'effet du confinement sur la T_g est proposée par McKenna [39]. Il montre que les mécanismes proposés par Kremer *et al.* pour expliquer les changements de T_g mesurés par d'autres groupes (problème de recuit, présence de solvant, dégradation chimique) ne peuvent pas rendre compte quantitativement des résultats obtenus. Cependant aucun consensus n'a encore été atteint sur le fait que les variations de T_g mesurées sur des films minces soient dus à de réels effets de confinement, ou bien à d'autres phénomènes.

Par ailleurs, l'interprétation des résultats de Tsagaropoulos et Eisenberg est remise en cause par Robertson *et al.* [40]. Ces derniers attribuent le second pic de $\tan\delta$ à une restriction de l'écoulement des chaînes adsobées à la surface des charges, et non pas à une modification de leur dynamique et donc de leur T_g. Ce serait donc la diffusion et la reptation des chaînes adsorbées qui seraient inhibées, sans que cela n'influe significativement sur la dynamique des chaînes. Le renforcement, quant à lui, serait principalement dû au réseau formé par les charges, sans avoir à faire intervenir l'immobilisation d'une partie du polymère [41]. Enfin, Ackoar *et al.* [42, 43] évoquent également le rôle prépondérant du réseau formé par les charges dans le comportement des élastomères chargés et la nécessité d'une percolation des charges pour obtenir un renforcement significatif. Le rôle de la matrice serait donc très mineur mais les chaînes de polymère adsorbées seraient importantes dans la création de ponts entre les particules, et donc dans la formation d'un réseau percolant.

- **Quelles difficultés d'interprétation ?**

Nous voyons ainsi qu'il n'existe pas de consensus sur l'origine du comportement particulier des élastomères renforcés. En particulier, le rôle des chaînes à proximité des charges semble important mais est encore assez mal explicité. La nature de ces chaînes, leur caractère vitreux ou non, est encore mal définie. Les différentes visions exposées précédemment montrent bien la difficulté à interpréter les résultats et mettent l'accent sur plusieurs points dont le contrôle est critique lors de l'étude des élastomères renforcés :

- la maîtrise des systèmes étudiés : les interactions particule - particule et particule - polymère doivent être bien contrôlées,
- l'état de dispersion des charges dans l'échantillon,
- la quantification du polymère immobilisé/adsorbé
- et l'influence de tous ces éléments sur le comportement mécanique des échantillons.

Nous allons voir dans la section suivante comment ces points ont été abordés lors de deux thèses précédentes au laboratoire.

1.2 Les thèses précédentes au laboratoire

Deux thèses ont déjà porté sur l'étude des propriétés mécaniques des élastomères renforcés au laboratoire : d'abord celle de Julien Berriot (2003) [1], suivie de celle de Thomas Chaussée (2008) [2]. Elles ont notamment permis la mise au point de systèmes modèles avec une architecture bien contrôlée, permettant ainsi une interprétation plus claire des résultats. Le travail présenté ici prend la suite directe de ces études et les échantillons étudiés sont ceux qui ont été synthétisés et caractérisés par Thomas Chaussée. Dans cette section nous allons donc rappeler les principaux résultats de ces précédents travaux.

1.2.1 Mise au point de systèmes modèles

Une des particularités de l'étude des élastomères renforcés au laboratoire est l'utilisation de systèmes modèles avec une architecture bien contrôlée. La mise au point de ces systèmes s'est faite au long des deux thèses précédentes. Ils se composent d'une dispersion de nanoparticules de silice monodisperses fonctionnalisées dans une matrice de poly(acrylate d'ethyle) (PEA). Ces systèmes permettent une meilleure compréhension que des systèmes industriels obtenus par malaxage puisqu'ils ne comportent ni additifs, ni agrégats et que la dispersion des charges est bien contrôlée. Pour obtenir un bon contrôle de la dispersion, la polymérisation est faite en présence des particules de silice. Pour cela, les charges doivent être stables et ne pas s'agréger, c'est pourquoi elles sont d'abord recouvertes d'un greffon. Le greffon, en plus de permettre la stabilisation des particules, permettra également de moduler l'interaction charge-matrice.

Synthèse des particules de silice

La première étape de la synthèse est la fabrication de particules sphériques de silice selon la méthode Stöber [44]. Elle se fait par hydrolyse - condensation du TEOS (TetraEthyl OrthoSilicate) en milieu basique :

$$\text{hydrolyse} \qquad Si(OC_2H_5)_4 + 4H_2O \longrightarrow Si(OH)_4 + 4C_2H_5OH \tag{1.12}$$

$$\text{condensation} \qquad Si(OH)_4 \longrightarrow SiO_2 + 2H_2O \tag{1.13}$$

$$\text{bilan} \qquad Si(OC_2H_5)_4 + 2H_2O \longrightarrow SiO_2 + 4C_2H_5OH \tag{1.14}$$

Cette synthèse se fait à partir d'une solution de TEOS dans l'éthanol en présence d'ammoniac et d'eau. Pour obtenir des silices bien monodisperses, la synthèse se fait en deux étapes : d'abord la nucléation de petites billes puis leur croissance. La croissance des billes de petite taille étant plus rapide que celle de grande taille, la polydispersité est réduite. Les silices obtenues sont de taille nanométrique avec un diamètre compris entre 26 et 83 nm.

Greffage des particules de silice

La réactivité de la surface des silices vient des groupements $-OH$ n'ayant pas réagit lors de la condensation. Ces sites réactifs sont utilisés pour la fonctionnalisation par des silanes. Les deux silanes utilisés dans cette thèse sont le TPM (3-(trimethoxysilyl)propyl methacrylate) et le C8TES (n-octyltriethoxysilane), représentés en Figure 1.5. Le TPM possède une fonction

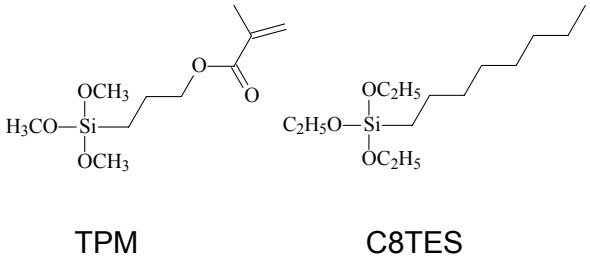

FIGURE 1.5 – Silanes utilisés lors de l'étude : TPM (3-(trimethoxysilyl)propyl methacrylate) et C8TES (*n*-octyltriethoxysilane)

acrylate qui est susceptible de réagir avec le monomère lors de la polymérisation, créant ainsi un lien covalent entre la silice et la matrice polymère. Le greffon C8TES en revanche ne peut pas créer de lien covalent avec le monomère. Dans ce cas, le lien avec la matrice polymère se fait par des liaisons hydrogène entre les fonctions acrylate des chaînes et les groupements $-OH$ résiduels à la surface de la silice.

La réaction entre les silanes et les groupements ethoxys à la surface de la silice se fait en milieu basique :

$$(SiO_2)_nSiO^- + Si(OR)_3R' \longrightarrow (SiO_2)_nSiO - Si(OR)_2R' + RO^- \tag{1.15}$$

Puisque la synthèse de la silice se fait en milieu basique, les silanes sont ajoutés directement dans le milieu réactionnel : dans une suspension à 5 % en masse de silice, une quantité de silane correspondant à 10 molécules par nm^2 de silice est ajoutée. La suspension est agitée pendant 24 heures puis le taux de greffage est contrôlé par analyse élémentaire. Le suivi du ratio du taux de carbone sur taux de silicium avant et après greffage permet de remonter aux taux de greffage. Ils sont compris entre 1.5 et 6 molécules par nm^2 selon les échantillons.

Polymérisation

Pour procéder à l'étape de polymérisation, la silice greffée doit être transférée par dialyse dans le monomère acrylate selon la méthode développée par Ford *et al.* [45–48], puis irradiée sous UV pour provoquer à la fois la polymérisation et la réticulation. Julien Berriot a montré que cette étape pouvait poser problème dans le cas des greffons qui ne créent pas de liaison covalente avec le monomère. En effet les particules de silice ont alors tendance à s'agréger à cause d'un phénomène de déplétion. Pour remédier à cela, Thomas Chaussée a du adapter le protocole de synthèse pour ces échantillons en procédant à une polymérisation en solvant.

Cas des silices avec greffon réactif (TPM) Dans le cas des greffons pouvant réagir avec le monomère, les silices greffées sont transférées par dialyse vers le méthanol puis vers le monomère

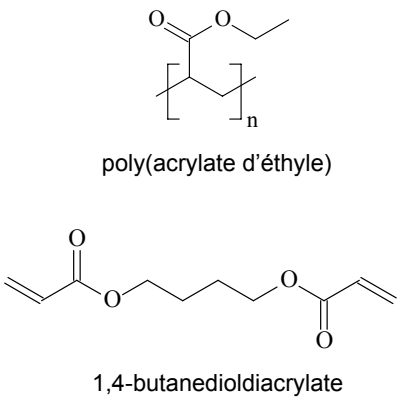

FIGURE 1.6 – Structure chimique du poly(acrylate d'éthyle) et du réticulant (1,4-butanedioldiacrylate) utilisés.

acrylate et on ajuste la concentration finale par dilution. La fraction volumique finale en silice est comprise entre 10 et 30 %. Un initiateur (Irgacure 819, 0.1 % en masse de monomère) et un réticulant (1,4-butanedioldiacrylate, 0.3 % molaire de monomère) sont ajoutés puis la solution est agitée pendant une heure. Elle est ensuite injectée dans un moule en verre et irradiée sous UV pendant une heure. L'échantillon est démoulé et recuit une nuit sous vide à 100 $°C$.

Cas des silices avec greffon non réactif (C8TES) Dans le cas de greffons ne pouvant pas réagir avec le monomère, la polymérisation se fait en solvant pour éviter les phénomènes de déplétion. Les conditions de la réaction ont été ajustées pour obtenir les mêmes propriétés pour une matrice PEA synthétisée en solvant et hors solvant. La suspension de silice greffée est transférée par dialyse vers l'acétone, puis elle est concentrée à environ 35 % en masse. La quantité de monomère suffisante est ensuite ajoutée, puis la quantité de solvant est ajustée par dilution ou évaporation pour obtenir un ratio solvant / monomère de 1. On ajoute 0.1 % en masse de monomère d'initiateur et 1.0 % molaire de monomère de réticulant avant d'irradier sous UV pendant 6 heures dans un moule en verre. L'échantillon est démoulé et le solvant évaporé à température ambiante pendant 24h. On procède ensuite au recuit pendant une nuit sous vide à 100 $°C$.

1.2.2 Mesure de l'état de dispersion des charges

La mesure de l'état de dispersion des particules de silice dans les échantillons se fait par diffusion de neutrons aux petits angles (Small Angle Neutron Scattering - SANS). Un faisceau de neutrons (longueur d'onde de l'ordre de 0.6 nm) est envoyé sur l'échantillon et interagit avec les noyaux des atomes présents dans l'échantillon. L'intensité diffusée par l'échantillon aux petits angles (inférieurs à 5°) est mesurée par un détecteur. Dans le cas d'une suspension de particules sphériques, l'intensité diffusée peut s'écrire :

$$I(q) = \Delta\rho^2 N_p V_p^2 P(q) S(q) \tag{1.16}$$

TABLE 1.1 – Caractéristiques des silices utilisées : diamètre moyen et polydispersité.

Nom	Diamètre moyen D_m (nm)	Facteur de distribution t	Ecart-type σ
MIST	27	50.0	0.51
T30	26	30.3	0.64
T50a	43	52.6	0.63
T50b	41	34.5	0.76
T100	83	71.4	0.76

où $\Delta\rho$ est le contraste de diffusion entre les particules de silice et la matrice polymère (de l'ordre de 3.9 $10^{10} cm^{-2}$), N_p est le nombre de particules diffusantes, ici le nombre de particules de silice, et V_p est le volume d'une particule diffusante. $P(q)$ est le facteur de forme, il décrit la forme, la taille et la polydispersité des particules. $S(q)$ est le facteur de structure et il décrit l'arrangement des particules dans la matrice [49].

Facteur de forme Le facteur de forme s'obtient en mesurant l'intensité diffusée par une solution très diluée de particules sphériques de silice. On peut en déduire la polydispersité des particules de silice grâce un modèle de Schultz :

$$f(D) = \left(\frac{t+1}{D_m}\right)^{t+1} \frac{D^t}{t!} \exp\left(-\frac{t+1}{D_m} D\right) \tag{1.17}$$

où D_m est le diamètre moyen et t est lié à la largeur de la distribution : $\frac{1}{t+1} = \frac{\langle D^2\rangle - D_m^2}{D_m^2}$. L'écart-type est donc donné par $\sigma(D) = \sqrt{\langle D^2\rangle - D_m^2} = \frac{D_m}{\sqrt{t+1}}$ et la polydispersité augmente lorsque t diminue. De plus pour des particules sphériques de diamètre D, le facteur de forme est :

$$P(q, D) = \left(\frac{3(\sin(qD/2) - qD/2\cos(qD/2))}{(qD/2)^3}\right)^2 \tag{1.18}$$

Finalement, le facteur de forme total s'écrit

$$P(q) = \frac{\int_0^\infty (\pi D^3/6)^2 P(q, D) f(D) \mathrm{d}D}{\int_0^\infty (\pi D^3/6)^2 f(D) \mathrm{d}D} \tag{1.19}$$

Un exemple de mesure expérimentale sur une solution diluée de particules de silices est présenté en Figure 1.7. On note la présence d'oscillations, typiques d'une forme sphérique, ainsi qu'une décroissance en q^{-4} aux grands vecteurs d'onde (loi de Porod), ce qui est caractéristique d'interfaces abruptes. L'ajustement de la fonction (1.19) aux mesures expérimentales permet de déterminer le diamètre moyen ainsi que la polydispersité des particules de silice. Un récapitulatif des résultats obtenus pour les silices choisies dans cette étude est présenté Table 1.1.

Facteur de structure Le facteur de structure décrit la position des centres de masse des particules dans la suspension. Il peut être décrit par analogie avec un gaz de sphères dures en

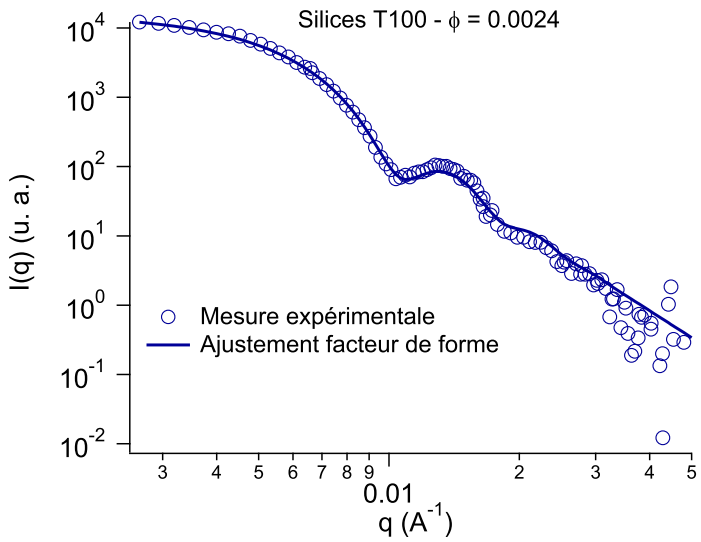

FIGURE 1.7 – Intensité diffusée en SANS par une solution diluée de particules de silice (Silices T100, fraction volumique de 0.0024). Le modèle représenté en trait plein donne un diamètre moyen de 83 nm et un facteur de distribution de $t = 71.4$, soit $\sigma = 0.76$ (Equation 1.19).

utilisant la solution approchée proposée par Percus et Yevick [50] :

$$\frac{1}{S(q)} = 1 + \frac{24\phi}{u^3}\left(a\left(\sin u - u\cos u\right) + b\left[\left(\frac{2}{u^2} - 1\right)u\cos u + 2\sin u - \frac{2}{u}\right]\right) + \frac{24\phi}{u^3}\left(\frac{\phi a}{2}\left[\frac{24}{u^3} + 4\left(1 - \frac{6}{u^2}\right)\sin u - \left(1 - \frac{12}{u^2} - \frac{24}{u^4}\right)u\cos u\right]\right) \quad (1.20)$$

avec ϕ la fraction volumique de particules, $u = qD$, $a = \frac{1+2\phi^2}{(1-\phi)^4}$ et $b = -\frac{3}{2}\frac{\phi(\phi+2)^2}{(1-\phi)^4}$. Ce modèle peut également être utilisé pour décrire des interactions répulsives longue portée qui créent autour des particules l'équivalent d'une coquille impénétrable [51]. Ainsi, le rayon déterminé par l'approximation de Percus-Yevick est égal au rayon de la particule plus la portée de l'interaction. Dans le cas des élastomères renforcés étudiés ici, l'ajustement du modèle de Perkus-Yevick aux données expérimentales donne accès à un rayon effectif des particules supérieur à leur rayon réel. Cela traduit l'existence d'interactions répulsives entre les particules et permet de déterminer la distance minimale entre particules voisines. Un exemple de courbes obtenues est présenté Figure 1.8 et un récapitulatif des caractéristiques des échantillons choisis pour cette étude est donné table 1.2.

Notons cependant que si cette méthode permet d'avoir accès une distance caractéristique, elle ne permet pas d'obtenir une image claire de l'arrangement des charges à l'intérieur de l'échantillon. L'existence ou non d'un ordre n'est par ailleurs pas clairement mis en évidence et la distribution des distances dans l'échantillon ne peut être ainsi obtenue.

Dans le présent travail nous allons décrire plus précisément l'arrangement des charges dans l'échantillon grâce à des simulations Monte-Carlo inverses. A partir du facteur de structure mesuré expérimentalement, nous allons simuler des arrangements de particules pouvant décrire ces mesures.

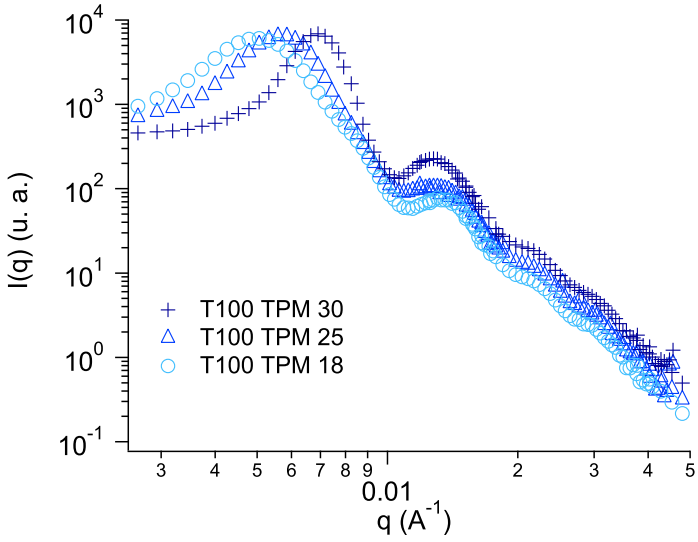

(a)

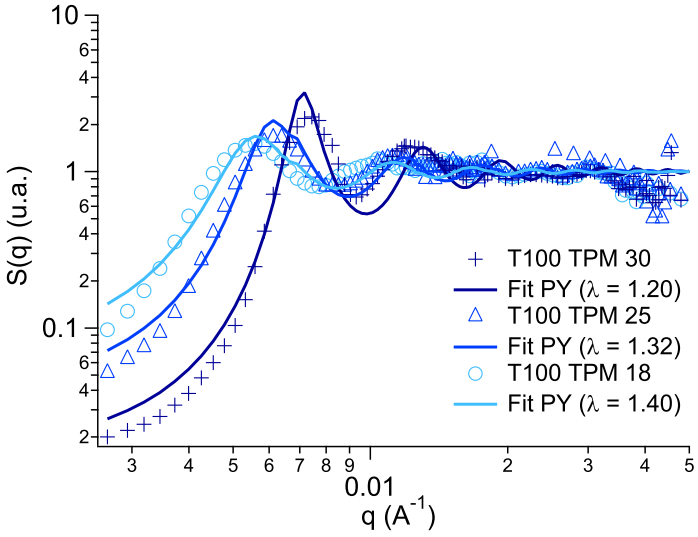

(b)

FIGURE 1.8 – Intensité diffusée en SANS pour les élastomères renforcés T100 TPM 30, 25 et 18 (a) et facteur de structure correspondant (b). Le facteur de structure est obtenu en divisant l'intensité diffusée par le facteur de forme selon l'équation (1.16). Il est ensuite décrit par le modèle de Percus-Yevick (équation (1.20)) et on en déduit le diamètre effectif des particules de silice qui est de $\lambda \times D_m$. Cela correspond à une distance minimale surface à surface entre particules voisines $h = (\lambda - 1)D_m$. On remarque bien que pour une même série d'échantillons renforcés, le premier pic du facteur de structure, caractéristique des distances moyennes entre particules, se déplace vers les plus grands q, *ie* les plus petites distances lorsque la fraction volumique de silice augmente.

1.2.3 Caractérisation de l'adhésion à l'interface : mesures de gonflement

Les mesures de gonflement en bon solvant permettent de mieux décrire les interactions à l'interface silice - polymère selon le type de greffon utilisé [52]. Dans le cas de greffons créant des liaisons covalentes à l'interface, on mesure une restriction du gonflement, alors qu'en l'absence de liaisons covalentes on mesure un gonflement plus important que dans la matrice pure, ce qui traduit une décohésion de la matrice à l'interface avec les charges. Le comportement des systèmes avec liaisons covalentes à l'interface est bien décrit par le modèle de F. Lequeux qui introduit

TABLE 1.2 – Caractéristiques des échantillons renforcés de l'étude. Les distances h données sont des distances surface à surface entre particules voisines.

Nom de l'échantillon	Diamètre moyen de la silice D_m (nm)	Densité de greffage Γ (nm^{-2})	Fraction volumique de silice ϕ_{Si}	Distance moyenne entre particules voisines h (nm)
MIST TPM 30	27	5.0	0.202	4.1
MIST TPM 25	27	5.0	0.163	5.4
MIST TPM 18	27	5.0	0.113	8.1
T50a TPM 30	43	3.2	0.216	11.3
T50a TPM 25	43	3.2	0.147	15.5
T50a TPM 18	43	3.2	0.113	21.0
T100 TPM 30	83	5.0	0.289	16.4
T100 TPM 25	83	5.0	0.174	27.1
T100 TPM 18	83	5.0	0.124	37.0
T30 C8TES 37	26	2.0	0.228	agrégé
T30 C8TES 30	26	2.0	0.169	agrégé
T30 C8TES 25	26	2.0	0.148	21.5
T30 C8TES 18	26	2.0	0.102	24.5
T50b C8TES 44	42	1.5	0.293	6.3
T50b C8TES 30	42	1.5	0.179	12.6
T50b C8TES 25	42	1.5	0.153	14.7
T50b C8TES 18	42	1.5	0.105	21.0

une coquille qui ne gonfle pas autour des particules. Cette coquille est principalement composée de greffons et son épaisseur dépend de la densité de greffage et de la qualité de l'adhésion à l'interface.

1.2.4 Mesure de la dynamique du polymère par RMN ^1H

Les expériences de Résonance Magnétique Nucléaire (RMN) sont particulièrement adaptées à l'étude de la dynamique des chaînes de polymère. En effet, le signal mesuré est celui de retour à l'équilibre d'un système de spins soumis à un champ magnétique intense, ainsi qu'au champ magnétique créé par les spins voisins. Ce signal est donc sensible à l'environnement local et est donc une bonne mesure de la dynamique moléculaire du système. Il est notamment sensible aux différentes contraintes topologiques qui réduisent la mobilité des chaînes : points de réticulation, enchevêtrements, attachement à la surface des particules. L'évaluation de la quantité de ces contraintes topologiques peut se faire par la mesure du temps de relaxation T_2. Dans les élastomères renforcés, trois temps T_2 peuvent être distingués, qui correspondent à trois régions : une couche de polymère immobilisé à la surface des renforts et présentant donc un T_2 très court, une couche intermédiaire de polymère mobile mais toujours lié au renfort avec un T_2 plus long et enfin une zone où le polymère est libre et se comporte donc comme dans la matrice polymère pure avec un temps T_2 encore plus long [53].

Structure du réseau En s'intéressant aux chaînes mobiles, éloignées de la surface des renforts, on peut étudier la structure du réseau de polymère. Les contraintes topologiques subies par ces chaînes induisent une anisotropie résiduelle qui est mesurée par une séquence d'échos de Hahn $(\pi/2, \tau, \pi, acq)$ à $T_g^{RMN} + 100K$. Dans le cas des élastomères renforcés où le greffon ne crée pas de liaison covalente entre la silice et le polymère, aucune modification de la dynamique des chaînes n'est mesurée par rapport à une matrice élastomère pure. En revanche, dans le cas où il existe des liaisons covalentes entre les renforts et le polymère, les fluctuations des chaînes sont restreintes par rapport au cas de la matrice. Dans ce cas, les surfaces de particules agissent comme des jonctions diffuses dans le réseau et la densité effective de jonctions est multipliée par un facteur compris entre 1.5 et 2 [54].

Dans cette thèse nous allons étudier la structure du réseau par une autre méthode RMN appelée Double Quantum (DQ). C'est une technique plus quantitative qui permet une détermination directe des couplages dipolaires résiduels et donc de l'orientation des chaînes de polymère.

Immobilisation des chaînes à l'interface Les chaînes situées aux interfaces avec les renforts étant moins mobiles, leur relaxation a lieu sur des temps plus courts et la séquence la plus adaptée pour leur étude est l'écho solide $(\pi/2, \tau, \pi/2, acq)$. Le signal mesuré est décomposé en deux contributions : c'est le produit d'une gaussienne décrivant le polymère immobilisé et d'une exponentielle correspondant à une phase mobile. En l'absence de liens covalents entre la silice et le polymère, la quantité de polymère immobilisé est plus faible que dans le cas où des liaisons covalentes lient le polymère à la silice. Dans les deux cas, la phase de polymère immobilisé diminue quand la température augmente. Le signal de ce polymère immobile correspond à celui de l'élastomère à $T_g + 5K$. Ce résultat est interprété par l'existence d'un gradient de T_g autour des particules solides. Les épaisseurs de polymère immobilisé mesurées en RMN sont bien décrites par l'approximation cœur-coquille du modèle de gradient de T_g de Long-Lequeux (équation (1.11)) avec une distance caractéristique du gradient de l'ordre de 0.3 nm. Ce n'est donc pas directement la notion de gradient qui est utilisée ici mais une approximation à deux composantes : une composante élastomère et une composante ralentie.

Dans cette étude, nous irons plus loin dans l'interprétation des données RMN avec l'utilisation directe d'un modèle de gradient de T_g. La séquence RMN que nous allons utiliser est le Magic Sandwich Echo (MSE) car elle permet une meilleure refocalisation des interactions dipolaires. Nous interpréterons ensuite les signaux mesurés directement en terme de gradient de T_g autour des charges.

1.2.5 Comportement mécanique : superpositions fréquence - température - fraction volumique

Le comportement mécanique des élastomères renforcés dépend très fortement de l'état de dispersion des particules dans l'échantillon et peut s'expliquer par l'existence d'un gradient de T_g autour des charges [32].

Propriétés mécaniques dans le régime linéaire La mesure des modules viscoélastiques dans le régime linéaire permet de comparer le comportement des élastomères chargés par rapport au comportement de la matrice pure, en fonction de la température et de la fréquence. Pour des

systèmes bien dispersés, on distingue peu de différence entre les systèmes chargés et non chargés. Dans le cas où la dispersion est moins bonne, avec la présence d'agrégats, on constate que la transition vitreuse est élargie vers les hautes températures et la loi WLF ne peut plus s'appliquer. Le renforcement - ratio du module élastique de l'élastomère chargé sur celui de la matrice pure - présente un pic asymétrique à environ $T_g + 10K$. L'augmentation du renforcement est très rapide aux basses températures et diminue lentement aux hautes températures. L'intensité du pic diminue avec la qualité de la dispersion des charges, l'augmentation de la température ou la diminution de la fréquence.

Une partie de ces observations peuvent également être interprétées par la présence d'un gradient de T_g autour des charges. Là encore, c'est en fait une approximation cœur-coquille du modèle de gradient de T_g qui est utilisée et qui n'est valable qu'à haute température. L'épaisseur de polymère vitreux déduite de ce modèle est donnée par l'équation (1.11) et est proportionnelle à $T_g^\omega/(T - T_g^\omega)$. Cette épaisseur varie donc avec la température et la fréquence et participe au renforcement tout comme les charges solides. Dans le cas des systèmes bien dispersés, des courbes maitresses sont obtenues lorsque le renforcement est tracé en fonction d'une fraction volumique effective de charges tenant compte du polymère vitreux. De plus, lorsque le renforcement est tracé en fonction de $T_g^\omega/(T - T_g^\omega)$, des courbes maîtresses sont également obtenues pour les hautes températures ($T > T_g + 50K$) [55]. A plus basse température en revanche, le gradient de T_g ne peut plus être approximé par une simple coque vitreuse et la superposition ne fonctionne plus. Le comportement des élastomères renforcés n'est donc pas décrit dans la zone de transition vitreuse.

Propriétés mécaniques dans le régime non linéaire : effet Payne Là encore l'état de dispersion est très important. L'amplitude de l'effet Payne et son apparition à de faibles déformations sont d'autant plus importantes que les charges sont moins bien dispersées dans la matrice. Cela peut s'interpréter par l'existence de couches vitreuses autour des charges qui peuvent former des ponts vitreux entre les particules. Ces ponts sont soumis à une forte amplification de contrainte et peuvent se plastifier, ce qui peut expliquer l'effet Payne [33, 34]. Par ailleurs, T. Chaussée a montré que cette non linéarité était supprimé dans le cas de l'ajout de solvant. Cela peut être corrélé à la diminution de l'épaisseur de couche vitreuse mesurée en RMN en présence de solvant et donc à la disparition des ponts vitreux.

Dans ce travail, nous allons utiliser une description plus précise des signaux mécaniques afin de voir si l'on peut y trouver des traits caractéristiques de la présence de polymère vitreux. Pour cela, nous ferons une analyse des signaux mécaniques en Large Amplitude Oscillatory Shear (LAOS) que nous interpréterons ensuite grâce au modèle de S. Merabia, P. Sotta et D. Long [].

1.3 Problématique

Cette thèse va porter sur trois axes principaux :

- **Analyse de la dynamique du polymère : interprétation en terme de gradient de T_g autour des charges**

  L'existence d'une couche de polymère immobilisé autour des particules a clairement été mise en évidence lors des thèses de J. Berriot et T. Chaussée. Ces mesures étaient compatibles avec l'existence d'un gradient de T_g autour des charges mais ne permettaient pas de le prouver directement. Dans le Chapitre 2, nous décrirons d'abord de nouvelles mesures en RMN sur ces systèmes qui ont été faites en collaboration avec le groupe de Kay Saalwächter à l'Université de Halle-Wittenberg (Allemagne). Ces mesures permettent une quantification plus rigoureuse des phases de différentes mobilités et nous mèneront au Chapitre 3 vers la mise en évidence de l'existence d'un *gradient* de T_g autour des charges, et non plus simplement l'existence de deux phases de polymère avec des mobilités différentes.

- **Analyse des non linéarités mécaniques : mise en évidence de la présence de ponts vitreux**

  Ensuite, nous nous intéresserons au comportement mécanique des élastomères renforcés et en particulier nous y rechercherons des marques éventuelles de la présence de polymère vitreux. Pour cela, une analyse très rigoureuse des signaux en mécanique non linéaire est nécessaire, notamment dans le cas où ces signaux peuvent devenir non sinusoïdaux. Dans le Chapitre 4 nous décrirons une méthode d'analyse des signaux de contrainte lors de la mesure de l'effet Payne. Nous mettrons ainsi en évidence le fait que, en plus de la caractéristique diminution de module mesurée dans les élastomères renforcés, il existe une non-linéarité des signaux à l'intérieur de chaque cycle de sollicitation, montrant à la fois des phénomènes de raidissement des chaînes et de rhéofluidification. Ces observations seront ensuite comparées qualitativement aux simulations obtenues par le modèle de renforcement par ponts vitreux de Samy Merabia, Paul Sotta et Didier Long du Laboratoire des Polymères et Matériaux Avancés de Lyon. Nous pourrons ainsi déterminer si ces non linéarités peuvent être attribuées à la présence de ponts vitreux dans les échantillons.

► **Lien entre arrangement des particules, épaisseur vitreuse et comportement mécanique**

Enfin, nous essaierons de faire un lien plus quantitatif entre l'arrangement microscopique des échantillons et leur comportement mécanique. L'arrangement des particules de silice dans les échantillons a été évalué dans les thèses précédentes par l'analyse des mesures SANS avec un modèle de Percus-Yevick. Cette approximation donne accès à la distance minimale entre les particules, mais ne renseigne pas sur leur arrangement les unes par rapport aux autres (aléatoire ou ordonné). Dans le Chapitre 5, nous interprèterons les données SANS au moyen de simulations Monte-Carlo inverses. Nous pourrons en déduire plus précisément l'arrangement des particules les unes par rapport aux autres ainsi que les distributions de distances dans les échantillons. Cette étude a été réalisée en collaboration avec Julian Oberdisse au Laboratoire des Colloïdes, Verres et Nanomatériaux de Montpellier. Ces résultats seront ensuite utilisés pour calculer les épaisseurs de polymère vitreux et immobilisé à partir des Chapitres 2 et 3. Finalement, connaissant ces épaisseurs et les distances entre particules, nous pourrons discuter l'existence de ponts vitreux et leur corrélation avec l'effet Payne dans les échantillons.

1.4 Problematics

This thesis will be articulated around three main axes :

- **Polymer dynamics analysis : interpretation in terms of T_g gradient around the particles**
  The existence of an immobilized polymer layer around the fillers has been clearly highlighted in the PhD thesis of J. Berriot and T. Chaussée. Those measurements were in agreement with the existence of a T_g gradient around the fillers, but they lacked direct evidence of this phenomenon. In Chapter 2, we will describe new NMR measurements on the same model systems, that have been done in collaboration with Kay Saalwächter's group in Halle-Wittenberg University (Germany). These results enable a better quantification of the polymer fractions with different types of mobility. It leads us (Chapter 3) to the direct interpretation of the data with a T_g *gradient*, as oppose to the existence of two distinct polymer phases with different dynamics.

- **Non linear mechanics analysis : link with the presence of glassy bridges**
  Then, we are interested in the mechanical behavior of the samples, in particular, potential signs of the presence of glassy polymer in the mechanical signals. For this, a rigorous analysis of the non linear signals is required, especially in the case where these signals can become non sinusoidal. In Chapter 4, we will describe a method for the analysis of the stress signals in oscillatory shear. We find that, in addition to the classical decrease of the elastic modulus with the strain amplitude (Payne effect), the signals exhibit a non linearity inside each cycle of solicitation, showing both strain-hardening and shear-thinning. Those observations are then qualitatively compared to simulations obtained with the glassy bridges reinforcement model developed by Samy Merabia, Paul Sotta and Didier Long at the LPMA in Lyon. We could then determine whether those non linearities can be attributed to the presence of glassy bridges in the samples.

▶ **Link between particles arrangement, glassy thickness, and mechanical behavior**

We attempt to make a more quantitative link between the microscopic composition of the samples and their mechanical behavior. In the previous PhD thesis, the dispersion state of the fillers has been evaluated through the analysis of small angle neutron scattering (SANS) experiments. A Percus-Yevick approximation enabled the description of the samples as liquids of hard spheres and gave access to the minimum distance between particles. However, it could not provide a more precise description of the particles arrangement, for example whether it is crystalline or random. In Chapter 5, we will interpret the SANS data using reverse Monte-Carlo simulations. We could then deduce directly the distribution of distances in the samples. This study has been done in collaboration with Julian Oberdisse at the LCVN in Montpellier. Those results are used to compute the glassy and immobilized thicknesses from Chapters 2 and 3's results. Finally, knowing both these thicknesses and the distances between particles, we will discuss the existence of glassy bridges and their correlation with the Payne effect.

Chapitre 2

Mesure par RMN ^{1}H de la dynamique du polymère dans les élastomères renforcés

Ce chapitre est une version augmentée de l'article paru en février 2011 : A Papon, K Saalwächter, K Schäler, L Guy, F Lequeux, H Montes. Low-Field NMR Investigations of Nanocomposites : Polymer Dynamics and Network Effects. *Macromolecules*, 44(4) :913-922, 2011.

Il décrit l'utilisation de méthodes RMN originales permettant une quantification du polymère immobilisé dans les élastomères renforcés modèles, ainsi que la mesure de la densité effective de contraintes topologiques dans ces échantillons.

Sommaire

Polymer dynamics in filled elastomers measured by ^{1}H NMR

This chapter is an extended version of the aricle published in February 2011 : A Papon, K Saalwächter, K Schäler, L Guy, F Lequeux, H Montes. Low-Field NMR Investigations of Nanocomposites : Polymer Dynamics and Network Effects. *Macromolecules*, 44(4) :913-922, 2011.

It describes the use of original NMR sequences allowing the quantification of the immobilized polymer in model filled elastomers, as well as the determination of the effective density of topological constraints in those samples.

Note : In this Chapter, the samples with TPM grafters are called CG (= Covalentely Grafted) and the ones with C8TES grafters are called NCG (= Non Covalentely Grafted). Here is the correspondance with notations of Table 1.2.

Sample name in Table 1.2	Sample name in Chapter 2
MIST TPM 30	T30 CG 30%
MIST TPM 25	T30 CG 25%
MIST TPM 18	T30 CG 18%
T50a TPM 30	T50 CG 30%
T50a TPM 25	T50 CG 25%
T50a TPM 18	T50 CG 18%
T100 TPM 30	T100 CG 30%
T100 TPM 25	T100 CG 25%
T100 TPM 18	T100 CG 18%
T30 C8TES 37	T30 NCG 37%
T30 C8TES 30	T30 NCG 30%
T30 C8TES 25	T30 NCG 25%
T30 C8TES 18	T30 NCG 18%
T50b C8TES 44	T50 NCG 44%
T50b C8TES 30	T50 NCG 30%
T50b C8TES 25	T50 NCG 25%
T50b C8TES 18	T50 NCG 18%

2.1 Introduction

As we have seen in the previous chapter, the reinforcement obtained by introducing solid fillers into an elastomer matrix is not a simple geometrical effect but it involves a modification of the polymer dynamics near the interface with the fillers.

The study of the polymer mobility in filled rubbers is thus of great importance and low-field proton NMR is a very well established method for this purpose. T_2 relaxometry has already permitted to distinguish between different polymer mobilities in filled rubbers and the presence of a layer of immobilised polymer of a few nanometers around the fillers has been detected in several systems [20–25].

The modification of the polymer dynamics near a solid surface has also been evidenced on thin polymer films deposited onto substrates [56]. In the case of strong interactions between the polymer and the substrate such as hydrogen bonds, the glass transition temperature has been shown to increase when the polymer film thickness decreases. This behavior can be described by a gradient of glass transition temperature near solid surfaces [31] :

$$T_g^f(z) = T_g^f(1 + (\delta/z)^{1/\nu}) \tag{2.1}$$

where $T_g^f(z)$ is the glass transition temperature of the polymer at a distance z from the substrate at the frequency f, T_g^f the glass transition temperature of the bulk polymer, δ a length related to the amplitude of the gradient and ν an exponent close to 1. This model, which comes from the description of the glass transition as a percolation phenomenon, describes the presence of immobilised polymer in filled rubbers that has been experimentally measured with NMR experiments [32, 53, 55].

We also pointed out that the mechanical non-linearity usually observed in filled rubber - known as Payne effect - is related to the stress-softening of the polymer glassy bridges between neighboring particles [33]. A better understanding of the polymer mobility around the fillers is thus of great importance since the presence of an immobilised polymer layer around the silica particles and the potential formation of glassy bridges between the particles govern the mechanical behavior of the filled samples.

The NMR sequences generally used to study polymer mobility in filled rubbers are the solid-echo pulse sequence to study the rigid polymer fraction (seen at short timescales) and the Hahn echo for the mobile fraction (at longer timescales). However, those methods are potentially subject to artefacts related to over-interpreted or inapplicable fitting models and parameters interdependencies [57, 58]. That is why we propose here to use two more reliable techniques.

On the one hand, we use magic-sandwich echo (MSE) to study the polymer relaxation at short timescales (less than 0.2 ms). The MSE refocuses the initial part of the free-induction decay (FID) and thus avoids the dead time issue. Compared with solid echo, it enables a better refocusing of multi-spin dipolar interactions and has been shown to be a robust method to investigate polymer mobility [59, 60].

On the other hand, multiple-quantum (MQ) experiments give access to much slower relaxation processes (0.1 ms to 3 ms), which are linked to the presence of topological constraints such as

cross-links and/or entanglements that are limiting the reorientations of the polymer segments. This method is more quantitative than T_2 relaxometry since it measures the residual dipolar coupling and thus the local dynamic order parameter on an absolute scale [57, 61–64]. These two complementary methods give us a broader view on the polymer dynamics in filled elastomers : the MSE enables the study of the polymer mobility and the determination of the immobilised polymer fraction, while MQ NMR gives us an insight into the cross-link density and homogeneity in the filled samples.

Another critical parameter in the study of the polymer dynamics in filled rubbers is the control of the dispersion of the fillers in the samples. In effect, if the polymer mobility is influenced by the presence of solid surface, it is then crucial to control the quantity of silica surface accessible to the polymer and thus the dispersion state of the fillers. This is why this study was conducted on model-filled samples with a much better controlled dispersion state than in conventional samples. We varied both the silica content and the particles diameter. Moreover, using two different synthesis methods, we were able to make filled samples with two kinds of "coupling" agents - the molecule coating the silica surface : one creating a covalent bond between the silica and the polymer, and the other just modifying the surface energy. In the latter case, the interaction between the filler and the matrix is mainly governed by hydrogen bonds between residual silica OH groups and the polymer chains. We could thus study the influence of the coupling agent on the polymer dynamics.

Model samples with a grafter creating a covalent bond between the silica and the polymer have already been studied in NMR and the presence of glassy polymer has been detected [32, 53, 55]. Here, the analysis of MSE-refocussed FIDs will give a more precise description of the polymer dynamics near the interface which is in agreement with the presence of a *gradient* of mobility that cannot be described with a core-shell approximation at low temperature. Moreover, with this method the presence of polymer with a slower dynamics could also be detected in samples with a weaker coupling between the silica and the polymer (hydrogen bonds). The relaxation of the polymer at long timescales has also been examined in a previous publication [54] with the study of Hahn or pseudo-solid spin-echoes. This analysis revealed an increase in the overall effective cross-link density compared to the amount of cross-linker introduced. It showed that the presence of solid particles plays a role in the effective crosslink density of filled rubbers. This result is now clarified by our MQ NMR measurements. In effect, we show here that if most of the elastomer has a slightly higher cross-link density than the reference matrix, a fraction of up to 30% of the polymer – most probably in the vicinity of the solid particles – has a far larger cross-link density. This effect had not been previously seen in conventional samples and is probably due to the good silica dispersion in those model samples.

In this chapter, we will first recall the sample synthesis and then expose some basic concepts in NMR and the two NMR methods used here. We will then expose the experimental results obtained from (MSE-refocussed) FIDs and MQ NMR. For each method, we will start with the study of the elastomer matrix before investigating the model filled samples.

2.2 Sample preparation and characterisation

Sample preparation

The model filled elastomers consist of grafted silica particles dispersed in a poly(ethylacrylate) matrix. Two kinds of grafter have been used : TPM (3-(trimethoxysilyl)propyl methacrylate), which can react with the monomer and thus create a covalent bond with the matrix (Covalently Grafted samples – CG), and C8TES (n-octyltriethoxysilane) with which there are only weak bonds between the silica particle and the polymer (Non-Covalently Grafted samples – NCG). The synthesis process has been described elsewhere [65] and we will here recall the main steps.

First, weakly polydispersed silica particles were synthesized using the procedure described by Stöber [44]. Then, the filled elastomers were obtained following the process developed by Ford et al. [45–48] for the TPM-grafted samples, and a process adapted by Berriot et al. for the C8TES samples [53]. For that, the silica particles were directly grafted in a diluted Stöber solution (particle volume fraction of 2%) with an excess amount of TPM or C8TES. The quantity of grafted coupling agent was determined by elemental analysis and is shown in Table 2.1. Then, the TPM-grafted particles were transferred by dialysis to methanol and then, again by dialysis, to the acrylate monomer. Various concentrations of silica were obtained by diluting the concentrated solution obtained after dialysis (20% in volume) with acrylate monomer. Finally, a photosensitive initiator (Irgacure from Ciba - 0.1 wt% to the monomer) and a cross-linker (butanediol diacrylate - 0.3 mol% to the monomer) were added and polymerization and cross-linking occurred simultaneously under UV illumination. The process used for C8TES-grafted silica was slightly different due to depletion issues observed during the synthesis. In effect, the colloidal stability is more difficult to preserve in the case of this coupling agent which does not create a covalent link with the polymer. The C8TES-grafted silica beads were first transferred to methanol by dialysis and then the desired amount of monomer was added. This way, the solution was kept diluted (around 6% in volume) so that the colloidal stability could be maintained. Part of the solvent was then evaporated by distillation at 50°C until a concentration of 20% in volume was reached. The polymerisation (same initiator and cross-linker than previously) was done in presence of solvent in order to reduce the depletion issues.

SANS measurements

The silica particles dispersion state was characterized with Small Angle Neutron Scattering (SANS) experiments [65]. Diluted solutions of silica particles gave access to the form factors and the structure factor could then be deduced by dividing the measured scattered intensity by the form factor. The intensity of the structure factor at low wavevectors q gives important information on the longscale arrangement of the silica particles in the samples. When the intensity is low in this regime, it means that the particles are very homogeneously distributed in the sample, otherwise, it shows the presence of aggregates. All the samples used here showed a rather good dispersion. The characteristics of the samples are presented in Table 2.1.

TABLE 2.1 – Samples characteristics. NCG = Non Covalently Grafted, CG = Covalently Grafted

Name	Mean silica diam. (nm) [a]	vol. fraction ϕ_{Si}	Graft density (nm^{-2}) [b]
T30-NCG-18%	26	0.10	2.0
T30-NCG-25%	26	0.15	2.0
T30-NCG-37%	26	0.23	2.0
T50-NCG-18%	42	0.10	1.5
T50-NCG-25%	42	0.15	1.5
T50-NCG-44%	42	0.29	1.5
T30-CG-20%	27	0.12	5.0
T30-CG-25%	27	0.16	5.0
T30-CG-30%	27	0.20	5.0
T50-CG-18%	42	0.11	3.2
T50-CG-25%	42	0.15	3.2
T50-CG-30%	42	0.22	3.2

[a] From SANS measurements ; [b] From elemental analysis.

2.3 New low-field ^1H NMR investigations

2.3.1 Basic concepts in NMR [1]

NMR is a characterisation technique widely used in the determination of the local properties of materials. Pulse NMR is based on the study of the relaxation of a set of magnetic spins placed in a intense static magnetic flux $\overrightarrow{B_0}$ and subject to short pulses of an electromagnetic flux $\overrightarrow{B_1}$. The signal measured is called the Free Induction Decay (FID). An accurate description of the MSE and MQ experiments would require a quantum mechanical treatment. However, for an easier visualization, we will here restrict our description of the pulse NMR method to a classical treatment [66]. This will give us the main features of the NMR spectra we will study in this chapter. We will then simply point out the advantages of the chosen methods compared to other, more widely used, techniques.

Nuclear precession

In classical mechanics, a magnetic moment placed in a magnetic flux $\overrightarrow{B_0}$ and making an angle θ with it is known to precess at the angular frequency $\omega_0 = -\gamma B_0$, where γ is the magnetogyric ratio of the considered nucleus. ω_0 is called the Larmor frequency. We generally consider not only one magnetic moment but a large ensemble of identic nuclei. Because of the static magnetic field, there is a net macroscopic magnetization $\overrightarrow{M}$ along the axis containing $\overrightarrow{B_0}$ (see Figure 2.1).

The rotating frame

In pulse NMR, we study the effect of the application of short pulses of a radiofrequency flux $\overrightarrow{B_1}$ placed perpendicularly to $\overrightarrow{B_0}$. For that, it is very convenient to use a coordinate system that rotates about $\overrightarrow{B_0}$ at the same frequency ω than $\overrightarrow{B_1}$. This coordinate system is called the rotating

1. This section, which is not in the original article, has been added for the sake of clarity. It introduces some classical NMR methods and compare them to the one chosen in this study.

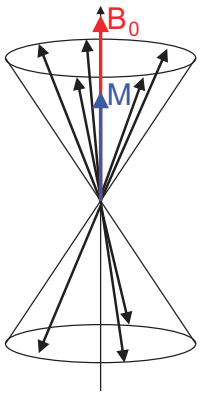

FIGURE 2.1 – Precession of an ensemble of magnetic moments in a static magnetic flux $\overrightarrow{B_0}$. The macroscopic magnetization $\overrightarrow{M}$ is along $\overrightarrow{B_0}$.

frame. The motion of the magnetic moment in the rotating frame can be described by the same equation than in the laboratory frame given that the magnetic flux applied $\overrightarrow{B}$ is replaced by an effective magnetic flux $\overrightarrow{B_{eff}} = \overrightarrow{B} + \overrightarrow{\omega}/\gamma$. If the only field applied is $\overrightarrow{B_0}$ and that the frame is rotating at the Larmor frequency $\omega = \omega_0 = -\gamma B_0$, we see that the effective flux is equal to zero so that the magnetic moment is static in the rotating frame. Now if a radiofrequency flux $\overrightarrow{B_1}$ at the same frequency than the rotating frame ω is added, the effective field obtained is $\overrightarrow{B_{eff}} = \overrightarrow{B_0} + \overrightarrow{\omega}/\gamma + \overrightarrow{B_1}$. Two cases have to be considered : the resonance condition if $\omega = \omega_0$ and the off-resonance condition if $\omega \neq \omega_0$

Resonance condition

If ω is equal to the resonance frequency ω_0, $\overrightarrow{B_0}$ is cancelled and the effective field is equal to $\overrightarrow{B_1}$, which is static in the rotating frame. In this case, the magnetic moment rotates about $\overrightarrow{B_1}$ in the rotating frame, at the Larmor frequency γB_1. Thus, if the radiofrequency flux $\overrightarrow{B_1}$ is applied for a time t, the magnetic moment go through an angle $\theta' = \gamma B_1 t$. For example, a $\pi/2$ pulse is a pulse long enough to make the magnetic moment turn by 90° (see Figure 2.2).

When $\overrightarrow{B_1}$ is turned off, the nuclei start to exchange energy with each others and the component of the magnetization in the(x,y) plane M_{xy} starts to decrease. The characteristic time of return to equilibrium with the other nuclei is call the spin-spin relaxation time T_2.

Moreover, the nuclear spin system also will come back to equilibrium with its surrounding and the component of $\overrightarrow{M}$ along the z axis comes back to its equilibrium value with a charateristic time T_1 called the spin-lattice relaxation time. In solids, T_2 is generally much shorter than T_1.

Off-resonance condition

Let us now consider the case where $\overrightarrow{B_1}$ and the rotating frame rotate at a frequency ω different from the resonance frequency. In this case, $\overrightarrow{M}$ precesses around the effective flux $\overrightarrow{B_{eff}}$ with

$$\| \overrightarrow{B_{eff}} \| = \left[(B_0 - \omega/\gamma)^2 + B_1^2 \right]^{1/2} \tag{2.2}$$

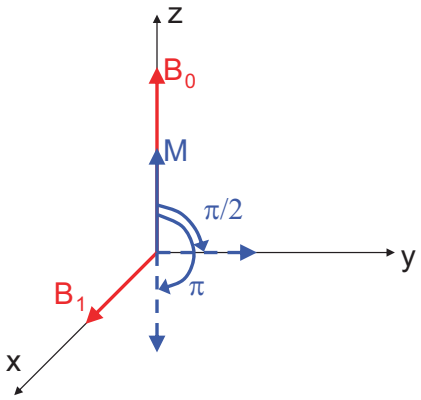

FIGURE 2.2 – Effect of the electromagnetic flux $\overrightarrow{B_1}$ in the rotating frame. The magnetization rotates around $\overrightarrow{B_1}$.

$$= (1/\gamma)\left[(\omega_0-\omega)^2+(\gamma B_1)^2\right]^{1/2} \tag{2.3}$$

at a frequency $\Omega = \left[(\omega_0-\omega)^2+(\gamma B_1)^2\right]^{1/2}$.

There might be different reasons for this condition to happen :

- the chemical shift of some of the nuclei,
- the magnetic field inhomogeneity : the ensemble of nuclei considered are not all located in the same part of the sample so that they do not experience exactly the same value of the static flux $\overrightarrow{B_0}$,
- dipolar fields : each nuclei experience not only the static field $\overrightarrow{B_0}$ but also the magnetic fields created by the neighboring nuclei.

As a consequence, the resonance frequency is not exactly the same for all the nuclei considered and thus some of them are in the off-resonance condition.

Free Induction Decay

All those effects contribute to the decrease of M_{xy} after a $\pi/2$ pulse. The measurement of the M_{xy} relaxation gives thus information on the local surrounding of the spins and thus on the materials properties. However, the direct measurement of the Free Induction Decay (FID) is prevented at short times because of the dead time of the instrumentation. In effect, the pulse applied is very intense compared to the M_{xy} measured and just after the application of $\overrightarrow{B_1}$, the receiver is not able to measure such a low intensity. Depending on the instrumentation used, this dead time lasts generally between 2 and 15 μs (see Figure 2.3). To tackle this problem, we use pulse sequences generating an echo of the FID. The pulse sequences refocus the magnetic moments and they can cancel some of the dephasing phenomenon described previously such as chemical shifts or dipolar couplings. The pulse sequence is chosen depending on the aim of the study.

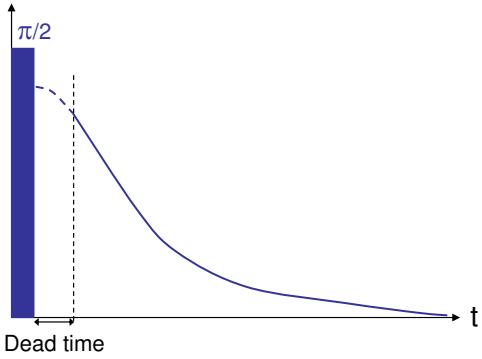

FIGURE 2.3 – The relaxation of M_{xy} after a $\pi/2$ pulse (FID) cannot be measured at short times because of the dead time of the instrumentation.

Study of rigid/mobile parts

The determination of hard/soft ratios in a material, for example in semi-cristalline polymers, is typically studied by the use of a solid echo. The corresponding pulse sequence is $(\pi/2, \tau, \pi/2, acquistion)$ and it enables a partial refocusing of the dipolar interactions and of the chemical shifts. For an elastomer, the relaxation curve can often be described with an exponential fonction. If the material is more rigid, the characteristic relaxation time will decrease. In the case of an heterogenous material with hard and soft phases, the relaxation curve will be superposition of a fast decaying signal at short times and a slower decaying signal at longer times. The fit of the curve with a sum of exponentials or stretched exponentials will give an estimation of the amount of each phase.

Instead of using the solid-echo sequence, we chose to use in this study a pulse sequence called the Magic Sandwich Echo because it leads to a better refocalisation of the dipolar interactions.

Study of topological constraints

The topological constraints experienced by the polymer chains, such as entanglements or crosslinks, are typically studied by Hahn echo. The pulse sequence is described in Figure 2.4 $(\pi/2, \tau, \pi, acquisition)$. It leads to the refocusing of the chemical shift dispersion as well as some of the effects of field inhomogeneity. This sequence enables the study of the spin relaxation at much longer timescales than the solid echo and is thus sensitive to polymer orientation constraints.

In this study, we will use a more quantitative method called Muliple Quantum NMR. It will give us acces directly to the residual dipolar couplings and thus to the local orientation of the polymer chains.

2.3.2 Minispec measurements

The NMR measurements were performed on a Bruker Minispec mq20 at 20 MHz proton resonance frequency. The sample temperature was controlled with a BVT3000 heater working with air or nitrogen gas at low temperature. For the experiments in presence of solvent (dichloroethane and toluene), the solvent was added to the sample in a conventional NMR tube. To

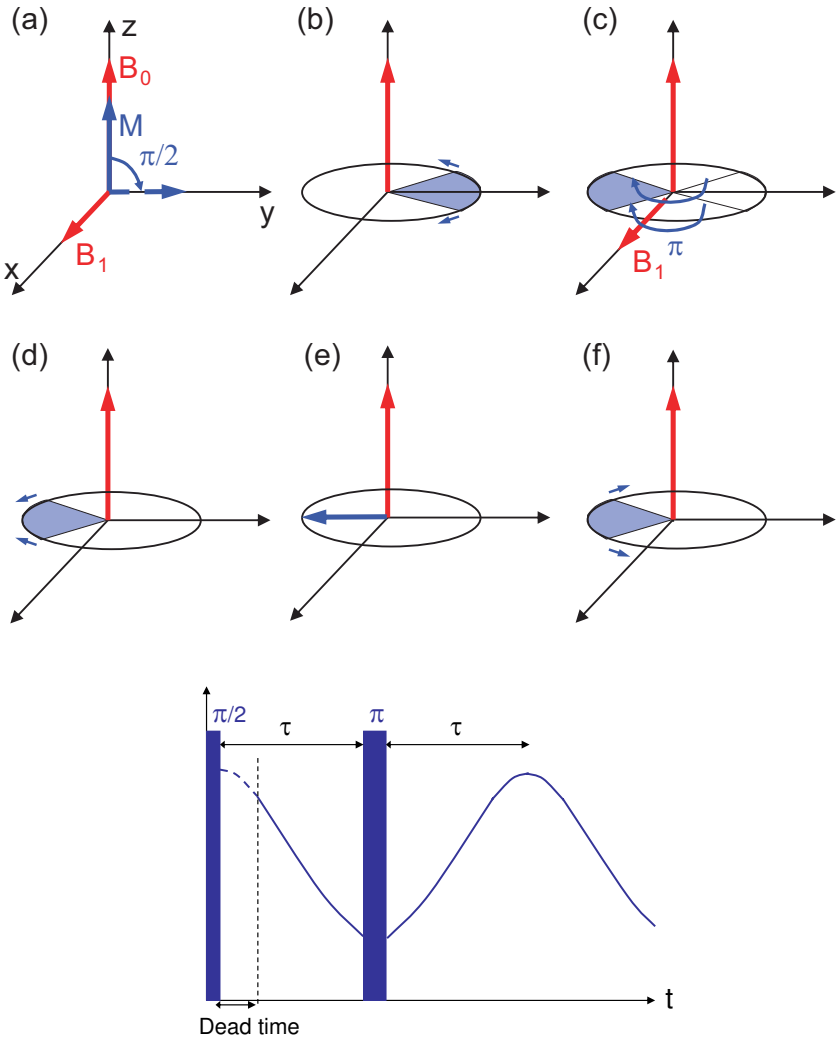

FIGURE 2.4 – The Hahn echo experiment. (a) First, a $\pi/2$ pulse is applied so that the magnetization M is along the y axis. (b) For a time τ the system relaxes. Because of field inhomogeneity, dipolar couplings and chemical shifts, the magnetic moments do not have exactly the same resonance frequency. In the rotating frame, they do not rotate at the same frequency so that the macroscopic magnetization in the xy plane M_{xy} decreases. (c) A π pulse is applied. (d) The system evolves for a time τ. Since the spins continue rotating in the same direction, they start to refocus. (e) At the time τ, the maximum of the echo is reached. (f) The refocussed-FID is measured, without the dead time issue.

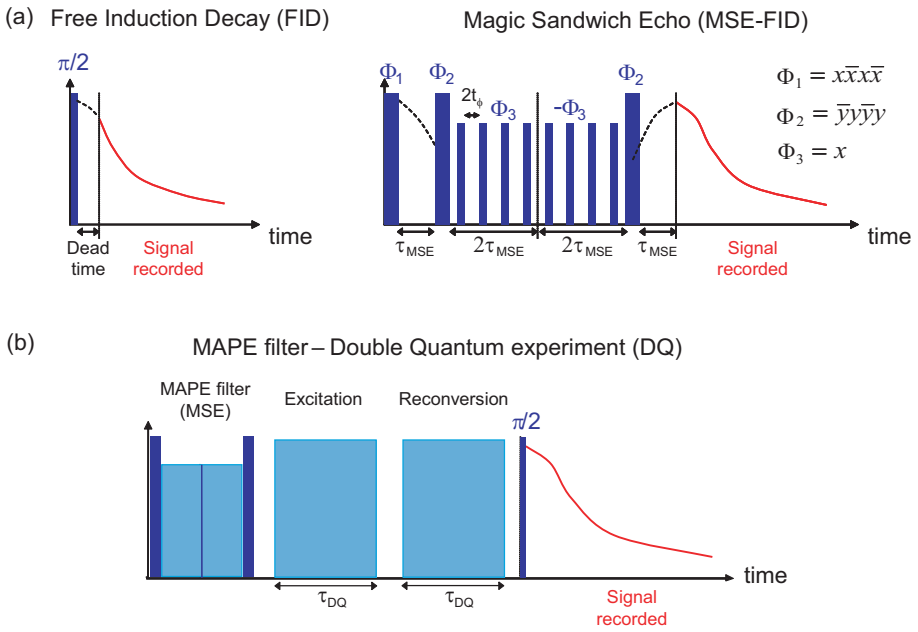

FIGURE 2.5 – NMR pulse sequences. Solid bars denote 90° pulses, and the grey-shaded areas represent groups of pulses. (a) The initial part of the free-induction decay (FID) is missing due the dead time of the receiver. That is why we use the magic-sandwich echo (MSE) to refocus the signal and thus measure the entire shape of the decay. This sequence is used to study the polymer mobility in the filled samples. (b) The multiple-quantum (MQ) experiment (see ref 63 for details) is preceded by a MAPE filter (effectively an MSE sequence with longer inter-pulse spacings t_ϕ) in order to remove the response of the immobilised polymer fraction from the signal. This sequence enables the study of the topological constraints in the samples such as cross-links and entanglements.

avoid evaporation, the tubes were flame-sealed after dipping in liquid nitrogen.

The minispec has typical $\pi/2$ pulse lengths of down to 2 μs (125 kHz nutation frequency), it shows a reliable phase cycling in $\pi/2$ steps with switching times in the 2 μs range, and has a minimum dwell time of 400 ns. It is thus very well adapted to solid-state pulse sequences. Each signal trace required 64 scans with around 1 s recycle delay (depending on the temperature).

2.3.3 Magic-Sandwich Echo

The rather long dead time of the low-field equipment (15 μs) is tackled by refocusing the free-induction decay (FID) signals with a magic-sandwich echo (MSE) pulse sequence. This sequence is much more efficient than the conventionally used solid-echo, which cannot properly refocus multi-spin dipolar interactions. The pulse sequence used is sketched in Figure 2.5 (a), and was designed to accommodate the finite phase switching time t_ϕ of the instrument. See refs 59, 60 for details.

2.3.4 Multiple-Quantum NMR

The precise procedure used for multiple-quantum (MQ) NMR experiments has been published previously [63], and we will here simply recall the principle of the measurement and the main

steps of the analysis.

The orientation of the polymer segments in a network can be described by an orientation autocorrelation function which for our NMR observable is the one of the second Legendre polynomial P_2. This time-dependent function gives the probability for a segment in a certain orientation at a time t_1 to be again in the same orientation at another time t_2. At short time differences $t_2 - t_1$, the polymer segments quickly loose their orientational memory due to fast local fluctuations, and the autocorrelation function decreases rapidly. At some point however, the longer-range or slower motions of the segments are hindered by the presence of topological constraints such as entanglements and cross-links. This leads to a very slowly decaying component in the autocorrelation function, which can almost be seen as a plateau. In this case the height of the plateau of the P_2 autocorrelation function corresponds to the square of a dynamic order parameter of the polymer backbone S_b.

The parameter S_b is directly proportional to the cross-link density and is thus characteristic of the network structure. It can be readily obtained by MQ experiments at temperatures far above T_g via the measurement of normalized double-quantum (DQ) build-up curves. (Higher-order MQ coherences do contribute to the signals at long times, but are negligible in the theoretical treatment.) The rise time of the DQ build-up curves depends on the residual dipolar coupling, which is proportional to S_b. The DQ build-up curves were measured at 393K and normalized in order to remove any temperature-dependent relaxation effects. The pulse sequence duration τ_{DQ} was varied between 0.01 and 70 ms, and for each value, the intensities of the DQ build-up curve (I_{DQ}) and a reference decay curve (I_{ref}) were measured. The sum of the two components contains the full magnetization of the sample and is used to normalize, at each time τ_{DQ}, the DQ build-up curves : $I_{DQ}^{norm} = I_{DQ}/(I_{ref} + I_{DQ})$. I_{DQ}^{norm} is then independent of the timescale of fast segmental fluctuations leading to intensity decay at long times. Thus the residual dipolar couplings that are representative of the network structure are reliably accessible.

In the case of our model filled samples, even if the MQ experiments were done at high temperature (393K, that is T_g + 120K), the filled rubbers still contained a fraction of rigid polymer. This immobilised polymer interferes with the early part of the build-up curves representing the mobile elastomer part, since at very short τ_{DQ}, also signals of rigid, strongly dipolar-coupled segments contribute to the DQ intensity. The used MQ pulse sequence is not very effficent for strongly dipolar-coupled systems due to the rather long cycle time, yet in order to completely remove such unwanted contributions, we used a MAPE (magic and polarization echo) as dipolar filter, which is addressed in more detail in ref 60. In essence, it is identical to the MSE sequence with exception of the last "sandwich" pulse, whose phase is opposite to the one of the first pulse. By increasing the overall cycle time of the central spin-lock part of the MSE sequence the echo becomes inefficient for strongly dipolar-coupled spins and their signal is correspondingly suppressed. A long echo duration τ_{MAPE} was realized by an increase of the interpulse spacing t_ϕ. The time τ_{MAPE} was adjusted so as to remove the rigid fraction for all the samples (0.164 ms). We will explain this point in more detail in the MQ NMR section. The polymer motion in the filled elastomers has thus been studied in the rubbery part of the sample. The pulse sequence used is schematically shown in Figure 2.5 (b).

2.4 Polymer mobility : FID and MSE measurements

The polymer mobility can in principle be investigated by simply studying the free-induction decay (FID) signal of the samples. A slow decay of the FID corresponds to the response of mobile polymer whereas a rapid decay shows the presence of less mobile polymer. However in our case the FID could not be directly exploited due to the rather long dead time of the receiver : the first 15 μs of the FID are missing and this part of the signal is very important since it contains the initial fast decay part and so the immobilised polymer response. To obtain information on the shape of the entire signal decay we thus referred to an echo in order to refocus the signal.

The FID after a short MSE sequence gives the entire shape of the decay and can generally be well fitted with a combination of stretched or compressed exponential (Weibullian) functions $e^{-(t/\tau)^b}$ (henceforth referred to as "modified" exponential). With $b = 2$, the function corresponds to a Gaussian decay which can be used to describe the behavior of a rigid polymer, whereas a simple or slightly stretched or compressed exponential ($b \approx 1$) will be able to describe a more mobile elastomer. The weight of each fit component gives the amount of mobile / less mobile polymer in each sample, but one needs to keep in mind that there is a (usually weak) signal decay during the echo time (true relaxation or imperfection effects), which needs to be accounted for. The general strategy is to fix as many as possible shape parameters (τ, b) of the individual components at pre-determined values and then use them in a multi-component fit to the FID signal, which is not subject to an intensity bias of the different components. Another point to mention is that we generally only fit MSE/FID data up to 0.25 ms since the decay at longer times is dominated by field inhomogeneities, the corresponding FID shape of which is not precisely known. The initial part is, however, generally well described by a simple modified exponential. Details on our curve-fitting strategy are described in ref. 60.

2.4.1 Glass-rubber transition in PEA

We will first look at the MSE signals of the poly(ethyl acrylate) (PEA) matrix at various temperatures around and in particular above the glass transition. The calorimetric T_g of PEA is about 250K [67]. However, glass transition effects on the NMR observables only set in several tens of K higher, i.e., when the segmental dynamics (α process) reaches correlation times of 0.1-0.01 ms, corresponding to the range where it is of the order of the inverse of the average dipolar coupling constant in the static limit. The MSE-refocussed FIDs shown in Figure 2.6 (a) reflect a typical motional-narrowing phenomenon in the mentioned temperature region, proving the influence of the glass-rubber transition. For a crude analysis, one can use the theory of Anderson and Weiss [68] to obtain an analytical (second-moment) approximation of a dipolar FID for a spin pair :

$$I_{\mathrm{FID}}(t) = \left\langle \cos \int_{\tau}^{t+\tau} \omega(\theta,\tau)\mathrm{d}\tau \right\rangle = \exp\left[-M_2\tau_c^2\left(e^{-t/\tau_c} + \frac{t}{\tau_c} - 1\right)\right] \tag{2.4}$$

The dipolar frequency $\omega(\theta,\tau)$ is proportional to $D \times P_2(\cos\theta)$, and the latter is a random function in time, owing to the orientation fluctuations of the internuclear vector described by θ. For the simple case of isotropic rotational diffusion, for which the autocorrelation function of $P_2(\cos\theta)$ is a simple exponential $\sim \exp[-t/\tau_c]$, standard procedures [69] can be used to arrive at the above

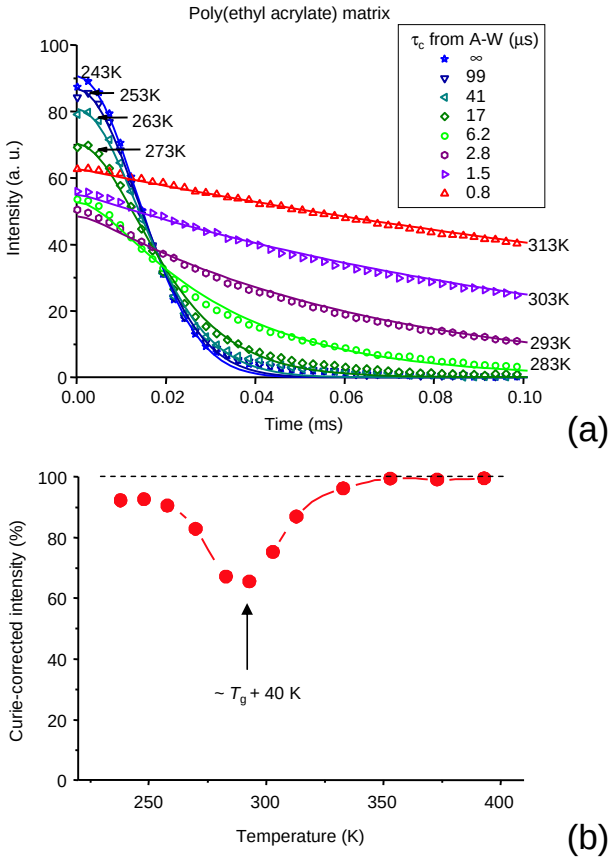

FIGURE 2.6 – (a) MSE-refocussed FID signals as a function of the acquisition time for a PEA matrix at various temperatures between 243K and 313K (symbols), and results of fits to eq. (2.4) (solid lines). The static second moment $M_2 \approx 5500$ ms^{-2} was obtained by a fit with $\tau_c \to \infty$ to the FID at 243K. (b) Initial intensity of the MSE-refocussed FIDs plotted as a function of the temperature. The intensities have been corrected according to the Curie law. The minimum in the signal intensity at around $T_g + 40$ K is expected for an MSE experiment, the refocussing action of which is perturbed by molecular motion in the 10-100 kHz range.

analytical result, where the second moment $M_2 \approx (9/20)D^2$ is related to the largest dipole-dipole pair couplings D in the system.

Eq. (2.4) provides a good fit to the experimental data, with correlation times in the realistic range (Figure 2.6 (a)). Note that the obtained τ_c is non-trivially related to a combination of main-chain segmental fluctuations (α process) as well as faster motions of the side-chains (β process). These are known to be coupled for the case of poly(alkyl methacrylates) [70], and similar complexity can be expected for PEA. A more complete analysis would of course have to embody a more complex form of the effective P_2 autocorrelation function, and one would also have to take into account that the high-temperature FIDs are already influenced by magnetic-field inhomogeneities or residual dipolar couplings related to cross-links. However, the general shape of the Anderson-Weiss function (Eq. 2.4) does not depend much on the specific form of the underlying correlation function, and is, over the whole τ_c range, well approximated by a simple modified exponential, $I_{\mathrm{FID}}(t) \sim \exp[-(t/\tau)^b]$, which justifies simple fitting approaches of the initial time range.

Figure 2.6 (b) provides a second confirmation of the typical signature of a glass-rubber transition. We plot the variation of signal intensity after the MSE, which exhibits the typical minimum in the intensity at a few tens of Kelvin above the glass transition. This behavior is characteristic of an MSE, which is a full dipolar/chemical-shift echo. The formation of such an echo is only possible either in the slow- or the fast-motion limit, but is impeded when molecular motion takes place on the time scale of the refocussed interaction (D^{-1}) and the echo (both $\sim 50\,\mu s$). The data demonstrate that in a more complex multi-component sample with a distribution in T_g, the parts that exhibit dynamics in the intermediate motional regime may be underestimated by up to 40%. This is why our quantitative analysis below relies on unrefocussed FID data.

2.4.2 At least three types of mobility in the filled rubbers

As seen in the first chapter, a gradient of glass transition temperature is expected around the silica particles, which should lead to a gradient of polymer mobility in the filled elastomers. To check this in our samples, we measured MSE-refocussed FIDs at a given temperature and fitted them with a linear combination of *experimental* MSE-FID signals of the pure PEA matrix at different temperatures (Figure 2.7, sample T50 NCG 44% at 333K). We chose to use experimental data as base functions rather than analytical representations, noting that the fits in Figure 2.6 (a) do not perfectly match the data.

We found that at least 3 components were needed to obtain an accurate representation. While a fit with seven components (PEA 253K, 263K, 273K, 283K, 293K, 303K and 333K) trivially matches the data extremely well, we note that with the three most significant components, PEA at 273K – that is glassy, at 303K – that is with an intermediate mobility, and at 333K – that is at the experiment temperature, the fit is still very good. A combination of only two components is however never sufficient to describe the experimental signal. This means that at least three different kinds of polymer mobility are present in the filled elastomers. This observation is in agreement with the existence of a gradient of T_g around the solid particles (which cannot be described with a simplistic core-shell approximation at low temperature).

2.4.3 Determination of the rigid polymer fraction

As we will see in the MQ experiment section, the CG samples contain a fraction of highly cross-linked polymer. We could then not use the MSE-FID signal of the PEA matrix (with 0.3 mol% of cross-linker, like the filled samples) to fit the MSE-FID signal of the CG samples. We thus decided to use an analytical fit composed of modified exponential functions, which can be applied to all the samples. We used three components, as two components were shown to not give a satisfactory fit for all the temperatures as we can see in Figure 2.9 (a). Reliable fitting was possible with all the parameters b and τ free except for the rigid (Gaussian) part where b_g was fixed to 2. The fitting function was thus

$$M(t) = M_0(a_g exp(-t/\tau_g)^{b_g} + a_i exp(-t/\tau_i)^{b_i} + a_n exp(-t/\tau_n)^{b_n}), \tag{2.5}$$

where g stands for glassy, i for intermediate and n for network.

The determination of the parameters was done using MSE-FID signals with different τ_{MSE} (see Figure 2.8). As τ_{MSE} increases (from 0.0126 ms to 0.123 ms), more and more of the solid

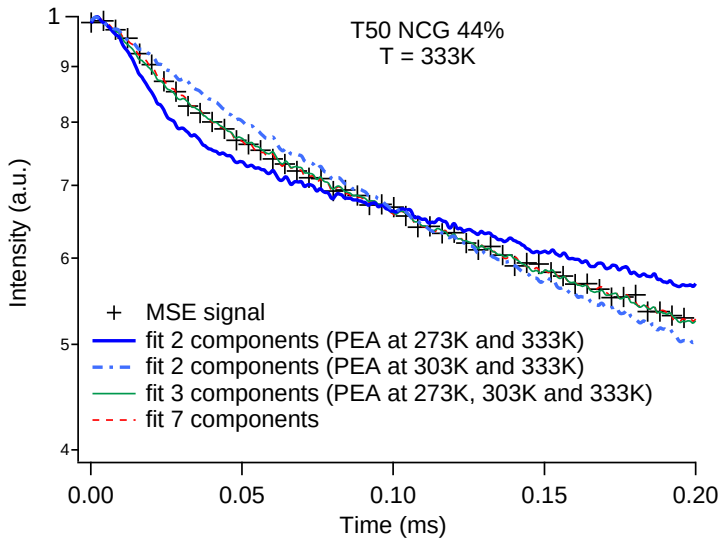

FIGURE 2.7 – MSE signal as a function of the acquisition time for the T50 NCG 44% sample at 333K fitted with different combinations of MSE signals of the PEA matrix between 253K and 333K. We see that at least 3 components are needed to fit the experimental signal, in agreement with the presence of a gradient of polymer mobility.

signal is lost. From $\tau_{MSE} = 0.083$ ms (here), all the rigid signal is lost and the MSE-FID signal can be fitted with simply one modified exponential. This curve is thus used for the determination of the parameters b_n and τ_n, which will then be kept constant. The three other parameters are determined by fitting the MSE-FID signal with the shortest τ_{MSE}. This is done on three MSE-FID signals with a short τ_{MSE} and an average value of each parameter is taken.

For all the samples we found similar parameters : $b_n \simeq 1$, $b_i \simeq 1.3$, $\tau_g \simeq 0.02$ ms, $\tau_i \simeq 0.06$ to 0.1 ms and $\tau_n \simeq 0.3$ to 1 ms depending on the temperature. A typical decomposition of the MSE-FID signal into three components is shown in Figure 2.9 (b). We can note here that τ_n is always smaller in the filled rubbers than in the matrix at the same temperature. The elastomer thus appears less mobile in the filled samples, which may simply be due to a higher effective cross-link density, as we will see in the MQ NMR section. However, the field inhomogeneity (shim limit and field distortions due to filler particles) may also play a role here, such that τ_n should not be over-interpreted. Simple Hahn-echo experiments could possibly yield better values, yet the MQ experiments are of course the route of choice for an in-depth characterization of the elastomer fraction.

Finally, keeping all those parameters fixed, we could fit the FID and find the fraction of each component a_g, a_i, a_n. In effect, even if the MSE-FID gives a well-refocused decay, there is still a loss of intensity especially for polymer just above T_g (as we can see in Figure 2.6 (b)). That is why, once the shape of the decay has been carefully fitted on the MSE-FID signals, we determine the amount of each component directly on the FID.

This analysis is done on all the samples at 313K, 333K, 353K, 373K and 393K, that is between $\sim T_g + 40$K and $T_g + 120$K. Examples of the variation of each component with the temperature are given in Figure 2.10 (a) and (c). We remark that the amount of "glassy" polymer does not vary much with the temperature and that for the CG samples, it is close to the fraction of protons

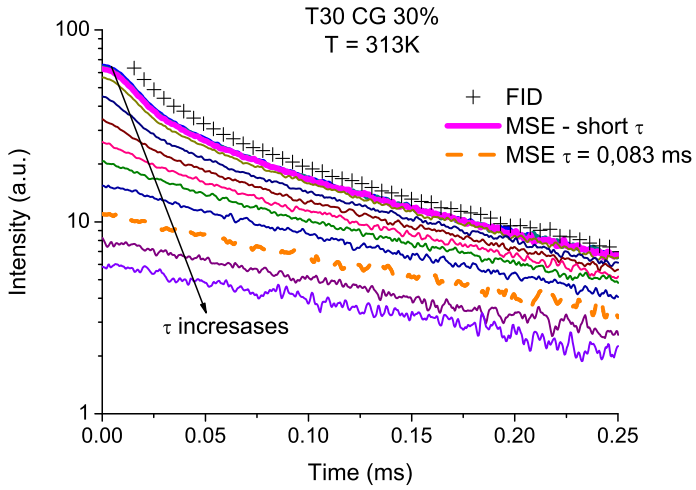

FIGURE 2.8 – FID and MSE-FID signals as functions of the acquisition time for the sample T30 CG 30% at 313K and for various τ_{MSE}. As τ_{MSE} increases, more and more of the initial fast decaying signal is lost. For $\tau_{MSE} \geq 0.083$ ms (that is below the dashed line), only the modified exponential signal remains and the parameters for the elastomer part can be determined : b_n and τ_n have here been determined on the curve corresponding to $\tau_{MSE} = 0.083$ ms. With MSE-FID curve at short τ_{MSE} (0.0126ms for the thick line), the parameters for the "intermediate" and "glassy" parts are extracted : b_i, τ_i and τ_g. Then, keeping all those parameters fixed, the FID is fitted in order to get the proportion of each component.

coming from the grafters and ethoxy groups around the silica particles. This latter quantity can be estimated thanks to elemental analysis and is shown in Figure 2.10 (a) and (c) as the shaded areas. For the NCG samples however, the glassy fraction is slightly smaller that the amount of grafter and ethoxy. In effect, in this case the grafters are rather long chains (8 carbons), not covalently linked to the polymer. They can thus be more mobile than the polymer and not be included in the glassy fraction.

From now on, we call "immobilised" polymer the sum of the "glassy" and "intermediate" parts.

2.4.4 Temperature and solvent addition have the same influence on the polymer mobility

At various solvent weight fractions, the amount of "glassy" and "intermediate" polymer was measured. The results obtained with toluene or dichloroethane were similar and the dichloroethane case is plotted in Figure 2.10 (b) and (d) for one CG and one NCG sample. We see that the amount of rigid polymer decreases with the solvent content, similarly to what happens with an increase of the temperature. In effect, the addition of solvent induces a decrease in the glass transition temperature due to an increase in the configurationnal entropy of the polymer chains [71], as shown in Figure 2.11 (a). This means that at constant temperature, the temperature difference $T - T_g$ is simply increased by swelling. We can show that solvent and temperature have exactly the same consequence on the polymer dynamics by plotting the amount of immobilised

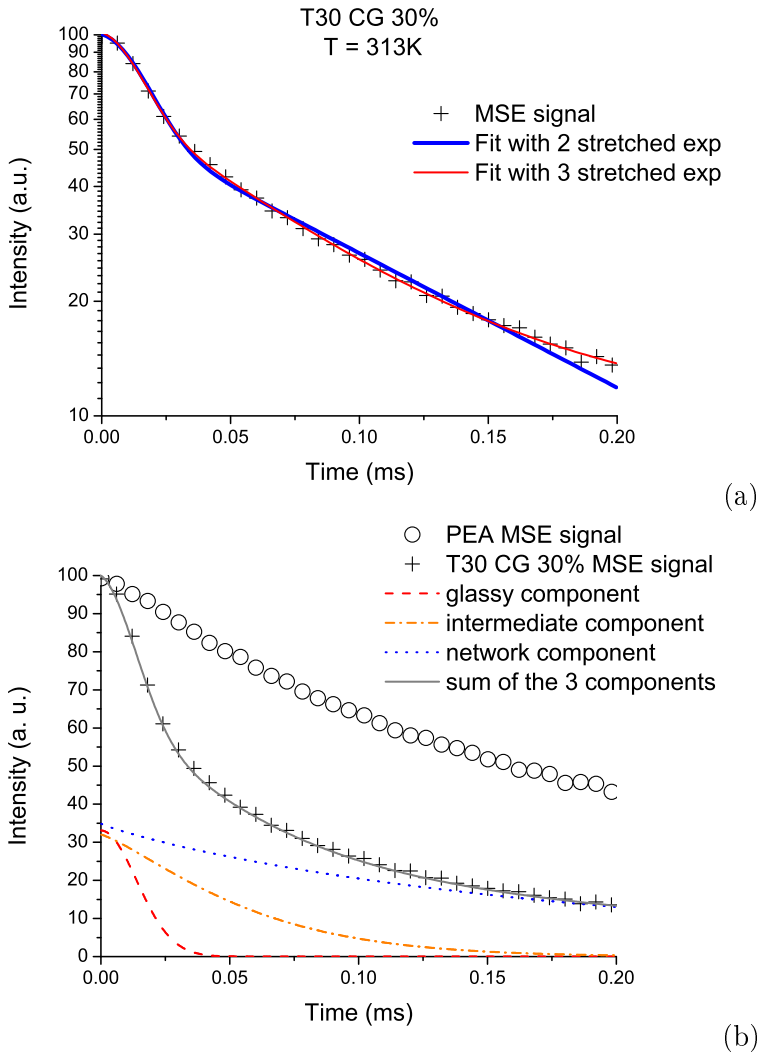

FIGURE 2.9 – MSE-FID signal as a function of the acquisition time for the T30 CG 30% sample at 313K fitted with the sum of 2 or 3 modified exponentials (a). Decomposition of the MSE-FID signal into 3 stretched exponentials (b).

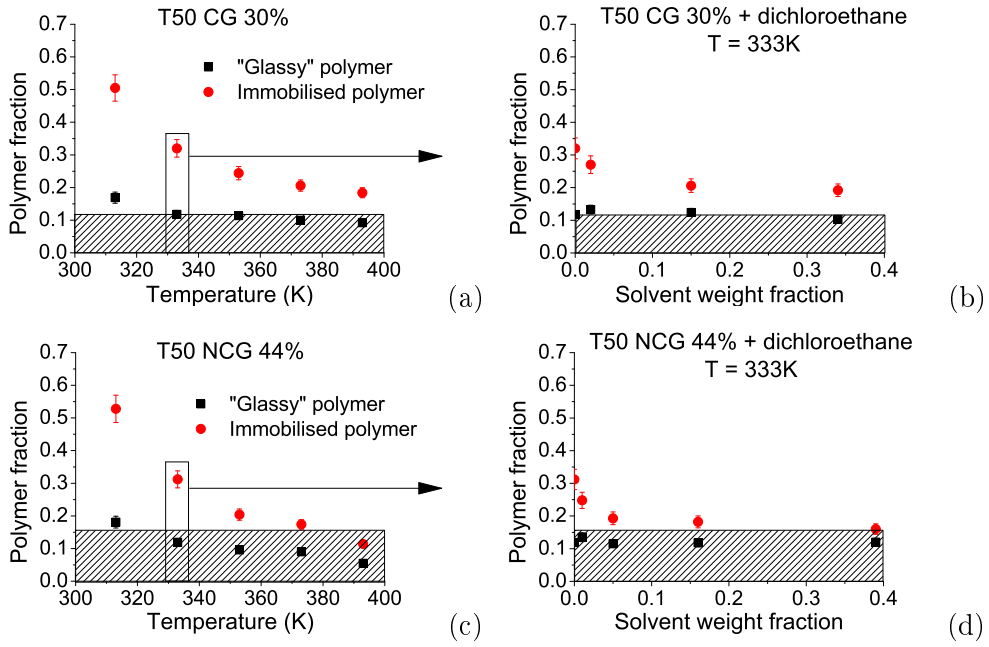

FIGURE 2.10 – Evolution of the immobilised polymer fraction as a function of the temperature (a) and (c) and as a function of dichloroethane weight fraction (b) and (d). The shaded areas correspond to the fraction of protons coming from the grafters and ethoxy groups on the silica particles (from elemental analysis). The boxes and arrows simply highlight the fact that the solvent effect has been studied at 333K, meaning that the first points (0% solvent) in the right figures correspond to the points in the boxes on the left figures.

polymer as a function of $T - T_g$. We see in Figure 2.11 that we indeed obtain master curves.

2.4.5 Influence of the silica content and of the grafting agent

The glassy and immobilised polymer fractions (a_g and a_g+a_i from eq.2.5) have been measured for all the samples at various temperatures and the results are plotted at each temperature in Figure 2.12 as a function of the silica specific surface (total silica surface per volume unit, $3\Phi/R_{Si}$ in m^{-1}, R_{Si} being the mean silica radius and Φ the silica volume fraction). The two sets of samples contain a fraction of immobilised polymer. Figure 2.12 shows that a covalent bond between the silica and the polymer matrix is not necessary to induce a gradient of T_g, an interaction - covalent or not - is sufficient. For the same silica specific surface, the NCG samples contain less immobilised polymer than the CG samples. This can be due to the different nature of the grafters - a stronger interaction in the case of covalent bonds which could lead to a larger range of interaction of the silica in the polymer network - but also to a different particles arrangement due to the different synthesis process used in each case (polymerisation without solvent for the CG samples, with solvent for the NCG samples).

At 313K, the interpretation of the plot is not clear and all the samples seem to show similar amounts of immobilised polymer. This is due to the fact that the temperature is too close to T_g, so that the FID decay shape of the PEA matrix cannot be separated well any more from the even more rigid surface material and the fits become ambiguous. The MSE-FID of pure PEA at 313K in Figure 2.6 (a) can in fact be fitted with either the given Anderson-Weiss function, or

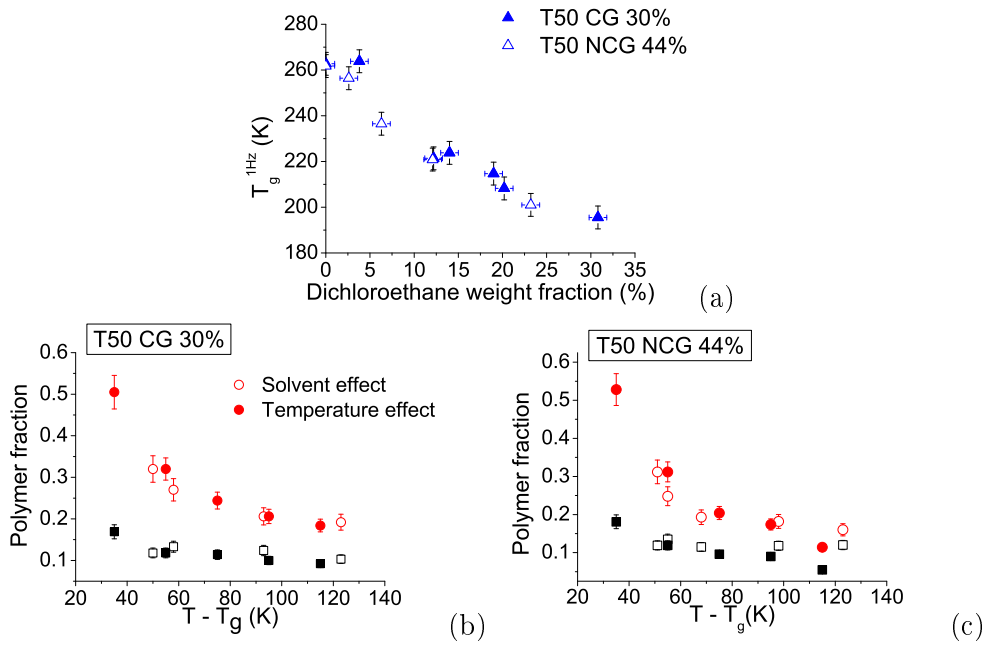

FIGURE 2.11 – Glass transition temperature as a function of the solvent weight fraction (a). Glassy (squares) and immobilised (circles) polymer fraction as a function of $T - T_g$ for T50 CG 30% (a) and T50 NCG 44% (b). Temperature (filled markers) and solvent (open markers) have the same effect on the polymer mobility.

a compressed exponential ($b > 1$), but also with a linear combination of a pure Gaussian and a pure exponential. The amount of immobilised polymer obtained at 313K is thus not only the polymer whose dynamics is modified by the proximity of the silica surface but it contains also part of the elastomer fraction approaching its glass transition.

Another important feature is that at high enough temperature (333 K to 393 K), the rigid polymer fraction is proportional to the silica specfic surface, so that the slope of the linear fit gives an approximate thickness of rigid polymer around the silica particles (Figure 2.12 (f)). In fact, two effects compensate each other : this approximate thickness is over-estimated because we do not take into account the curvature of the silica particles, but it is also under-estimated because it also misses the overlap effect when the particles are in average closer than the rigid thickness.

2.5 Cross-linking inhomogeneities : MQ NMR measurements

MQ experiments give an insight into the orientation of the polymer segments in the network and thus on the topological constraints like cross-links and entanglements. We will first see the effect of a change in cross-link density in a PEA matrix on the DQ build-up curves and then see that the two sets of filled samples show very different responses.

2.5.1 PEA matrix : evolution of the DQ signal with the crosslink density

First, the DQ build-up curves of PEA matrix with different cross-link densities are shown in Figure 2.13. Since the residual dipolar couplings are the origin of the appearance of a DQ

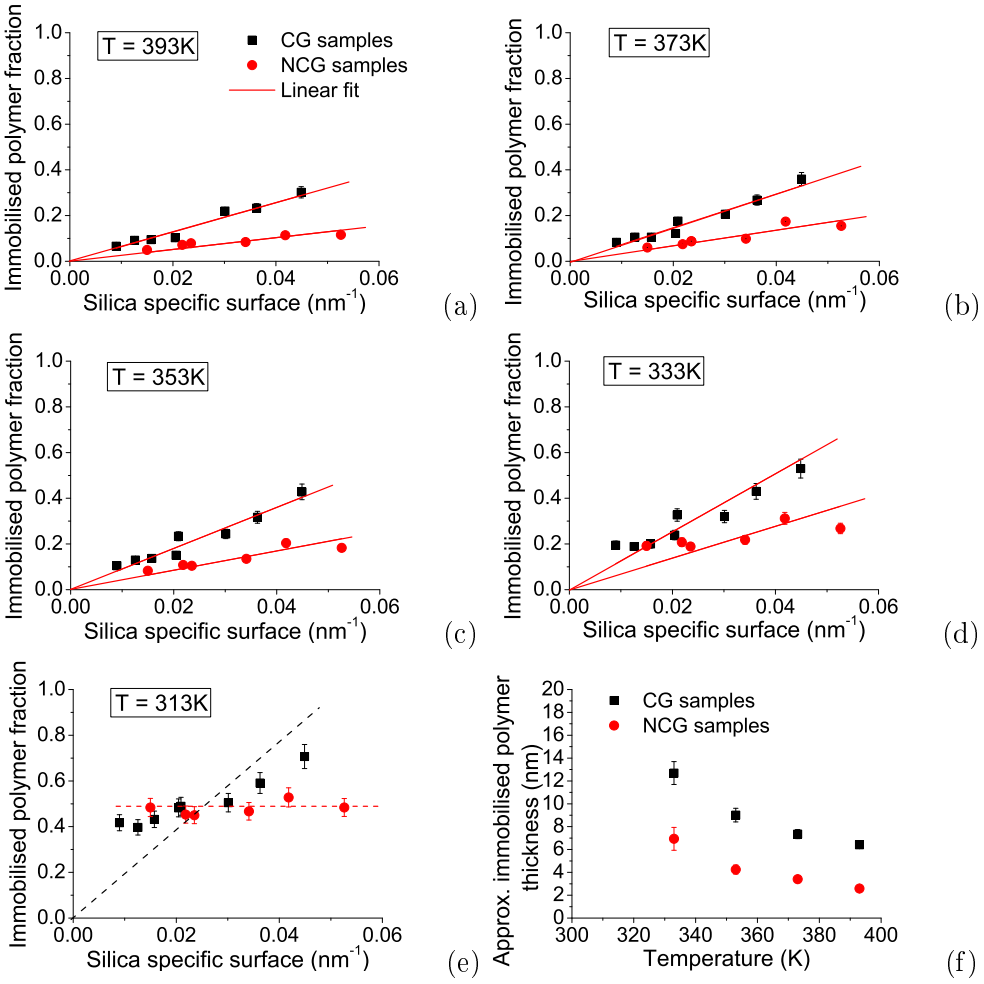

FIGURE 2.12 – Fraction of immobilised polymer as a function of the silica specific surface at 393K (a), 373K (b), 353K (c), 333K (d), 313K (e). For each set of samples, a linear fit of the experimental points is shown. The slopes of those curves give an approximate thickness of immobilised polymer, which is plotted as a function of the temperature in (f). At 313K, the temperature is too close to T_g and the linear fit is not possible anymore.

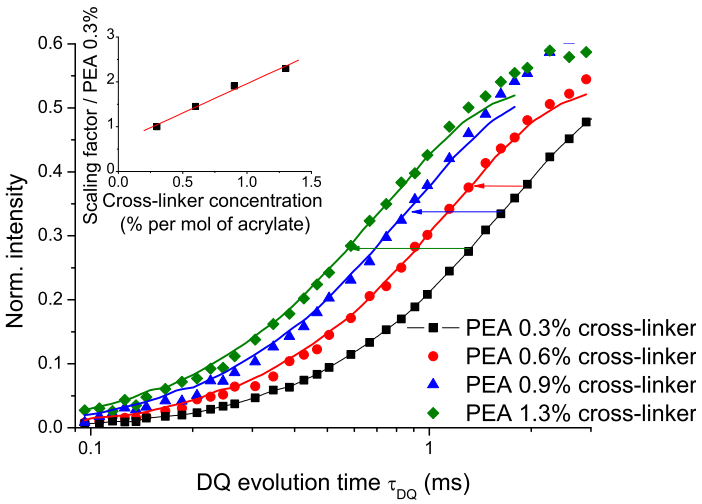

FIGURE 2.13 – DQ build-up curves for PEA matrix with various cross-link density (T = 393K). In the inset, the scaling factor applied to the reference PEA 0.3 mol% cross-linker curve to superpose it to the curve of the PEA matrix with a higher cross-link density. A higher cross-link density is thus seen as a shift (scaling on a linear scale) of the DQ build-up curve to the shorter times.

signal build-up and their strength is directly proportional to the cross-link density, it is clear that a higher cross-link density results in a time scaling of the DQ build-up curve in cases where the microstructure (homogeneity) of the networks is similar. If we take the PEA matrix with 0.3 mol% of cross-linker as the reference (that is the same quantity of cross-linker as used for the filled samples), we can fit the higher cross-linked PEA matrix by simply scaling this curve along the time axis (corresponding to an additive shift on a logarithmic scale). In the inset, we confirm that the scaling factor used depends linearly on the cross-linker concentration used in the synthesis. Note that we could in this case not use an analytical fit of the DQ build-up curves, as done in previous publications [62, 64] because of the inhomogeneous behavior of the PEA matrix due to its side chains ("spin system inhomogeneity"). A similar yet less serious complexity of the experimental response is for instance exhibited by styrene-butadiene-rubber with its different monomer units and the pending phenyl group, as discussed in ref. 64.

2.5.2 Filled elastomers : necessity of a MAPE filter to remove the immobilised polymer signal

The DQ experiments are performed at 393K, where the rigid polymer fraction is the lowest. However, this rigid polymer exhibits strong dipolar couplings, and we have to suppress its (weak) contribution to the DQ signal in order to study only the changes of the elastomer fraction. For that, we place a MAPE dipolar filter – similar to the MSE we used previously – before the DQ sequence. Increasing the filter length τ_{MAPE} leads to a rapid decrease in the Gaussian part of the signal until the response becomes more or less singly exponential (see Figure 2.14). For the sample with the largest rigid fraction (T30 CG 30%), we see that at $\tau_{MAPE} = 0.164$ ms only the elastomer response is present. The value of τ_{MAPE} was kept constant for all the filled samples

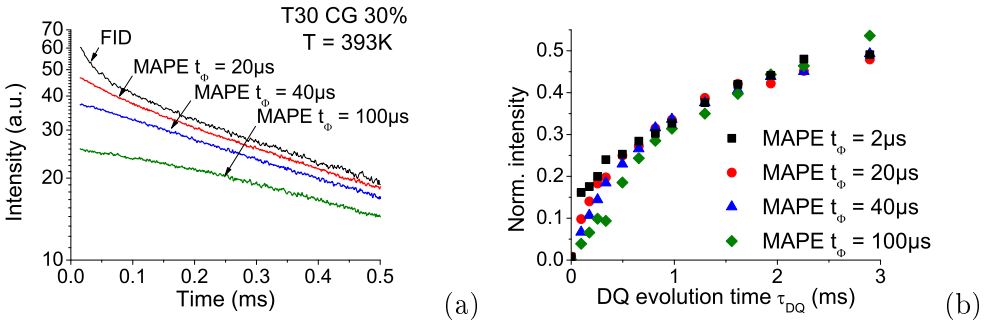

FIGURE 2.14 – Adjustment of the MAPE filter. As t_ϕ is increased in the MAPE filter, the solid-like response in the FID response (as a function of the acquisition time) decreases (a). The filter time chosen is $t_\phi = 40\mu s$, which corresponds to pure elastomer response. The corresponding DQ build-up curves are presented in (b).

and the DQ study will thus be limited to the elastomer part of the filled samples. It was checked that this filter had no influence on the DQ build-up curves of the PEA matrix.

As expected, the temperature also had no influence on the DQ build-up curves of the pure matrix networks, which is due to the normalization process explained in the "Samples and experimental methods" section. However, this is not the case for the filled samples. In effect, changing the temperature leads to a change in the amount of immobilised polymer and thus in the quantity of signal suppressed by the MAPE filter so that τ_{MAPE} would have to be adjusted to each temperature, in all cases with the criterion that the signal exhibits only one component. Here we will restrict our study to a fixed temperature of 393K.

2.5.3 Higher effective crosslink density for the CG samples

Figure 2.15 shows the DQ build-up curves of the NCG samples, compared with the reference PEA matrix. It shows that all the curves can be fitted with the slightly time-scaled (shifted) reference curve. It means that the elastomer part of the NCG samples is homogeneously cross-linked with an effective cross-linked density slightly above 0.3 mol% cross-linker.

The behavior of the CG samples is very different (see Figure 2.16). In this case, the DQ build-up curves are not superimposed on the reference and are shifted to shorter DQ evolution time, meaning that they are more cross-linked than expected. The DQ build-up curves could not be fitted with only the time-scaled DQ build-up curve of the PEA matrix, which means that the samples are not only more highly cross-linked, but also that they are not homogeneous. We can model the response of the CG samples by a sum of two pure-matrix components, time-scaled to a different degree. This shows that the use of a grafting agent like TPM creating covalent bonds between the silica particles and the matrix has an influence on the cross-link density around the silica particles. This is an observation that was not made in any conventional filled elastomer system [64]. We attribute this to the good particle dispersion, the homogeneous surface grafting density, and the consequently large volume fraction of affected material.

An attempt of quantification of the amount of polymer with a higher cross-link density has been made, however, we need to keep in mind that, due to the MAPE filter, we are probing only *part* of the polymer and that it is dependent on the τ_{MAPE} chosen. Although we set τ_{MAPE}

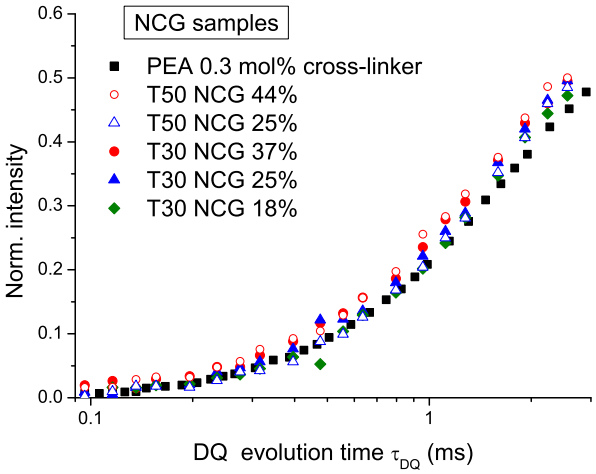

FIGURE 2.15 – The DQ build-up curves of the NCG samples can be fitted by the curve of the reference PEA matrix slightly shifted (time-scaled). The NCG samples are thus homogeneously cross-linked with an effective cross-linker concentration slightly above 0.3 mol%.

such that mostly the glassy part of the signal was suppressed, we of course have to consider that there is a smooth gradient in T_g, which is likely coupled to an inhomogeneity on the effective cross-link density.

For the fits, the scaling factors obtained were around 1.2 for the main component and ranged between 5 and 10 but with a rather high uncertainty for the other component. We thus decided to fix the second scaling factor to 7.5 (which corresponds approximately to 5 mol% of cross-linker, see Figure 2.6 (b)) and keep only two parameters free : the shift factor of the main fraction of the elastomer and the quantity of polymer with a higher cross-link density. The results are representative only of the elastomer fraction of each sample, but it can be expected that rigid (glassy) polymer located close to the silica particles has an even higher effective cross-link density. The total amount of highly cross-linked polymer would thus be the sum of the immobilised polymer fraction (determined by MSE-FID at 393K) and the fraction of elastomer with a higher cross-link density extracted from the fits. This quantity is obviously linked to the silica specific surface (see Figure 2.17).

2.6 Conclusion

In this study of model filled elastomers, we showed through MSE-FID NMR experiments the existence of a fraction of immobilised polymer and more precisely of at least three kinds of polymer mobility. This is in agreement with the existence of a *gradient* of polymer mobility, which can be interpreted as a gradient of glass transition temperature in the vicinity of the solid particles, as it has been shown for thin polymer films deposited on a substrate and interacting through hydrogen bonds [56]. An increase in the temperature or the addition of solvent both induce a decrease in the immobilised polymer fraction. In effect, in both cases $T-T_g$ is increased, either by increasing T or by decreasing T_g, and thus the polymer mobility is increased.

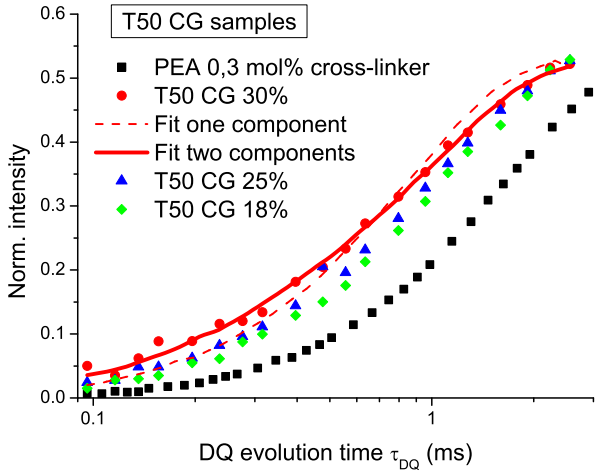

(a)

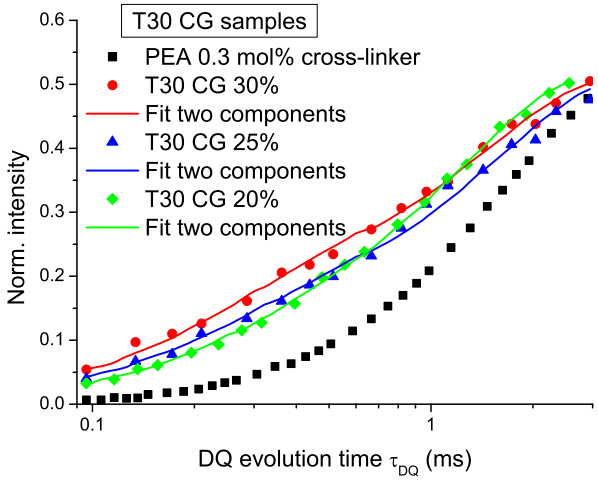

(b)

FIGURE 2.16 – The DQ build-up curves of the CG samples are not superimposed on the one of the reference PEA matrix meaning that the CG samples appear more cross-linked than the polymer matrix with the same amount of cross-linker introduced (0.3mol% to the monomer). In (a), the DQ build-up curve of the T50 CG 30% sample cannot be fitted with only one time-shifted PEA curve (thin line), we need to use a combination of two time-scaled PEA curves (thick line), meaning that the sample is heterogeneously cross-linked.

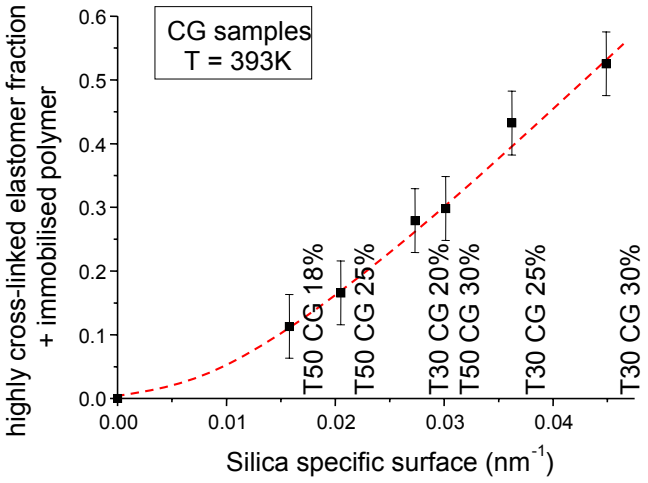

FIGURE 2.17 – Amount of highly cross-linked polymer plus immobilised polymer at 393K plotted as a function of the silica specific surface (scaling factor fixed to 7.5). The line is a guide for the eye.

The effect of the coupling agent has also been investigated. Whether the grafter creates a covalent bond between the filler or not does not change the overall behavior : in both cases there is a gradient of mobility, even if the amount of immobilised polymer is slightly less when the interaction between the filler and the polymer is not covalent.

MQ NMR experiments then pointed out the presence of a fraction of highly crosslinked polymer in the case of the covalently grafted samples but not for the non-covalently grafted samples. The presence of a highly crosslinked polymer fraction had not been previously detected in conventional systems and is most likely the result of the good particle dispersion in our model samples. It remains to be investigated in how far this effect is relevant for the reinforcement mechanisms in conventional (aggregated) filled elastomers, where the fraction of polymer in the vicinity of the fillers is obviously much smaller.

From those observations we can finally conclude that a connection – i.e. a covalent bond or a strong adsorption (as in the system PDMS-silica [72]) – between the filler and the polymer is not a necessary prerequisite for the existence of a gradient of T_g, even if it is probably responsible for a highly cross-linked polymer fraction. This indicates that the gradient of glass transition temperature is related more to the presence of an *interaction* between the fillers and the polymer than to a *connection* between them.

This study enabled the decomposition of the NMR signals of model filled rubbers into three parts with different mobilities : elastomer, glassy and intermediate. It also gives us the tools to go further in our interpretation and analyse the polymer dynamics directly in terms of T_g gradient around the fillers. In Chapter 3, we use the NMR signals of the pure elastomer at different temperatures and a T_g gradient model to describe the NMR signals of the filled samples.

Chapitre 3

Mise en évidence d'un gradient de température de transition vitreuse autour des charges par des mesures de RMN et DSC

Ce chapitre met en évidence l'existence d'un gradient de température de transition vitreuse autour des particules solides. Il s'agit d'un manuscrit soumis à PRL.

Sommaire

T_g gradient in nanocomposites : evidence by NMR and DSC

This chapter shows the existence of a gradient of glass transition temperature around the solid particles. It is a manuscript that has been submitted to PRL.

3.1 Introduction

The question of the existence of a gradient of glass transition temperature T_g in elastomers near a solid surface has been debated for many years now. In thin polymer films first, Keddie *et al.* [29], Fryer *et al.* [56] or Rotella *et al.* [73] showed a modification of T_g depending on the interaction between the solid surface and the polymer. An increase in T_g is observed near the surface in the case of a strong interaction and a decrease in the case of a weak interaction. But there is thus no clear consensus on the existence of a T_g gradient in thin films as of now [39] and it is the same in the field of filled elastomers. From the 70's, NMR experiments have shown the existence of different polymer mobility domains in filled elastomers [20, 23] and Struik has pointed out the presence of glassy polymer in those systems through aging experiments [27]. Those observations can be interpreted as the existence of an increase in T_g close to the surface of the solid particles due to attractive interactions between the fillers and the elastomer. Using a T_g gradient approach and combining NMR and mechanical experiments, we also have indirectly shown that this interpretation would correctly describe the behavior of model filled elastomers [32, 55]. However, this explanation has not reached a consensus and some authors claim that even if the polymer chains adsorbed onto the fillers can be seen as immobilized, it has no effect on the segmental dynamics of the chains and thus on their glass transition temperature [40–42].

In this study, we show that in the case of model filled elastomers we can explicitly evidence the existence of a T_g gradient around the fillers. This conclusion is based on the interpretation of recent polymer dynamics measurements both in solid state ^1H NMR and in Differential Scanning Calorimetry (DSC). In effect, we recently showed that, in model filled rubbers, part of the polymer had a slowed-down dynamics [74]. We show here that this "immobilized" polymer is in fact glassy and that it is due to a T_g gradient near the filler surface. We will demonstrate that the NMR relaxation curves of the model filled elastomers can be fitted with the ones the pure elastomer matrix taking into account a T_g gradient around the fillers. We will show the robustness of this model by its ability to describe the behavior of the systems even in presence of solvent and to predict their behavior in DSC - T_g measurement and physical aging. This is the first time we explicitly use a T_g gradient model to interpret data and not simply a core-shell approximation.

3.2 NMR measurements : determination of the parameters of the T_g gradient model

Our model samples are composed of a poly(ethyl acrylate) (PEA) matrix with monodispersed silica particles with a diameter of 28, 42 or 87 nm, grafted with either a coupling agent creating a covalent link between the silica and the polymer (TPM : 3-(trimethoxysilyl)propyl methacrylate) or a covering agent shielding part of the hydrogen bonds between the residual -OH groups on the silica surface and the polymer (C8TES : *n*-octyltriethoxysilane) [65]. For PEA, T_g = 253 K at 1 Hz and 273 K at NMR frequencies around 10 kHz, following the WLF law.

We will first show that we can fit the NMR relaxation curves of the filled rubbers using simply the NMR curves of the pure PEA matrix with a T_g gradient. We base our interpretation on the

T_g gradient model proposed by Long and Lequeux [31], following the work done in thin films by Fryer *et al.* [56]. In the case of strong interactions between the polymer and the surface, the gradient can be written as follows

$$T_g(z) = T_g^{\infty}\left(1 + \frac{\delta}{z}\right) \tag{3.1}$$

where z is the distance from the solid surface, T_g^{∞} the glass transition temperature in the bulk and δ the characteristic length of the gradient.

The fitting method consists thus in integrating the PEA response around an isolated particle, taking into account the T_g gradient :

$$M^{FR}(T,t) = \frac{\int_{V_{tot}} M^{PEA}(T - T_g(z), t)\mathrm{d}V(z)}{V_{tot}} \tag{3.2}$$

The volume of integration corresponds to the mean polymer volume per silica particle : $V_{tot} = \frac{1-\phi_{Si}}{\phi_{Si}} 4/3\pi R_{Si}^3$, where R_{Si} is the silica particle radius and ϕ_{Si} the volume fraction of silica in the sample. Of course this is only a mean value and it is thus not a very accurate but it will not have any major consequence on our calculations since the most important part of the integral is the one close to the silica surface, where the polymer chains are immobilized.

Moreover, we have to take into account the presence of the grafters in our model samples. Since they are covalently attached to the silica surface, the grafters are mainly seen as immobilized, as it has been shown by NMR in Ref. [74]. We will thus consider a T_g gradient starting from a distance e_0 from the solid surface. The origin of z in equation (5.5) has to be interpretated as the distance $R_{Si} + e_0$ from the center of the particule.

To apply our fitting method we then need a description of the NMR curves of the pure PEA matrix at various temperatures. We have previously shown that the NMR relaxation of the PEA matrix - measured with a Magic Sandwich Echo sequence (MSE) that refocuses the Free Induction Decay (FID) - can be fitted with the Andersen-Weiss equation [74]

$$M^{PEA}(T,t) = \exp\left[-M_2\tau_c(T)^2\left(e^{-t/\tau_c(T)} + \frac{t}{\tau_c(T)} - 1\right)\right] \tag{3.3}$$

The parameter M_2 is found to be 5500 ms^{-2}, and τ_c depends on the temperature and can be fitted according to the Vogel-Fulcher relation

$$\tau_c(T) = \tau_0 \exp\left(\frac{A}{T - T_0}\right) \tag{3.4}$$

where $A = 1260$ K^{-1} , $\tau_0 = 3.10^{-4}$ μs and $T_0 = 156$ K. The temperature T_0 would be expected around $T_g + C_2^g \simeq T_g +$ 50 K $\simeq$ 200 K [75]. The discrepancy can be attributed to the fact that the values taken for τ_c are only apparent values and are rather inaccurate at lower temperatures due to the influence of beta process. Nevertheless, our aim is to simply to describe the NMR signal of the PEA at any given temperature and those equations give a good representation of the data measured.

In the following, we will consider the fits until the time $t = 0.04$ ms, which is a time span that includes both the "immobilized" response with a characteristic time of 0.02 ms and the elastomer

response. It is thus an appropriate time span to do describe the polymer behavior taking into account in an equal manner the immobilized response and the elastomer one. We also take into account the loss in intensity due to the MSE sequence [74]. At last, we know how to analytically describe the PEA relaxation at any temperature between T_g - 20 K and T_g + 120K.

The fitting method consists then in integrating the PEA response around a particle :

$$\begin{aligned} M^{FR}(T,t) &= \frac{V_{imm.}M^{PEA}(T-T_g^{max}(z),t)}{V_{tot}} \\ &+ \frac{\int_{V_{gradient}} M^{PEA}(T-T_g(z),t)\mathrm{d}V(z)}{V_{tot}} \end{aligned} \tag{3.5}$$

where $V_{imm.} \simeq 4\pi R_{Si}^2 e_0$, $\mathrm{d}V(z) = 4\pi(R_{Si}+e_0+z)^2\mathrm{d}z$, $V_{gradient} + V_{imm.} = V_{tot}$ and $T_g(z)$ is described by Eq.(5.5). In practice, we use a cut-off in $T_g(z)$ at $T_g^{max} = T$ + 20K to avoid the divergence, without noticeable sensitivity on the computed signal (see Figure 3.1). The first term

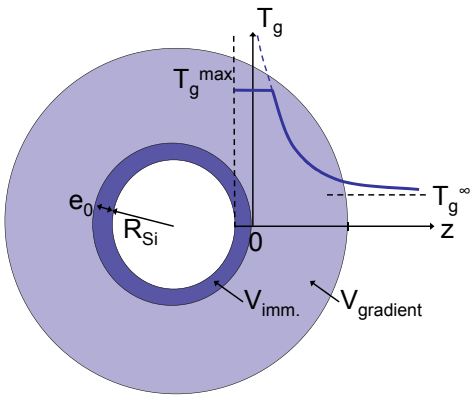

FIGURE 3.1 – Schematic representation of the glass transition temperature gradient in the vicinity of a particle, with a cut-off at T_g^{max}. The volume V_{imm} represents the immobilized protons at the surface of the particle, corresponding to a thickness e_0.

of this equation describes the reponse of the immobilized molecules at the surface of the filler. They are the protons belonging either to the grafters or to the polymer chains very near the grafters. We describe their dynamics by the one of the matrix 20K below its T_g, which is enough to account for their immobility in the experimental range of time [74].

First, we fit at the same time the whole set of experimental NMR measurements at various temperatures between 313 and 393 K. The standard deviation is calculated for each parameter pair (e_0, δ) and a minimum is clearly found (see inset of Figure 3.2(a)). We can see in Figure 3.2(a) that the fitting curves corresponding to this parameter pair describe very well the experimental measurements. This has been done on various samples, with different silica amounts and sizes and different grafters with similar results. Thus, with only two parameters, we can fit five curves corresponding to behaviors at different temperatures. For the first time it shows explicitly that a T_g gradient can phenomenologically describe very well the polymer dynamics in filled elastomers. The typical value we found for e_0 is 2 nm in the case of the grafter TPM, which is in agreement with the expected grafter thickness. In the case of the grafter C8TES, the value obtained is smaller, around 0.5 nm, because this grafter is expected to be more mobile since

it is not covalently linked to the polymer. This is in agreement with the previous results from Ref.[74]. Regarding the characteristic length of the gradient δ, we found it to be between 0.1 and 0.2 nm for all the samples, which is of the order of magnitude that we had previously estimated with a core-shell approximation [33]. In order to test more accurately the value of δ, we take e_0 as deduced from the previous fit and examinate whether δ depends on the temperature. Whereas the previous fit was done for all the temperatures at the same time, here we fit the NMR curves independently at each temperature, with the parameter δ free. In the inset of Figure 3.2(b) we show that no significant change in δ is found within our temperature range, neither with the TPM grafter, nor with the C8TES. The coefficient δ, characteristic of the interaction between the filler surface and the the polymer, is thus independent of the temperature between T_g + 40K and T_g + 120K. This proves that the polymer dynamics in filled elastomers can be described by a gradient of glass transition temperature around the fillers.

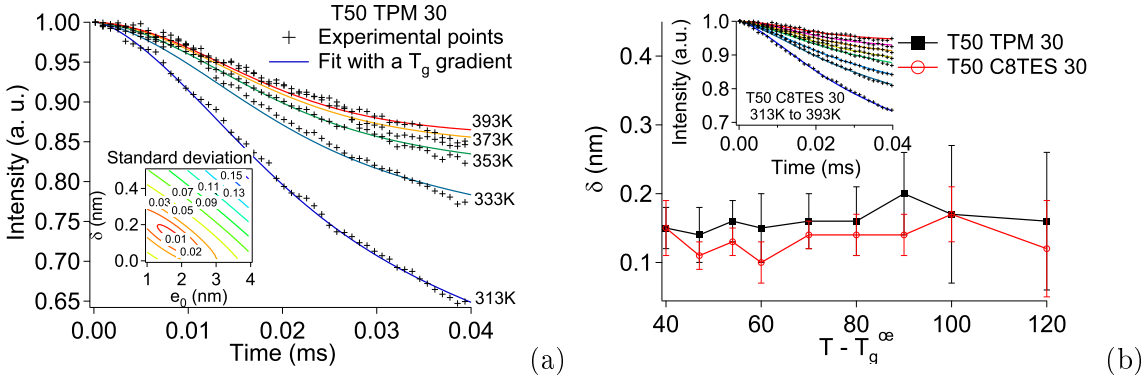

FIGURE 3.2 – MSE refocused Free Induction Decay for filled elastomers fitted with the MSE curves of the PEA matrix taking into account a T_g gradient around the fillers. The crosses are used for the experimental signals and the lines for the fits. (a) The fit is done at all the temperatures with the parameters (e_0, δ) minimizing the standard deviation with the experimental points (inset). For the sample considered here, R_{Si} = 21.5 nm and ϕ_{Si} = 0.216. In the inset, the standard deviation calculated for each parameter pair shows a minimum. (b) The fit is done independently at each temperature, with e_0 fixed from the previous fit. δ is thus the only free parameter and it is determined for each temperature. For the sample considered here, R_{Si} = 21 nm and ϕ_{Si} = 0.179. We see that δ does not depend on the temperature in this temperature range, neither with the TPM nor with the C8TES grafters.

3.3 Effect of solvent addition

Moreover, we will see that this description is still suitable in the case of the addition of solvent, which is known to decrease the T_g of the elastomer. With this T_g gradient model, we can correlate the change in the NMR relaxation curves with the change in the T_g measured in DSC, both for the PEA matrix and the filled elastomers.

First, we look at the pure PEA matrix in presence of solvent. We can check that the evolution of the parameter τ_c with the temperature is simply shifted due to the addition of solvent. Figure 3.3(a) shows that all the curves can be superimposed if we take into account a shift in temperature

$\Delta T_g(\phi)$. Moreover, Figure 3.3(c) shows a good agreement between the T_g shift measured here and the one measured in DSC.

Then, we can look at the NMR relaxation curves of the filled rubbers and fit them with the parameter pair (e_0, δ) that has been obtained in the previous dry case, and keep only one free parameter, the glass transition temperature in the bulk T_g^∞, which is expected to change in presence of solvent. We see in Figure 3.3(b) that $T_g^\infty(\phi)$ decreases in proportion to the amount of solvent ϕ as expected. We see in Figure 3.3(c) that the T_g shifts deduced from the T_g gradient model and the ones measured in DSC are very well correlated. This is another evidence that a T_g gradient model describes well the polymer dynamics in filled rubbers.

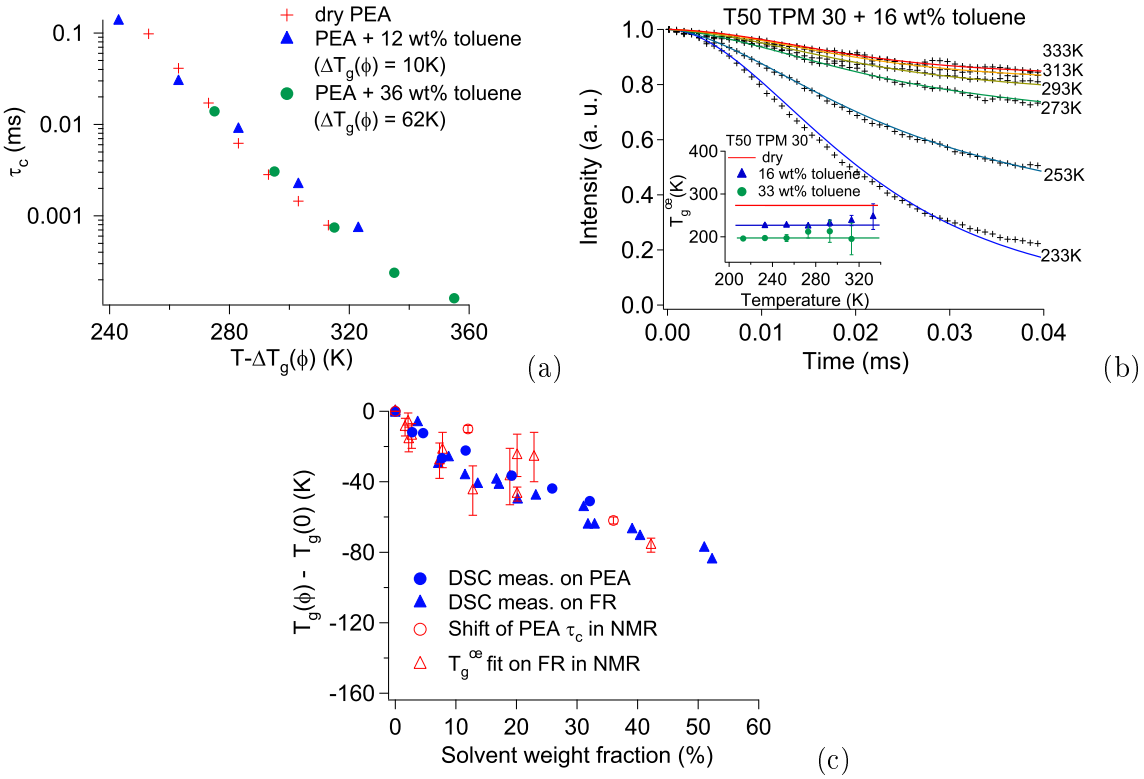

FIGURE 3.3 – (a) *PEA matrix.* The parameter $\tau_c(T)$ for the dry PEA matrix and the matrix with $\phi = 12$ and 36 $wt\%$ toluene are superimposed when the x-axis is shifted by a factor $\Delta T_g(\phi)$. This value is thus the T_g shift due to the presence of solvent, as measured by NMR. We see in (c) that it corresponds well to the T_g shift measured in DSC. (b) *Filled elastomers.* The MSE refocused Free Induction Decay of filled samples with solvent can be fitted with the T_g gradient model with only one free parameter : the T_g^∞ which is the T_g in the bulk PEA with solvent. The parameter pair (e_0, δ) is not expected to change with the addition of solvent and is thus fixed at its value in the dry case. The sample used is the same than in Figure 3.2(a). In the inset, T_g^∞ at different temperatures for 16 and 33 wt% toluene. (c) *PEA and filled elastomers.* Comparison between T_g shifts measured in NMR and in DSC. FR = Filled Rubbers. For the PEA, the T_g shift is measured from the shift applied to $\tau_c(T)$ and for the filled elastomers, it comes from the fits with the parameter T_g^∞.

3.4 DSC measurements : T_g determination and physical aging

Finally, another classical signature of the glass transition in elastomers is their DSC response so we have examined the validity of our model with this technique.

First, in Figure 3.4(a) we compare the T_g measured on a filled sample with the prediction from the T_g gradient model. The results are obtained at a cooling/heating rate of 10 K.min^{-1}. In a similar manner than previously, we integrated the heat capacity of the PEA matrix $c_p^{PEA}(T-T_g(z))$ around one silica particle, taking into account the gradient $T_g(z)$ with the parameters determined previously from the NMR relaxation curve. There is thus no adjustable parameter and we can see that the prediction is in very good agreement with the experimental DSC measurement, both in the amplitude of the transition and in the shift of T_g.

In the end, we will show the robustness of the model with the fit of the heat capacity of filled rubber after aging from the DSC measurements of the pure elastomer matrix. For that we measured $c_p^{PEA}(T_a, T)$ for the PEA matrix after aging 10 hours at various temperatures T_a between 223 and 253 K (see Figure 3.4(b)). For convenience, we worked on the difference $\Delta c_p(T_a, T) = c_p^{aged}(T_a, T) - c_p^{unaged}(T)$. As previously, we fit the behavior of a filled sample by integration around a filler

$$\begin{aligned} \Delta c_p^{FR}(T_a, T) &= \frac{V_{imm.} \times \Delta c_p^{PEA}(T_a - T_g^{max}, T - T_g^{max})}{V_{tot}} \\ &+ \frac{\int_{V_{gradient}} \Delta c_p^{PEA}(T_a - T_g(z), T - T_g(z)) \mathrm{d}V(z)}{V_{tot}} \end{aligned} \tag{3.6}$$

Here, we fix the parameter e_0 to the value found in NMR and we let δ free. We see in Figure 3.4 (c) that the fit from the T_g gradient model is rather close from the experimental measurement done in DSC, with a parameter δ very close from the one found in NMR (~ 0.15 nm). If the temperature of the peak is very well described, the amplitude of the peak is more difficult to reproduce since it also depend on the quality of the contact of the sample with the heating plate during the DSC measurement, which is hardly reproducible from a sample to another. The agreement between the experimental curve and the prediction confirms nevertheless that this model of T_g gradient around the particles is able to describe the polymer relaxation seen through NMR experiment or through DSC experiment with the same parameters.

3.5 Conclusion

We see through all those different experiments that the behavior of filled elastomers can be very well described using the behavior of the pure elastomer matrix and a T_g gradient in the vicinity of the fillers. This is the first direct interpretation of experimental data using explicitly a gradient and the strength of the model has been shown through its ability to describe both NMR measurements with and without solvent and DSC measurements.

As a conclusion, the amplitude of the slowing down of the polymer in nanocomposites has to be interpretated as a distribution of glass transition temperatures following the $T_g^{\infty}(1 + \delta/z)$ law.

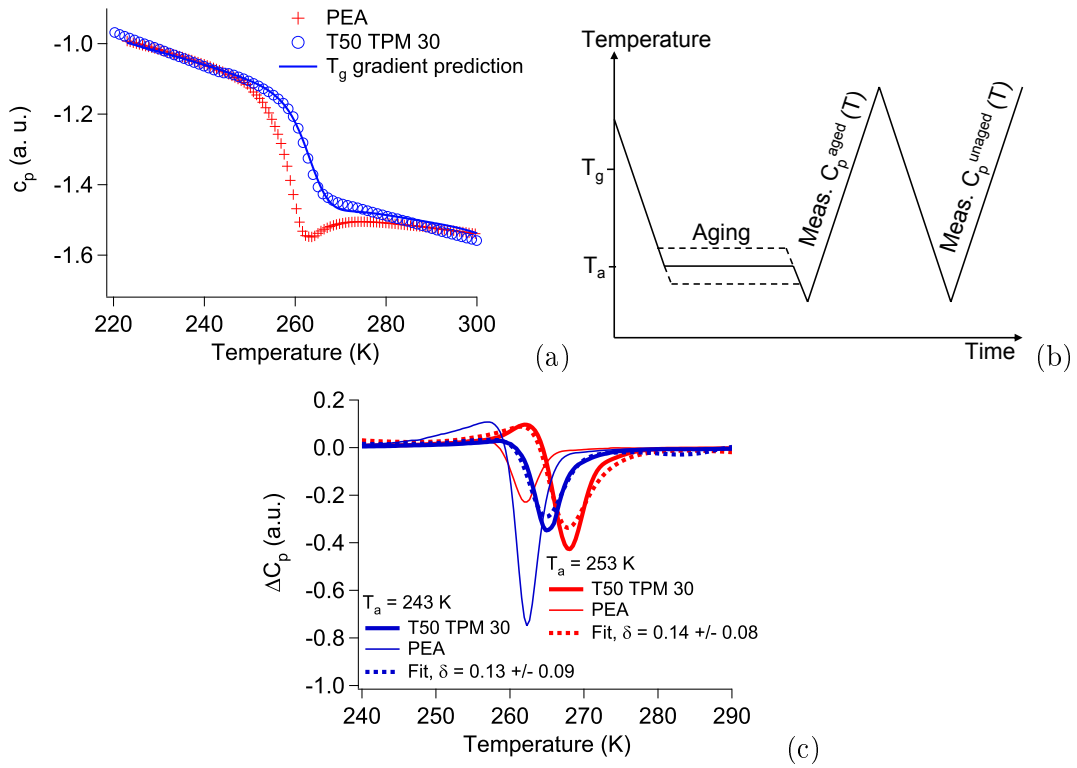

FIGURE 3.4 – (a) Heat capacity measurement for the pure PEA matrix (crosses) and a filled sample (open circles). The sample is the same than in Figure 3.2(a). The line is the prediction for the filled sample made from the behavior of the pure matrix and a T_g gradient. (b) Thermal profile used for the aging experiments. The cooling and heating rates are all 10 K.min^{-1}. (c)$\Delta c_p(T_a, T)$ measured for the PEA matrix (thin line) and the same filled sample than in (a) (thick line) aged at the temperatures 243 and 253 K. The fit obtained with the T_g gradient model is plotted with a dashed line. The parameter e_0 was fixed at the value obtained from the NMR fit and δ was free. The values found for δ are very close to the ones obtained from the NMR fit.

In this Chapter we have described the polymer dynamics in filled elastomers in terms of T_g gradient around the fillers. Using a T_g gradient model and the behavior of the pure elastomer matrix, we have been able to describe the NMR signals of the filled samples at different temperatures and with the addition of solvent, as well as the behavior of the samples in calorimetry. In Chapter 4, we are interested in the mechanical behavior of the samples. In particular, we examinate whether their non linear behavior at large strain amplitude can be related to the presence of glassy polymer.

Chapitre 4

Comportement mécanique des échantillons modèles : deux types de non linéarités

La première partie de ce chapitre présente l'analyse des signaux de contrainte lors de sollicitations sinusoïdales et a été publiée en 2010 : A Papon, H Montes, F Lequeux, and L Guy. Non linear rheology of model filled elastomers. Journal of Polymer Science Part B : Polymer Physics, 48(23), 2490-2496, 2010.

La deuxième partie compare ces résultats expérimentaux aux simulations obtenues avec le modèle de renforcement par ponts vitreux de S Merabia, P Sotta et D Long. Il s'agit d'un manuscrit d'article rédigé en collaboration avec ce groupe.

Sommaire

Mechanical behavior : two types of non linearity

In the first part of this chapter, we describe the stress signal analysis during oscillatory shear experiments. This part has been published in 2010 : A Papon, H Montes, F Lequeux, and L Guy. Non linear rheology of model filled elastomers. Journal of Polymer Science Part B : Polymer Physics, 48(23), 2490-2496, 2010.

In the second part, we compare those experimental results to the simulations obtained with the glassy bridges reinforcement model of S Merabia, P Sotta and D Long. It is a manuscript written in collaboration with this group.

Note : In this Chapter, the samples with TPM grafters are called CG (= Covalently Grafted) and the ones with C8TES grafters are called NCG (= Non Covalently Grafted). Here is the correspondence with notations of Table 1.2.

Sample name in Table 1.2	Sample name in Chapter 4.1
MIST TPM 30	T30 CG 3
MIST TPM 25	T30 CG 2
MIST TPM 18	T30 CG 1
T50a TPM 30	T50 CG 3
T50a TPM 25	T50 CG 2
T50a TPM 18	T50 CG 1
T100 TPM 30	T100 CG 3
T100 TPM 25	T100 CG 2
T100 TPM 18	T100 CG 1
T30 C8TES 37	T30 NCG 3
T30 C8TES 30	T30 NCG 2
T30 C8TES 25	T30 NCG 1
T50b C8TES 44	T50 NCG 3
T50b C8TES 30	T50 NCG 2
T50b C8TES 25	T50 NCG 1

Please also note that the characteristic size of the T_g gradient model is called β in section 4.2, instead of δ in the rest of the thesis.

4.1 Two types of non linearity : Payne effect but also strain-stiffening and shear-thinning

Filled elastomers are composites obtained by dispersing solid fillers - typically carbon black or silica particles - into an elastomer matrix. This is a very efficient way of improving the properties of rubber : it increases its elastic modulus as well as its fracture and abrasion resistance. It is clear that this is not a simple geometrical effect due to the presence of a solid fraction into the polymer, but a consequence of the modification of the polymer dynamics near the interface with the fillers [4, 10, 11, 14]. One example of this complex behavior is the well-known Payne effect [3, 9, 76–83] : whereas unfilled elastomers exhibit a constant elastic modulus for strain amplitudes up to 100% during cyclic strain experiments, filled rubbers show a significant decrease in their elastic modulus for strain amplitudes typically from a few percents. It is often assumed that in this strain domain, filled elastomers exhibit a quasi-harmonic behavior. It means that under sinusoidal solicitation, they have a quasi-sinusoidal response [4, 84].

In this paper, we will show that for some samples however the non linearity in the response is significant - that is, a sinusoidal strain give rise to a non sinusoidal stress - and that we need to take it into account so as not to loose information. We base our analysis on the method developed by Cho et al. [85] to describe Large Amplitude Oscillatory Shear (LAOS). This method - described in the next section - allows the decomposition of a non linear stress signal into an elastic and a viscous part. Then, we extract in each part a linear and a non linear term. This method enables us to decouple two phenomena that are superimposed in the mechanical response of our filled rubbers : the Payne effect and a strain-stiffening phenomenon. We also observe a correlation between the two effects and show that strain-stiffening has several intricate origins, most probably including Payne effect and finite extensibility of polymer chains confined between solid particles.

4.1.1 Background on Large Amplitude Oscillatory Shear analysis

LAOS is the study of materials through the application of large sinusoidal strains. When the strains are large enough, the response of the material becomes non linear, meaning that it cannot be described simply by sinusoidal waves. There are several ways of describing non linearity. The first one is the Fourier Transform analysis. In that case, the non linearity is described by the amplitude of the higher harmonics [86–93]. Otherwise, a graphical representation of the non linearity can also be obtained with Lissajous curves. But in both cases, it is hard to find an interpretation of the information obtained and to link it to the physical properties of the material.

Cho's method [85] is derived from a generalization of the linear regime. In the linear regime, the storage modulus G' and the loss modulus G'' describe the elastic and viscous behavior of the material and depend only on the strain amplitude in a cyclic solicitation. In the non linear regime however, when the response of the material is not a simple sine wave, those moduli cannot be extracted simply. That is why Cho introduces a generalized storage and loss moduli with a physical meaning. We will start explaining the method in the linear regime and then extrapolate the non linear case.

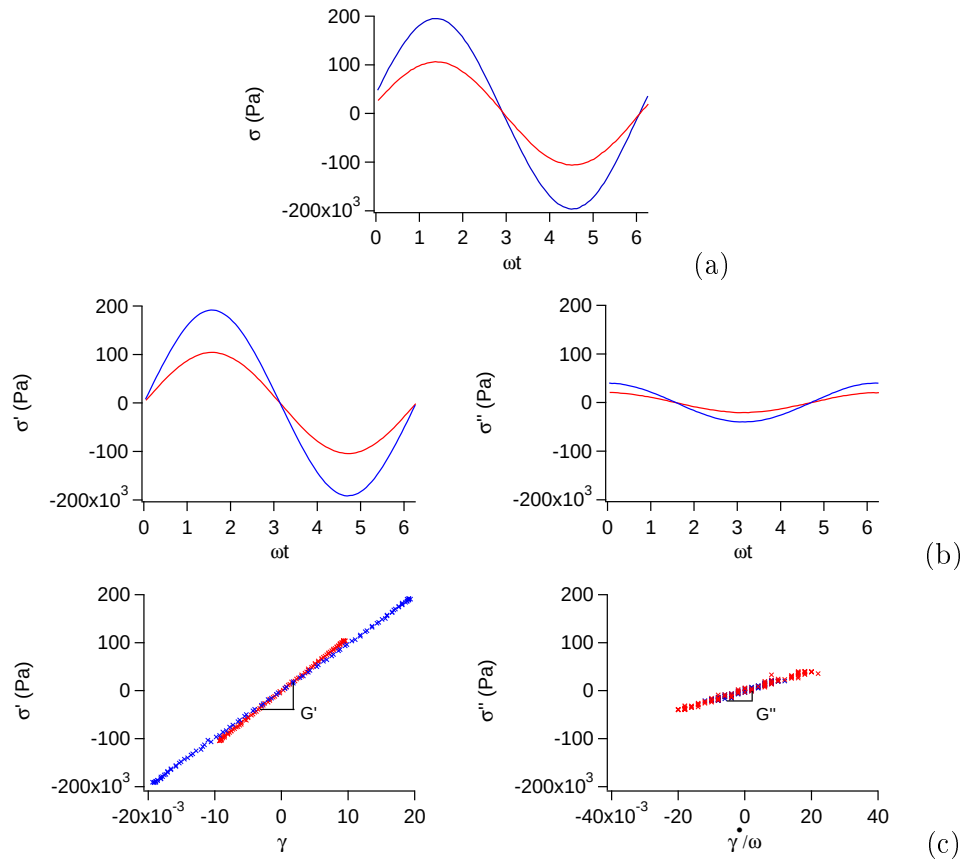

FIGURE 4.1 – Cho's decomposition in the linear case for two different strain amplitudes (γ_0 = 1% and 2%, sample T50-NCG-3). Stress σ as a function of ωt during one strain cycle (a) and its decomposition into odd (σ' - elastic) and even (σ'' - viscous) parts (b). σ' and σ'' plotted as a function of γ and $\dot{\gamma}/\omega$ respectively are straight lines with slopes equal to G' and G'' respectively (c).

In the linear case, we classically write the stress as :

$$\sigma(t) = G'\gamma(t) + G''\dot{\gamma}(t)/\omega \tag{4.1}$$

The total stress is thus the sum of an elastic stress $\sigma' = G'\gamma$ and a viscous one $\sigma'' = G''\dot{\gamma}/\omega$. If the strain applied is a sine wave $\gamma = \gamma_0 sin(\omega t)$, the elastic stress is the part of the signal in phase with the strain - that is a sine wave too - and the viscous stress is the part in phase with $\dot{\gamma}$ - that is a cosine wave. If we put it in other words, the elastic stress is the odd part of the stress and the viscous stress is the even part. Moreover, we see that if we plot the elastic stress $\sigma' = G'\gamma$ as a function of γ for one cycle of solicitation, we will obtain a straight line with a slope equal to G'. Similarly, $\sigma'' = G''\dot{\gamma}/\omega$ plotted as function of $\dot{\gamma}/\omega$ will give a straight line with a slope equal to G''. This situation is described in Figure 4.1.

From geometrical considerations, Cho extrapolates this decomposition method to the non linear case. Applying a sinusoidal strain $\gamma = \gamma_0 sin(\omega t)$ in this context, one measures a non linear but periodic stress $\sigma(t)$. It can thus be decomposed in a unique way into the sum of its odd -

$\sigma'(t)$ - and even - $\sigma''(t)$ - parts :

$$\sigma(t) = \sigma'(t) + \sigma''(t) \tag{4.2}$$

with

$$\sigma'(t) = (\sigma(t) - \sigma(-t))/2 \tag{4.3}$$
$$\sigma''(t) = (\sigma(t) + \sigma(-t))/2 \tag{4.4}$$

Cho then introduces the generalized moduli Γ' and Γ'' describing the elastic and viscous behavior of the sample similarly to the linear case :

$$\sigma'(t) = \Gamma'\gamma(t) \tag{4.5}$$
$$\sigma''(t) = \Gamma''\dot{\gamma}(t)/\omega \tag{4.6}$$

In the linear case, the generalized moduli correspond thus exactly to the storage and loss moduli G' and G'' and they only depend on the strain amplitude. In the non linear case however, the moduli also depend on the value of $\gamma(t)$ and $\dot{\gamma}(t)$ inside one cycle of strain, meaning that σ' vs γ and σ'' vs $\dot{\gamma}/\omega$ will not be straight lines anymore. It will thus enable the analysis of the viscoelastic behavior of a sample inside each cycle.

This method has the advantage over a simple harmonic decomposition to give a more physical and visual interpretation of the results. It has already been used to analyze many viscoelastic fluids (gastropod pedal mucus, worm-like micelle solution [94, 95], fibrin gels [96], PDMS [97]and amphiphilic polymer solution [98]). Here we use it to analyze the non linear behavior of filled elastomers. Inside one cycle of high strain, we could observe strain-stiffening and shear-thinning behaviors, similar to what observed Ma [99] with keratin and Xu et al. [100] and Semmrich et al.[101] with actin filament networks.

4.1.2 Signal analysis : elastic/viscous and linear/non linear decompositions

We performed the mechanical measurements on an Anton Paar MCR 501 rheometer in simple shear strain with a plate-plate geometry. The samples were cylinders of 8 mm in diameter and 2 mm thick and were glued on the rheometer plates with a cyanoacrylate glue (Loctite 406). The measurements were done at $30°C$ ($= T_g + 50\ °C$) and 0.1 Hz. The rheometer was interfaced with a computer so that the strain and stress signals could be directly recorded and analyzed. The samples characteristics are given in Table 4.1.

Decomposition into elastic and viscous parts

A sinusoidal strain is applied to the samples and the amplitude is increased progressively. The stress and strain signals are recorded. For each strain amplitude, we wait for the transient regime to be over before analyzing the signal (about 20 cycles). We will show here the curves obtained for the sample T50-CG-3 as an example, the general behavior being similar for all the samples (Figure 4.2). At high strain, it is clear that the stress is not a sinusoidal wave anymore,

TABLE 4.1 – Samples characteristics. NCG = Non covalently grafted (C8TES grafters), CG = Covalently grafted (TPM grafters). h is the surface-to-surface distance between particles determined from SANS measurements with a Percus-Yevick approximation.

Name	Mean silica diam. (nm) [a]	vol. fraction ϕ_{Si}	h (nm)[a]	Graft density (nm^{-2})[b]
T30-NCG-1	26	0.15	21.5	2.0
T30-NCG-2	26	0.17	aggregated	2.0
T30-NCG-3	26	0.23	aggregated	2.0
T50-NCG-1	42	0.15	20.5	1.5
T50-NCG-2	42	0.18	16.4	1.5
T50-NCG-3	42	0.29	9.3	1.5
T30-CG-1	27	0.11	8.7	5.0
T30-CG-2	27	0.16	6.8	5.0
T30-CG-3	27	0.20	5.4	5.0
T50-CG-1	42	0.11	21.5	3.2
T50-CG-2	42	0.15	15.9	3.2
T50-CG-3	42	0.22	6.5	3.2

[a] From SANS measurements ; [b] From elemental analysis.

non linearity is appearing. It is even more obvious when plotted as a Lissajous curve (stress vs strain), where the curve is more and more deviating from the ellipse obtained in the linear case. An important consequence of the non linearity is that the moduli measured by the rheometer have no clear physical meaning in this regime and that a more precise analysis of the stress signal is required.

Thus, we start by decomposing the stress signal σ into elastic and viscous parts (σ' and σ'' respectively), as proposed by Cho et al [85]. (Figure 4.3 - method described in the Background section)

Then we plot σ' and σ'' as a function of γ and $\dot{\gamma}/\omega$ respectively (Figure 4.4). In the linear regime (low strain), we obtain straight lines which slopes are G' and G'' respectively (see Figure 4.1). But as we can see, it is not the case anymore in the non linear regime, so that we introduce the generalized moduli Γ' and Γ'', which are functions of $\gamma(t)$ and $\dot{\gamma}(t)/\omega$ in each cycle of solicitation (see Eq.(4.13)).

Decomposition into linear and non linear terms

In order to study those generalized moduli, Ewoldt et al. [94, 95] chose to decompose the stress in Chebyshev series. However, as the interpretation of the various coefficients obtained is rather complex, we chose to limit our decomposition to two terms : one describing the linear behavior, the other describing the non linear one. For that, we find a Taylor expansion of Γ' and Γ'' by fitting $\sigma' = \Gamma'\gamma$ and $\sigma'' = \Gamma''\dot{\gamma}/\omega$ with a polynomial of degree 3 in γ and $\dot{\gamma}/\omega$ respectively.

$$\Gamma' = \Gamma'_0 + \Gamma'_2\gamma^2 \quad (4.7)$$

$$\Gamma'' = \Gamma''_0 + \Gamma''_2(\dot{\gamma}/\omega)^2 \quad (4.8)$$

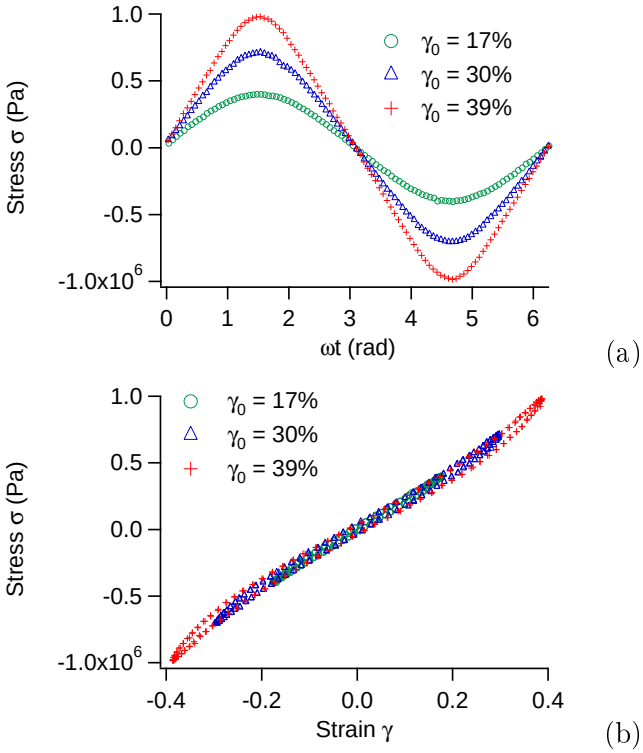

FIGURE 4.2 – Stress σ as a function of ωt (a) and as a function of strain γ (b) during one cycle of sinusoidal strain applied with an amplitude $\gamma_0 = 17$, 30 and 39%. Sample T50-CG-3.

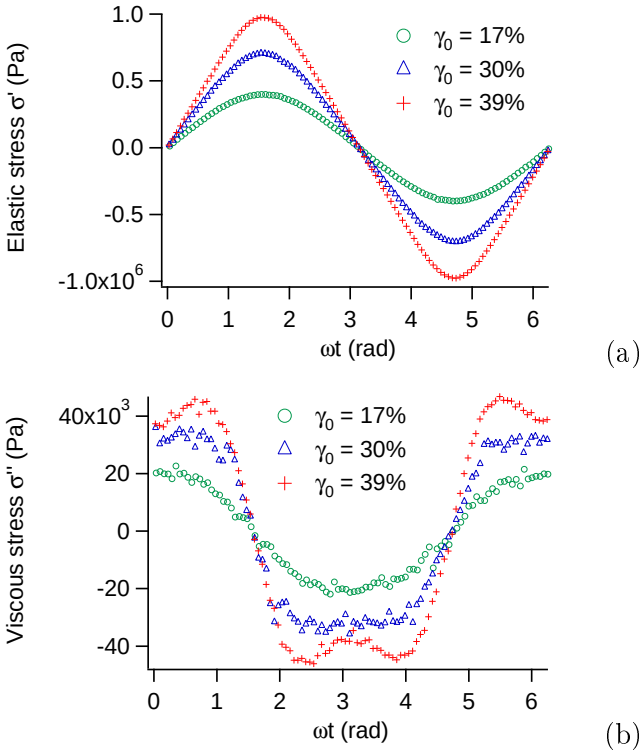

FIGURE 4.3 – Elastic stress σ' (a) and viscous stress σ'' (b) as a function of ωt during one cycle of sinusoidal strain applied with an amplitude $\gamma_0 = 17$, 30 and 39%. Sample T50-CG-3.

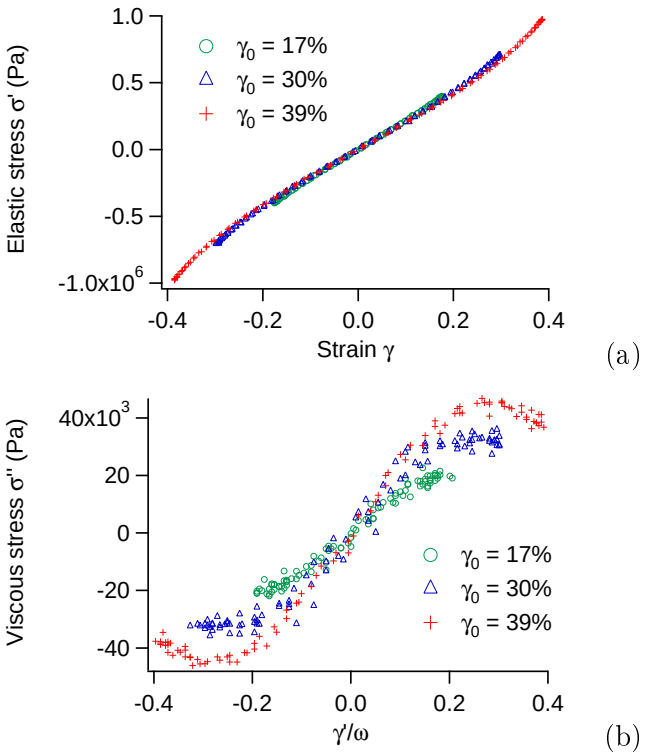

FIGURE 4.4 – Elastic stress σ' (a) and viscous stress σ'' (b) as a function of strain γ and $\dot{\gamma}/\omega$ respectively during one cycle of sinusoidal strain applied with an amplitude $\gamma_0 = 17, 30$ and 39%. Sample T50-CG-3.

Γ'_0 and Γ''_0 are thus the slopes at the origin in Figure 4.4, while Γ'_2 and Γ''_2 take into account the deviation from the linear behavior of σ' and σ'' respectively. For all the samples, we could observe an intra-cycle strain-stiffening ($\Gamma'_2 > 0$ - in one strain cycle, that is σ' increases more abruptly with γ at high γ) and shear-thinning ($\Gamma''_2 < 0$ - in one strain cycle, that is σ'' increases more smoothly with $\dot{\gamma}$ at high $\dot{\gamma}$).

Here, we have to put the emphasis on the fact that the coefficients we are measuring are not accurate due to the plate-plate geometry we used and the inhomogeneous strain field it introduces. In effect, we consider here a non linear stress with terms of order 3 and we would have to take this into account in the calculation from the measured torque. The measured torque is linked to the stress as follows :

$$M = \int_0^R \sigma(r) \times r \times 2\pi r dr \tag{4.9}$$

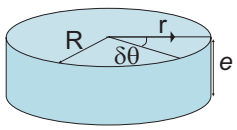

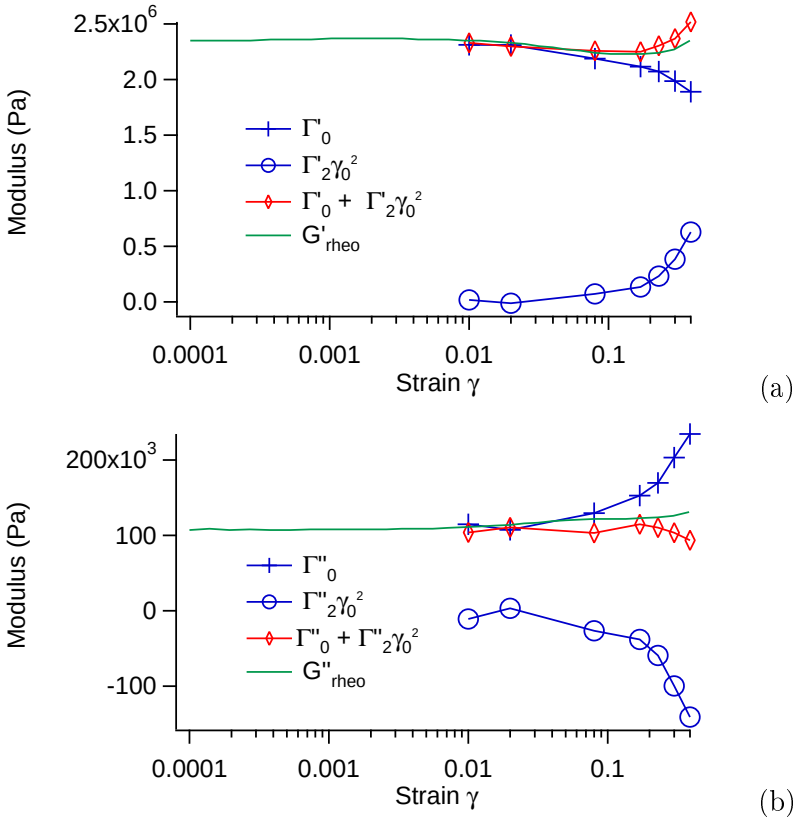

FIGURE 4.5 – Evolution of the linear and non-linear term of the elastic (a) and viscous (b) moduli with the strain amplitude γ_0. Comparison with the values given by the rheometer. Sample T50-CG-3.

Using a Taylor expansion of degree 3 for the stress and with the strain at a distance r of the center of the sample being $\gamma(r) = \frac{r\delta\theta}{e}$, we have :

$$\sigma(r) = \Gamma'_0 \frac{r\delta\theta}{e} + \Gamma'_2 (\frac{r\delta\theta}{e})^3 \tag{4.10}$$

For the torque we find

$$M = \frac{\pi R^3}{2} (\Gamma'_0 \gamma + \frac{2}{3} \Gamma'_2 \gamma^3) \tag{4.11}$$

Since the factor applied by the rheometer to the measured torque to get the stress is $\frac{2}{\pi R^3}$, we see that we would need to apply a corrective factor of $3/2$ to the coefficient Γ'_2 we measure (for a term of higher order Γ'_n, the corrective factor would be $(n+4)/4$). However, doing this we would not be able to compare our values with the ones of the rheometer anymore. That is why we choose here to keep the raw values of Γ'_2, but we need to keep in mind that their actual values are higher by a factor $3/2$.

4.1.3 Evolution of the non linearity with the strain amplitude

We can then study the variations of Γ'_0, Γ''_0, Γ'_2 and Γ''_2 with the strain amplitude γ_0 (Figure 4.5). An example of sample with a non-covalent bond between silica and polymer is given in Figure 4.6 (sample T30-NCG-1).

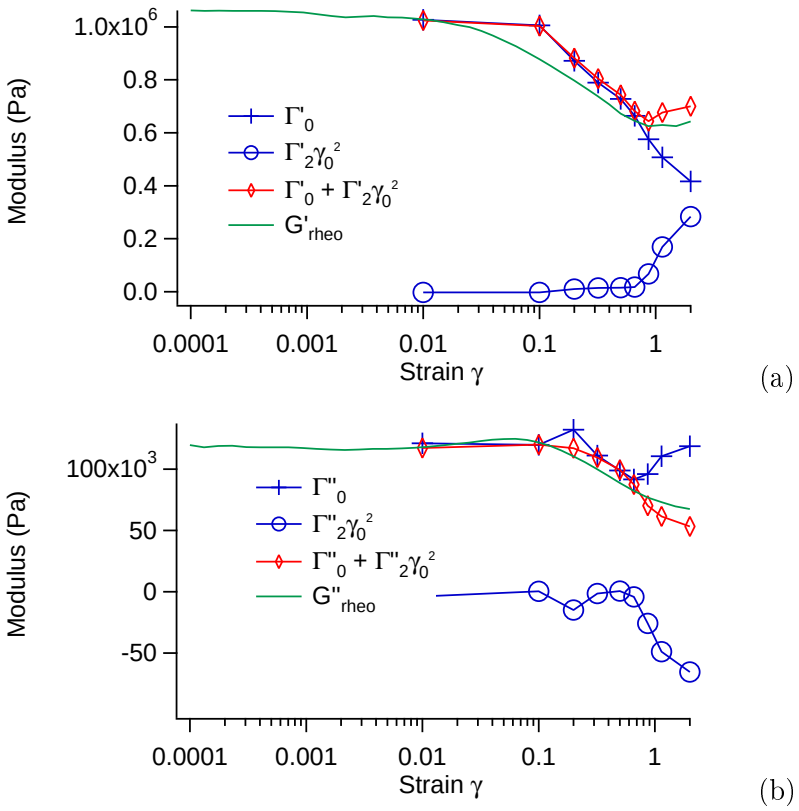

FIGURE 4.6 – Evolution of the linear and non-linear term of the elastic (a) and viscous (b) moduli with the strain amplitude γ_0. Comparison with the values given by the rheometer. Sample T30-NCG-1.

On all the samples we can observe the same general behavior, more or less pronounced depending on the structure of the sample. Γ'_0 decreases with γ_0 : it corresponds to the Payne effect - a decrease in the storage modulus with the strain amplitude. Γ'_2 is positive, describing a strain-stiffening behavior, while Γ''_2 is negative, describing a shear-thinning behavior. Γ'' present a classical behavior corresponding to the Payne effect : it presents a maximum when Γ' is decreasing. However, the respective contributions of Γ''_0 and Γ''_2 are complex and will be discussed in the next section. Here, we will focus on Γ'.

In absolute value, Γ'_2 and Γ''_2 increase with γ_0, which means that the non linearity effects become more and more significant as the strain amplitude increases. We also notice that for both Γ' and Γ'', the sum of the two components - linear and non-linear, is comparable to the moduli given by the rheometer. It is worth noting that from strain amplitudes of a few tens of percents, both phenomena - Payne effect and non-sinusoidal signals - are superimposed and can not be distinguished by simply looking at the moduli given by the rheometer.

4.1.4 Link between strain-stiffening and Payne effect

We will here focus on the elastic modulus extracted with Cho's method, since it corresponds to the main part of the stress signal. We have decomposed it into a linear term (corresponding to the sinusoidal part of the stress - Γ'_0) and a non linear one (accounting for the non sinusoidal part of the stress - Γ'_2).

The Payne effect is described by the variation of $\Gamma'_0(\gamma_0)$ and not by the moduli given by the rheometer because of the contribution of non linear term. It can be interpreted as the strain softening of the glassy bridges between particles [34].

The non linear term Γ'_2 describes a strain-stiffening at high elongations, appearing sooner or later depending on the samples. In order to compare the strain-stiffening of the various samples, we can choose to simply look at the ratio of the non linear term divided by the linear one $\Gamma'_2(\gamma_0)/\Gamma'_0(\gamma_0 = 0)$. This objective analysis will give us a hint on the physical origin of the strain-stiffening and its potential link with the Payne effect.

We first plot the ratio $\Gamma'_2(\gamma_0)/\Gamma'_0(\gamma_0 = 0)$ as a function of γ_0 (Figure 4.7). As a first approximation, we will consider that this parameter is independent of the strain amplitude and use an average value for each sample.

We can then compare this parameter with the Payne effect and see if they are correlated. If the non linear effects can be assessed with the value of $\Gamma'_2(\gamma_0)/\Gamma'_0(\gamma_0 = 0)$, it is more difficult to find a simple criterion measuring the amplitude of the Payne effect (we do not see the high strain plateau in our experiments). We choose here as a criterion the strain amplitude at which the elastic modulus has decreased by 10% ($G'(\gamma_c) = 0.9G'(0)$). This way, if this strain γ_c is low, it means that the Payne effect is large. We plot this criterion as a function of the strain amplification factor (Figure 4.8).

We clearly see in this figure that the two sets of samples are driven apart and that for each set the Payne effect is correlated with the non linearity : strain-stiffening increases with the Payne effect. Moreover, at one given Payne effect amplitude, we see that the strain-stiffening is larger for the CG samples compared with the NCG samples. This means that the strain-stiffening does not only come from the Payne effect. Another origin of this effect might be a finite extensibility

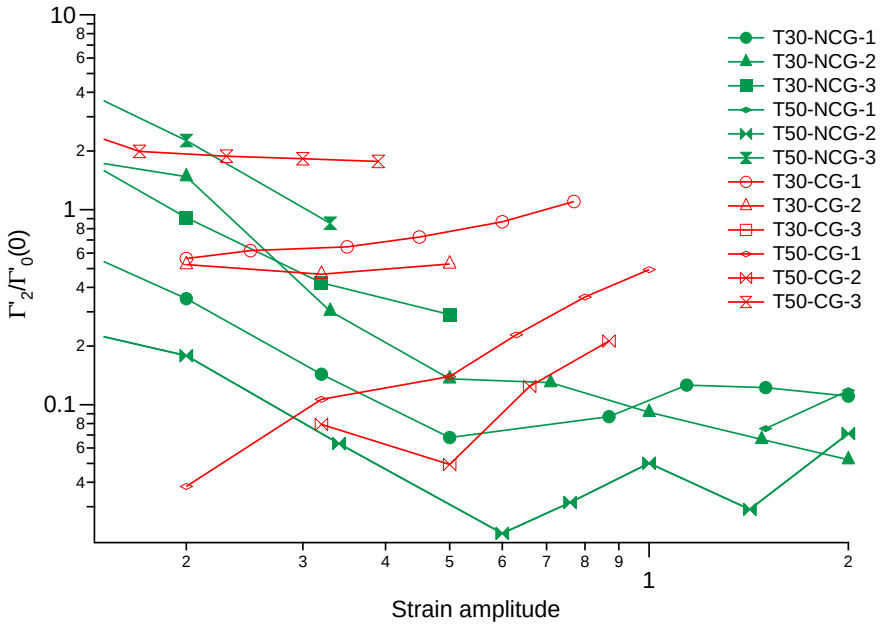

FIGURE 4.7 – Non linear parameter $\Gamma'_2(\gamma_0)/\Gamma'_0(\gamma_0 = 0)$ as a function of the strain amplitude γ_0. As a first approximation, we will consider that this ratio is independent of the strain amplitude and use an average value.

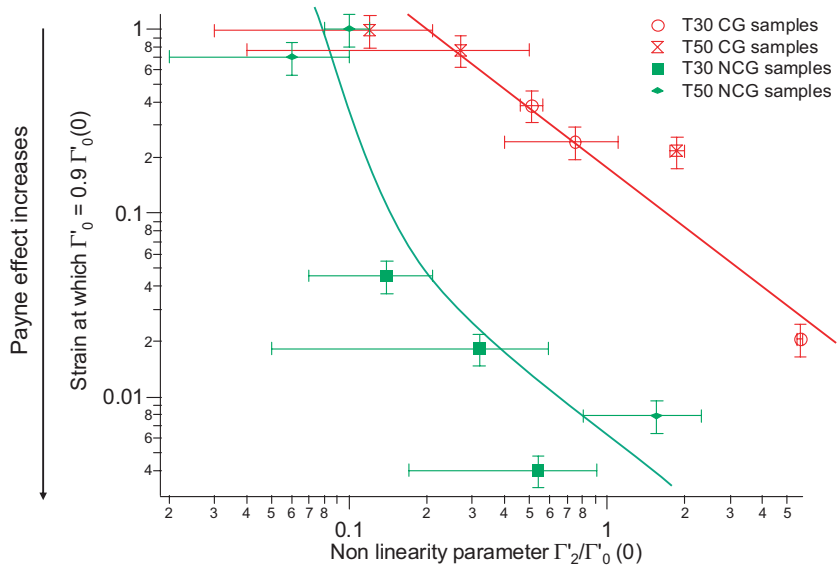

FIGURE 4.8 – Correlation between the Payne effect and the non linearity parameter $\Gamma'_2(\gamma_0)/\Gamma'_0(\gamma_0 = 0)$. The lines are guides for the eye. We see that the NCG samples have a larger Payne effect than the CG samples, and that the Payne effect increases with the non linearity parameter.

phenomenon. In effect, when the strain is so high that some of the polymer chains are completely stretched out, the stress increases drastically. In filled elastomers, since the silica particles cannot be distorted, we can easily imagine that the effective strain felt by the polymer confined between solid particles is higher than the macroscopic strain applied. Thus, the confined polymer could show finite extensibility. For the NCG samples, the lesser significance of the strain-stiffening might be due to a slippage effect of the matrix at the surface of the particles, which could lower the strain amplification between the particles. This argument could also explain why, if we look at one given non linearity parameter, the NCG samples have a larger Payne effect than the CG samples [102].

4.1.5 Conclusion

Thanks to LAOS analysis and using Cho's approach, we were able to get an insight into filled rubber mechanics and properties. The study focused on the non linear behavior of model filled elastomers with various amount of silica, various sizes of silica particles and different coupling agents. The samples showed a general trend of simultaneous strain-stiffening and shear-thinning behavior during one cycle of solicitation. This behavior was quantified for all the samples and for various strain amplitudes. We thus pointed out that from a few tens of percents of strain, Payne effect and strain-stiffening are superimposed, and the method we described allows to analyze them separately.

From those results, we could then see a correlation between the Payne effect and strain-stiffening in filled rubbers. We could also show that the Payne effect is not the only origin of strain-stiffening. Another cause might be the finite extensibility of polymer chains confined between silica particles, where the local strain is increased. Slippage at the surface the silica particles in the case of NCG samples has also probably a role to play in the amplitude of both the Payne effect and the strain-stiffening.

There are thus several intricate effects leading to non linearity in filled elastomers and this study showed that the classical Payne effect analysis provides only a part of the mechanics involved at low deformation.

In this section, we have highlighted the existence of two kinds of non linearity in the mechanical behavior of model filled samples : a decrease in the elastic modulus with the strain amplitude (Payne effect) but also strain-hardening and shear-thinning inside each cycle of solicitation at large strain amplitude. However, the physical interpretation of these intra-cycle non linearities is not clear. In the next section, we compare these experimental observations to simulations obtained with the glassy bridges reinforcement model. We show that the simulations also exhibit strain-hardening and shear-thinning, suggesting that they might be associated to the presence of glassy bridges in the samples.

4.2 Correlation with the glassy bridge reinforcement model

In the previous section, we put into light the apparition of non sinusoidal stress signal at high strain amplitude in oscillatory shear. We will here compare those experimental results to simulations obtained with a model of reinforcement by glassy bridges.

The section is organized as follows. First, we recall in section 4.2.1 the non linear quantities studied and the experimental results obtained on model filled elastomers in large amplitude oscillatory strain (LAOS). Then, section 4.2.2 is the theoretical part of the paper, the physical ingredients of the glassy bridge reinforcement model (GBRM) and its numerical resolution are explained. Finally, in section 4.2.3 the results of the simulations are discussed and compared to the experimental data.

4.2.1 Recall - Definition of the non-linear problem and experimental results

Here we aim at quantifying the non-linear behavior of filled elastomers submitted to large amplitude sinusoidal deformations. Both the in-phase and out-of phase responses need to be defined in the non-linear regime. The method is briefly recalled, starting from the linear case, and then generalized to the non-linear case.

Following Cho et al. [85], as well as some other authors [94, 95, 103, 104], the stress is decomposed into an elastic and a viscous part. In the linear regime, the stress ensuing a sinusoidal strain $\gamma(t)$ can classically be written as

$$\sigma(t) = G'\gamma(t) + G''\dot{\gamma}(t)/\omega \tag{4.12}$$

It is the sum of two terms : one in-phase with the strain corresponding to the elastic response $\sigma' = G'\gamma$ and one in quadratic phase with the strain corresponding to the viscous response $\sigma'' = G''\dot{\gamma}/\omega$. Thus, for an applied strain $\gamma = \gamma_0 sin(\omega t)$, the elastic stress σ' is a sine wave – odd part – and the viscous part σ'' a cosine – even part. Then, when σ' is plotted as a function of γ – respectively σ'' as a function of $\dot{\gamma}/\omega$ –, a straight line with a slope G' – respectively G'' – is obtained.

If a large amplitude sinusoidal strain is applied, the measured stress is non-linear, but still periodic. It can thus be decomposed in a unique way into odd – σ' – and even – σ'' – parts :

$$\sigma(t) = \sigma'(t) + \sigma''(t) \tag{4.13}$$

with

$$\sigma'(t) = (\sigma(t) - \sigma(-t))/2 \tag{4.14}$$

$$\sigma''(t) = (\sigma(t) + \sigma(-t))/2 \tag{4.15}$$

Similarly to the linear case, Cho et al then introduces the generalized moduli Γ' and Γ'' :

$$\sigma'(t) = \Gamma'(\gamma(t))\gamma(t) \tag{4.16}$$

$$\sigma''(t) = \Gamma''(\dot{\gamma}(t))\dot{\gamma}(t)/\omega \tag{4.17}$$

An equivalent analysis may be performed in the frequency domain. For an applied deformation $\gamma(t) = \gamma_0 \sin(\omega t)$, the in-phase and out-of phase stress responses $\sigma'(t)$ and $\sigma''(t)$ are given respectively by

$$\sigma'(t) = \sum_{n=1}^{\infty} a_n(\gamma_0, \omega) \sin(n\omega t) \tag{4.18}$$

$$\sigma''(t) = \sum_{n=1}^{\infty} b_n(\gamma_0, \omega) \cos(n\omega t) \tag{4.19}$$

Because σ' and σ'' are odd functions of γ and $\dot{\gamma}$ respectively, a_n and b_n are non-zero only for odd values of n. The dissipated energy per period is :

$$W = \int_0^T \sigma''(t)\dot{\gamma}dt = W = \gamma_0 b_1(\gamma_0, \omega)\pi \tag{4.20}$$

where $T = 2\pi/\omega$ is the period. W depends only on $b_1(\gamma_0, \omega)$. In the limit of small deformation amplitudes, the storage and dissipative moduli are related to the coefficients a_1 and b_1 by

$$\gamma_0 G'(\omega) = a_1(\omega) \tag{4.21}$$

$$\gamma_0 G''(\omega) = b_1(\omega) \tag{4.22}$$

In [105, 106] the non-linear dependence of the first harmonics (which dominate the response) writes :

$$\gamma_0 G'(\gamma_0, \omega) = a_1(\gamma_0, \omega) \tag{4.23}$$

$$\gamma_0 G''(\gamma_0, \omega) = b_1(\gamma_0, \omega) \tag{4.24}$$

as predicted by the GBR model was discussed and compared to the results published by Payne. Here the whole non-linear dependence of σ' and σ'' as a function of the deformation amplitude is considered and compared to experimental data. To be more specific, we consider here the expressions of σ' and σ'' as a function of γ and $\dot{\gamma}$ respectively, and the Fourier series expansion is calculated up to the order $n = 3$ only. We will see that in both experimental results and simulations, contributions from higher harmonics are indeed negligible. Up to the 3rd harmonics, one has

$$\sigma'(t) = a_1(\gamma_0, \omega) \sin(\omega t) + a_3(\gamma_0, \omega) \sin(3\omega t) \tag{4.25}$$

which reads

$$\sigma'(t) = (a_1 + 3a_3) \sin(\omega t) - 4a_3 \sin^3(\omega t) = (a_1 + 3a_3)\frac{\gamma(t)}{\gamma_0} - 4a_3(\frac{\gamma(t)}{\gamma_0})^3 \tag{4.26}$$

A similar development for σ'' leads to

$$\sigma''(t) = (b_1 - 3b_3) \cos(\omega t) + 4b_3 \cos^3(\omega t) = (b_1 - 3b_3)\frac{\dot{\gamma}}{\gamma_0\omega} + 4b_3(\frac{\dot{\gamma}}{\gamma_0\omega})^3 \tag{4.27}$$

Two samples are presented here : T50 CG 30% (silica diameter = 42 nm, grafting density =

3.2 nm^{-2}, silica volume fraction = 0.22) and T30 NCG 25% (silica diameter = 26 nm, grafting density = 2 nm^{-2}, silica volume fraction = 0.15).

Contrary to the linear case, the generalized moduli (defined in Eq.(4.17)) depend on the strain and shear rate during one cycle of solicitation, according to Eq. (4.26) and (4.27). Up to the 3rd harmonics, the generalized moduli defined in Eq.(4.17) are written in the form of Taylor expansions with only two terms, one describing the linear behavior and the other one the non-linear behavior :

$$\Gamma' = \Gamma'_0 + \Gamma'_2\gamma^2 \quad (4.28)$$

$$\Gamma'' = \Gamma''_0 + \Gamma''_2(\dot{\gamma}/\omega)^2 \quad (4.29)$$

The curves obtained by plotting σ' vs γ and σ'' vs $\dot{\gamma}(t)/\omega$ are thus not straight lines anymore. As an example, the signal analysis is shown in Figure 4.9 for the sample T30 NCG 25%. In order to quantify the non linearity, according to Eq.(4.29), the curves are fitted with polynomials of degree 3. Here the inhomogeneity of the strain field in the plate-plate geometry has to be taken into account. It was shown that a correction factor of $3/2$ has to be applied to the experimentally measured non-linear terms Γ'_2 and Γ''_2 (see section 4.1). This correction is applied in all following experimental results.

In order to describe the non-linear behavior of the elastic part, the slopes p_0, p_1 and p_2 in the σ' vs γ curve are used, as described in Figure 4.10 :

- p_0 is the slope of the curve at low strain in the linear regime, it corresponds to $\Gamma'_0(\gamma_0 = 0)$ (γ_0 is the strain amplitude),
- p_1 is the slope at the origin, it corresponds to $\Gamma'_0(\gamma_0)$,
- p_2 is the slope at large strain, it corresponds to $\Gamma'_0(\gamma_0) + 3 \times 3/2 \times \Gamma'_2(\gamma_0)\gamma_0^2$ (factor $3/2$ coming from the plate-plate correction mentioned above).

Using this analysis, the ratios p_1/p_0 and p_2/p_0 can be plotted as a function of the strain amplitude. At small strain amplitudes, we expect both ratios to tend to 1, since in the linear case $p_2 = p_1 \longrightarrow p_0$. At higher strains, it is observed that p_1 decreases and that $p_2 \geq p_1$, which corresponds to Payne effect and strain-hardening respectively (Figure 4.10). As temperature decreases, the amplitude of the Payne effect is expected to increase, which is indeed what is observed in Figures 4.11 and 4.12(a). The strain-hardening phenomenon, probed by the variation of p_2/p_0, seems to be less sensitive to temperature (see Figures 4.11 and 4.12(b)). Thus, the temperature dependence indicates that the variation of p_2 cannot be attributed to the strain-softening of glassy bridges only.

The elastic stress is plotted as a function of strain in Figure 4.13, at different temperatures, for a strain amplitude 100%. The main result here is that strain hardening is observed, and that it is more pronounced at low temperatures. Thus, in these samples and at these temperatures, the strain hardening cannot be explained by the finite extensibility of the chains only. The viscous stress as a function of the strain rate $\dot{\gamma}$ is also plotted in Figure 4.13 for the same temperatures. The higher harmonics contributions to the elastic stress are plotted in Figure 4.13.(c). It is

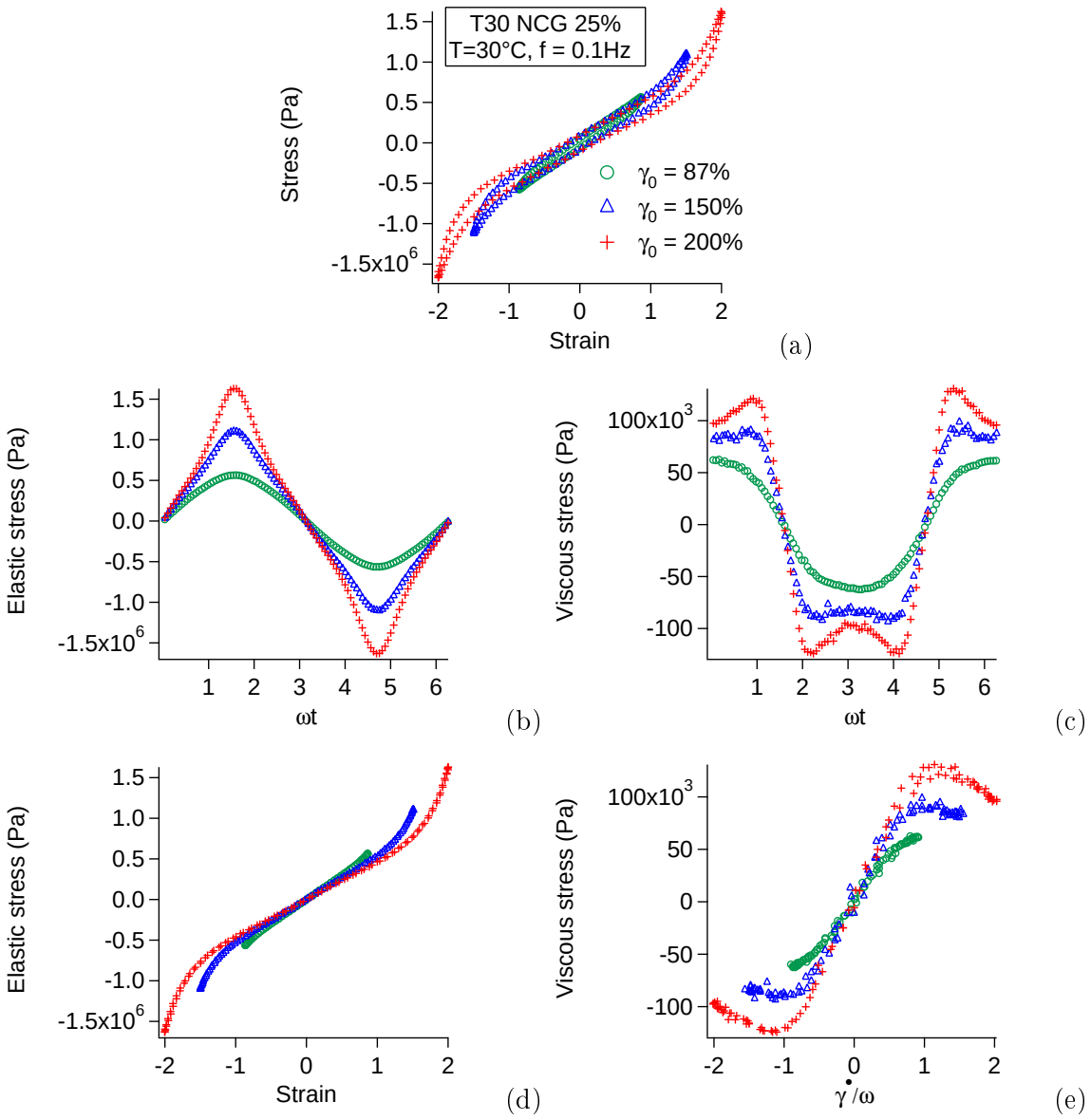

FIGURE 4.9 – Signal analysis for the sample T30 NCG 25%. (a) Lissajoux plot : stress vs strain. As the strain amplitude is increased, the Lissajoux plot is more and more deviating from the elliptic shape obtained in the linear case. (b) Elastic stress (odd part of the total stress signal) vs time. (c) Viscous stress (even part of the total stress signal) vs time. (d) Elastic stress vs strain : the curve is not a straight line at large strain and shows a strain-hardening behavior. (e) Viscous stress vs $\dot{\gamma}(t)/\omega$: the non-linearity is seen as a rheofluidification.

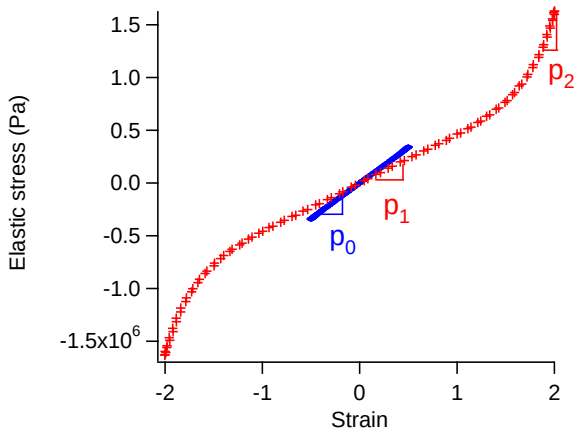

FIGURE 4.10 – Elastic stress σ' as a function of the strain γ inside one strain cycle. p_0 is the slope of the curve at low strain amplitude, in the linear regime. p_1 and p_2 are the slopes in the non-linear regime at small and large strain amplitudes respectively.

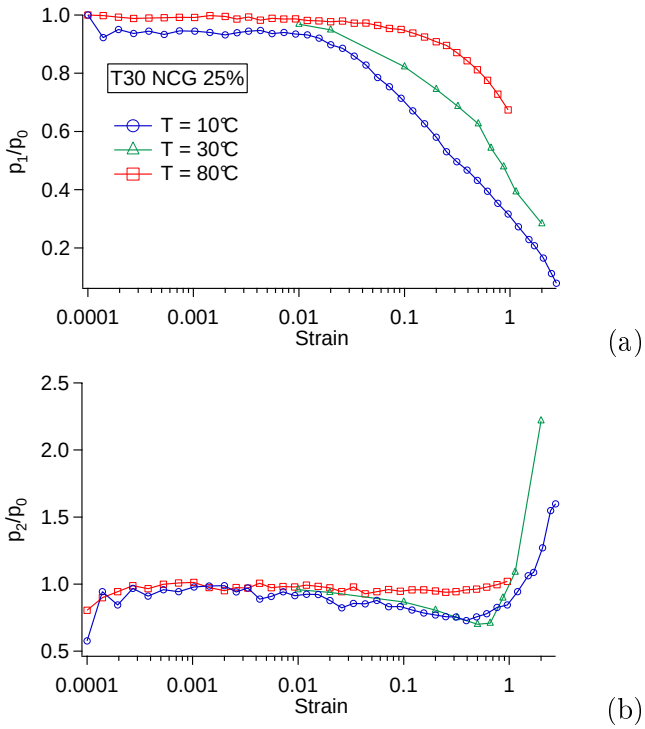

FIGURE 4.11 – The ratios p_1/p_0 (a) and p_2/p_0 (b) vs strain amplitude at different temperatures (10°C, 30°C and 80°C) for the sample T30 NCG 25%. As temperature decreases, the Payne effect becomes larger so that p_1/p_0 decreases more abruptly. p_2/p_0 first follows this decrease and then increases due to the large strain-hardening phenomenon.

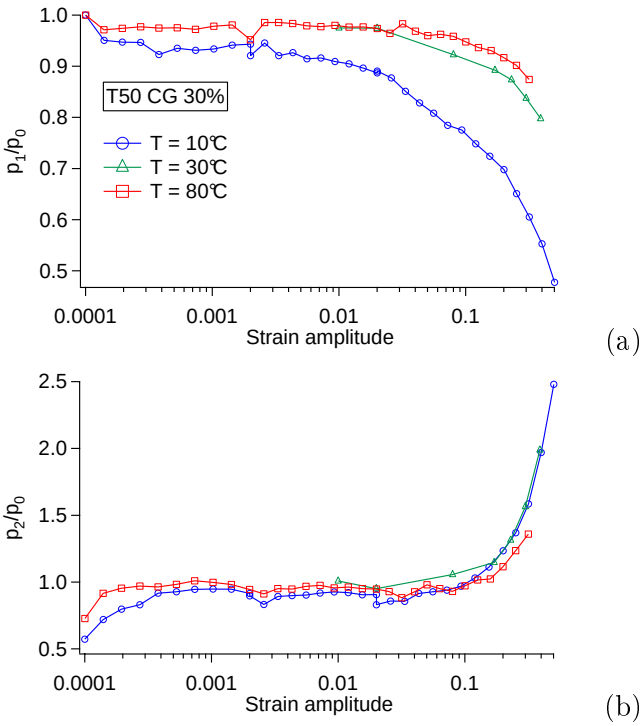

FIGURE 4.12 – The ratios p_1/p_0 (a) and p_2/p_0 (b) vs strain amplitude at different temperatures (10°C, 30°C and 80°C) for the sample T50 CG 30%. Again the Payne effect is larger at lower temperature but it is smaller than for the T30 NCG 25% sample so that p_2/p_0 seems to be a monotonic increasing curve.

observed that higher harmonic amplitudes are indeed small, and that a_3 is negative, which is the signature of the strain hardening behavior (see Eq.(4.26)).

4.2.2 Description of the model

Shift of the glass transition temperature T_g in the vicinity of the fillers

In the GBR model, it was proposed that the reinforcement is the consequence of an increase of the glass transition of the matrix in the vicinity of the fillers [31, 107]. This shift is given by [33, 105]

$$T_g(z,\sigma) \approx T_g\left(1+\left(\frac{\beta}{z}\right)^{1/\nu}\right) - \frac{\sigma}{K} \approx T_g\left(1+\frac{\beta}{z}\right) - \frac{\sigma}{K} \tag{4.30}$$

where z is the distance to a filler from an interface, T_g is the bulk glass transition temperature of the pure rubber and $\nu \approx 0.88$. The first term in the right hand side of Eq.(4.30) is the effect of the interaction between the fillers and the matrix. The second term is the decrease of T_g due to the local stress σ, which is the plasticizing effect of an applied stress. K depends on the polymer. It relates the yield stress σ_y to the temperature T and the polymer glass transition temperature T_g by $\sigma_y = K(T_g - T)$. K is of the order of 10^6 Pa.K^{-1} typically [108]. The value of the length β depends on the matrix-filler interaction. In a film with strong substrate/polymer interactions, the increase of T_g can be as large as 50 K at a distance of 10 nm [109–111], which corresponds to a value of β of 1.5 nm.

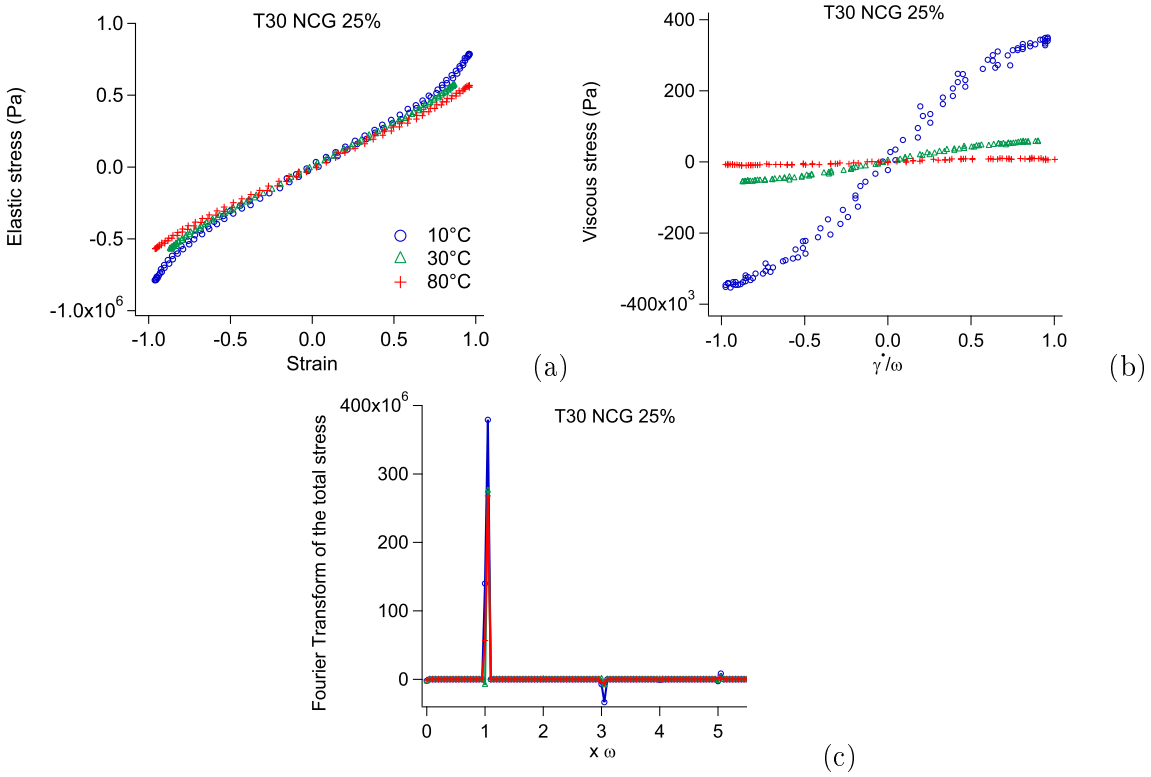

FIGURE 4.13 – Signal analysis for the sample T30 NCG 25%. (a) Elastic stress (odd part of the total stress signal) vs time, for the same deformation amplitude at three different temperatures. One observes strain hardening at low temperatures. (b) Viscous stress (even part of the total stress signal) vs time for the same experiments. (c) Fourier transform of the total stress in the same experiments. One observes that the 5th harmonic is negligible.

When glassy layers overlap, the macroscopic shear modulus G' is related to the shear modulus of the glassy polymer G'_g through geometrical effects. Indeed, a macroscopic deformation ϵ is amplified locally in between the fillers by an amplification factor λ, which is the ratio between the diameter of the fillers and the distance between two neighboring fillers. In a plane normal to the direction of elongation, the stress is supported by glassy bridges which represent an area fraction $\Sigma < 1$. Both parameters λ and Σ depends on the considered systems. The macroscopic modulus is thus given by

$$G' \approx G'_g \lambda \Sigma \tag{4.31}$$

Assuming that the fillers are spherical particles of 10 nm diameters with typical interparticle distance of a few nanometers, we deduce that λ is of the order of a few units and Σ is of the order of a few 10^{-2}, depending on the ratio between the glassy layer thickness and the nearest neighbor distance. Since $G'_g \sim 10^9$ Pa, we obtain a macroscopic shear modulus of about 10^8 Pa, which corresponds to very strong reinforcement.

When a macroscopic deformation ϵ of a few percents is applied to the sample, the local stress σ is of the order of $\sigma \sim \lambda \epsilon G'_g \sim 10^8$ Pa. With $K \sim 10^6$ Pa K^{-1} [108], a local T_g reduction of 100 K is obtained. Therefore, glassy bridges yield, which results in a decrease of the shear modulus, for macroscopic deformations of the order of a few %. This is indeed comparable to the Payne effect [112], which is a sharp decrease of the elastic modulus in this range of deformation.

Life-time of glassy bridges : aging

Glassy bridges are not permanent. Within a glassy bridge in-between two neighboring particles, at equilibrium, we assume that the polymer locally has the dominant relaxation time τ_α given by the William-Landel-Ferry (WLF) law of the corresponding polymer [113], modified by the T_g shift due to interfacial effects and the local stress σ. We assume that the life-times (breaking times) of glassy bridges are comparable to the local dominant relaxation times τ_α of the glassy bridges. The breaking time is thus given by

$$\log\left(\frac{\tau_\alpha(z,\sigma)}{\tau_g}\right) = \log\left(\frac{\tau_{WLF}(T - T_g(z,\sigma))}{\tau_g}\right) = -\frac{C_1(T - T_g(z,\sigma))}{C_2 + (T - T_g(z,\sigma))} \tag{4.32}$$

where $T_g(z,\sigma)$ is given by Eq.(4.30), $\tau_g = 100$ s (the relaxation time at T_g) and T is the temperature. C_1 and C_2 are the WLF parameters of the considered polymer [113].

Eq.(4.32) gives *the equilibrium value of the breaking time*, which is obtained when the distance z, the local stress σ and the temperature T have been maintained fixed for a long time. In general, the breaking time depends on the history of the glassy bridge and is denoted $\tau_\alpha(t)$. Its evolution (aging) is discussed now. We assume that, at any time, a glassy bridge has a probability for breaking per unit time, dP/dt, given by

$$dP = \alpha \frac{dt}{\tau_\alpha(t)} \tag{4.33}$$

where α is a number of the order of 1. We will assume $\alpha = 0.3$ to 0.4 in the following. When a glassy bridge breaks, the local stress σ is relaxed and drops to a much smaller value, which

is the rubbery contribution. Immediately after breaking, we assume that τ_α relaxes to a value $\tau_{min} \sim \dot{\gamma}^{-1}$, where $\dot{\gamma}$ denotes the local deformation rate. The local breaking time $\tau_\alpha(t)$ undergoes a subsequent evolution, analogous to an aging process [114]. Thus, the evolution of the breaking time of a glassy bridge, $\tau_\alpha(t)$, is given by

$$\frac{\partial \tau_\alpha(t)}{\partial t} = 1 \tag{4.34}$$

if

$$\tau_\alpha(t) \leq \tau_{WLF}(T - T_g(z,\sigma)) \tag{4.35}$$

and by definition, we set the time τ_α to be bounded by the time $\tau_{WLF}(T - T_g(z,\sigma))$ given by Eq.(4.32).

It was shown that the kinetics of yield and rebirth of glassy bridges described by Eq. (4.33), (4.34) and (4.35) is a key feature for explaining the dependence of $G'(\omega)$ and $G''(\omega)$ on the strain amplitude (Payne effect), and especially the presence of the peak of $G''(\omega)$ at intermediate strain amplitude for strongly reinforced elastomers [105, 112]. It is also essential for understanding the plastic behavior of filled elastomers [4, 106]. As we shall see, this kinetics is also key for understanding the higher harmonic response of filled elastomers.

Modeling

The model described above needs to be solved numerically. The degrees of freedom are the centers of mass of the fillers. The diameter d of the fillers sets the unit length scale. The equations of the dynamics are non inertial. The equation of motion for particle i is :

$$\vec{F}^i_{el} + \vec{F}^i_{hs} + \vec{F}^i_{Hydro} = \vec{0} \tag{4.36}$$

where $\vec{F}_{el}$ is the elastic force between two neighboring particles and is the sum of the contributions of the glassy bridges and of the rubbery matrix. $\vec{F}_{hs}$ is the hard core repulsion between fillers and $\vec{F}_{Hydro}$ is the friction force between two neighboring particles. The elastic force is given by

$$\vec{F}_{el}(\vec{r}) = -k_\infty(\vec{r} - l_0\vec{u}) - k_0(\vec{R}_{ij} - \vec{R}^{ref}_{ij}) \tag{4.37}$$

l_0 is the equilibrium length of the rubbery springs, $\vec{r}$ is the vector joining the centers of the two particles, and $\vec{u}$ is the unit vector joining the two particles. To represent the effect of the rubbery matrix (of typical elastic modulus 1 MPa), we set $k_\infty = 1$. This spring constant sets the unit of modulus. All the results will therefore be expressed in units of MPa. The glassy modulus, 10^9 Pa, is typically 3 orders of magnitude larger than the rubbery modulus. However, due to the geometric effects mentioned above, when translated in terms of spring stiffness, this quantity has to be rescaled by the product $\lambda\Sigma$ which we choose to be 10^{-2}-10^{-1}. The glassy spring constant is thus set to $k_0 \sim 10 - 100$. $\vec{R}_{ij} = \vec{R}_i - \vec{R}_j$ and $\vec{R}_i$ is the vector position of filler i.

When the breaking of a glassy bridge occurs at a time t, the glassy contribution cancels, and the subsequent glassy contribution at time $t' > t$ involves the displacement relative to the

parameter	physical value	value in the simulation
number of particles		$N_{sites} = 5000$
volume fraction	$10 - 40\%$	40 %
filler diameters	10 nm	$d = 1.0$
connectivity of springs		$n = 10$
rubbery modulus	5.10^5 Pa	$k_\infty = 1$
glassy modulus	10^9 Pa	$k_0 = 10$ to 100
Glass transition temperature T_g of the pure rubber	213 K	$T_g = 213$ K
Temperature of the experiment T	T	$T = 263$ K
Typical deformation rate	1 s^{-1}	$\dot{\gamma} = 1$ s^{-1}
Dissipative modulus at large deformation amplitudes	10^6 Pa	$\zeta = 4$ s
coefficient β	≈ 0.5 nm	0.02 to 0.04
coefficient K	10^6 Pa.K^{-1}	0.3
coefficient α	$\lesssim 1$	0.4

TABLE 4.2 – Parameters of the model. In addition to the glass transition temperature of the matrix, one needs the complete WLF law of the considered polymer.

new reference state $\vec{R}_{ij}^{ref} = \vec{R}_{ij}(t)$ corresponding to the relative positions of the fillers when the last breaking occurred. The viscous force between two neighboring particles in our simulations is written as

$$\vec{F}_{Hydro} = -\zeta(\vec{v}^1 - \vec{v}^2) \tag{4.38}$$

The life-time of the glassy bridges is the result of a dynamical evolution calculated according to Eq.(4.32), (4.33), (4.34), and (4.35). This dynamical evolution depends on the local glass transition temperature (Eq.(4.32)), which allows the calculation of the time scales in physical units (seconds).

More details regarding the implementation of the model into a numerical code are given in [115–117]. In [105] we discussed in more detail how the physical parameters of the system can be translated into the parameters of the simulation. The parameters and the corresponding values used in our simulations are summarized in Table (4.2).

4.2.3 Simulations : Results and discussion

We have considered a system of 5000 particles with a volume fraction $\Phi = 40\%$. To describe the dynamics of the glassy springs, the WLF parameters of polyisoprene (PI) [118], for which $T_g = 213$ K, have been used. The parameter K which describes the stress-softening in Eq.(4.30) has been taken to be 0.3 MPa·K^{-1}. The other parameters characterizing the network of soft springs and the hardcore interactions between particles are the same as in our previous studies and are fixed [105, 106]. We have considered two values of the parameter β : 0.04 and 0.02, and two values for the parameter k_0 : 10 and 100. For each value of β and k_0, simulations have been performed at various temperatures, from $T = 263$ K $= T_g + 50$ K up to $T = 323$ K $= T_g + 110$ K. A sinusoidal deformation $\gamma(t) = \gamma_0 \sin(\omega t)$ with a fixed pulsation $\omega = 1$ s^{-1} has been imposed. As the model systems may be more dissipative than the experimental systems because of the large value of the friction ζ, the viscous contribution $\sigma(t) = G''_{\text{high T}}\gamma_0 \cos(\omega t)$, where $G''_{\text{high T}} \simeq 3.86$ MPa is the loss modulus measured at high temperature for the smallest value of β ($T = 323$ K,

$\beta = 0.02$), has been removed from the stress. Note in particular that, for these parameter values, the apparent modulus is found to be independent of the strain amplitude (there is no Payne effect), and thus in this regime the viscous stress originates only from the friction between particles.

The elastic response of a sample defined by the following parameters : $\beta = 0.04$ and $T = 323$ K is shown in Figure 4.14. The stress versus strain curves, the elastic and viscous stress as a function of time and the elastic and viscous stress as a function of strain and strain rate are shown. A strain-hardening behavior is observed. The parameters chosen here correspond to a moderate reinforcement, and a relatively high temperature. The main features observed in the experiments (Figure 4.9) are reproduced qualitatively. The elastic stress at several temperatures and for two different values of β : 0.02 and 0.04 is plotted as a function of strain in Figure 4.15. The corresponding viscous stress (for $\beta = 0.02$ only) is plotted in Figure 4.16. A hardening of the elastic stress is observed at the extremities of the cycle. The stronger the reinforcement, and the lower the temperature, the larger the hardening effect. The observed behavior is also qualitatively similar to that observed experimentally in Figure 4.11. Regarding the viscous stress, a behavior qualitatively similar to that of the experimental data, in which the viscous stress goes through a maximum at intermediate strain rates, is observed.

We interpret the strain hardening as the consequence of the slowing down of the strain rate at the extremities of the cycle. When the strain rate slows down, glassy bridges can recover relatively long relaxation times more efficiently as compared to faster strain rates. By relatively long, we mean relaxation times which are not too small as compared to the deformation period. The corresponding glassy bridges will therefore contribute more efficiently to the elastic response. We define the distributions of relaxation times $P(\log \tau)$ as the number of glassy springs having a relaxation time larger than τ. In Figure 4.17, the distribution $P(\log \tau)$ in systems undergoing a sinusoidal deformation of amplitude $\gamma_0 = 0.5$ are plotted at different instantaneous values of the strain $\gamma(t)$. We consider a relatively strongly reinforced system ($\beta = 0.04$; $T = 263$ K), and the same system at higher temperature ($T = 323$ K). Indeed, one can see in Figure 4.17 that the number of glassy bridges with breaking times between 10^{-1} s and 1 s is larger for values of $\gamma(t)$ close to the maximum $\gamma_0 = 0.5$. When the strain rate slows down, the relaxation time of glassy bridges can increase, whereas at high values of the strain rate the glassy bridges break more frequently. This is the same mechanism as the one we discussed in [106] for accounting for the unique plastic properties of filled elastomers. Indeed, it was argued in [106] that when a static strain is applied and maintained constant for a long time, the glassy bridges recover long relaxation times in this new imposed deformation state, thus creating a new reference state corresponding to a plastic deformation with respect to the initial state at rest (before the static strain has been applied). The same mechanism is at work in the dynamical situations discussed in this paper. The observed hardening is the consequence of the larger life-times of the glassy bridges at the extremities of the deformation cycles : thus this does not correspond to strain hardening, but to what we propose to name "slowing down hardening", a property which should be observed in self-healing systems in general.

The behavior of the dissipative stress, and in particular the peak observed in both the ex-

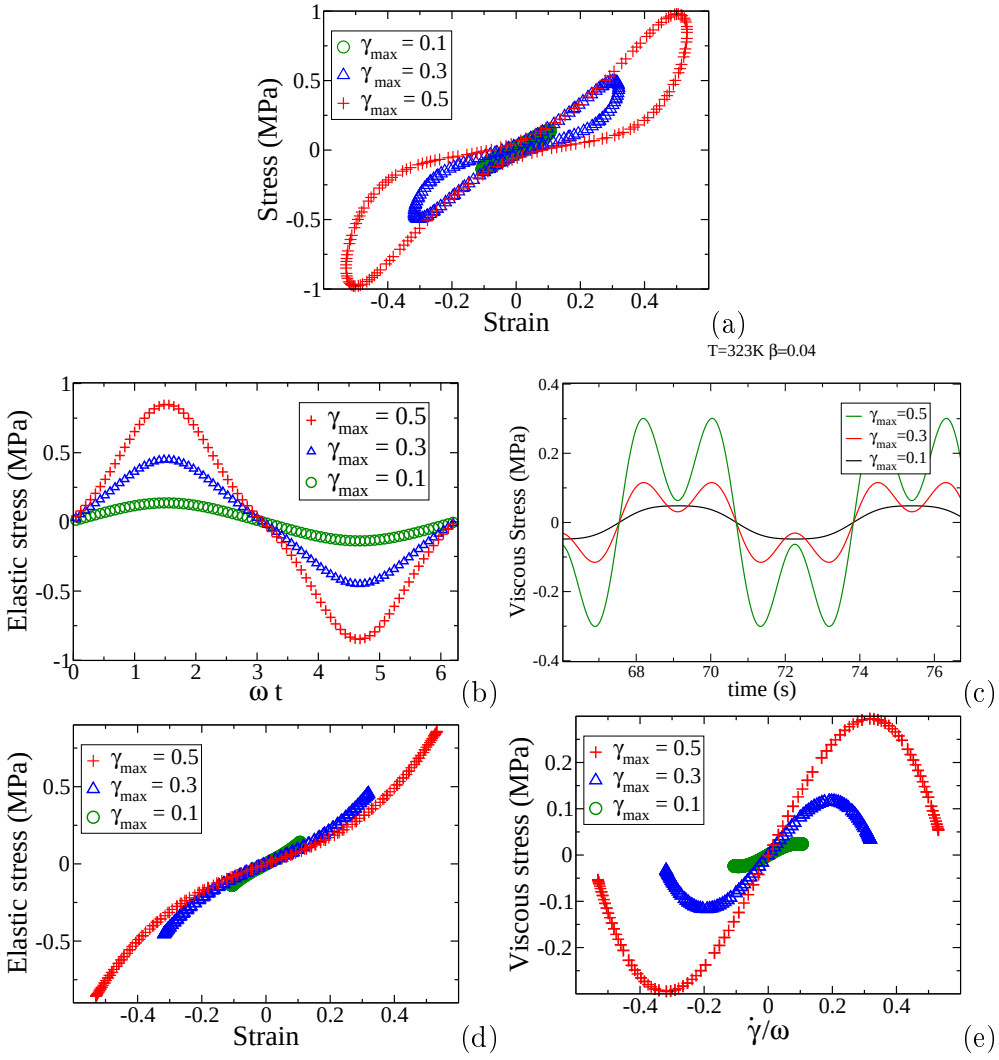

FIGURE 4.14 – Stress curves simulated with the model with $\beta = 0.04$, $k_0 = 100$ and $T = 323$ K (using the WLF parameters of PI with $T_g = 213$ K). Other parameters are $\Phi = 40\%$; $K = 0.3$; $\zeta = 4$ s ; pulsation $\omega = 1$ s^{-1}. The contribution to the stress due to the friction between particles has been substracted as explained in the text. (a) Lissajous plot : stress vs strain. (b) Elastic stress vs time. (c) Viscous stress vs time. (d) Elastic stress vs strain : the curve at large amplitude shows strain-hardening. (e) Viscous stress vs $\dot{\gamma}(t)/\omega$: the non-linearity is seen as a rheofluidification. Compare to experimental results in Figure 4.9.

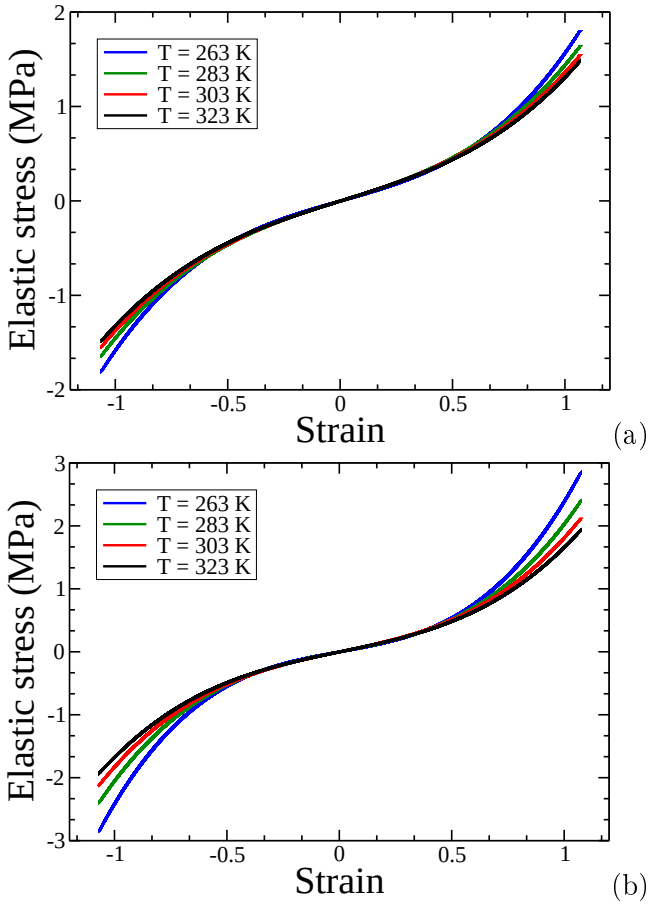

FIGURE 4.15 – Simulations : elastic stress as a function of strain at different temperatures. The parameters are $\beta = 0.02$, $k_0 = 100$ (a) and $\beta = 0.04$, $k_0 = 100$ (b). A temperature dependent hardening is observed at the extremities of the cycle, due to a slowing down of the deformation rate. The stronger the reinforcement, and the lower the temperature, the larger the effect.

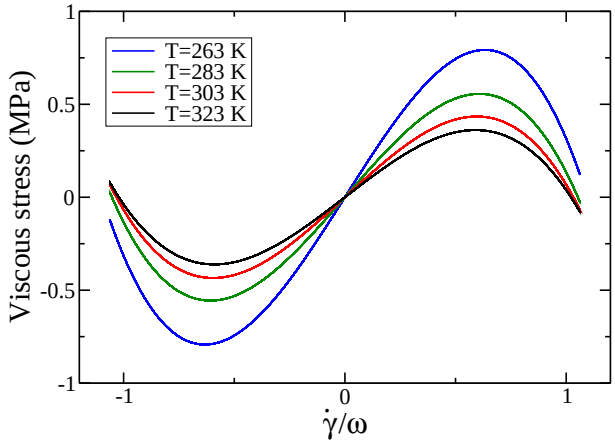

FIGURE 4.16 – Simulations : viscous stress in a sample with $\beta = 0.02$, $k_0 = 100$, $\gamma_0 = 100\%$, at different temperatures.

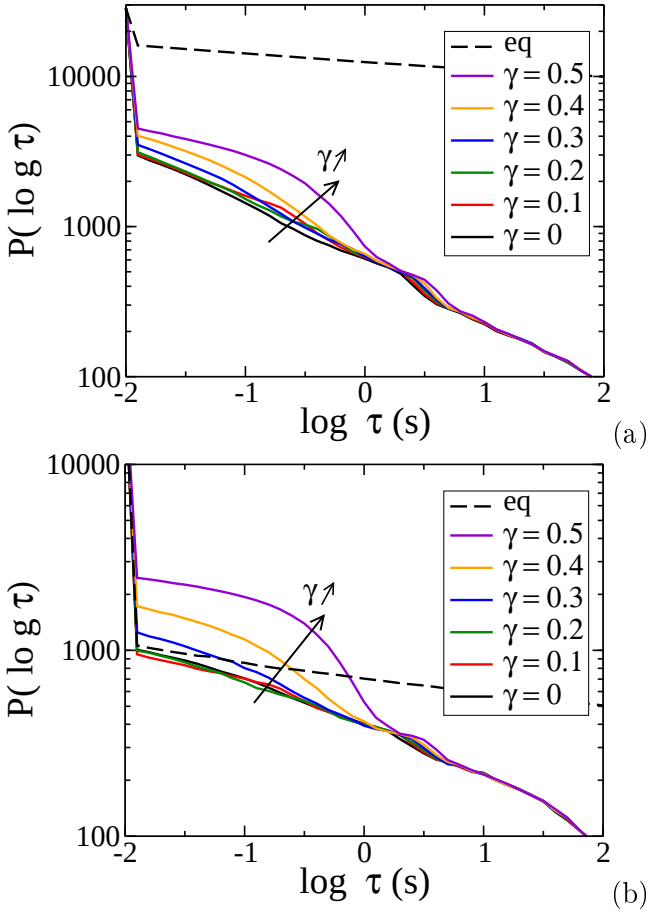

FIGURE 4.17 – Distribution of relaxation times of glassy bridges $P(\log\tau)$ of systems undergoing a sinusoidal deformation with an amplitude $\gamma_{max} = 0.5$, plotted at different values of the instantaneous strain $\gamma(t)$:from bottom to top, $\gamma = 0\,;\ 0.1\,;\ 0.2\,;\ 0.3\,;\ 0.4$ and γ_{max}. $P(\log\tau)$ is the number of glassy springs having a relaxation time larger than τ. The total number of glassy bridges is $\simeq 25000$. (a) reinforced system ($\beta = 0.04\,;\ T = 263$ K), for which p_2 is smaller than p_0 (see Figure 4.18) ; (b) a moderately reinforced system ($\beta = 0.04\,;\ T = 323$ K) for which p_2 is larger than p_0 (see Figure 4.18). Other parameters are the same as in Figure 4.14. Dashed curves show the distributions prior to deformation. In the moderately reinforced system (b), the number of glassy springs having a lifetime comparable at least to the deformation period, $\tau \sim 1$ s, may be larger than at equilibrium. In this case, the slope p_2 is larger than p_0.

periments and in the simulations (see Figures 4.9 and 4.14 respectively), may also be explained by this mechanism. Let us consider the behavior of the viscous stress as a function of $\dot{\gamma}$. We consider the extremum of the instantaneous strain $\gamma(t = 3T/4) = -\gamma_0$ at the lower extremity of the deformation cycle (T is the period of the applied deformation). At this point, $\dot{\gamma} = 0$ and the viscous stress is zero. Close to this point, the life-times of the glassy bridges are comparatively large, because of the 'slowing down hardening' effect discussed above. Then, $\dot{\gamma}$ increases and $\sigma''(t)$ first increases linearly (as can be seen in Figures 4.9 and 4.14), because the distribution of glassy bridge life-times is not yet modified as compared to the situation at the extremum, at time $t = 3T/4$. As the strain rate, as well as the instantaneous strain, increases further, the distribution shifts to shorter times, as it is observed in Figure 4.17. The sample then becomes less dissipative, which corresponds to the peak of $\sigma''(t)$. The same is true at the upper extremity of the cycle at $t = T/4$, where $\gamma(t = T/4) = \gamma_0$.

As discussed in [105], the dissipation in filled elastomers has three different origins. The most obvious one is that of the matrix, far from the polymer-filler interfaces. The second one is due to the transition region between the matrix and the glassy layer. The third one is due to the kinetics of rupture and rebirth of glassy bridges, which is of interest here. This third source of dissipation becomes efficient at intermediate deformation amplitudes γ_0. Indeed, at small γ_0, the life-time distribution of the glassy bridges is not modified by the deformation and remains the same than that of the sample at rest. The rupture and rebirth of glassy bridges do not contribute significantly to the dissipation. At intermediate to large values of γ_0, the distribution is shifted towards smaller time scales and may thus contain a significant fraction of life-times comparable to the deformation period. Then, the kinetics of rupture and rebirth of glassy bridges contributes significantly to the dissipation. This is also the reason why the dissipative stress plotted as a function of $\dot{\gamma}$ increases when the deformation amplitude increases, as seen in Figures 4.9, 4.13, 4.14, 4.21 and 4.22. Note that at even higher strain amplitudes, the effect of glassy bridges decreases because their life-times become shorter. This leads to a decrease in G'' at large deformation amplitudes [105] and to the presence of a peak for G'' as a function of γ_0 at intermediate values of γ_0. This is not observed here because the strain amplitudes are not large enough and/or the systems are not sufficiently reinforced.

The ratios p_1/p_0 and p_2/p_0 are plotted as a function of the strain amplitude in Figures 4.18 and 4.19, at different temperatures and for the same parameter values as in Figure 4.15. Figure 4.18 shows that p_1/p_0 decreases more abruptly, i.e. the Payne effect becomes larger, when temperature decreases. The ratio p_2/p_0 decreases with the strain amplitude at low temperatures, while it increases at high temperatures. Figure 4.19 shows that at high temperatures, the Payne effect is modest and nearly independent of temperature in the considered temperature range. At all the temperatures considered, the ratio p_2/p_0 increases with the strain amplitude, following a curve which is nearly independent of temperature, except for the lowest considered temperature ($T = 263$ K).

We have proposed above that the elastic modulus at the extrema of the strain cycle $\gamma(t) = \gamma_0$ can be larger than that at $\gamma(t) = 0$ (for a given deformation amplitude γ_0) because glassy bridges

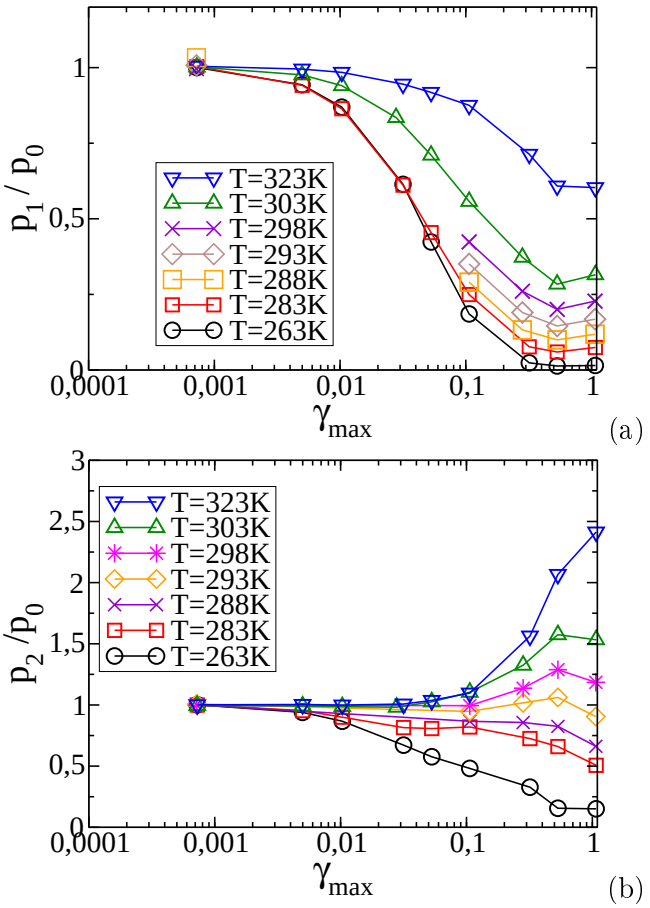

FIGURE 4.18 – Simulations : the ratios p_1/p_0 (a) and p_2/p_0 (b) vs strain amplitude at different temperatures ($T = 263$ K, 283 K, 303 K and 323 K) for $\beta = 0.04$ and $k_0 = 100$. As temperature decreases, the Payne effect becomes larger so that p_1/p_0 decreases more abruptly. p_2/p_0 decreases with the strain amplitude at low temperatures, while it increases at high temperatures. Other parameters are the same as in Figure 4.14. Compare to Figure 4.11.

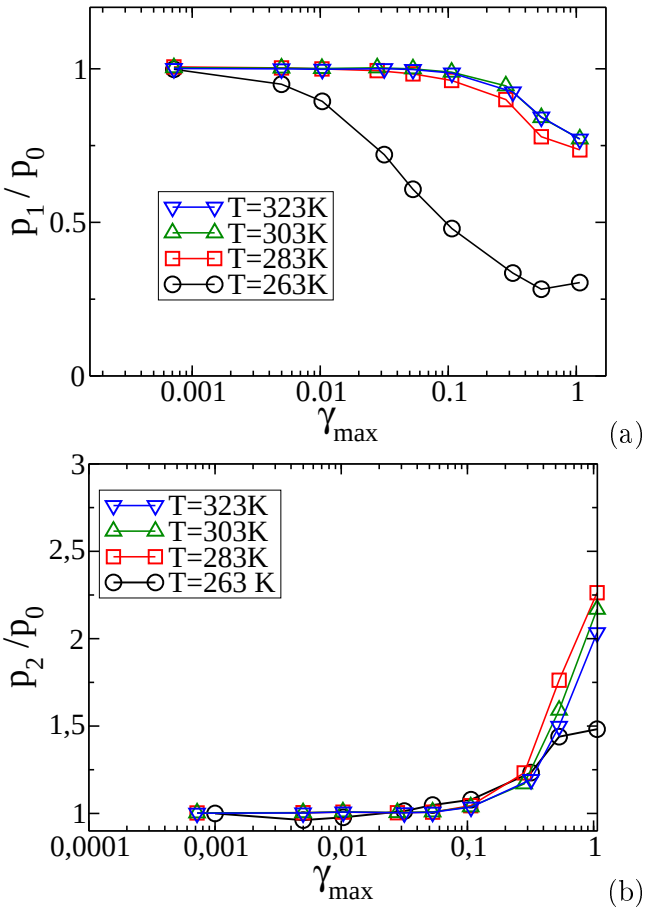

FIGURE 4.19 – Simulations : the ratios p_1/p_0 (a) and p_2/p_0 (b) vs strain amplitude at different temperatures ($T = 263$ K, 283 K, 303 K and 323 K) for a small value of $\beta = 0.02$ and $k_0 = 100$. At high temperatures, the Payne effect is modest and nearly independent of temperature. At all the considered temperatures, the ratio p_2/p_0 increases with the strain amplitude, following a curve which is nearly independent of temperature. Other parameters are the same as in Figure 4.14. Compare to Figure 4.12.

can build relatively long relaxation times around positions for which $\dot{\gamma} = 0$. On the other hand, one might expect that the elastic modulus should be smaller than p_0 there. This is the case in strongly reinforced systems, with large Payne effect : the "slowing down hardening" cannot compensate for the strong amplitude of the Payne effect, as can be seen in Figures 4.18 for a system with $\beta = 0.04$ at $T = 263$ K.

On the other hand, for moderately reinforced systems (the system with $\beta = 0.04$ considered in Figure 4.18 at high temperatures ($T = 303$ K or 323 K) and the system with $\beta = 0.02$ in Figure 4.19 at any temperature), the slope p_2 is larger than p_0, as it is also the case experimentally (see Figures 4.11 and 4.12). We have argued that the finite extensibility of the chains cannot be the reason for this increase, because of the temperature dependence of p_2 (see Figure 4.13 and related discussion). Finite extensibility is not incorporated in the simulations anyway. We propose the following explanation : the applied deformation changes the distribution of distances between fillers, and can bring some of them closer together. This results in a shift of glassy bridges lifetimes towards longer times and thus possibly in a stiffening of the sample at large deformation amplitudes as compared to the undeformed state. The distributions of distances $N(z)$ between the centers of mass of neighboring particles are plotted in Figure 4.20 at different instantaneous values of the strain. The results for a relatively strongly reinforced sample ($\beta = 0.04$ and $T = 263$ K) are plotted in Figure 4.20(a).

No shift towards smaller distances is observed in this case. In the case of a moderately reinforced system ($\beta = 0.04$ and $T = 323$ K, Figure 4.20.(b)), it is observed that some fillers can come closer together under applied strain as compared to the equilibrium system, thus leading to a stiffening at large deformation amplitudes. The difference regarding the distribution of distances between the initial, undeformed system, and the one at the maximum deformation amplitude might seem tiny. However, one must bear in minds that the reinforcement parameter β is not very large ($\beta = 0.04$), and that the temperature is relatively high ($T = 323$ K). The glassy layer thickness e_g, given by [32, 55]

$$e_g = \beta \frac{T_g}{T - T_g} \tag{4.39}$$

is of the order of 0.09. As a consequence, the polymer layers situated between fillers further apart that $z \approx 1.2$ are more than 60 K above their glass transition, and do not contribute to the building of glassy bridges. Only fillers closer than $z \approx 1.2 - 1.1$ contribute significantly to the reinforcement. We see thus that the elastic forces within the material can bring some fillers closer together as compared to the initial undeformed sample, and lead to values of p_2 larger than p_0.

From these discussions, we deduce that the simulated system which is closest to the experimental system T50 CG 30 % corresponds to the parameters $\beta = 0.02$ and $k_0 = 100$. The simulated system which is the closest to the experimental system T30 NCG 25% corresponds to the parameters $\beta = 0.04$ and $k_0 = 100$.

To further illustrate how the non-linear behavior depends on the reinforcement parameters k_0, β and T, the stress/strain curve, the elastic stress as a function of the strain and the viscous stress as a function of the strain rate are shown for a system with $\beta = 0.04$ and $k_0 = 10$ at

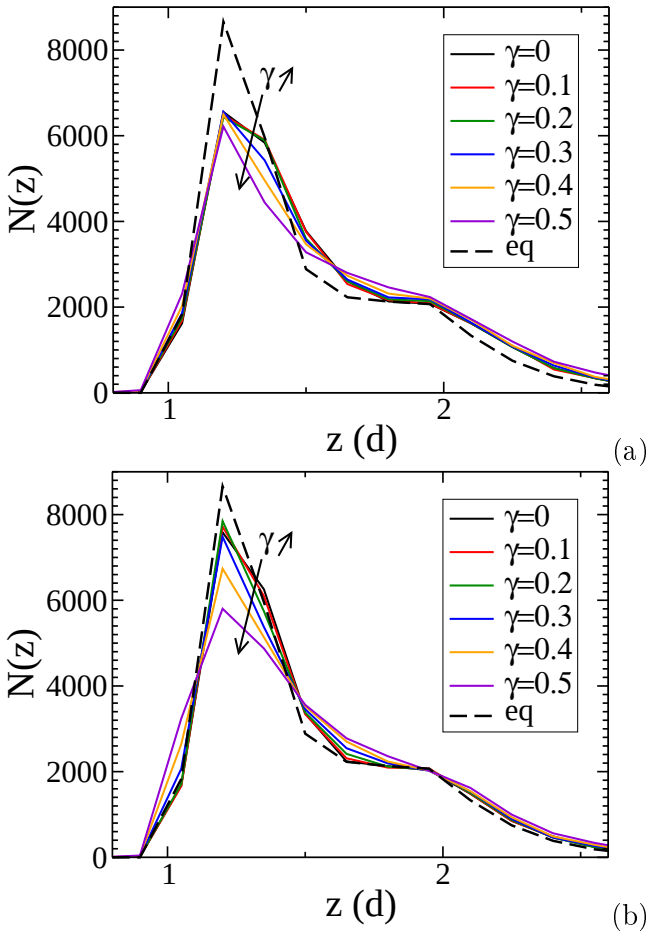

FIGURE 4.20 – Distribution of distances $N(z)$ between the centers of mass of neighbouring particles for systems undergoing a sinusoidal deformation of amplitude $\gamma_{\max} = 0.5$, plotted at different values of the instantaneous strain : from top to bottom, $\gamma = 0\,;\ 0.1\,;\ 0.2\,;\ 0.3\,;\ 0.4$ and $\gamma_{\max}$. $N(z)$ is the number of pairs whose center of mass lies between z and $z + \Delta z$, with $\Delta z = 0.15d$. The total number of distinct pairs of particles is $\simeq 25000$. (a) reinforced system ($\beta = 0.04\,;\ T = 263$ K) ; (b) a moderately reinforced system ($\beta = 0.04\,;\ T = 323$ K). Other parameters are the same as in Figure 4.14. Dashed curves show the equilibrium distributions prior to deformation. Note that at 323 K and at maximum strain, two neighbouring particles may come very close to each other, consistently with the large value of p_2 compared to p_0. See text for more explanations.

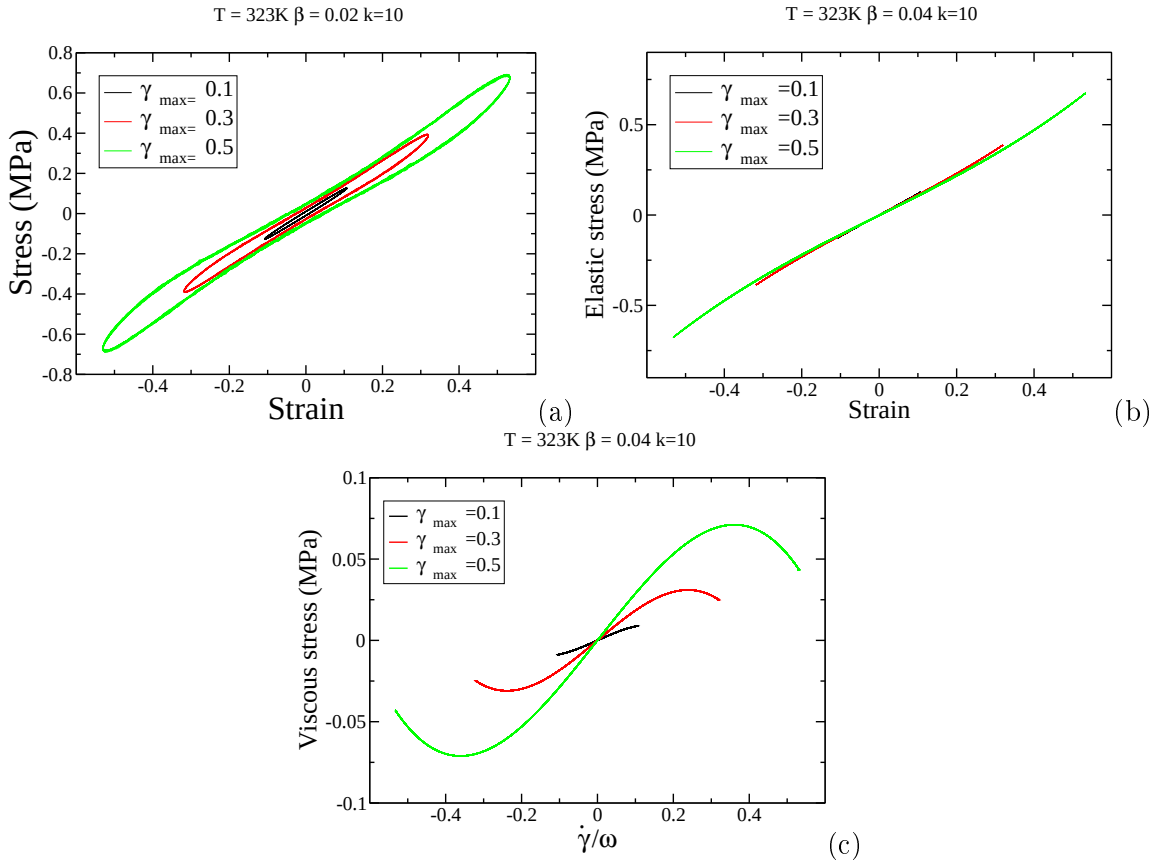

FIGURE 4.21 – Simulations : stress/strain curve (a), Elastic stress (b) and viscous stress (c) of a sample with $\beta = 0.04$, $k = 10$, $T = 323$ K.

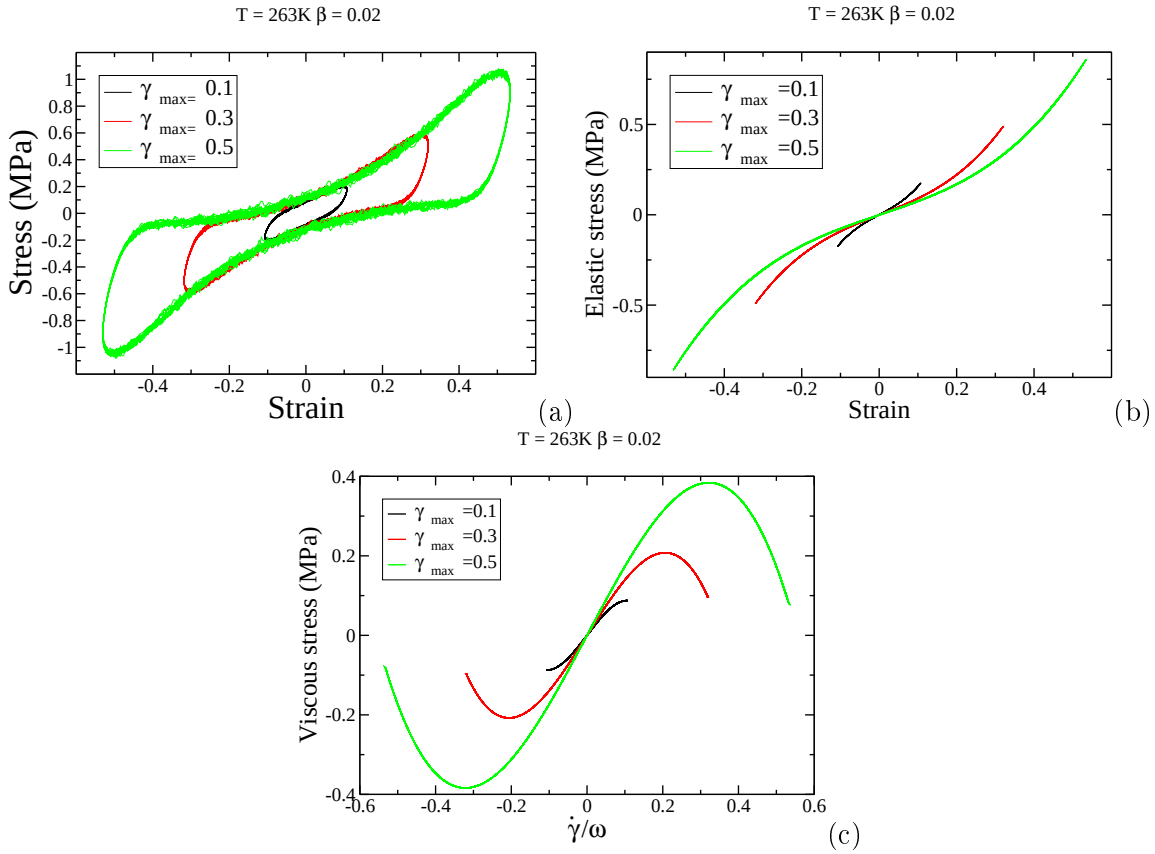

FIGURE 4.22 – Simulations : stress/strain curve (a), Elastic stress (b) and viscous stress (c) of a sample with $\beta = 0.02$, $k = 100$, $T = 263$ K.

$T = 323$ K (Figure 4.21) and for a system with $\beta = 0.02$, $k_0 = 100$, $T = 263$ K (Figure 4.22). In this latter case, the cubic contribution to the viscous strain dominates at large strain rates. In some cases, the viscous stress may show values of opposite sign than the strain rate for large values of the latter, as it is observed in Figure 4.16. The contributions of the harmonics ω, 3ω and 5ω to the elastic stress are plotted in Figure 4.23. It is observed that $a_5(\omega)$ is indeed negligible for the considered systems and deformation amplitudes. Only $a_3(\omega)$, though much smaller than $a_1(\omega)$, is not negligible. The stronger the reinforcement, the larger the amplitude of $a_3(\omega)$. Note that since it is negative, it leads to strain hardening at large deformation amplitude. Thus, the "slowing down hardening" is due to the contribution of the third harmonics. On the other hand, a_3 is quite small compared to the apparent "slowing down hardening" observed in Figure 4.15. The hardening is defined by the slope $p_2 = \frac{d\sigma'(t)}{d\gamma}$. According to Eq.4.26, one has

$$p_2(\gamma(t) = \gamma_0) = \frac{d\sigma'(t)}{d\gamma} = (a_1 + 3a_3)/\gamma_0 - 12a_3/\gamma_0 = (a_1 - 9a_3)/\gamma_0 \tag{4.40}$$

Thus, even if a_3 is small as compared to a_1, it can lead to a significant hardening because of the factor 9 in this equation.

A last point deserves to be discussed, it is the specific features of the non-linear behavior of filled elastomers. It is often thought that a non-linear behavior under periodic solicitations at frequency ω should necessarily result in the appearance of contributions to higher frequency harmonics 3ω, 5ω,..., which is the case in particular when the stress is a non-linear, non-retarded function of the deformation x with a constitutive relation of the type : $\sigma(x) = k^{(1)}x + k^{(3)}x^3 + k^{(5)}x^5 + ...$ Under these circumstances, large higher harmonic contributions are indeed associated to a strongly non-linear behavior. On the contrary, as we have discussed, it is well known that filled elastomers have a strong non-linear behavior, in the sense that the elastic modulus $G'(\gamma_0, \omega) = a(\gamma_0, \omega)/\gamma_0$ strongly depends on γ_0, which is the Payne effect, whereas higher harmonics are very small, as we have seen both in experimental results and in simulations. Filled elastomers thus behave as non-linear materials as regards their response to deformation of increasing amplitudes, but almost as linear materials under permanent oscillatory shear of fixed amplitude. We propose the following explanation for this apparent paradox. Filled elastomers can be described by two different moduli : a first one, which corresponds to the elastomeric matrix, with infinite life-time ; a second one, which corresponds to a high frequency glassy modulus. The deformation amplitude γ_0 essentially modifies the life-time of glassy-bridges, and thus modifies their contribution to the mechanical response, but does not change the glassy modulus itself. In particular, for deformation amplitudes larger than a few percents, or ten percents, depending on the systems, the difference between the initial distribution of relaxation times and the distribution during the experiment is huge (see Figure 4.15). On the other hand, the variation of the distribution of relaxation times during a given shear experiment can be quite small as is shown in the same figure. In a first approximation, one can consider that the applied periodic deformation modifies the distribution of relaxation time. In the absence of additional effects, the response to a permanent oscillatory shear would be rigorously harmonic. However, as we have discussed, the life-times of glassy bridges evolve slightly during the deformation cycle, which results in small anharmonicities. The amplitude of the anharmonicities depends on the

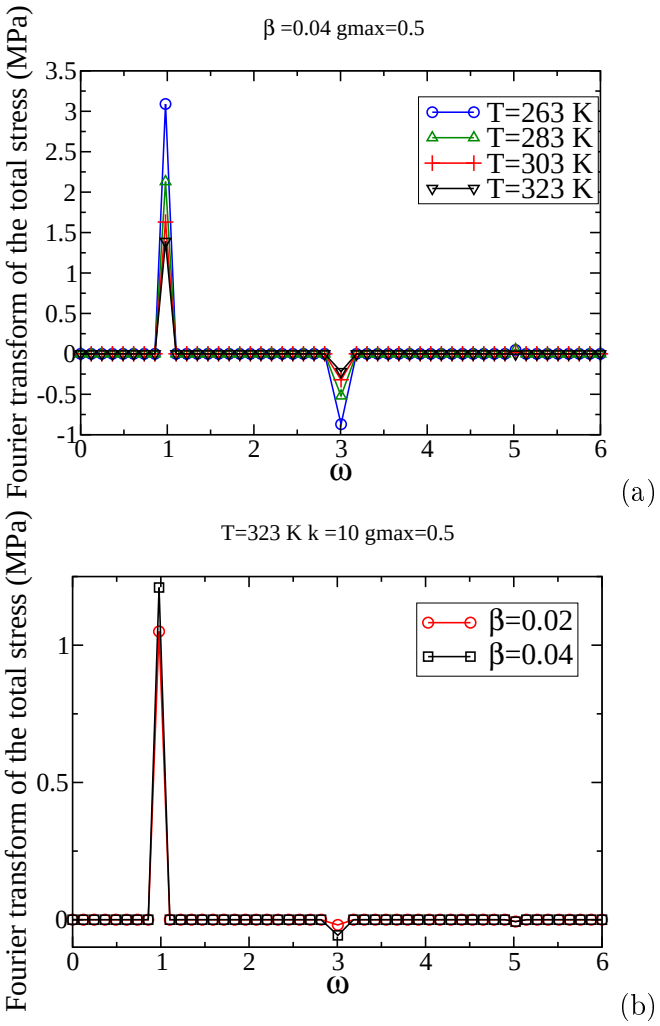

FIGURE 4.23 – Fourier components of the total stress for systems deformed with an amplitude $\gamma_0 = 0.5$. $k_0 = 100$ (a) and $k_0 = 10$ (b). Different values for β and for the temperature are considered.

fraction of glassy bridges which are able to build life-times comparable to (though necessarily smaller than) the deformation period in the vicinity of the extremities of the deformation cycles. One can thus expect that the non-harmonic response should be relatively larger, i.e. the ratio between the third and the first harmonic contributions should increase, for large amplitude and very low frequency oscillatory shear cycles, that is by increasing γ_0 and decreasing ω such that the product $\gamma_0\omega$ decreases. Indeed, when ω goes to zero, such periodic deformations come close to the static deformations considered in [106] where it was shown that the glassy bridges build a new reference state corresponding to the applied deformation. This new reference state corresponds to a plastic deformation of the material. If the waiting time is long enough, the mechanical properties around this new state are very close to that of the initial system around its former reference state. As a consequence, one might expect that anharmonicities should be larger at very low frequencies. This will be tested in further studies.

4.2.4 Conclusion

We have shown that the GBR model can account for the non-linear behavior of filled elastomers submitted to large amplitudes oscillatory shear experiments. Though they might be present in some experiments, and certainly at sufficiently large deformation amplitudes, the finite extensibility of the chains did not dominate the non-linear response of the studied samples. The non-linear response was shown to be the consequence of the kinetics of destruction and rebirth of glassy bridges, which is also key for explaining the non-linear Payne effect, as well as some unique feature of the plastic and recovery behavior of filled elastomers. No new adjustable parameter has been introduced as compared to earlier papers [105, 106]. Essentially all the considered parameters assumed the same values as compared to earlier studies, except for the reinforcement parameter β which assumed smaller values since the systems considered in this paper are less reinforced than the systems considered in [105, 106]. Our point of view is that filled elastomers systems can be described by two elastic moduli : a rubbery one, and a glassy one, and the distribution of relaxation times associated to the glassy component. The applied strain does not change the elastic moduli, but modifies the life-time distribution and thus, in particular, modifies the contribution of the glassy modulus. Thus, the main features of the non-linear response during periodic oscillations is the following : the strain amplitude changes drastically the distribution of relaxation times as compared to the initial undeformed system (Payne effect). The higher harmonic contributions are the results of fluctuations of the distribution of relaxation times during one period, and are a much smaller effect. The behavior of filled elastomers is at odds as compared to systems which could be described by a non-linear and non-retarded constitutive relation of the type $\sigma(x) = k^{(1)}x + k^{(3)}x^3 + k^{(5)}x^5 + ...$, for which there might be no possible distinction between the non-linear behavior and the higher harmonics contributions. It appears that the glassy layer picture is able to explain various aspects of the mechanical behavior of filled elastomers : the reinforcement amplitudes as compared to Payne's experiments [112] ; the Payne effect ; the recovery effects and specific features of the plastic properties of filled elastomers [4]. On the other hand, as we discussed in [105], it is hard to explain even the amplitude of the reinforcement by an increase of entanglement density in the vicinity of the fillers as proposed in [119]. Indeed, the very presence of the observed non-harmonicities is a strong indication that relaxation takes place on time scales comparable to the period, and thus that glassy dynamics

is involved.

In this Chapter, we have described the non linear mechanical behavior of the samples. Using a qualitative comparison with the glassy bridge reinforcement model, we showed that the strain-hardening and shear-thinning experimentally observed inside a cycle of solicitation at large strain amplitude could be attributed to the destruction/rebirth kinetics of glassy bridges. It is now interesting to determine more quantitatively the presence of glassy bridges between the particles in our samples. In the next Chapter, we investigate the particles dispersion in the samples and use the polymer dynamics results obtained in Chapters 2 and 3 to open a general discussion on the presence of glassy bridges and their link with the mechanical behavior of the samples.

Chapitre 5

Discussion générale : Arrangement des particules, épaisseur vitreuse et propriétés mécaniques

Ce chapitre a pour but la mise en relation de la composition microscopique des échantillons et leur comportement macroscopique.

Tout d'abord, l'arrangement des particules dans chaque échantillon est déterminé grâce à des simulations Monte-Carlo inverses à partir de résultats de diffusion de neutrons. Ensuite, les résultats des chapitres 2 et 3 sont discutés en fonction de l'arrangement des particules et des épaisseurs caractéristiques de polymère vitreux et immoblisé sont extraites. Enfin, à partir de ces épaisseurs et de la dispersion des charges, nous déduisons la présence ou non de ponts vitreux entre les particules, ce que nous essayons ensuite de relier à l'amplitude de l'effet Payne.

Sommaire

General discussion : Particles arrangement, glassy thickness and mechanical properties

The aim of this chapter is to discuss the relationship between the microscopic composition of the samples and their macroscopic behavior.

First, the particles arrangement in the samples is determined through reverse Monte-Carlo simulations from neutron scattering measurements.Then, the results of chapters 2 and 3 are discussed taking into account the fillers dispersion, and characteristic glassy and immobilized polymer thicknesses are extracted. Finally, with those thicknesses and the fillers arrangement, we deduce the presence or not of glassy bridges between the particles, that we can correlate to the Payne effect amplitude in the samples.

5.1 Introduction

In chapter 3, we have interpreted the polymer dynamics in filled elastomers in terms of glass transition temperature gradient around the fillers. For that we have used a model of T_g gradient assuming that the particles were isolated from each other. We did not take into account the fact that the neighboring particles could be a perturbation if the T_g gradients were overlapping. In order to check to which extent this hypothesis is valid, we need to be aware of the arrangement of the fillers in the samples. In the same way, in order to translate the glassy and immobilized polymer volume fractions obtained in Chapter 2 in thicknesses around the particles, we also need to know the particles arrangement in the samples so that we can take into account the possible overlap of layers from neighboring particles.

A useful tool for the determination of the silica particles arrangement is the Small Angle Neutron Scattering (SANS) technique. As it has been exposed in the first chapter (section 1.2.2), SANS measurements have been done on the samples and have been interpreted using a Percus-Yevick approximation. The samples were described as hard spheres liquids with a random arrangement of the particles. This model showed the presence of an excluded volume around the particles, which is characteristic of a repulsive interaction between the fillers. We could thus obtain the minimum distance between the surface of the particles h (see Table 1.2).

However, if this description works well for the well dispersed samples with a rather low silica volume fraction, it is more difficult to use it for more concentrated or not so well dispersed samples. That is why we will use in this chapter another method to interpret the SANS measurements, namely reverse Monte-Carlo simulations. It will give us the opportunity to find the distribution of distances between particles in each sample. The principle of this simulation is to compare the experimental SANS curve to the one computed for a box of particles. At each step of the simulation, a particle is moved in the box and the new SANS signal is calculated. The step is accepted if the new computed signal is closer from the experimental one. In the end, the box of particles should give a good description of the fillers arrangement in the sample.

In this chapter, we will first describe the Monte-Carlo simulations and the obtaining of the interparticle distances in each sample. The program is an adaptation of the one developed by Julian Oberdisse at the Laboratoire des Colloides Verres et Nanomatériaux in Montpellier. Then, we will use this result to discuss the results obtained in chapters 2 and 3 on the polymer dynamics in filled elastomers : first the validity of the isolated particles hypothesis taken in chapter 3 and then the determination of the thicknesses with each method. Finally, we will discuss the pertinence of those thicknesses to describe the mechanical behavior of the samples and in particular their Payne effect.

5.2 Particles dispersion : Reverse Monte-Carlo simulations

The determination of the particles arrangement is done through reverse Monte Carlo simulations which have been done in collaboration with Julian Oberdisse at the Laboratoire des Colloides Verres et Nanomatériaux in Montpellier. The program has been adapted from the one developed in this laboratory to be used on our systems.

5.2.1 Program structure

Initialization

First, we choose the number of particles N_{tot} on which the simulation will be done. The mean diameter D_m of the particles is fixed, as well as the polydispersity. The particle volume fraction in the sample determines the size of the box where the particles will be introduced. The particles are placed in the box in an initial configuration that can be either a random or a crystalline arrangement. Then the pair correlation function corresponding to this configuration is calculated. It corresponds to the probability of finding the center of a particle at a given distance from the center of another particle. Then, the structure factor is deduced and compared to the experimental one and the standard deviation between the two, χ^2, is calculated. The total number of steps in the simulation is also chosen, as well as the initial thermal energy. This parameter simulates a temperature effect and will enable the acceptation of energetically unfavorable steps in the simulation. We will come back to the influence of this parameter in a coming section.

Loop

Then there is the succession of Monte-Carlo steps. At each step, the program chooses a random particle and makes it move of one step in a random direction. Then we check that it is not colliding with another particle, otherwise, the particle is replaced in its initial position and another one is chosen and moved, until there is no collision. With this new configuration, the pair correlation function and the structure factor are updated, taking into account the local changes in the particles arrangement. This method is faster in terms of calculation time than a complete recalculation. Then, depending on the new value of the standard deviation, the step can be accepted or refused. If χ^2 has decreased or increased moderately - depending on the thermal energy - the step is accepted and another step is done. Otherwise, the step is refused, the particle is replaced in its initial position and another step is done. In order to simulate an annealing step, the thermal energy is decreased by multiplying it by a factor 0.9 every N_{tot} steps.

End

At the end, a complete recalculation of the structure factor is done and compared to the experimental one. An example of the results obtained is given in Figure 5.1. In the final configuration, the polymer volume fraction corresponding to a given thickness around each particle is calculated. This computation allows to take into account the possible overlap of neighboring layers.

5.2.2 Simulation parameters

Some of the parameters are fixed for all the simulations : the mean silica diameter is determined from SANS measurements of diluted silica solutions (see Chapter 1 - section 1.2) and the polydispersity is fixed to 10% for all the samples. The size of one Monte-Carlo step is 0.5 nm, which is short enough to give a good precision in the final configuration.

The parameters we have investigated are : the range of q where the structure factor can be fitted, the influence of the initial Boltzmann energy chosen, the number of particles and the

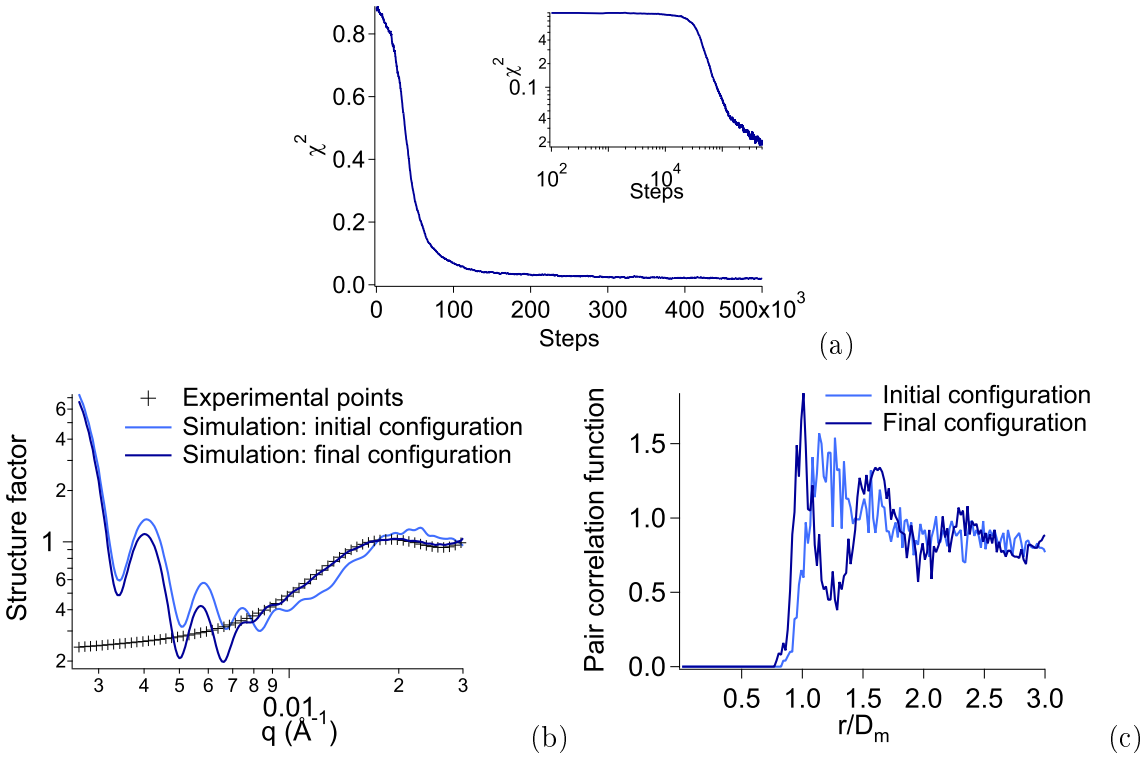

FIGURE 5.1 – Results of a reverse Monte-Carlo simulation on the sample MIST TPM 25% (R_{Si}=13.5 nm, $\phi_{Si} = 0.163$) with an initial thermal energy of 0.01, $N_{tot} = 1000$ particles and 500 000 steps in the simulation. The initial configuration is a random one. (a) Evolution of the standard deviation between the experimental and computed structure factor (log-log scale in the inset). In the inset we see that the system is still evolving at the end of the simulation but the system is already very close from the experimental results after 100 000 steps. (b) Experimental structure factor (markers), structure factor in the initial configuration (light blue) and in the final configuration (dark blue). The oscillations seen at low q are due to the finite size of the simulation box. The standard deviation is calculated from $q = 8.10^{-3}$ Å^{-1}. (c) The pair correlation function in the initial configuration (light blue) and in the final configuration (dark blue) as a function of r/D_m, where D_m is the mean diameter of the particles. In the initial random state there is no preferred distance, whereas peaks of first, second etc neighbors are appearing in the final configuration, showing some order in the particle arrangement.

initial particles configuration.

Fitting q range

The fitting range, that is the q range on which the standard deviation χ^2 is calculated, has to be carefully chosen for each sample. In effect, at low q, the computed curve shows large oscillations due to the finite size of the box in which the simulation is done - the box is similar to a Heaviside function which gives rise to a *sinc* function in the reciprocal space. Thus the fit cannot start before those oscillations are lower in intensity than the experimental structure factor. Moreover, at large q, the experimental signal is not well defined mainly due to the noise of the experiment so that a fit in this range of q would not be pertinent. The fitting range has thus to be chosen in-between those two regions for each sample.

Boltzmann energy

The thermal energy - or Boltzmann energy - is simulating an annealing of the sample. The parameter entered is its initial value, then it is decreased as the simulation advances (we multiply it by a factor 0.9 every N_{tot} steps). To see the influence of this parameter, we choose initial values between 0.001 and 10 and compare the evolution of the simulations, other things being equal. We see in Figure 5.2 that the final configuration is not noticeably modified. The final χ^2 value and pair correlation function are very similar, the main change is in the way the system attains its final configuration. If the initial thermal energy is high, more unfavorable steps are allowed which enables a better exploration of the space but also delays the finding of a more favorable configuration. The decrease in χ^2 is thus expected to come later if the initial Boltzmann energy is higher. For the next simulations, we chose an initial thermal energy of 0.01.

Number of particles in the box

Increasing the number of particles on which the simulation is done reduces the edge effects but also increases drastically the calculation time to reach the point of convergence. The results of simulations with various amount of particles are exposed in Figure 5.3. It shows that the final configurations have slightly different standard deviations χ^2 as well as a different shape of the pair correlation function. When N_{tot} is increased, the peaks in the pair correlation function are less pronounced following a more significant averaging process due to the larger box used. Moreover, if the number of particles is too small, we also see a decrease in the pair correlation function at large distances, due to the finite size of the box. We have thus to find a compromise between the calculation time and the accuracy of the pair correlation function. We see that for $N_{tot} \geq 8000$ the maximum value of the pair correlation function and the integral of its first peak start to stabilize, so it seems a good choice to take $N_{tot} = 8000$ particles for the coming simulations.

Initial configuration

It is also essential to check that the initial configuration has no influence on the point of convergence of the simulation. In Figure 5.4 we clearly see that the various initial random configurations all lead to a similar final configuration. For a crystalline initial configuration, the initial

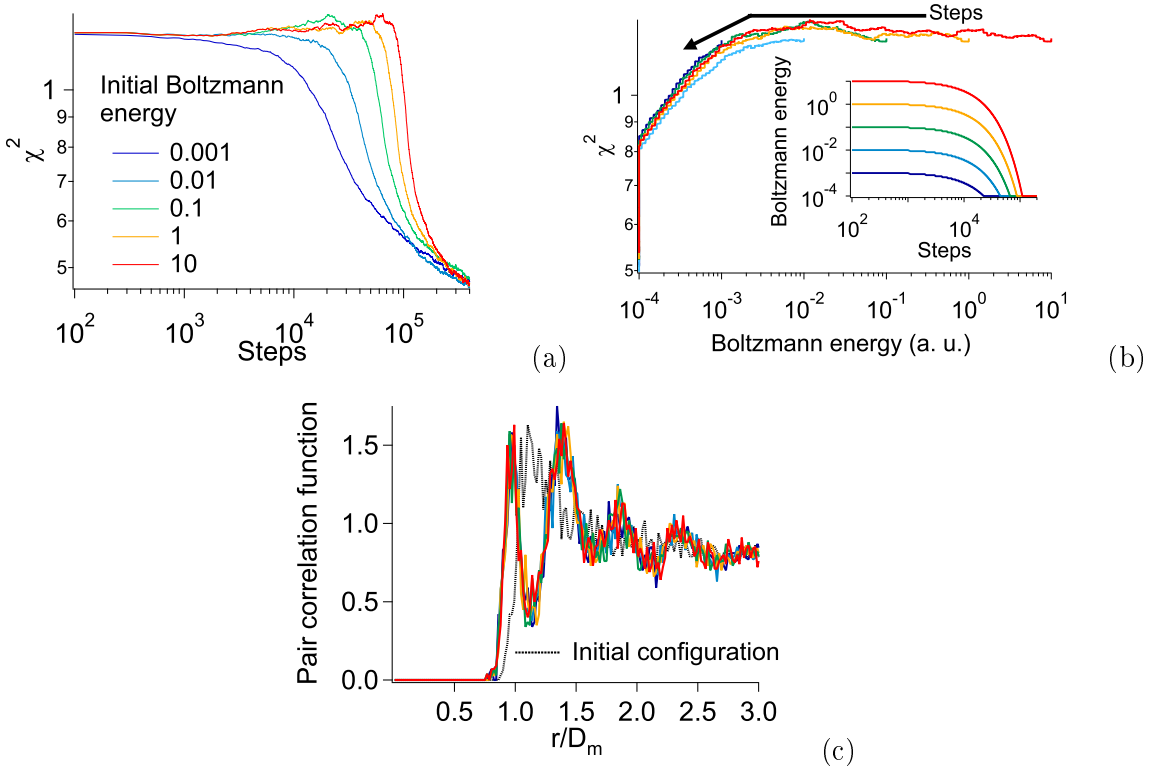

FIGURE 5.2 – Effect of the initial thermal energy on the evolution of the reverse Monte-Carlo simulation (sample MIST TPM 30%, $N_{tot} = 1000$ particles). Standard deviation χ^2 as a function of the Monte-Carlo steps (a). In (b), we present a parametric plot of χ^2 as a function of the thermal energy during the simulation for various initial thermal energies. We see that the curve is very similar for all the different initial thermal energies. In the inset, we see the evolution of the thermal energy in the simulation : it is multiplied by a factor 0.9 every N_tot steps. (c) represents the pair correlation function in the initial configuration (dash line) and in the final ones (plain lines). If the initial thermal energy is higher, the system takes a larger number of steps before starting to converge, but the final configuration is not significantly different. For the next simulations we will put the initial thermal energy at 0.01.

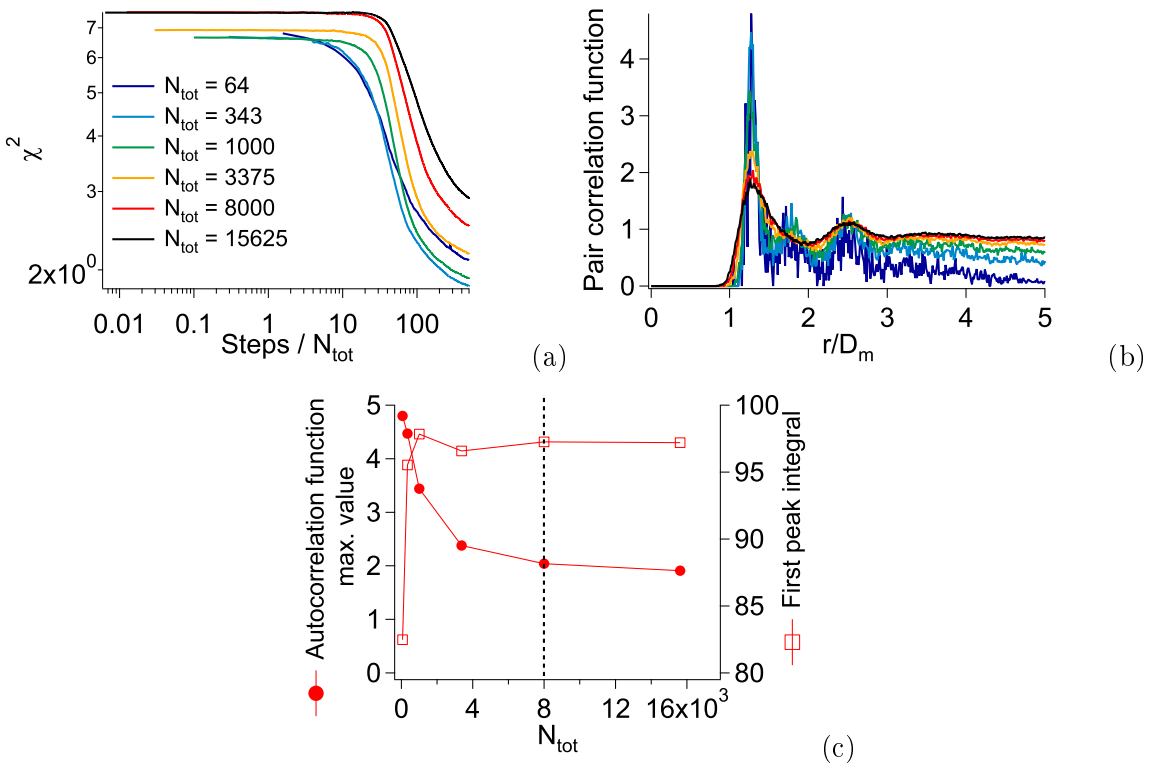

FIGURE 5.3 – Effect of the number of particles in the simulation. Standard deviation as a function of Monte-Carlo steps divided by the total number of particles N_{tot} (a), and pair correlation function after simulation with between 64 and 15 625 particles (b) (sample T50 TPM 30%). The more particles there are in the simulation, the more averaging there is in the pair correlation function. Increasing the number of particles decreases the importance of the edge effects and allows a better determination of the distances distribution but it also drastically increases the calculation time. In (c) we presents the evolution of the maximum value of the pair correlation function and the integral of its first peak as a function of the number of particles. Both values start to stabilize at N_{tot}=8000, which is thus the value we will take for the following simulations.

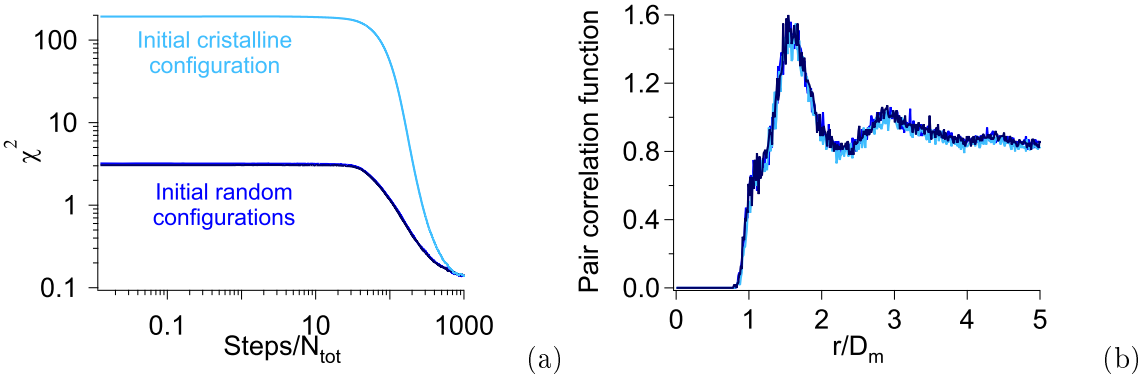

FIGURE 5.4 – Effect of the initial configuration on the reverse Monte-Carlo simulation. Standard deviation (a) and pair correlation function (b) for simulations with various random and crystalline initial configurations (sample T50 TPM 25%). The method is validated since the final configuration does not depend on the initialization of the simulation.

standard deviation is much higher, but the final configuration is not noticeably different from the previous cases. This confirms the robustness of the simulation and its independence to the initial configuration chosen. For the following simulations, we will take random initial configurations.

5.2.3 Results : distribution of the interparticle distances

The parameters being chosen, the simulation is done for all the samples of the study. We are interested in the pair correlation function, which is giving the distribution of distances in the sample, as well as in the mean distance between first neighbors.

Figures 5.5 and 5.6 present the experimental and computed structure factors and the pair correlation functions for all the samples. From those results, we can compare the samples in terms of number and distance of the first neighbors.

We can obtain the mean distance between neighboring particles (center to center) by integration of the first peak (fp) of the pair correlation function $g(r)$,

$$d = \frac{\int_{fp} r g(r) 4\pi r^2 dr}{\int_{fp} g(r) 4\pi r^2 \mathrm{d}r} \tag{5.1}$$

In order to get a more precise value of the mean surface to surface distance between neighboring particles we have to take into account the particles polydispersity. For that we start from the particles positions after simulation and directly compute the mean surface to surface distance over the first neighbors. This is the method we will use in the following.

The number of first neighbors can be obtained by integration of the first peak of the pair correlation function

$$n = \int_{fp} g(r) \frac{N_{tot}}{V_{tot}} 4\pi r^2 \mathrm{d}r \tag{5.2}$$

The results are gathered in Table 5.1 and compared to the results obtained with the Percus-Yevick approximation (h_{PY}) and with the value expected for a random close packing arrangement $h_{RCP} = 2R_{Si}\left[\left(\frac{\phi_{RCP}}{\phi_{Si}}\right)^{1/3} - 1\right]$ where $\phi_{RCP} = 0.64$.

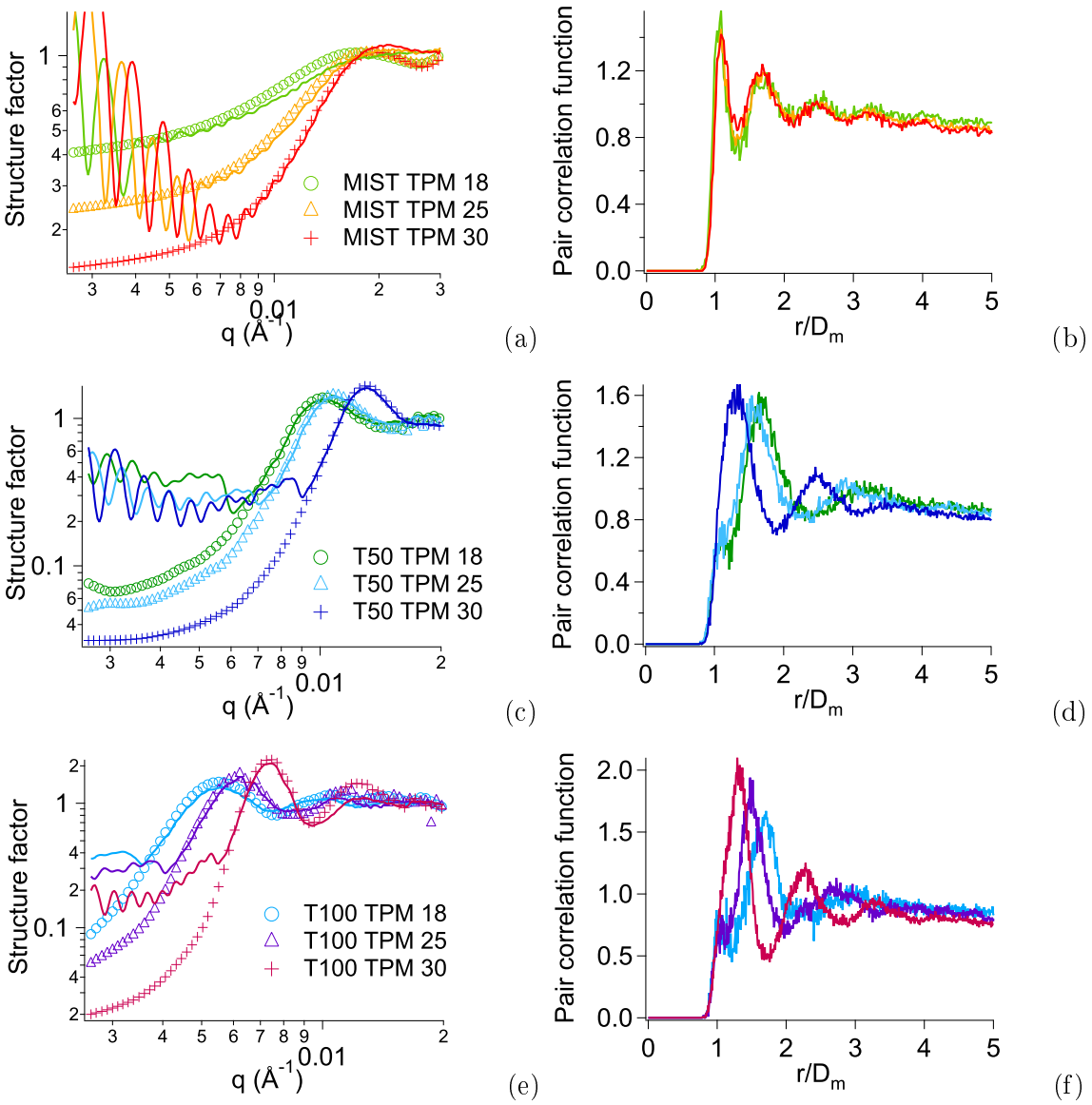

FIGURE 5.5 – Simulation results for the TPM samples. Experimental structure factor (markers) and computed ones (plain lines) and pair correlation function for the MIST TPM samples (D_m=27 nm) (a) and (b), for the T50 TPM samples (D_m=43 nm) (c) and (d) and for the T100 TPM samples (D_m=83 nm) (e) and (f). The pair correlation functions are all exhibiting distinct peaks, showing the existence of some order in the samples.

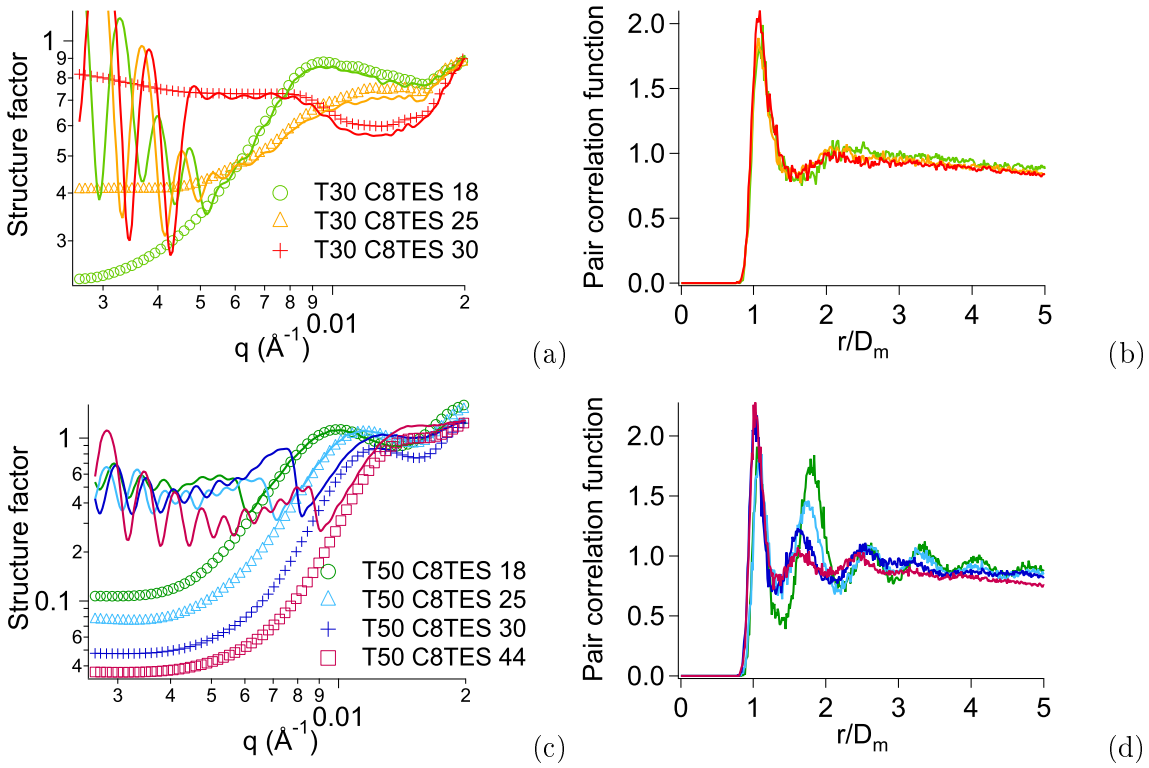

FIGURE 5.6 – Simulation results for the C8TES samples. Experimental structure factor (markers) and computed ones (plain lines) and pair correlation function for the T30 C8TES samples (D_m=26 nm) (a) and (b), for the T50 C8TES samples (D_m=42 nm) (c) and (d). The T30 C8TES samples exhibit no specific order contrary to the T50 C8TES samples.

TABLE 5.1 – Distance between neighboring particles (surface to surface) according to the Reverse Monte-Carlo simulations (RMC), the Percus-Yevick approximation (PY), a Random Close Packing arrangement (RCP) and the number or firsts neighbors according to the RMC simulations.

Sample name	h_{RMC} (nm)	h_{PY} (nm)	h_{RCP} (nm)	Number of first neighbors
MIST TPM 30	3	4.1	12.6	2
MIST TPM 25	3	5.4	15.6	2
MIST TPM 18	2	8.1	21.1	1
T50 TPM 30	21	11.3	18.8	12
T50 TPM 25	34	15.5	27.3	14
T50 TPM 18	37	21	33.7	14
T100 TPM 30	30	16.4	25.1	11
T100 TPM 25	48	27.1	45.2	11
T100 TPM 18	57	37	60.4	11
T30 C8TES 30	6	agg.	15.4	5
T30 C8TES 25	6	agg.	16.4	4
T30 C8TES 18	6	agg.	22.0	3
T50 C8TES 44	4	6.3	12.2	5
T50 C8TES 30	4	12.6	21.7	3
T50 C8TES 25	7	14.7	25.1	3
T50 C8TES 18	7	21	33.9	2

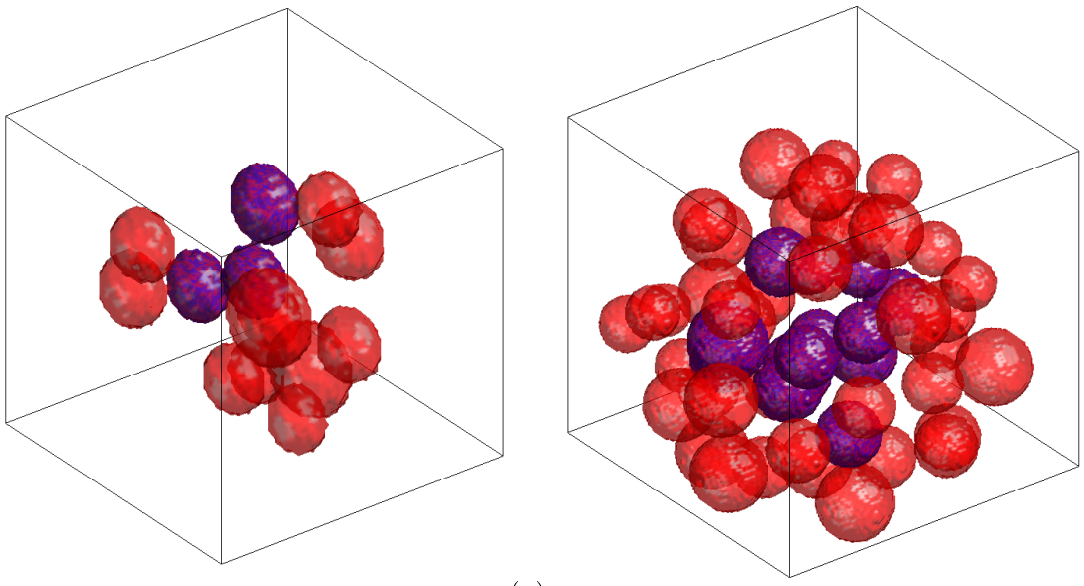

(a) (b)

FIGURE 5.7 – 3D representation of the silica particles arrangement in the samples MIST TPM 30 (a) and T50 TPM 30 (b) (at different scales). A particle is chosen and its first neighbors are represented in blue and the second ones in red.

From those results we clearly see that we have two kinds of samples : the samples T50a TPM and T100 TPM have a high number of first neighbors at a rather large distance between neighboring particles, which is characteristic of a good dispersion state, whereas the other samples have only few neighbors very close from each other, meaning that they are not so well dispersed. As an example, Figure 5.7 (a) is a 3D representation of the first and second neighbors of a silica particle in the sample MIST TPM 30, as obtained after the simulation. We clearly see that the particles are almost in contact with each other. On the contrary, Figure 5.7 (b) shows that the first neighbors of a silica particle in the sample T50 TPM 30 are much further away from each other.

For the well dispersed samples, the surface to surface distances h obtained from the simulations are higher than the one coming from the Percus-Yevick approximation (see Figure 5.8). This can be explained by the fact that h_{RMC} is a mean value over the first neighbors whereas h_{PY} is characteristic of a repulsive interaction and is thus a minimum distance between particles. Moreover, we observe that the distances obtained with the reverse Monte-Carlo simulations are rather close from the distances expected for a random close packing arrangement, which confirms the good dispersion state of those samples.

Now that the particles arrangement is known for the various samples, we are able to interpret more precisely the previous results on the dynamical behavior of the polymer chains obtained by NMR (Chapters 2 and 3).

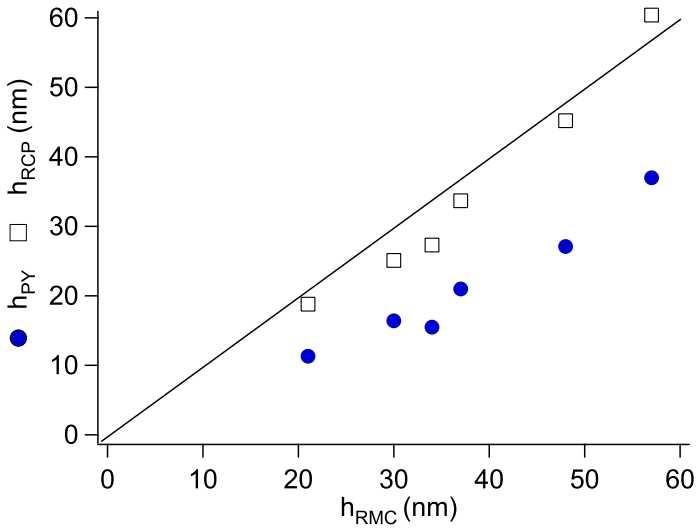

FIGURE 5.8 – Comparison of the mean distance between the surfaces of neighboring particles of the T50 and T100 TPM samples from the reverse Monte-Carlo simulation (h_{RMC}) with the distance from the Percus-Yevick approximation (h_{PY}) and the distance for a Random Close Packing arrangement (h_{RCP}). The line is the first bisector. h_{RMC} is close to h_{RCP} and larger than h_{PY}.

5.3 Consequences on the NMR results

Knowing the arrangement of the particles in each sample, we are now able to further interpret the NMR measurements. In Chapter 2, we described the NMR signals with the sum of three streched exponentials and deduced a glassy and an immobilized polymer fraction at each temperature. Based on the particle arrangement obtained with the RMC simulations, we can now translate those volume fractions into polymer thicknesses. Regarding the second analysis method, that is the T_g gradient model described in Chapter 3, we can now check the validity of the hypothesis of isolated particles we took.

5.3.1 Thicknesses as deduced from the NMR measurements and particle dispersion - Method 1

In Chapter 2, we have decomposed the polymer chains dynamics in our model filled elastomers into three parts : one with the pure elastomer mobility, one with a very restricted mobility (called glassy part) and one with an intermediate mobility. From the analysis of the NMR signals, we could extract the volume fraction of each of those parts. Now that the particle arrangement is known for each sample, we can translate those volume fractions into layer thicknesses around the particles. For that, we compute for each sample the volume fraction corresponding to a given layer thickness around the particles in the box obtained at the end of the simulation (see Figure 5.9(a)). Then, the thickness corresponding to the glassy and immobilized volume fractions are interpolated from those curves. We thus obtain the glassy and immobilized thicknesses for all the samples (see Figure 5.9(b)). The results are similar for all the samples with glassy thicknesses between 2 and 6 nm depending on the temperature for the TPM samples, 1 and 3

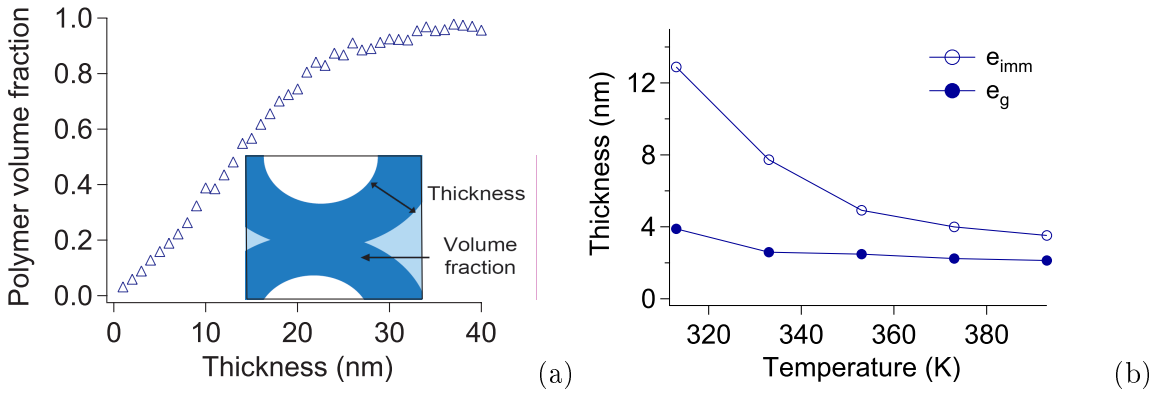

FIGURE 5.9 – Glassy and immobilized thicknesses determination - Sample T50 TPM 25. (a) From the reverse Monte Carlo simulations, we get the particles arrangement of each sample. For the particles configuration obtained after the simulation, we compute the volume fraction (over the total polymer volume) corresponding to a given thickness around each particle. (b) From the volume fractions of glassy and immobilized polymer measured in NMR (Chapter 2), we can then interpolate the corresponding thickness and plot it as a function of the temperature. The results are very similar for all the samples.

nm for the C8TES samples and immobilized thicknesses between 5 and 15 nm for all the samples.

5.3.2 Validity of the T_g gradient model - Method 2

We considered in the T_g gradient model that the particles were isolated. In this hypothesis, the relationship between the layer thickness around the particles and the polymer volume fraction corresponding writes :

$$\phi = \left[\left(1 + \frac{e}{R_{Si}}\right)^3 - 1\right] \frac{\phi_{Si}}{1 - \phi_{Si}} \tag{5.3}$$

In Figure 5.10, we compare this to the curve obtained with the particle arrangement after the Monte-Carlo simulations. As we will see in the next section, the characteristic glassy polymer thickness deduced from the T_g gradient model is below 6 nm at the lowest temperature for all the samples.

We clearly see in this figure that, in this range of thickness, the two curves are very close from each other. We can thus conclude that our approximation of isolated particles is valid for in the temperature range considered.

5.4 Discussion on the glassy and immobilized polymer thicknesses around the particles

In Chapters 2 and 3 we used two different methods to analyze the NMR signals of model filled samples : a decomposition in three parts and a gradient. Using the particle arrangement deduced from RMC simulations, we translated the volume fractions measured with the first method into glassy and immobilized thicknesses and checked the validity of the isolated particles hypothesis taken in the second method. In order to compare the two methods, we first extract a

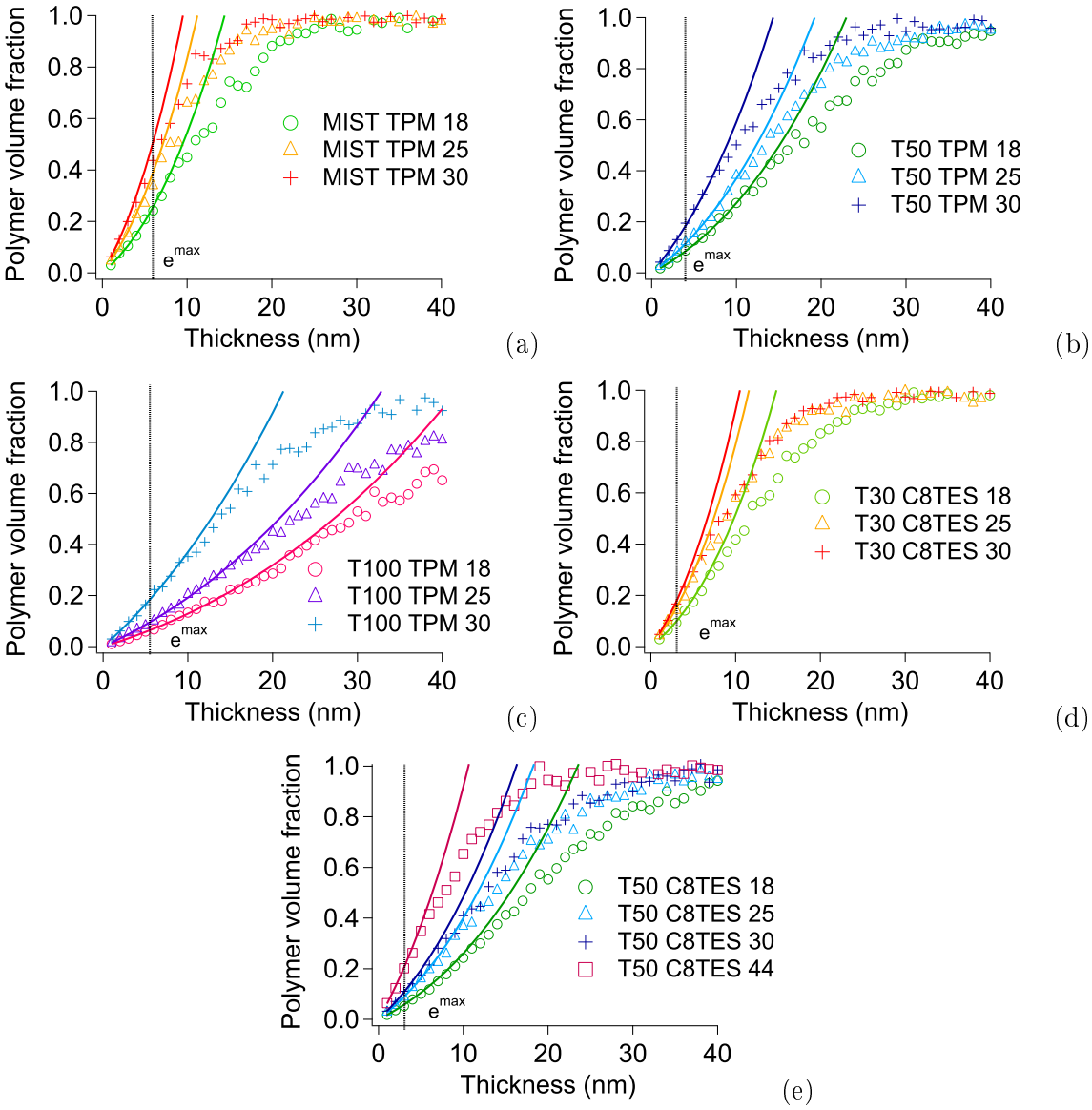

FIGURE 5.10 – Validity of the isolated particles hypothesis in the T_g gradient model. The polymer volume fraction corresponding to a given thickness around the particles is plotted in the hypothesis of isolated particles (plain lines) and in the case of the particles arrangement obtained after the Monte-Carlo simulations (markers) for all the samples : (a) MIST TPM 18, 25 and 30, (b) T50 TPM 18, 25 and 30, (c) T100 TPM 18, 25 and 30, (d) T30 C8TES 18, 25 and 30 and (e) T50 C8TES, 18, 25, 30 and 44. In each case, the two curves are close enough for thicknesses smaller than the glassy thickness deduced from the T_g gradient model. The isolated particles hypothesis is thus sufficient to describe the system in the temperature range we have considered.

characteristic thickness from the T_g gradient method and then discuss the difference in sensitivty of the two analysis.

Thicknesses as deduced from the T_g gradient approach - Method 2

To be rigorous, the thickness of polymer in the glassy state corresponds to the criterion $T_g(e) = T$, that is $T_g^\infty \left(1 + \frac{\delta}{e-e_0}\right) = T$ according to the T_g gradient model (see Figure 5.12(a)). However, in Chapter 2, we not only encountered glassy polymer but also polymer with an intermediate mobility between elastomer and glassy. It seems thus interesting to extend the previous criterion to a broader one : $T_g(e) = T - \Delta$, and test different values for Δ. In Figure 5.12(b), we compare the variation of $e(\Delta)$ with the temperature for Δ = 0K, 20K and 37K with the glassy and immobilized thicknesses obtained with the first analysis method. We see that the glassy thickness corresponds rather well to $e(\Delta = 20K)$, that is to polymer below its T_g plus 20K in the gradient model. The immobilized thickness on the other hand cannot be described by any Δ value. It seems thus that the T_g gradient describes well the polymer fraction that is strongly slowed-down by the presence of the fillers, but that is fails describing a longer-range, more moderate alteration of the dynamics.

Another interesting criterion to define a characteristic thickness in this model is to consider the evolution of the elastic modulus around the particles. From mechanical measurements, we can plot the elastic modulus G' of the pure PEA matrix as a function of $T - T_g$ (the glass transition being the one at 1 Hz - see Figure 5.11(a)). Then, from Chapter 3 we can plot for each sample the variation of T_g as a function of the distance from the particle z (Figure 5.11(b)). Finally, interpolating for each distance z the value of G' corresponding to $T - T_g(z)$, we obtain the variation of the elastic modulus G' as a function of the distance from a particle (Figure 5.11(c)). We see that this variation is very sharp and a good cut-off to extract a thickness can be the distance $e_{G'/G'_0=2}$ at which $G' = 2G'_0$ where G'_0 is the elastic modulus of the pure elastomer at the temperature considered.

We observe in Figure 5.12(b) that this criterion also corresponds well to the glassy thickness e_g and $e(\Delta = 20K)$. And, in the same way than previously, we are not able to find a criterion allowing the description of the immobilized thickness.

It opens thus a discussion on the difference of sensitivty of the two methods.

Discussion on the sensitivity of each analysis method

As we have seen, the T_g gradient model can account only for the glassy fraction measured with the stretched exponentials analysis, and not for the intermediate part. We can thus wonder what might cause this difference between the two analysis.

One difference between the two analysis methods is the fitting range considered : 0-200 μs for the stretched exponentials fits, 0-40 μs for the gradient fit. The shorter range chosen in the second method was to prevent the network part to be too preponderant compared to the glassy part (restricted to 0-20 μs) and to reduce the eventual solvent and crosslink density effects in the network part. This precaution was especially important for the TPM samples, which exhibit a higher effective crosslink density than expected, as shown by the DQ experiments in Chapter

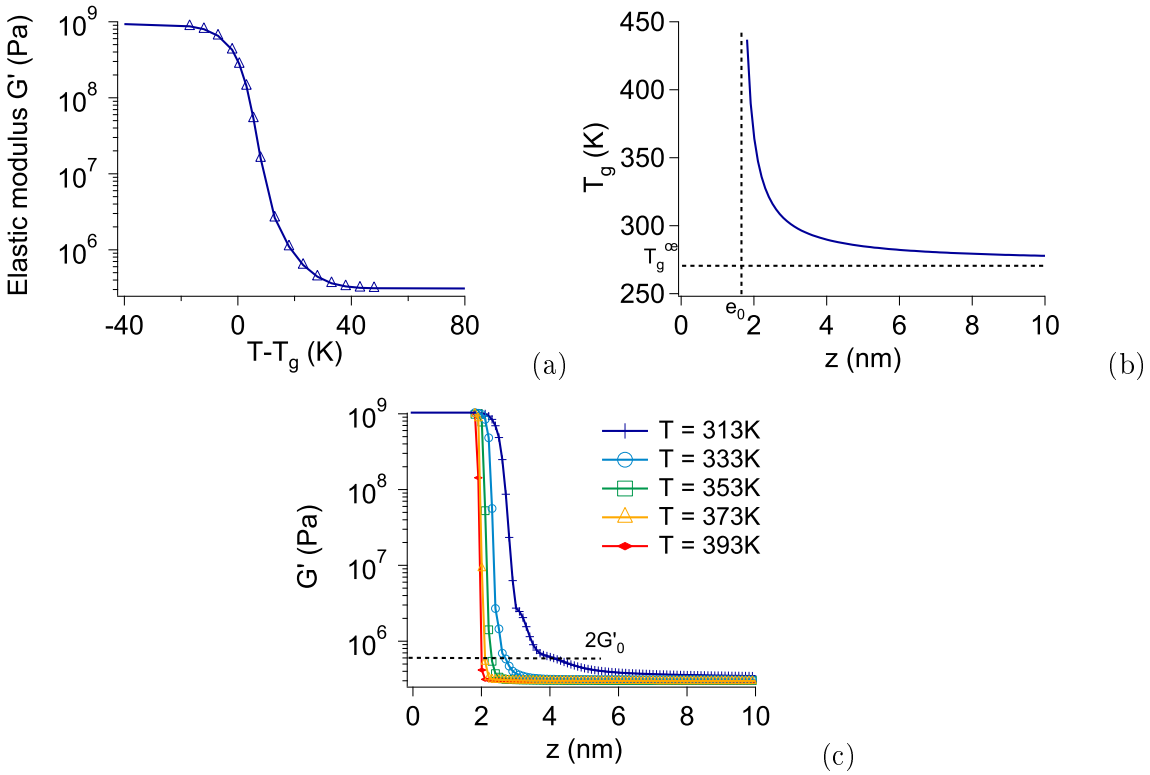

FIGURE 5.11 – Immobilized thickness determination from the modulus variation in the T_g gradient model - Sample T50 TPM 25. (a) Elastic modulus G' as a function of $T-T_g$ from oscillatory shear measurements at 1Hz for the pure PEA matrix. (b) In the filled elastomer, variation of the glass transition temperature with the distance to a particle $T_g(z)$. In this way, at each distance z corresponds a temperature $T - T_g(z)$ and thus a modulus. (c) We can then plot the elastic modulus variation with the distance to a particle $G'(z)$. A criterion to define an "immobilized" polymer thickness is to take the thickness e_m at which the modulus is twice the one of the pure matrix at the same temperature $G'(e_m) = 2G'_0$.

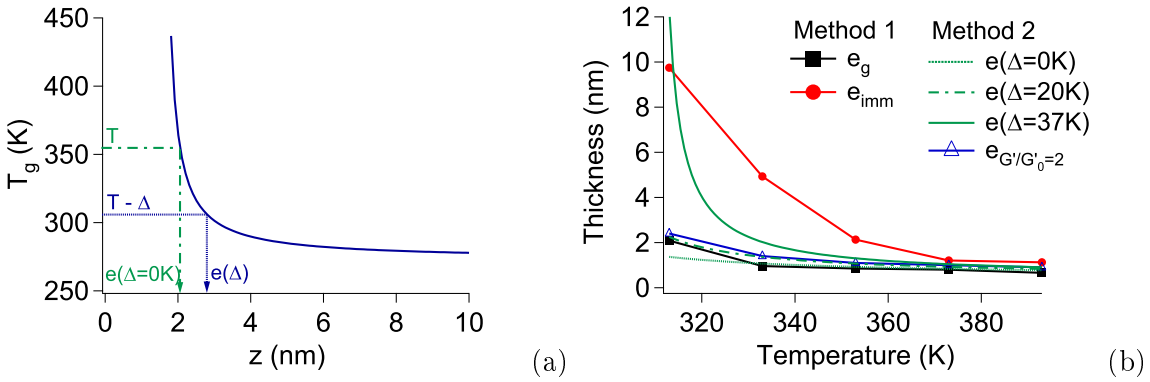

FIGURE 5.12 – (a) Determination of the thickness corresponding to the criterion $T_g(e) = T - \Delta$. (b) Comparison of different thicknesses deduced from the T_g gradient model - Sample T50 C8TES 30. The thickness extracted from the modulus variation near a particle $e_{G'/G'_0=2}$ is compared to the one corresponding to $T = T_g(e) + \Delta$ with Δ=0, 20 and 37K, as well as with the glassy and immobilized thicknesses. We see that the "glassy" thickness is very close to $e_{G'/G'_0=2}$ and $e(\Delta = 20\text{K})$. The immobilized thickness on the other hand cannot be described by any Δ value. The results are very similar for all the samples.

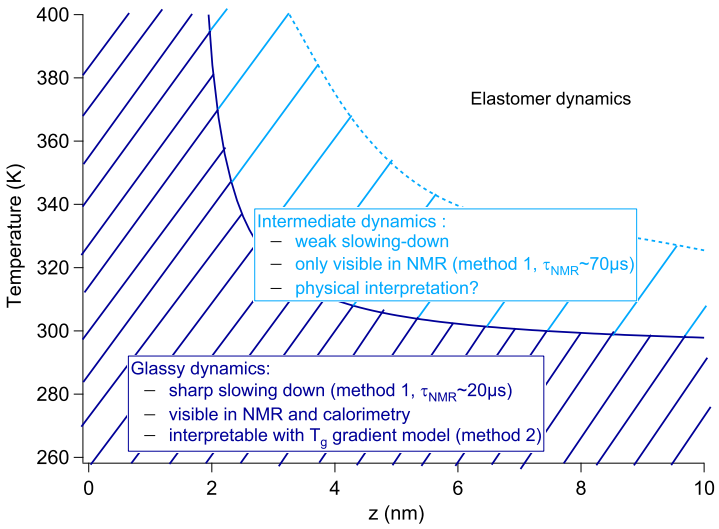

FIGURE 5.13 – Schematic representation of the polymer mobility zones we have encountered in this study. The glassy zone (corresponding to polymer at a temperature below $T_g(z)$+20K) is seen with both NMR analysis methods, as well as in calorimetry, and can be interpreted with a T_g gradient model. The intermediate zone, on the other hand, corresponds to a much weaker polymer dynamics slowing-down and is seen only in NMR with the analysis method 1.

2 (section 2.4.3). This way, the fit was more stable and less dependent on the variation of the network behavior with the addition of solvent. The drawback is that with a shorter fitting range, we might be less sensible to a slowing down of the dynamics at longer scale range, that is to the intermediate part obtained in Chapter 2.

Then, the T_g gradient model might also fail to describe a longer-range slower dynamics because of the form of the gradient model itself, which might be too sharp compared to reality. In our analysis, we chose to take the exponent ν of the original formula $T_g(z) = T_g^\infty \left(1 + \left(\frac{\delta}{z}\right)^{1/\nu}\right)$ equal to one, but we could think that a higher value would give a better descrition. In fact, preliminary results showed that changing the ν value did not change much the results. It might thus be useful to test a different shape of T_g gradient.

To sum up, a schematic repesentation of the typical dynamics encountered in our study is drawn in Figure 5.13. The stretched exponentials analysis shows that the NMR technique is very sensitive to small changes in the polymer dynamics. In effect, it isolates not only the glassy fraction, which is due to the T_g gradient, but also the intermediate fraction which is due to a much lighter slowing down of the polymer dynamics. As we have seen in Chapter 3, this second contribution is not visible in calorimetry, where the curves can be interpreted using only the T_g gradient model, but we can wonder whether it has an influence on the mechanical behavior of the samples.

5.5 Link with the mechanical properties : Payne effect and glassy bridges

In the previous section, we have extracted thicknesses of polymer with different mobilities : a glassy thickness obtained through both the stretched exponentials method (method 1) and the gradient model (method 2), and an immobilized thickness obtained only with the stretched exponentials fits. We are now interested in knowing which of those two thicknesses is more relevant to describe to the mechanical behavior of the filled elastomers and in particular their Payne effects.

Knowing the glassy and immobilized layers thicknesses around the particles, as well as the particles arrangement, we can compute the average number of "glassy" and "immobilized" bridges per particle for each sample, that is the average number of particles linked to a given one by glassy or immobilized polymer. For that, we integrate the pair correlation function obtained after the Monte Carlo simulations for r between 0 and $D_m + 2e$:

$$n = \int_0^{D_m+2e} g(r)\frac{N_{tot}}{V_{tot}}4\pi r^2 \mathrm{d}r \tag{5.4}$$

This is very similar to the calculation of the number of first neighbors (equation 5.2) but this time the integration is over a distance equal to $D_m + 2e$ where e is either the glassy or immobilized thickness at the temperature considered.

The Payne effect is measured for various samples at different temperatures. We chose here to present the amplitude of Payne effect at a given strain amplitude γ_0 : $\frac{G'(\gamma_0)-G'(0)}{G'(0)}$. At each temperature, we interpolate the amount of glassy bridges from the NMR measurements, taking into account the frequency change. We choose to do the interpolation following the value of $\frac{T_g}{T-T_g}$, based on Long and Lequeux's model.

Based on the interpretation of the Payne effect by a plastification of glassy bridges, we would expect to obtain the same Payne effect amplitude for a given amount of glassy bridges, whatever the temperature or the sample considered. Figures 5.14 and 5.15 present the variation of the amplitude of Payne effect for the TPM and C8TES samples as a function of the average number of glassy (a) and immobilized (b) bridges per particle. We observe that TPM and C8TES samples exhibit very similar Payne effect amplitude for a given value of glassy or immobilized bridges, meaning that this represantation enables the comparison of very different samples. However, the number of glassy bridges seems slightly too small to make all the curves collapse on a master curve, whereas the number of immobilized bridges seems too large (the curves are scattered in the opposite order). This means that describing the Payne effect as a function of the number of glassy bridges seems pertinent but that the relevant thickness to use might be in-between the glassy and immobilized thicknesses. It is also interesting to note in Figure 5.14 (a) and 5.15 (a) that the samples exhibit a significant Payne effect even if the average number of glassy bridges per particle is one or less. This lacks coherence with the interpretation of the Payne effect by the plasticization of the glassy bridges, since there are only few of them and that they could not constitute any network. In this sense, considering the immobilized bridges seems more pertinent

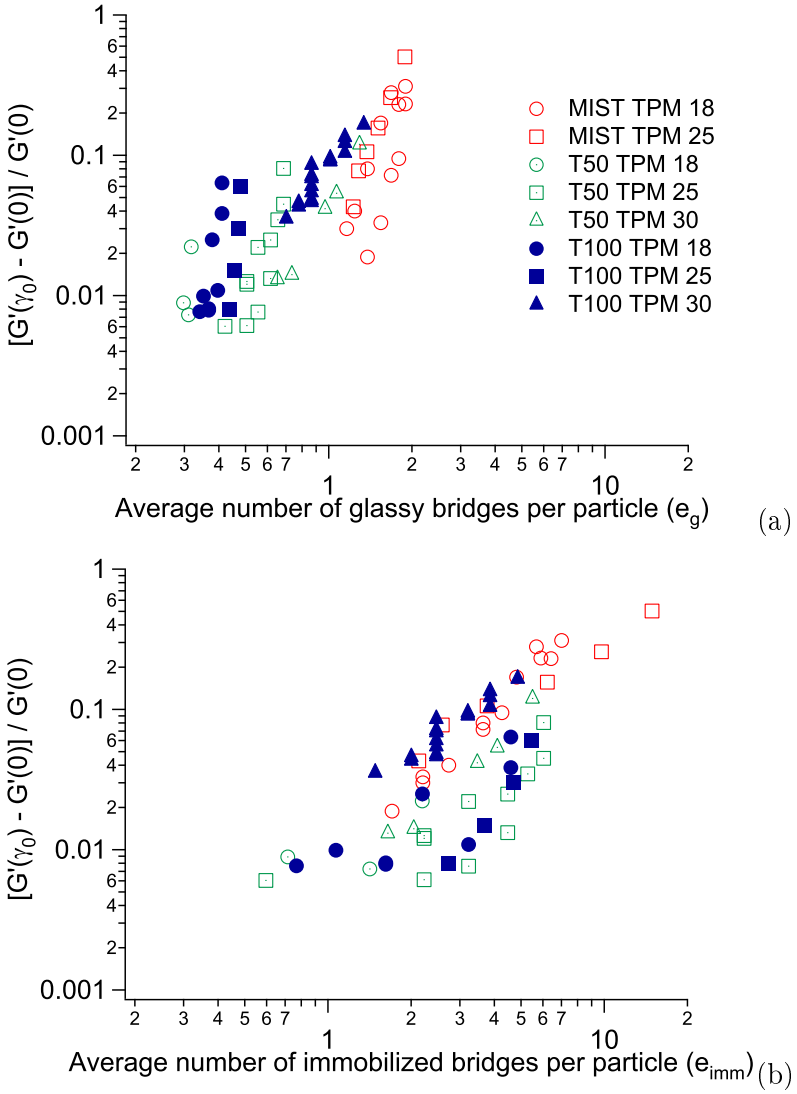

FIGURE 5.14 – Payne effect amplitude as a function of glassy bridges quantity - TPM samples. The amplitude of Payne effect $\frac{G'(\gamma_0)-G'(0)}{G'(0)}$ at a strain amplitude γ_0 =15% is plotted as a function of the average number of glassy (a) or immobilized (b) bridges per particle.

since there are in average 2 to 6 bridges connected to one particle, which means that it forms a kind of immobilized skeleton throughout the sample. In any case, we see that at least part of the polymer with an intermediate mobility is involved in the Payne effect. It opens the question on how polymer exhibiting only slightly altered dynamics can affect significantly the mechanical properties of filled rubbers (Figure 5.16).

5.6 Conclusion

In this chapter we have first determined the particles arrangement in each model filled elastomer studied and extracted two types of samples. T50 TPM and T100 TPM samples show a very good dispersion state, whereas MIST TPM and C8TES samples are not so well dispersed. The reverse Monte-Carlo simulations gave us access to the interparticle distances distribution in each

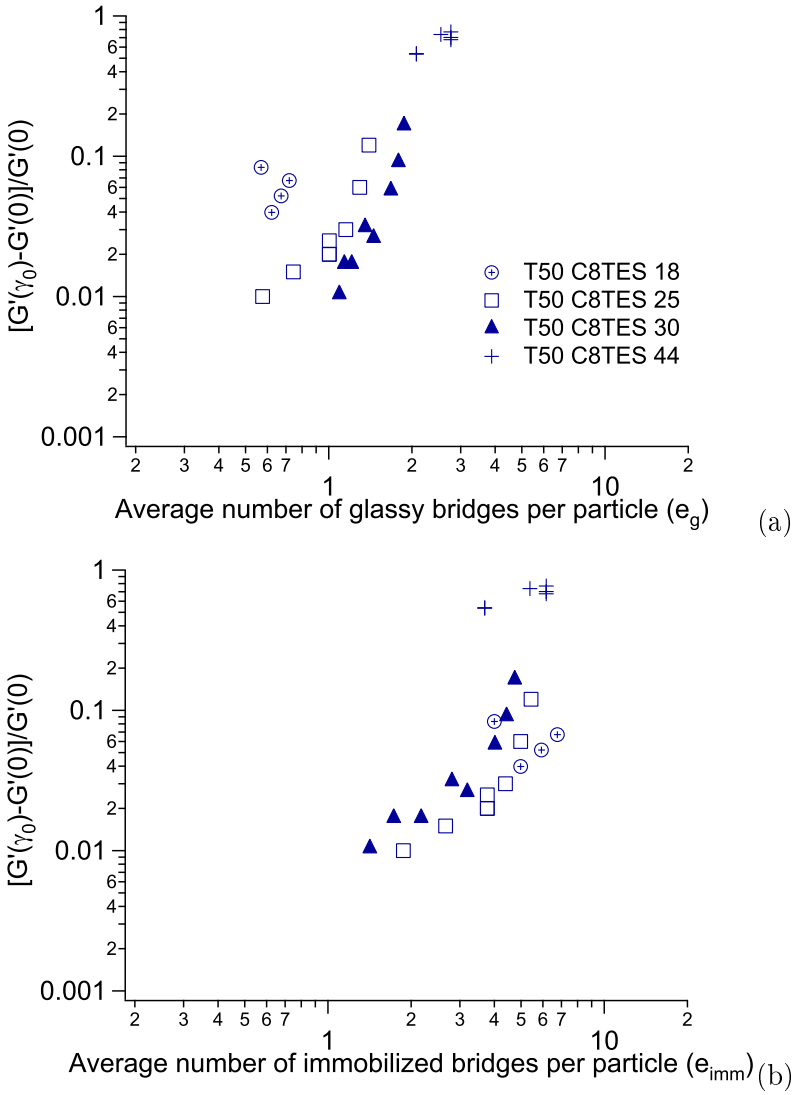

FIGURE 5.15 – Payne effect amplitude as a function of glassy bridges quantity - C8TES samples. The amplitude of Payne effect $\frac{G'(\gamma_0)-G'(0)}{G'(0)}$ at a strain amplitude γ_0 =15% is plotted as a function of the average number of glassy (a) or immobilized (b) bridges per particle. Similar results are obtained at higher strain amplitudes

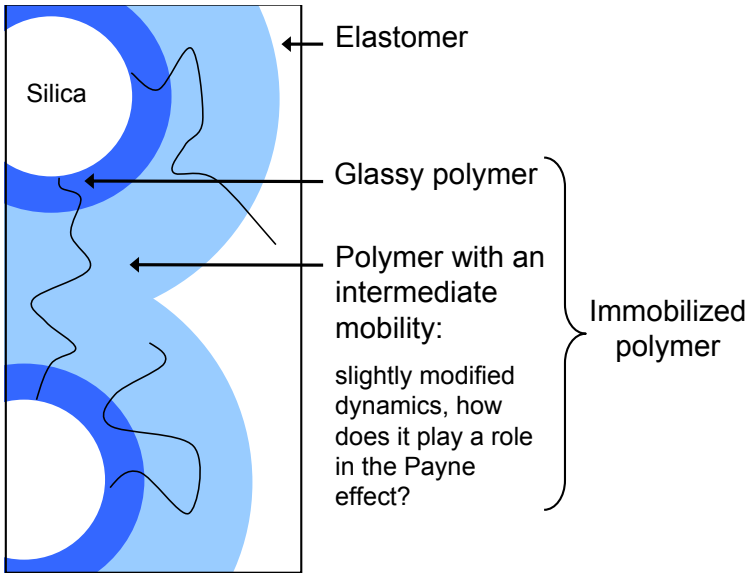

FIGURE 5.16 – Glassy and immobilized thicknesses

sample and we could thus deduce the thicknesses corresponding to the glassy and immobilized polymer volume fractions obtained in Chapter 2, as well as validate the hypothesis of isolated particles taken in Chapter 3. We showed that the thicknesses obtained with the T_g gradient model corresponds rather well to the glassy layer determined with the stretched exponentials analysis of the NMR signals. However, the gradient model could not account for the immobilized thicknesses from Chapter 2. This might be due to the shorter fitting range used in Chapter 3 but also to the shape of the gradient which might be too sharp to describe a slight polymer dynamics slowing-down at a longer scale. Having those two characteristic thicknesses, we wondered which one was relevant to describe the mechanical behavior of the filled samples. For that we plotted the amplitude of Payne effect as a function of the average number of glassy or immobilized bridges between particles. We observed that none of those curves gave a satisfactory master curve for different samples and temperatures but that we would need to use a thickness in-between the glassy and immobilized ones in order to get a good description. This means that the mechanical behavior is governed by longer-range interactions than only the glassy layer. Of course it opens the question on how to determine this relevant thickness and to investigate its physical state.

In this Chapter, we have compared the results obtained on the polymer dynamics in Chapters 2 and 3 and linked them to the mechanical behavior of the samples. The T_g gradient model used in Chapter 3 is coherent with the glassy layer obtained in Chapter 2, but it cannot describe the polymer with an intermediate mobility that might be situated at a larger distance from the solid particles. Another gradient shape might thus be useful to describe the whole polymer dynamics. This slightly slowed-down polymer is important since it seems to play a role in the mechanical behavior of the samples and it remains to investigate how it is involved.

Conclusion générale

Les élastomères renforcés sont des matériaux composites qui sont utilisés depuis plus d'un siècle dans l'industrie sans que leur comportement mécanique ne soit encore complètement compris. L'ajout de charges solides dans un élastomère modifie en effet de façon complexe le comportement des chaînes de polymères et ainsi transforme les propriétés mécaniques de façon non triviale. Lors de cette étude sur des systèmes modèles, nous avons mis en rapport la composition microscopique des échantillons - épaisseur de polymère immobilisé autour des charges et état de dispersion des particules - avec leur comportement mécanique macroscopique.

Tout d'abord, nous avons étudié ces élastomères renforcés modèles par RMN, afin de mieux comprendre deux aspects de la dynamique des chaînes de polymère : d'une part les mouvements diffusifs des chaînes sur de longues portées et qui sont dues aux contraintes topologiques du réseau (réticulation et enchevêtrements) et d'autre part les fluctuations plus rapides, à courte portée, qui sont associées à une dynamique vitreuse. Nous avons étudié les contraintes topologiques du réseau élastomère grâce à une séquence Double Quantum qui permet d'isoler la première contribution et ainsi d'accéder à la densité de réticulation effective. Nous avons alors mis en évidence l'existence d'une surréticulation effective dans le cas des échantillons avec greffon créant un lien covalent entre la silice et le polymère (greffon TPM - 3-(trimethoxysilyl)propyl methacrylate). Dans le cas d'interactions plus faibles (liaisons hydrogène, greffons C8TES - *n*-octyltriethoxysilane), aucune surreticulation n'est observée. Par ailleurs, la séquence de Magic Sandwich Echo nous a permis de déterminer, de façon plus quantitative que l'Echo de Hahn, la contribution provenant du polymère ayant une dynamique plus lente que celle de la matrice élastomère. Nous avons alors pu identifier au moins trois sortes de mobilité. Pour cela nous avons décrit le signal RMN avec la somme de trois fonctions : une gaussienne décrivant un comportement vitreux, une exponentielle décrivant un comportement élastomère et une exponentielle étirée décrivant un comportement intermédiaire entre les deux précédents. Nous avons ainsi pu quantifier le polymère immobilisé et montrer que l'ajout de solvant et l'augmentation de la température avaient le même effet : la diminution de la quantité de polymère rigide.

Les résultats concernant l'existence de polymère immobilisé sont compatibles avec l'existence d'un gradient de transition vitreuse autour des charges mais ne permettent pas de prouver directement son existence. C'est pour cela que nous avons ensuite utilisé une autre methode d'analyse des signaux RMN en utilisant, cette fois, le modèle de gradient de température de transition vitreuse T_g proposé par Long et Lequeux [31]. Ainsi, à partir d'une description analytique des signaux de la matrice pure (équation d'Andersen-Weiss) et du modèle de gradient de T_g, nous avons pu extraire les deux paramètres permettant de décrire les signaux RMN des élastomères

renforcés entre T_g + 40K et T_g + 120K. Ces deux paramètres sont, e_0 qui représente l'épaisseur vitreuse due aux greffons et qui est donc indépendante de la température, et δ la longueur caractéristique du gradient de T_g. Les valeurs obtenues pour e_0 sont de l'ordre de 2 nm pour les échantillons avec greffons TPM et 0.5 nm pour les C8TES, ce qui correspond bien aux valeurs estimées d'après les taux de greffage. La valeur de δ, quant à elle, est indépendante du type de greffon et se situe entre 0.10 nm et 0.26 nm selon les échantillons. Ces valeurs correspondent bien aux estimations faites lors des précédentes études sur ces systèmes et correspond par ailleurs à la taille caractéristique mise en jeu lors de la transition vitreuse [120]. Ce modèle de gradient permet également de décrire les signaux RMN dans le cas de l'ajout de solvant, en tenant simplement compte de la modification de la valeur de T_g dans l'élastomère pur. Par ailleurs, nous avons pu vérifier la validité du modèle sur des expériences de DSC. De la même manière que précédemment, nous avons pu prédire le comportement en DSC des élastomères renforcés (mesure de T_g et vieillissement physique) à partir du comportement de la matrice pure et du modèle de gradient. Ces différentes mesures ont donc permis de confirmer de façon directe l'existence d'un gradient de T_g autour des charges dans les élastomères renforcés.

En outre, nous avons étudié les propriétés mécaniques non linéaires des systèmes modèles en rhéologie. Afin de détecter d'éventuelles preuves de la présence de polymère vitreux dans les comportements mécaniques des échantillons, nous avons analysé directement les signaux de contrainte mesurés lors de déformations sinusoïdales. Nous avons alors pu mesurer non seulement le classique effet Payne - diminution du module élastique lorsque l'amplitude de déformation dépasse quelques pour-cents - mais aussi une non-harmonicité qui est généralement négligée dans les études. En se basant sur une méthode d'analyse proposée par Cho[85] pour décomposer le signal de contrainte totale en une partie élastique et une partie visqueuse, nous avons identifié deux effets : un raidissement au cours du cycle dans la partie élastique, et une rhéofluidification dans la partie visqueuse. Ces contributions non linéaires ont été quantifiées et leur évolution a pu ainsi être suivie en fonction de l'amplitude de déformation et de la température. Nous avons ensuite montré que ces caractéristiques pouvaient être expliquées par la présence de ponts vitreux dans les échantillons grâce à la comparaison de nos résultats expérimentaux avec des simulations issues du modèle de renforcement par ponts vitreux de S. Merabia, P. Sotta et D. Long. En effet, le même comportement non linéaire est attendu dans ce modèle où les particules sont reliées entre elles par des ponts vitreux pouvant se plastifier. Le raidissement et le rhéofluidification observés lors de chaque cycle de sollicitation peuvent donc s'expliquer par la cinétique de destruction - reformation des pont vitreux sous l'effet de la déformation imposée.

Enfin, un autre paramètre important dans l'étude des systèmes modèles est la connaissance de leur état de dispersion afin de pouvoir finalement relier la composition microscopique des échantillons à leur comportement mécanique. Dans ce but, nous avons utilisé les données de diffusion de neutrons aux petits angles pour effectuer des simulations Monte-Carlo inverses. Des particules sont placées dans une boite et la position d'une bille est modifiée à chaque pas de la simulation. Le pas est accepté si le facteur de structure calculé pour la boite se rapproche du facteur de structure mesuré expérimentalement, sinon il est refusé. Le système converge alors vers une configuration pouvant représenter l'arrangement des particules de silice dans chaque système

et nous obtenons ainsi la distribution des distances dans chaque échantillon. Connaissant l'arrangement des particules, nous pouvons ensuite revenir sur les précédents résultats concernant la dynamique du polymère afin de les comparer plus précisemment. A partir des descriptions avec la somme de trois exponentielles étirées des signaux de RMN, nous avions obtenu les fractions volumiques de polymère immobilisé que nous pouvons maintenant traduire en termes d'épaisseur et les comparer aux épaisseurs obtenues à partir du modèle de gradient de T_g. Nous observons alors que le modèle de gradient de T_g décrit bien l'épaisseur vitreuse mesurée par l'analyse avec les exponentielles étirées mais ne peut rendre compte des épaisseurs immobilisées, c'est-à-dire du polymère ayant une mobilité intermédiaire. Cela peut provenir du fait que le modèle choisi décrit un changement trop brusque de T_g par rapport à la réalité et ne permet pas de rendre compte d'une légère modification de mobilité à plus longue portée. Nous avons finalement deux épaisseurs caractéristiques, vitreuse et immobilisée, et nous pouvons donc nous demander laquelle est la plus pertinente pour décrire le comportement mécanique des échantillons et en particulier leur effet Payne. Nous avons pour cela voulu tracer l'amplitude de l'effet Payne à une déformation donnée en fonction du nombre moyen de ponts vitreux ou immobilisés par particule, c'est-à-dire le nombre moyen de particules reliées à une particule donnée uniquement par du polymère vitreux ou bien immobilisé. Nous avons alors constaté qu'aucune de ces deux épaisseurs ne permettaient d'obtenir une courbe maitresse pour plusieurs échantilons et températures et que l'épaisseur pertinente pour décrire l'effet Payne devait se situer entre ces deux valeurs. Cela montre que le polymère vitreux seul ne permet pas d'expliquer le comportement mécanique des élastomères renforcés, et qu'il est nécessaire de considérer le rôle que peut jouer au moins une partie du polymère faiblement ralenti.

Cette thèse ouvre de plus des perspectives de travail dans plusieurs directions :

- l'amélioration du modèle de gradient de T_g afin de mieux décrire un ralentissement faible des chaînes de polymère à plus longue portée,
- l'utilisation de la connaissance de l'arrangement des particules dans chaque échantillon, pour utiliser directement le modèle de renforcement par ponts vitreux avec les bons paramètres physiques et ainsi essayer d'obtenir une description quantitative du comportement des échantillons,
- la modification de la nature du greffon pour étudier le comportement d'échantillons dans le cas de liens plus faibles entre la silice et le polymère.

General conclusion

Filled elastomers are nanocomposites that have been used for more than a century in industry without their mechanical behavior being fully understood. The addition of solid particles in an elastomer matrix modifies the behavior of the polymer chains in a complex way and thus transforms the mechanical properties in a non-trivial manner. In this study on model systems, we have related the microscopic composition of the samples, e.g. thickness of immobilized polymer surrounding the fillers and dispersion state of the particles, with their macroscopic mechanical behavior.

First, we studied these model filled rubbers by NMR, in order to obtain a better understanding of two aspects of the polymer chains dynamics : the slow, long-range, diffusive motion of the chains, which are controlled by the topological constraints in the network (crosslinks and entanglements), and the faster short-range fluctuations, which are associated with glassy dynamics. We studied the topological constraints in the network with a Double Quantum sequence that isolates the first aspect and thus gives us access to the effective crosslink density. We then demonstrate that, in the case of samples with grafters creating a covalent bond between the silica and the polymer chains (3-(trimethoxysilyl)propyl methacrylate (TPM) grafters), the effective crosslink density is inhomogeneous and much higher than expected. However, this observation was not made in the case of weaker interactions (hydrogen bonds, *n*-octyltriethoxysilane (C8TES) grafters). Regarding the second aspect, the Magic Sandwich Echo sequence allowed to determine, more quantitatively than with the Hahn echo, the contribution coming from the polymer having a slower dynamic than that of the elastomer matrix. We were then able to identify at least three kinds of mobility. This required fitting the NMR signal with the sum of three functions : a Gaussian describing a glassy behavior, an exponential describing an elastomer behavior and a stretched exponential describing an intermediate behavior between the previous two. We were then able to quantify the immobilized polymer fraction and showed that the addition of solvent or an increase in the temperature had the same effect : it leads to a reduction in the amount of rigid polymer.

The results regarding the existence of immobilized polymer are compatible with the existence of a glass transition temperature gradient around the fillers but do not directly prove its existence. To address this issue, we have used another analysis method of the NMR signals : we employ the model of glass transition temperature (T_g) gradient proposed by Long and Lequeux [31]. From an analytical description of the pure matrix NMR signals (Anderson-Weiss equation) and from the T_g gradient model, we were able to extract the two parameters allowing the descrip-

tion of the NMR signals of the reinforced elastomers at temperatures between T_g + 40K and T_g + 120K. These two parameters are, e_0, which represents the glassy thickness due to the grafter and is therefore independent of the temperature, and δ, the characteristic T_g gradient length. The values obtained for e_0 are of the order of 2 nm for the samples with TPM grafters and 0.5 nm for C8TES grafters, which corresponds rather well to the values estimated from the grafting density. The value of δ appears to be independent of the grafter's type and lies between 0.10 nm and 0.26 nm depending on the sample. These values also correspond well to estimates made in previous studies on the same systems and is similar to the characteristic length into play in the glass transition [120]. The T_g gradient model also allows the description of the NMR signals of the filled rubbers in the case of the addition of solvent, taking into account only the change in the T_g value in the pure elastomer. In addition, we were able to check the validity of the model on DSC experiments. In the same way as before, we could predict the behavior of reinforced elastomers in DSC (T_g measurement and physical aging) from the behavior of the pure matrix and the gradient model. These various measurements have directly confirmed the existence of a T_g gradient around the solid particles in filled elastomers.

Furthermore, we studied the nonlinear mechanical properties of our model systems using rheometry. In order to detect the presence of glassy polymer in the mechanical behavior of the samples, we analyzed the stress signals directly measured in oscillatory shear. We were able to measure not only the classic Payne effect - a decrease in the elastic modulus when the strain amplitude exceeds a few percent - but also a non-harmonic behavior that is generally neglected in the studies. Based on the analysis method proposed by Cho[85] to decompose the total stress signal in an elastic and a viscous part, we have identified two effects in each cycle of solicitation : a strain-hardening in the elastic part and shear-thinning in the viscous part. These nonlinear contributions have been quantified and their evolution could thus be monitored as a function of strain amplitude and temperature. We then showed that these characteristics could be explained by the presence of glassy bridges in the samples by comparing our experimental results with simulations from the glassy bridges reinforcement model of S. Merabia, P. Sotta and D. Long. Indeed, the same nonlinear behavior is expected in this model where the particles are connected by glassy bridges that can be plasticized. The strain hardening and shear thinning observed in every cycle of solicitation can then be explained by the kinetics of destruction - rebirth of the glassy bridges as a result of the imposed strain.

Finally, another important parameter in the study of model systems is the knowledge of their dispersion state in order to finally relate the microscopic composition of the samples to their mechanical behavior. For this purpose, we used data from small angle neutron scattering to perform reverse Monte Carlo simulations. Particles are placed in a box and the position of a random filler is changed at every step of the simulation. The step is accepted if the structure factor calculated for the box is closer to the experimentally measured structure factor, otherwise, it is denied. The system then converges to a configuration that can represent the arrangement of silica particles in each system and we obtain the distribution of distances in each sample. Knowing the arrangement of the particles, we can then return to the previous results on the dynamics of the polymer in order to compare them more precisely. From the descriptions with

the sum of three stretched exponentials of the NMR signals, we obtained the volume fraction of immobilized polymer that we can now translate in terms of thicknesses and compare them with thicknesses obtained from the T_g gradient model. We observe that the T_g gradient model describes the glassy thickness measured with the stretched exponentials analysis, but that it cannot account for the total immobilized thickness measured with this method. This might be because the model we chose describes a change of T_g that is too sharp compared to reality and does not account for a slight change in mobility at longer range. In the end we have two characteristic thicknesses, glassy and immobilized. To determine which one is the most relevant to describe the mechanical behavior of the samples, and in particular their Payne effect, we plotted the Payne effect amplitude at a given strain as a function of the average number of glassy or immobilized bridges between particles, that is, the average number of particles connected to a given particle with only glassy or immobilized polymer. Neither of these two thicknesses obtained a master curve for various samples and temperatures. The relevant thickness to describe the Payne effect is most likely between these two values. It means that the glassy polymer alone cannot explain the mechanical behavior of the samples and that at least part of the slightly slowded-down polymer has to be considered.

This PhD work also opens up several work directions :

- the improvement of the T_g gradient model in order to better describe the slight dynamics slowdown of the polymer chains at longer range
- the use of the knowledge of the particles arrangement in each sample in order to directly use the glassy bridges reinforcement model with the right physical parameters and thus try to get a quantitative description of the behavior of samples
- the change of the grafter's nature to study the behavior of the samples in the case of weaker links between silica and polymer.

Résumé

Les élastomères renforcés sont utilisés couramment dans l'industrie des pneumatiques depuis plus d'un siècle. Cependant la compréhension de leur propriétés mécaniques n'est toujours pas complète. En effet, l'ajout de charges solides dans une matrice élastomère modifie de façon complexe le comportement des chaînes de polymère. C'est un sujet important dans le contexte industriel actuel car une meilleure compréhension de ces systèmes pourrait permettre une diminution de la consommation d'énergie des véhicules.

Pour faciliter l'étude de ces systèmes, il est important de bien contrôler leur composition. Or dans les systèmes industriels obtenus par malaxage de l'élastomère avec les charges solides, de nombreux agrégats sont présents ce qui rend les échantillons difficiles à caractériser. C'est pour cela que J. Berriot et T. Chaussée ont mis au point des systèmes modèles où l'état de dispersion des charges est bien contrôlé. La fabrication de ces systèmes se fait en trois étapes : d'abord la synthèse de particules de silice sphériques et monodisperses par la méthode Stöber, ensuite leur greffage par des agents de couplage (ici TPM - 3-(trimethoxysilyl)propyl methacrylate) - permettant un lien covalent entre la silice et le polymère) ou de recouvrement (ici C8TES - *n*-octyltriethoxysilane - le polymère interagissant alors directement avec les groupes ethoxys résiduels de la silice), et enfin leur dispersion dans une solution de monomère qui est ensuite polymérisée et réticulée (ici du poly(acrylate d'éthyle) - PEA).

Cette thèse poursuit l'étude de ces systèmes suivant trois directions principales : d'abord l'étude de la dynamique des chaînes de polymère par RMN, ensuite l'analyse de leur comportement en mécanique non linéaire en rhéologie et enfin la détermination de l'arrangement des particules, afin de pouvoir relier la composition microscopique des échantillons à leur comportement macroscopique mécanique. En particulier, nous nous attachons à la démonstration de l'existence d'un gradient de T_g autour des charges solides et à l'importance de l'existence d'une couche de polymère vitreux autour des particules dans le comportement mécanique des échantillons.

Etude de la dynamique du polymère par RMN

Nous avons tout d'abord étudié la dynamique des chaînes de polymère par RMN, en collaboration avec K. Saalwächter à l'université de Halle-Wittenberg (Allemagne). Le premier aspect étudié concerne les fluctuations à longue portée des chaînes, qui sont régies par les contraintes topologiques du réseau (enchevêtrements et points de réticulation). Pour cela, nous avons utilisé une séquence appelée Double Quantum (DQ) qui permet d'isoler cette contribution de la relaxation des chaînes. Par ailleurs, les fluctuations à plus courte portée des chaînes sont étudiées

par une séquence de Magic Sandwich Echo (MSE) qui permet une meilleure description de la relaxation des chaînes que l'echo de Hahn.

Etude du réseau : surréticulation effective dans le cas des greffons TPM

Les échantillons d'élastomères renforcés étudiés contiennent tous un taux de réticulant de 0.3% molaire par rapport au monomère. Afin de connaitre l'homogénéité et la densité effective de réticulation dans ces échantillons, nous comparons leurs courbes obtenues en DQ avec celle obtenue pour une matrice pure contenant le même taux de réticulant. Dans le cas des échantillons avec greffons C8TES, on observe une réticulation homogène et légèrement supérieure à celle de la matrice pure. En revanche, dans le cas des greffons TPM, on observe une réticulation très inhomogène et bien supérieure à celle de la matrice pure. Nous pouvons décrire ces courbes avec la somme de deux composantes : une ayant une réticulation légèrement supérieure à la matrice, l'autre étant très largement surréticulée par rapport à la matrice. Nous avons montré que la fraction de polymère très surréticulé est corrélée à la surface développée en silice dans chaque échantillon. La présence de particules de silices liées de façon covalente au réseau de polymère augmente donc la quantité effective de contraintes topologiques ressenties par les chaînes de polymère.

Etude de la dynamique locale des chaînes : existence de polymère rigide et interprétation par un gradient de T_g autour des charges

D'autre part, la séquence MSE nous permet de suivre la relaxation des chaînes de polymère en fonction du temps à différentes températures. Les courbes obtenues pour la matrice pure peuvent être décrites par une expression analytique (équation de Andersen-Weiss) qui peut se simplifier en une exponentielle au-dessus de T_g (comportement élastomérique) et en une gaussienne au-dessous de T_g (comportement vitreux). Nous étudions ensuite les élastomères renforcés entre T_g + 40K et T_g + 120K. Nous constatons alors que le signal correspondant ne peut être simplement décrit par une exponentielle, mais qu'il est nécessaire d'utiliser au moins trois composantes. Nous le décrivons ainsi avec la somme de trois fonctions : une exponentielle (écrivant un comportement élastomérique), une gaussienne (décrivant un comportement vitreux) et une exponentielle étirée (décrivant un comportement intermédiaire). Un exemple de décomposition est décrit en Figure 5.17

Cette méthode d'analyse permet de quantifier le polymère immobilisé (vitreux ou intermédiaire) pour différents échantillons et de suivre son évolution en fonction de la température ou de l'ajout de solvant. Nous avons ainsi constaté que la quantité de polymère immobilisé est corrélée à la surface développée en silice dans chaque échantillon. Cela montre bien que cette fraction de polymère est due à la présence de surfaces solides dans l'échantillon. Par ailleurs, nous avons montré que la fraction de polymère immobilisé dépend de la variable $T - T_g$. En effet, cette fraction diminue de façon similaire lorsque l'on augmente la température ou que l'on fait diminuer la température de transition vitreuse de la matrice élastomère en ajoutant du solvant.

Ces constatations sont compatibles avec l'existence d'un gradient de température de transition vitreuse T_g à proximité des particules solides mais ne le prouve pas directement. C'est pourquoi

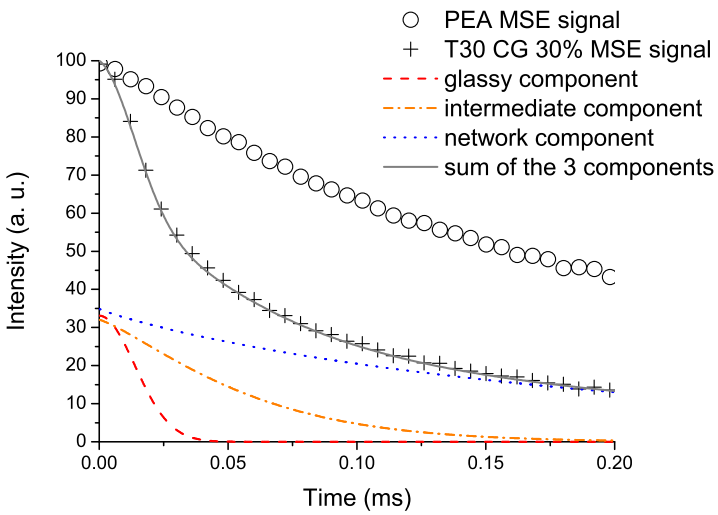

FIGURE 5.17 – Signal MSE à T_g + 40K pour l'échantillon T30 CG 30% (croix - diamètre de la silice 27 nm, greffon TPM, 20% vol. de silice) et la matrice pure PEA (cercles). Le signal de l'élastomère renforcé peut être décomposé en trois contributions : une vitreuse, une élastomère et une intermédiaire (lignes pointillées).

nous nous sommes ensuite attachés à décrire directement les signaux RMN avec un modèle de gradient de T_g. Pour cela, nous sommes partis du modèle de Long-Lequeux [31] qui décrit l'évolution de T_g avec la distance à une surface solide z :

$$T_g(z) = T_g^{\infty}\left(1 + \frac{\delta}{z}\right) \tag{5.5}$$

T_g^{∞} est la température de transition vitreuse à une distance infinie (*ie* en masse) et δ est la taille caractéristique du gradient. De plus, nous supposons que les greffons sont très fortement immobilisés (dans un état vitreux) et sont donc insensible à la température. Nous faisons donc commencer le gradient de T_g non pas à la surface de la silice mais à une distance e_0 qui représente l'épaisseur due aux greffons. Nous avons vu par ailleurs que nous pouvions décrire le signal de la matrice à toutes les températures par une expression analytique (Andersen-Weiss). Nous pouvons ainsi décrire le signal des élastomère renforcés à partir du comportement de la matrice pure et du modèle de gradient de T_g avec simplement deux paramètres : e_0 et δ. En Figure 5.18, nous voyons la forme de gradient de T_g choisie (avec un maximum à T_g^{max} pour éviter une divergence) ainsi que la description des signaux par ce modèle. On voit bien l'obtention d'un couple de paramètres optimal pour la description des signaux à toutes les températures. Les valeurs de e_0 obtenues sont de l'ordre de 2 nm pour les greffons TPM et 0.5 nm pour les C8TES, ce qui correspond bien à ce qui peut être estimé à partir des densités de greffage. Les valeurs de δ sont elles situées autour de 0.18 nm, ce qui correspond bien aux précédentes estimations faites sur ces systèmes.

Cette méthode a également été utilisée avec succés pour décrire les signaux RMN des échantillons dans le cas de l'ajout de solvant. Nous avons en effet pu décrire les signaux RMN avec les mêmes paramètres e_0 et δ que précédemment, en ne modifiant que la valeur de T_g^{∞}. Nous avons alors obtenus des valeurs de T_g^{∞} très similaires à celles mesurées en DSC pour la matrice seule en présence de solvant. Le même profil de gradient permet également de prévoir la variation de

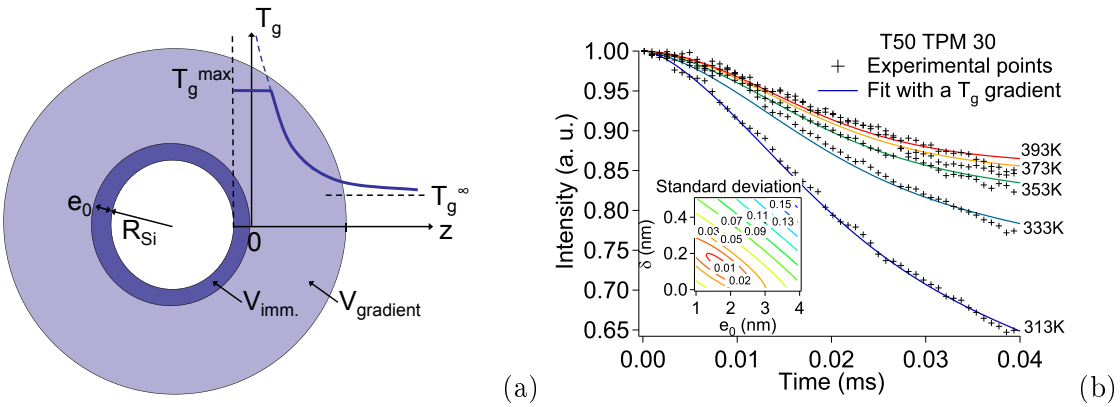

FIGURE 5.18 – (a) Représentation schématique du modèle de gradient de T_g utilisé, avec une coupure à T_g^{max}. V_{imm} représente le volume occupé par les greffons, correspondant à une épaisseur e_0. (b) Signaux RMN pour un échantillon renforcé entre T_g + 40K et T_g + 120K (croix) et description par un modèle de gradient de T_g (lignes). En insert, l'évolution de l'écart-type entre le signal expérimental et le fit en fonction des deux paramètres e_0 et δ. On observe bien un minimum pour un couple de paramètre donné.

flux de chaleur lors de la transition vitreuse et lors du vieillissement physique des élastomères renforcés, à partir du flux mesuré pour la matrice pure. Cela permet de confirmer la robustesse du modèle utilisé.

Nous nous sommes ensuite intéressés au comportement mécanique des échantillons afin d'y détecter un signe éventuel de la présence de polymère vitreux.

Mécanique non linéaire : effet Payne mais pas seulement

L'étude du comportement mécanique des systèmes a été faite en cisaillement sinusoidal, et nous nous sommes particulièrement intéressés au comportement aux grandes déformations. Le comportement attendu pour les élastomères renforcés est une diminution significative du module élastique avec l'amplitude de déformation (effet Payne), tout en gardant des signaux de contrainte sinusoidaux.

Analyse des signaux de contrainte

Afin d'étudier précisément le comportement des échantillons, nous avons analysé directement les signaux de contrainte obtenus lors de sollicitations sinusoïdales. Nous avons d'abord décomposé le signal en une partie élastique et une partie visqueuse en suivant la méthode proposée par Cho [85]. Cela revient en fait à faire une décomposition en partie impaire (en phase avec la déformation sinusoidale donc partie élastique, notée σ') et partie paire (en quadrature avec la déformation donc partie visqueuse, notée σ''). En traçant, à l'intérieur d'un cycle, la partie élastique de la contrainte en fonction de la déformation, on obtient, en régime linéaire, une droite de pente le module élastique G'. De même, en traçant la contrainte visqueuse en fonction du taux de cisaillement divisé par la pulsation on obtient une droite de pente G''. Dans le cas de nos élastomères renforcés modèles, on voit en Figure 5.19 que ce n'est plus le cas à haute déformation.

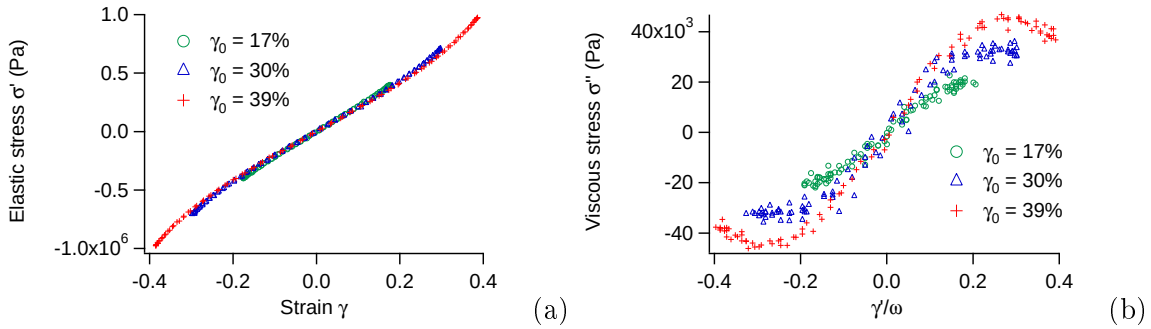

FIGURE 5.19 – Contrainte élastique σ' (a) et visqueuse σ'' (b) en fonction de la déformation γ et de $\dot{\gamma}/\omega$ respectivement à l'intérieur d'un cycle de sollicitation à des amplitudes de déformation $\gamma_0 = 17$, 30 et 39%. Echantillon T50-CG-30%.

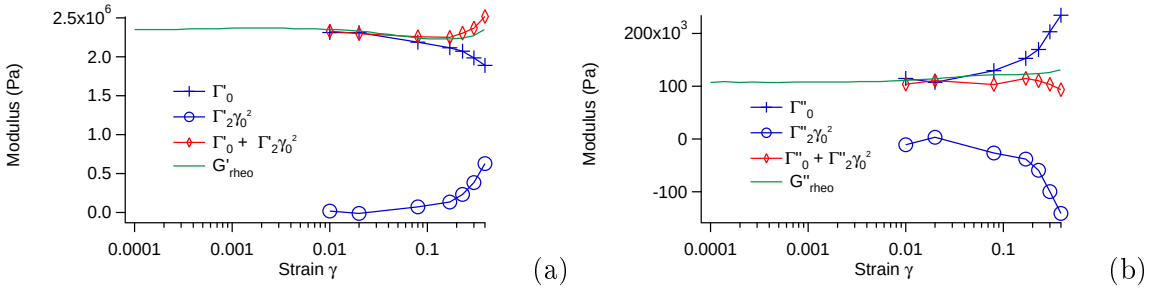

FIGURE 5.20 – Evolution des termes linéaire et non linéaire des modules élastique (a) et visqueux (b) avec l'amplitude de déformation γ_0. Comparaison avec les valeurs données par le rhéomètre. Echantillon T50-TPM-30%.

Il y a apparition de non linéarités à l'intérieur de chaque cycles de sollicitation.

Mise en évidence d'un raidissement et d'une rhéofluidification

En observant les non linéarités à l'intérieur d'un cycle de sollicitation (*ie* à une amplitude de déformation donnée), on constate que la contrainte élastique augmente fortement avec la déformation instantanée γ, ce qui correspond à un raidissement, tandis que la contrainte vitreuse diminue avec le taux de cisaillement, ce qui correspond à une rhéo-fluidification. Le signal de contrainte n'étant plus sinusoidal, les modules mesurés par le rhéomètre n'ont plus de sens physique et nous devons introduire des modules généralisés définis par $\sigma' = \Gamma'\gamma$ et $\sigma'' = \Gamma''\dot{\gamma}/\omega$. Afin de quantifier ces phénomènes non linéaires, nous décrivons les courbes précédentes avec des équations du type :

$$\Gamma' = \Gamma'_0 + \Gamma'_2\gamma^2 \quad (5.6)$$

$$\Gamma'' = \Gamma''_0 + \Gamma''_2(\dot{\gamma}/\omega)^2 \quad (5.7)$$

Cela nous permet d'identifier un terme linéaire et un terme non linéaire dans chaque partie et de suivre leur évolution avec l'amplitude de la déformation imposée (Figure 5.20).

Les termes linéaires Γ'_0 et Γ''_0 correspondent aux pentes à l'origine dans les figures 5.19 (a) et (c) respectivement. On observe une diminution de Γ'_0 avec l'amplitude de déformation, ce qui

correspond bien à l'effet Payne et une augmentation de Γ_0'', ce qui décrit une dissipation d'énergie. Le terme non linéaire Γ_2' est positif puisqu'il décrit un changement pente croissant, tandis que Γ_2'' est négatif puisqu'il correspond à un changement de pente décroissant. On observe, comme l'on pouvait s'y attendre, que ces termes non linéaires augmentent en valeur absolue avec l'amplitude de déformation. Le rhéomètre donne, quant à lui, une valeur qui correspond environ à la somme des termes linéaire et non-linéaire.

Pour mieux comprendre à quoi peuvent être dues ces non linéarités, nous allons comparer ces résultats expérimentaux à des simulations obtenues par le modèle de renforcement par ponts vitreux de S. Merabia, P. Sotta et D. Long.

Lien avec le modèle de renforcement par ponts vitreux

L'effet Payne peut être expliqué par la plastification d'une fraction de plus en plus importante de ponts vitreux lorsque les sollicitations sont de plus grande amplitude. Le modèle de renforcement par ponts vitreux décrit bien cet effet en représentant ces ponts par des ressorts qui peuvent être détruits et recontruits au cours des sollicitations. Ce modèle reproduit également qualitativement les caractéristiques non linéaires que nous avons observées expérimentalement : raidissement et rhéofluidification à l'intérieur de chaque cycle de sollicitation. Cela montre que ce sont des traits qui peuvent s'expliquer par la cinétique de destruction-reconstruction des ponts vitreux. En effet, lorsqu'on se place au maximum de déformation instantanée, on est au minimum du taux de cisaillement, ce qui laisse plus de temps aux ponts pour se reformer et pourrait ainsi expliquer le raidissement observé.

Arrangement des particules et épaisseurs vitreuses : quel lien avec l'effet Payne ?

Nous avons vu que l'étude RMN des échantillons permettait de mettre en évidence la présence de polymère vitreux et que par ailleurs le comportement mécanique de ces sytèmes présentait des traits pouvant qualitativement s'expliquer par l'existence de ponts vitreux entre les particules. Afin d'essayer d'obtenir un lien plus quantitatif entre la présence de ponts vitreux et le comportement non linéaire des échantillons, nous avons besoin de déterminer précisément l'arrangement des particules. Connaissant ensuite les fractions de polymère immobilisé, nous pourrons en déduire la présence ou non de ponts vitreux et la relier à l'effet Payne mesuré sur les échantillons.

Arrangement des particules : simulations Monte-Carlo inverses

Pour déterminer l'arrangement des particules dans chaque échantillons, nous avons interprété les mesures de diffusion de neutrons aux petits angles (SANS) grâce à des simulations Monte-carlo inverses. Lors de ces simulations, nous considérons une boite dans laquelle nous plaçons des particules solides (leur taille et leur fraction volumiques étant connues pour chaque échantillon). A chaque pas de la simulation, une particule au hasard est déplacée d'un pas et le facteur de structure correspondant à cette nouvelle configuration est calculé. S'il se rapproche du facteur expérimental mesuré en SANS, le pas est accepté, sinon il est refusé et la particule est replacée

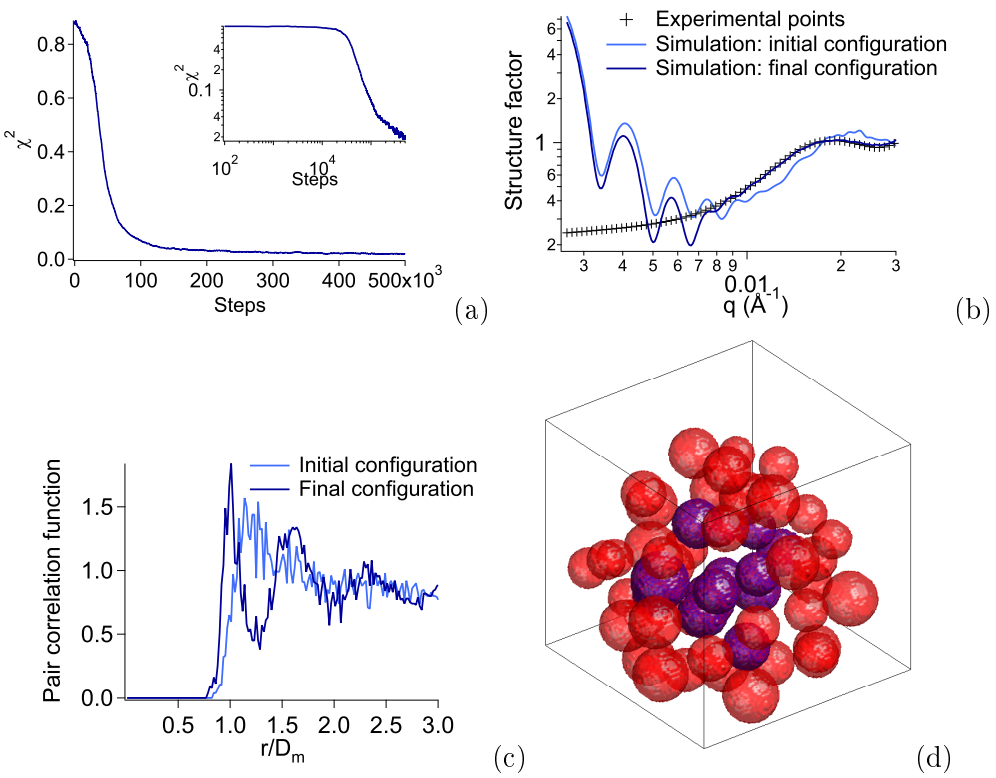

FIGURE 5.21 – (a), (b) et (c) : résultats d'une simulation Monte-Carlo inverse pour l'échantillon MIST TPM 25% (diamètre de la silice 27 nm, fraction volumique 16%) avec 1 000 particules, 500 000 pas et une configuration initiale aléatoire. (a) présente l'évolution de l'écart type entre la facteur de structure expérimental et simulé au cours de la simulation. En (b), comparaison du facteur de structure expérimental (croix) avec celui obtenu dans la simulation, dans la configuration initiale (ligne bleu clair) et finale (bleu foncé). Les oscillations à bas q sont dues à la taille finie de la boite. En (c), comparaison des fonctions de corrélation de paire dans les configurations initiale (bleu clair) et finale (bleu foncé) en fonction de r/D_m où D_m est le diamètre moyen des particules. Des pics apparaissent, montrant l'établissement d'un certain ordre dans l'arrangement des particules. (d) est une représentation 3D de l'arrangement des particules obtenus pour l'échantillon T50 TPM 30%. Une particule est choisie et ses premiers voisins sont représentés en bleu et les seconds en rouge.

dans sa position initiale. Le système évolue alors vers une configuration pouvant représenter l'état de dispersion des charges dans l'échantillon. Un exemple de simulation est présenté en Figure 5.21.

Calcul des épaisseurs vitreuses et lien avec l'effet Payne

Une fois l'arrangement des particules connu pour chaque échantillon, nous pouvons revenir sur les résultats de dynamique du polymère. En particulier, nous pouvons maintenant traduire les fractions volumiques de polymère immobilisé, obtenues par l'analyse des signaux de RMN par la somme de trois fonctions, en épaisseurs, en tenant compte de leur éventuel recouvrement. Nous en déduisons donc une épaisseur vitreuse e_g et une épaisseur immobilisée e_{imm} correspondant au polymère vitreux et avec une mobilité intermédiaire. Par ailleurs, à partir du modèle de gradient, nous pouvons calculer une épaisseur $e_{G'/G'_0=2}$ qui correspond à la distance à laquelle le module du

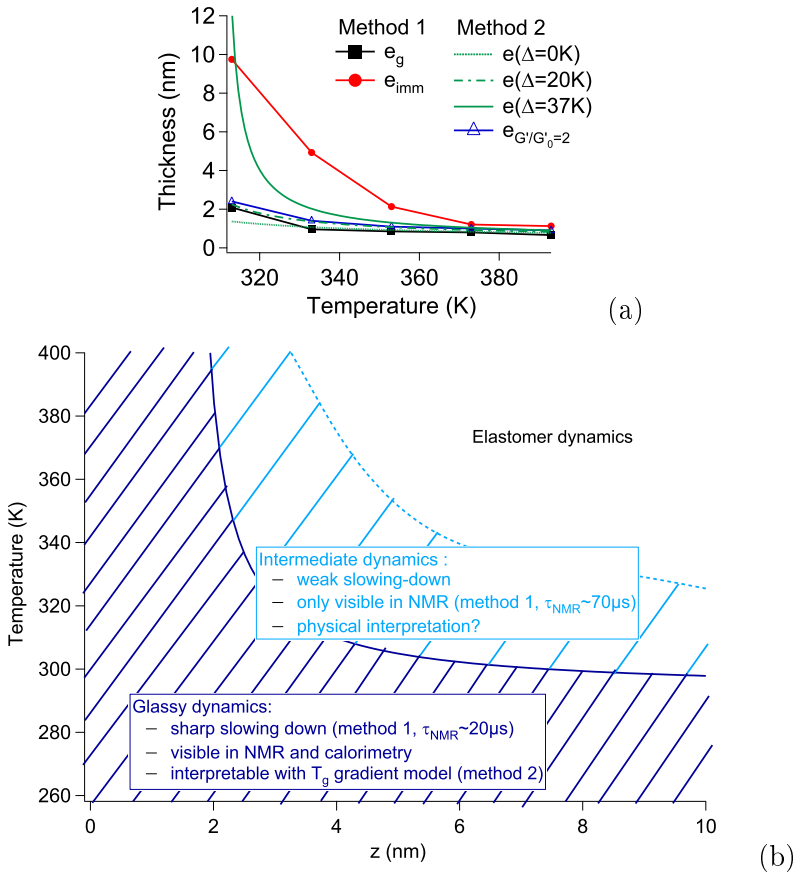

FIGURE 5.22 – (a) Comparaison des différentes épaisseurs obtenues lors de l'étude de la dynamique du polymère : e_g et e_{imm} à partir de l'analyse des signaux avec la somme de trois fonctions, $e_{G'/G'_0=2}$ et $e(\Delta)$ obtenues à partir du modèle de gradient de T_g. $e(\Delta)$ est l'épaisseur correspondant à $T = T_g(e) + \Delta$ avec Δ=0, 20 ou 37K. On constate qu'$e_{G'/G'_0=2}$ et $e(\Delta)$ sont très proches de e_g. Par contre e_{imm} n'est jamais décrit par le modèle de gardient. (b) Représentation schématique des différentes zones de mobilité rencontrées dans cette étude. La zone vitreuse (correspondant à du polymère en-dessous de $T_g(z)$+20K) est observée en RMN, ainsi qu'en DSC, et peut être interprétée par l'existence d'un gradient de transition vitreuse. En revanche la zone intermédiaire, qui correspond à un changement beaucoup plus faible de dynamique, n'est observé qu'en RMN avec la première méthode d'analyse.

polymère est égal à deux fois celui de la matrice élastomère. Par ailleurs, cette épaisseur peut se traduire en termes d'écart à T_g. On voit en Figure 5.22 que $e_{G'/G'_0=2}$ correspond au polymère qui est en dessous de sa T_g plus 20K, ce qui correspond également à l'épasseur vitreuse mesurée avec la première méthode. En revanche, l'épaisseur immobilisée ne peut être décrite avec le modèle de gradient de T_g. Cela montre que le modèle choisi permet de bien décrire la variation abrupte de T_g proche de la particule mais ne permet pas de rendre compte d'une modification plus fine de la dynamique du polymère à plus longue échelle.

Nous avons donc finalement deux épaisseurs caratéristiques : une correspondant à une très forte modification de la dynamique à courte portée e_g et une décrivant une modification plus légère mais à plus longue portée e_{imm}. On peut se demander laquelle serait la plus pertinente pour décrire le comportement mécanique des échantillons. Pour cela, nous avons tracé l'amplitude de l'effet Payne à une déformation donnée en fonction du nombre moyen de ponts vitreux

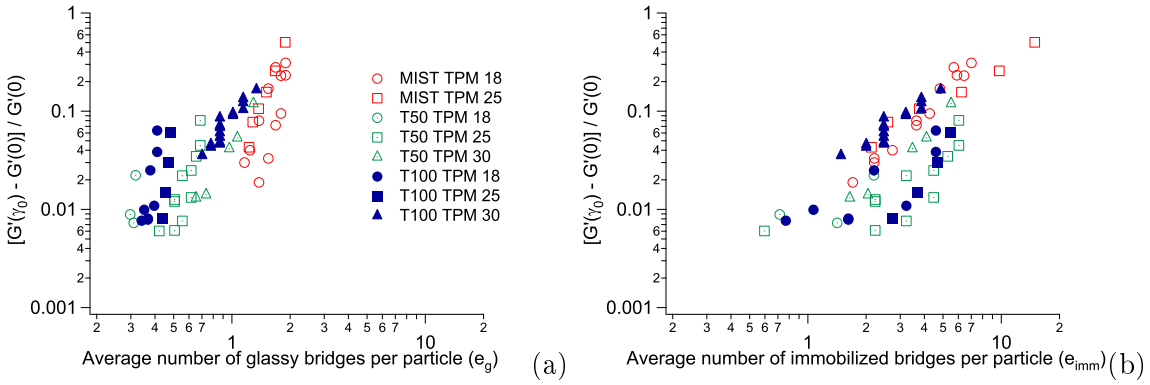

FIGURE 5.23 – Amplitude de l'effet Payne $\frac{G'(\gamma_0)-G'(0)}{G'(0)}$ à une déformation γ_0 =15% en fonction du nombre moyen de ponts vitreux (a) ou immobilisés (b) pour les échantillons TPM.

ou immobilisés par particule. Nous voyons en Figure 5.23 que nous n'obtenons pas de courbes maîtresse pour différents échantillons et différentes températures. Cela peut signifier que l'épaisseur permettant la description du comportement mécanique des échantillons se situe entre e_g et e_{imm}. Ainsi, pour expliquer le comporteemnt mécanique des élastomères renforcés, il serait nécessaire de considérer non seulement le polymère vitreux à l'interface avec les charges mais aussi une partie du polymère faiblement ralenti sur une plus longue portée.

Annexe

Cette annexe présente un article publié en 2010 et qui traite de l'influence de l'état de dispersion des particules solides sur le comportement mécanique des échantillons renforcés modèles.

This annex presents an article published in 2010 on the influence of the fillers dispersion state on the mechanical properties of model filled elastomers.

H Montes, T Chaussée, A Papon, F Lequeux, and L Guy. Particles in model filled rubber : dispersion and mechanical properties. EPJE 31(3), 263-268,2010.

Particles in model filled rubber: dispersion and mechanical properties

Hélène Montes, Thomas Chaussée,* Aurélie Papon, and François Lequeux
PPMD-SIMM, Soft Matter Science and Engineering,
UMR 7615 CNRS/UPMC/ESPCI ParisTech, 10 rue Vauquelin, F-75231 Paris Cedex 5, France

Laurent Guy
Rhodia Opérations, 15 rue Pierre Pays, BP 52, F-69660 Collonges-au-Mont-d'Or, France

We have been able to design model filled rubbers with exactly the same chemical structure but different filler arrangements. From these model systems, we show that the particle arrangement in the elastomeric matrix controls the strain softening at small strain amplitude known as the Payne effect, as well as the elastic modulus dependence on the temperature. More precisely, we observed that the Payne effect disappears and the elastic modulus only weakly depends on the temperature when the particles are well separated. On the contrary, samples with the same interfacial physical chemistry but with aggregated particles show large amplitudes of the Payne effect and their elastic modulus decreases significantly with the temperature. We discuss these effects in terms of glassy bridge formation between filler particles. The observed effects provide evidence that glassy bridges play a key role on the mechanical properties of filled rubbers.

PACS numbers:
Keywords:

INTRODUCTION

Dispersing colloïdal particles in an elastomeric matrix is an every day operation in the rubber industry. It is an efficient way of improving many mechanical properties of the rubber such as its elastic modulus, fracture resistance, abrasion resistance etc. It has also been clear for many years that the introduction of solid particles has not only a trivial geometrical role on the mechanics, but also modifies the polymer dynamics of the matrix [1–4]. However, it is very difficult to identify properly the respective geometrical and dynamical roles of the particles since they are usually both controlled by the same parameter: a "coupling" agent that coats the particles surface. By acting on the particles/polymer interactions, this molecule not only affects the particle arrangement but also the dynamics of the polymer near the particle. It is then clear that any breakthrough in this domain will require the independent mastering of both the polymer dynamics at the interface and the filler arrangement. We propose here a method to drive appart those two phenomenon and obtain samples with the same interfacial physical chemistry - that is same coupling agent and graft density - but with either aggregated or non aggregated particles. We have compared the mechanical response of those two sets of samples and it clearly shows that the particle arrangement strongly controls the temperature dependence of the elastic modulus as well as the amplitude of the Payne effect [5–8] - a softening of the elastic modulus observed in cyclic strain experiments, characteristic of filled rubbers. Samples with well dispersed fillers show a very weak Payne effect and almost no temperature dependence of the elastic modulus, whereas samples with aggregated particles exhibit on the contrary a large amplitude of the Payne effect and a significant temperature dependence of their elastic modulus. The paper is organised as follows: we will first recall some previous results we obtained on our model samples before explaining our synthesis and characterisation methods. We will then present the results of the mechanical experiments we performed and finally conclude on the role of the filler arrangement on the mechanical response of those model reinforced elastomers.

BACKGROUND

For this study we used model systems with a covalent binding between the silica particles and the polymer matrix. We previously showed that in these samples there is a gradient of glass transition temperature in the vicinity of the particles [9, 10]. This gradient is similar to the one observed in thin polymer films [11] and it can be described as:

$$T_g^\omega(z) = T_g^\omega(1 + (\delta/z)^v) \quad (1)$$

where z is the distance to the particle surface, ω the frequency used for the measurement, v an exponent close to 1 (it will be taken equal to 1 in this paper), T_g^ω the bulk glass transition temperature, $T_g^\omega(z)$ the one at distance z from the particle interface and δ a length that may depend on the interface molecular structure, typically around 1 nm in our case. Far above the glass transition - between T_g + 50 K and T_g + 100 K - the gradient of glass transition temperature around the particles is very sharp so that we can consider that the particle is surrounded by a glassy layer whose thickness can be

deduced from equation (1):

$$e_g(T,\omega) = \delta \frac{T_g^\omega}{T - T_g^\omega} \quad (2)$$

In this regime, we can thus see the sample as a soft matrix in which solid particles surrounded by solid glassy shells are dispersed. This equation is also a way to evaluate δ. NMR measurements give access to the fraction of glassy polymer, which can be translated in terms of glassy thickness e_g. δ is obtained by plotting e_g as a function of $\frac{T_g^\omega}{T-T_g^\omega}$ [9].

In order to assess the effect of the particles on the polymer dynamics, it is useful to normalize the elastic modulus of the filled sample by the one of the pure matrix. This quantity is usually called the reinforcement R. If there were no modification of the polymer dynamics, R should be independent of the temperature because the mechanical modulus of the silica - about 10 GPa - is very large compared to the one of the matrix -less than 100 MPa in the range of temperature studied here. In practice, most of the filled rubber samples exhibit a complex temperature dependence of the reinforcement typically with a huge maximum around 20 K above the glass transition of the matrix. This behavior will be described and discussed in a further publication but it clearly shows that the particles have a large effect on the polymer dynamics. As explained elsewhere [12], the reinforcement verifies the following frequency - temperature superposition law between 50 K and 100 K above the matrix glass transition:

$$R(T,\omega) = f(\frac{T_g(\omega)}{T - T_g(\omega)}) \quad (3)$$

where f is a function that depends on the type of sample. When we compare it to equation (2) we understand that in this regime the reinforcement is a function the glassy shell thickness only.

Another characteristic behavior of reinforced elastomers is known as the Payne effect. It is a softening of the elastic modulus of filled rubber observed in cyclic strain experiments for strain values typically between 0.1% and 10% - although the matrix without particles is in a linear regime for strain amplitude larger than 100%. This effect is also due to the modification of the polymer dynamics by the particles. As to our samples, we have shown that it is related to the presence of glassy bridges between the fillers and that it only depends on the $T-T_g^\omega$ difference for a given sample. It is also well known that the strain softening of glassy polymer occurs at a yield stress that depends on the distance to the glass transition and that is roughly equal to:

$$\sigma_y \cong K(T - T_g(\omega)) \quad (4)$$

where K is about 1 MPa.K^{-1}. As a consequence, the field of yield stress in the sample depends only on the thickness of the glassy layer. Hence we obtain the following relation for the Payne effect [12]:

$$R(T,\omega,\gamma) \cong g(\frac{T_g(\omega)}{T - T_g(\omega)}, \gamma) \quad (5)$$

where γ is the strain amplitude, and g a function depending on the sample.

Table I: Characteristics of the samples

Name	Mean silica diam. (nm) [a]	Si vol. fraction	$h^{a,b}$ (nm)	Graft density (nm^{-2})[c]
Set (a) - 1	41	0.22	8	3.2
Set (a) - 2	41	0.15	15	3.2
Set (b) - 1	42	0.19	agg	3.3
Set (b) - 2	42	0.14	agg	3.3

[a] From SANS measurements; [b] h = mean distance between neighboring silica particles surfaces, agg = aggregated; [c] From elemental analysis.

SAMPLES AND EXPERIMENTAL TECHNIQUES

The sample preparation has been described previously [13]. In this work we showed that the dispersion state of the fillers depends on the grafting density and on the synthesis procedure. From these observations, we developed two protocols to get filled samples with different dispersion states starting from the same colloidal solution of grafted silica particles in acrylate monomers. The samples used in the present work were synthesized starting from silica particles with almost the same size ($\simeq$ 42 nm) and grafting density ($\simeq$ 3.3 molecules/nm^2, see Table I). The silica beads were grafted with TPM, a silane ended by a methylacrylate function, [14–17]. Then, the fillers were transferred from their initial solvent to ethylacrylate monomers using slightly different protocols. Set (a) was prepared with a concentration step performed at room temperature, trough a dialysis in acrylate monomers. For set (b), the silica suspension was concentrated using a distillation performed at 50ïC. This was sufficient to obtain very different particle arrangements for the two sets. Finally, we polymerized and cross-linked the samples using UV agents. The grafter copolymerized with the polymer and we thus obtained a very good and reproducible dispersion of silica particles embedded in an elastomeric matrix. The dispersion state has been measured using Small Angle Neutrons Scattering (SANS).

SANS experiments

We performed Small Angle Neutrons scattering using the KWS2 (FKZ, Juelich, Germany) and PAXY

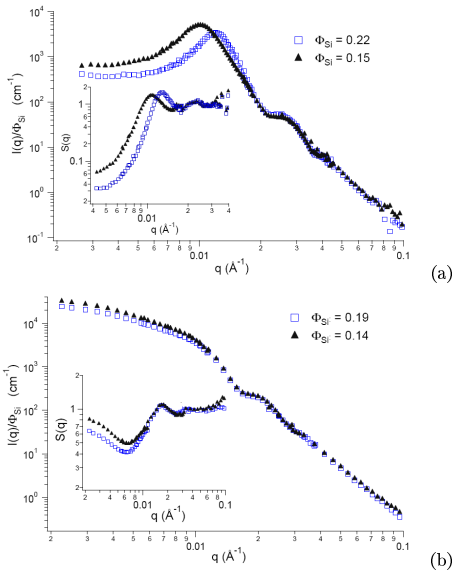

Figure 1: Scattered intensity and corresponding structure factor S(q) (inset) of ethylacrylate elastomers reinforced with silica particles grafted with TPM molecules. (a) Samples with very good silica dispersion states: silica diameter 41 nm, graft dentity 3.2 molecules/nm^2, silica volume fraction (square): 0.22; (triangle): 0.15 (b) Samples with partly aggregated particles: silica diameter 42 nm, graft dentity 3.3 molecules/nm^2, silica volume fraction (square): 0.19; (triangle): 0.14

(LLB,Saclay, France) and D16 (ILL, Grenoble, France). The contrast between silica and polyethylacrylate is the source of scattering we measured. The structure factors of the samples were obtained by dividing the scattered intensity by the one of the dilute particles, as described in Ref.13. We plotted the structure factors of the two sets of samples in Fig. 1. Two features are essential for the understanding of the signal. Firstly, for low and decreasing wave vectors - below 0.1 nm^{-1} - we probe the particle arrangement at a scale of about 5 particle diameters. If the intensity is low in this regime, it means that the particles are homogeneously distributed - a perfect gas has a zero low-q structure factor intensity. We observe that the structure factors measured for the samples of set (a) decrease with q, meaning that the fillers are very well dispersed.

The situation is very different for set (b) where the structure factor increases with an exponent of the order of -0.5. This behavior corresponds to the response of a fractal aggregate with a fractal dimension of 1/2. It

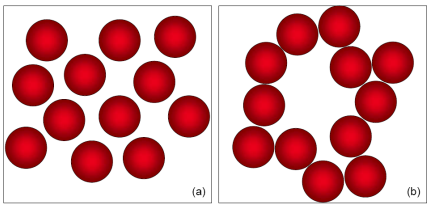

Figure 2: Schematic representation of the two types of samples: Set (a) with well dispersed particles and set (b) with partly aggregated particles.

means that, in those samples, the particles are forming very open aggregates.

The second important feature of the structure factor is the position of its first peak. This peak position roughly corresponds to the distance between first neighbours and we can see that in case (a) it varies with the silica concentration. Actually, this structure factor can be fitted by the one of a simple liquid of hard spheres, using Percus Yevick approximation and it appears that the structure factor we measured corresponds to the one of a simple liquid with a particle diameter larger than the real one. This defines a kind of excluded volume around each particle from which we can deduce a typical distance h between the surface of neighboring particles. This distance h is equal to 8 and 15 nm for respectively silica volume fractions of 0.22 and 0.15. On the contrary, samples from set (b) exhibit a peak that is characteristic of a flocculated sample. It means that in thoses samples the particles are nearly in contact and form aggregates . Thus, the analysis of the samples behavior at small q-vectors and of the first peak position leads to the following conclusion: set (a) is constituted of very well dispersed particles, while particles in set (b) form open aggregates. This last set of samples is indeed a network of particles - as commonly presumed in industrial samples [1, 18]. In Fig. 2, we have pictured a schematic representation of the two types of samples.

Mechanical measurements

The mechanical measurements have been performed in a torsion mode on cylindrical samples, using a RDA2 rheometer and a plate/plate geometry. The samples are glued on the plates with Loctite 406. Glass transition temperature - used in the frequency-temperature superposition (equation (3)) is determined as the frequency of the maximum of the loss modulus, for each temperature. Elastic moduli have been measured in the 10^{-2} Hz - 10Hz frequency range, for various temperatures.

4

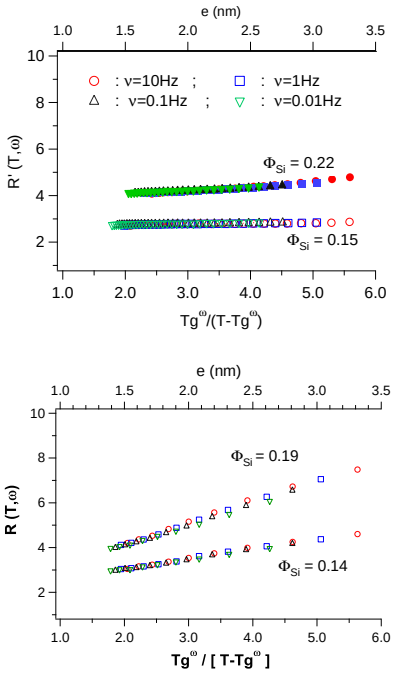

Figure 3: Effect of the particle dispersion on the reinforcement R as a function of the reduced variable $\frac{T_g(\omega)}{T-T_g(\omega)}$. This reduced variable is proportional to the glassy layer thickness e (upper axis) from equation (2). For each sample, the reinforcement was measured at different temperatures and frequencies. (a) Reinforcement measured on samples with very good dispersion states for two silica volume fractions : 0.22 and 0.15. (b) Reinforcement measured on samples with partly aggregated particles for two silica volume fractions : 0.19 and 0.14

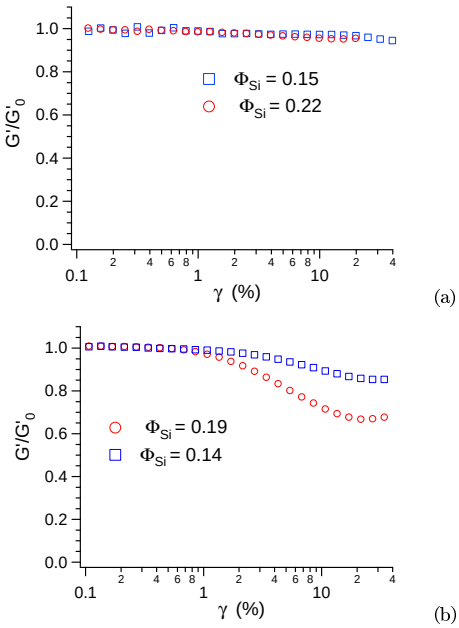

Figure 4: Effect of the particle dispersion on the strain dependence of the shear modulus (Payne effect). Data of the modulus were normalized by the modulus measured in the linear regime. Measurements were performed at 1Hz and $T = T_g + 50K = 303K$, ie. at $\frac{T_g}{T-T_g} = 5$. (a) Results obtained on samples with very good dispersion states for two silica volume fractions : 0.22 and 0.15. (b) Results obtained on samples with partly aggregated particles for two silica volume fractions : 0.19 and 0.14

The reinforcement - elastic modulus of the filled sample divided by the one of the pure matrix, R - is plotted in Fig. 3 as a function of the reduced variable $\frac{T_g^\omega}{T-T_g^\omega}$ (lower axis) and versus the glassy layer thickness (upper axis) - we saw in equation (2) that these two quantities are proportional. R verifies the frequency - temperature superposition. From samples (a) to (b), it is clear that the slope of the reinforcement with glassy layer thickness increases with the disorder of the particles arrangement. The elastic moduli G', normalized by the elastic moduli at zero strain G'_0, are plotted in Fig. 4 as a function of strain. The elastic modulus is independent of the strain amplitude for set (a), while it decreases significantly for set (b). Thus set (a), unlike set (b), exhibits neither a temperature dependence of its reinforcement, nor a Payne effect. The data clearly show that the respective positions of the fillers in an elastomer control the existence of a Payne effect.

DISCUSSION

Let us first discuss the results obtained on set (a). The distance h between the particles - respectively 8 and 15 nm - is large compare to the typical thickness of the glassy layer - 3.5 nm - so that there is no glassy bridge between the particles. Moreover, within the present temperature range, the glassy layer thickness varies from 1.5nm to 3.3 nm. The volume fraction of the solid phase - $\Phi(1+e_g/r)^3$

- where Φ is the silica volume fraction and r the particles diameter, varies then from 0.26 to 0.33. According to the phenomenological law for the geometrical reinforcement for filled rubbers known as the Guth and Gold law [19],

$$R \approx 1 + 2.5\Phi + 14\Phi^2 \quad (6)$$

we can estimate the increase of reinforcement due to the increase of the volume fraction of the solid phase, that is the particles surrounded by their glassy layer. One finds that the reinforcement variation in the explored range of temperature varies from 2.6 to 3.3 while experimental results show a variation from 4.1 to 4.8. Thus, the small increase estimated using the Guth and Gold law is in qualitative agreement with our measurements but the absolute value of the reinforcement estimated by the Guth and Gold law is higher than the one observed experimentally. This is actually due to an underestimation of the elastic modulus of the polymer network in the presence of particles due to the additional covalent bonds between polymer and particles surfaces - observed by NMR [20]. To summarize, in set (a) in which the distance between particles is larger than the thickness of two glassy layers, the growth of the glassy layer for decreasing temperature does not induce any spectacular modulus variation. And as shown in Fig. 4, there is not any significant Payne effect.

Let us now consider the set of samples (b). In that case, most of the particles are very close to their neighbors, so that if the temperature is lowered and that the glassy layer thickness increases, it reinforces drastically the glassy bridges linking the particles. Let us estimate the diameter of the glassy bridges as a function of the temperature. If $e_g(T)$ is the glassy thickness corresponding to the temperature T and since $e_g(T) \ll r$, the temperature dependence of the glassy bridge diameter writes as follows (Fig. 5):

$$d(T) \simeq \sqrt{8 \times e_g(T) r} \quad (7)$$

It varies typically from 15 to 24 nm in the explored range of temperature ($e(T)$ is given in Fig. 3). Thus, decreasing slightly the temperature in sample (b) induces a strong mechanical bridging of the particles, and thus a large increase of the rigidity of the network of filled particles. This effect increases strongly the elastic modulus. If we take into account only the solid volume fraction, and if we use Guth and Gold equation as previously, we find that the reinforcement goes from 2.2 to 2.8 in the explored temperature range for the 0.19 silica volume fraction. The experimental value gives a variation of the reinforcement from 3.9 to 7.5, thus an absolute variation larger by a factor of about 2 than the one considering only the volume fraction argument. Furthermore, since the samples from this set exhibit a significant Payne effect, it shows that there is a correlation between the presence of glassy bridges in the sample and the amplitude of the Payne effect. In effect, as the glassy bridges support a considerable amount of stress in the skeleton formed by the particles and glassy polymer, they are subject to strain softening, which might cause the Payne effect. As a conclusion, this study on two sets of samples clearly demonstrates that the Payne effect exists only if there are glassy bridges between neighboring particles.

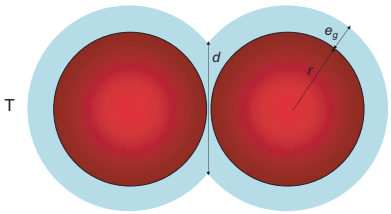

Figure 5: Schematic representation of two neighboring particles at a temperature T at which the glassy thickness is e_g. A glassy bridge of diameter d is created.

CONCLUSION

This paper presents the mechanical behavior of two sets of reinforced elastomers differing only by their particle arrangement. We used model systems with a covalent bonding between the polymer and the particles, in which we previously showed that the polymer at the surface of the particle is in the glassy state, forming a glassy shell. The two sets of samples are made up of the same polymer matrix and fillers coated with the same coupling agent and graft density, but one set has very well dispersed particles whereas the other one includes large aggregates. The fact that the two sets exhibit very different mechanical behaviors shows the key role that plays the particle arrangement. The elastic modulus of samples with well separated particles only weakly depends on the temperature and we can only hardly see on them the strain softening effect known as Payne effect. This can be understood as the shells of glassy polymer around the particles are not bound to each other. On the contrary, in the case of aggregated particles, we observe a large Payne effect and a significant dependence of the elastic moduli on the temperature. In effect, the glassy shells are here in contact with each other and it forms a network of particles bound by glassy polymer. This skeleton supports most of the stress in the sample so that the glassy bridges are

subject to strain softening, which account for the Payne effect observed. As a conclusion, this new study confirms that, in these model systems, the glassy bridges between neighboring particles are responsible for the Payne effect.

ACKNOWLEDGEMENT

We acknowledge Y. Bomal for many discussions, W. Pykhout Hinzen, L. Noirez and B. Deme for their help and support on SANS measurements on KW2 in FZ-Juelich, PAXY in LLB and D16 in ILLL.

---

* *now in Dow Corning*

[1] G. Heinrich and M. Kluppel, in *Filled Elastomers Drug Delivery Systems* (Springer Berlin / Heidelberg, 2002), vol. 160 of *Advances in Polymer Science*, pp. 1–44.
[2] M. Wang, Rubber Chemistry and Technology **71**, 520 (1998).
[3] L. Chazeau, J. Brown, L. Yanyo, and S. Sternstein, Polymer Composites **21**, 202 (2000).
[4] M. Kluppel, in *Filler-Reinforced Elastomers/Sanning Force Microscopy* (Springer Berlin / Heidelberg, 2003), vol. 164 of *Advances in Polymer Science*, pp. 1–86.
[5] A. Payne, Journal of Applied Polymer Science **6**, 368 (1962).
[6] A. Payne and W. Watson, Rubber Chemistry and Technology **36**, 147 (1963).
[7] A. Payne, *Reinforcement of elastomers* (Interscience, New-York, 1965), g. kraus ed.
[8] J. Harwood, L. Mullins, and A. Payne, Journal of Applied Polymer Science **9**, 3011 (1965).
[9] J. Berriot, H. Montes, F. Lequeux, D. Long, and P. Sotta, Macromolecules **35**, 9756 (2002).
[10] J. Berriot, H. Montes, F. Lequeux, D. Long, and P. Sotta, Europhysics Letters **64**, 50 (2003).
[11] D. Fryer, R. Peters, E. Kim, J. Tomaszewski, J. de Pablo, P. Nealey, C. White, and W. Wu, Macromolecules **34**, 5627 (2001).
[12] H. Montes, F. Lequeux, and J. Berriot, Macromolecules **36**, 8107 (2003).
[13] J. Berriot, H. Montes, F. Martin, M. Mauger, W. Pyckhout-Hintzen, G. Meier, and H. Frielinghaus, Polymer **44**, 4909 (2003).
[14] H. Sunkara, J. Jethmalani, and W. Ford, Chemistry of Materials **6**, 362 (1994).
[15] J. Jethmalani and W. Ford, Chemistry of Materials **8**, 2138 (1996).
[16] J. Jethmalani, W. Ford, and G. Beaucage, Langmuir **13**, 3338 (1997).
[17] J. Jethmalani, H. Sunkara, W. Ford, S. Willoughby, and B. Ackerson, Langmuir **13**, 2633 (1997).
[18] G. Heinrich, M. Kluppel, and T. Vilgis, Current Opinion in Solid State & Materials Science **6**, 195 (2002).
[19] E. Guth and O. Gold, Phys. Review **53**, 322 (1938).
[20] J. Berriot, F. Martin, H. Montes, L. Monnerie, and P. Sotta, Polymer **44**, 1437 (2003).

Bibliographie

[1] J Berriot. *Existence et rôle d'un gradient de température de transition vitreuse sur les propriétés mécaniques d'un élastomère renforcé.* PhD thesis, Université Paris 6, 2003.

[2] T Chaussée. *Effet de la physico-chimie des interfaces sur les propriétés mécaniques des élastomères renforcés.* PhD thesis, Université Paris 6, 2008.

[3] AR Payne. *Reinforcement of elastomers.* Interscience, New-York, G kraus edition, 1965.

[4] L Chazeau, JD Brown, LC Yanyo, and SS Sternstein. Modulus recovery kinetics and other insights into the Payne effect for filled elastomers. *Polymer composites*, 21(2) :202–222, 2000.

[5] A Einstein. A new determination of the molecular dimensions. *Annalen der Physik*, 19(2) :289–306, 1906.

[6] HM Smallwood. Limiting law of the reinforcement of rubber. *Journal of applied physics*, 15(11) :758–766, 1944.

[7] E Guth and O Gold. On the hydrodynamical theory of the viscosity of suspensions. *Phys. Review*, 53 :322, 1938.

[8] E Guth. Theory of filler reinforcement. *Journal of applied physics*, 16(1) :20–25, 1945.

[9] G Kraus. Mechanical losses in carbon-black filled rubbers. *Applied Polymer Symposia*, (39) :75–92, 1984.

[10] G Heinrich and M Klüppel. Recent advances in the theory of filler networking in elastomers. In *Filled Elastomers Drug Delivery Systems*, volume 160 of *Advances in Polymer Science*, pages 1–44. Springer Berlin / Heidelberg, 2002.

[11] M Kluppel. *The Role of Disorder in Filler Reinforcement of Elastomers on Various Length Scales*, pages 1–86. 2003.

[12] G Huber and TA Vilgis. Universal properties of filled rubbers : Mechanisms for reinforcement on different length scales. *Kautschuk Gummi Kunststoffe*, 52(2) :102–107, 1999.

[13] AI Medalia. Morphology of aggregates. *Journal of Colloid and Interface Science*, 32(1) :115, 1970.

[14] MJ Wang. Effect of polymer-filler and filler-filler interactions on dynamic properties of filled vulcanizates. *Rubber Chemistry and Technology*, 71(3) :520–589, 1998.

[15] JM Funt. Dynamic testing and reinforcement of rubber. *Rubber Chemistry and Technology*, 61(5) :842–865, 1988.

[16] PG Maier and D Goritz. Molecular interpretation of the Payne effect. *Kautschuk Gummi Kunststoffe*, 49(1) :18–21, 1996.

[17] E Chabert, R Dendievel, C Gauthier, and JY Cavaille. Prediction of the elastic response of polymer based nanocomposites : a mean field approach and a discrete simulation. *Composites Science and Technology*, 64(2) :309–316, 2004.

[18] M Klüppel. The role of disorder in filler reinforcement of elastomers on various length scales. In *Filler-Reinforced Elastomers/Sanning Force Microscopy*, volume 164 of *Advances in Polymer Science*, pages 1–86. Springer Berlin / Heidelberg, 2003.

[19] G Heinrich, M Kluppel, and TA Vilgis. Reinforcement of elastomers. *Current opinion in solid state and materials science*, 6(3) :195–203, 2002.

[20] S Kaufman, WP Slichter, and DD Davis. Nuclear magnetic resonance study of rubber - carbon black interactuons. *Journal of Polymer Science Part A-2 Polymer Physics*, 9(5) :829–839, 1971.

[21] JC Kenny, VJ McBrierty, Z Rigbi, and DC Douglass. Carbon-black filled natural rubber .1. structural investigations. *Macromolecules*, 24(2) :436–443, 1991.

[22] YC Ou, ZZ Yu, A Vidal, and JB Donnet. Effects of alkylation of silicas on interfacial interaction and molecular motions between silicas and rubbers. *Journal of Applied Polymer Science*, 59(8) :1321–1328, 1996.

[23] VM Litvinov and PAM Steeman. EPDM-carbon black interactions and the reinforcement mechanisms, as studied by low-resolution h-1 NMR. *Macromolecules*, 32(25) :8476–8490, 1999.

[24] JW ten Brinke, VM Litvinov, JEGJ Wijnhoven, and JWM Noordermeer. Interactions of stober silica with natural rubber under the influence of coupling agents, studied by H-1 NMR T-2 relaxation analysis. *Macromolecules*, 35(27) :10026–10037, 2002.

[25] G Leu, Y Liu, DD Werstler, and DG Cory. NMR characterization of elastomer-carbon black interactions. *Macromolecules*, 37(18) :6883–6891, 2004.

[26] R Ruggerone, V Geiser, S Dalle Vacche, Y Leterrier, and JAE Manson. Immobilized polymer fraction in hyperbranched polymer/silica nanocomposite suspensions. *Macromolecules*, 43(24) :10490–10497, 2010.

[27] LCE Struik. The mechanical and physical aging of semicrystalline polymers .1. *Polymer*, 28(9) :1521–1533, 1987.

[28] G Tsagaropoulos and A Eisenberg. Direct observation of two glass transitions in silica filled polymers - implications for the morphology of random ionomers. *Macromolecules*, 28(1) :396–398, 1995.

[29] JL Keddie and RAL Jones. Glass transition behavior in ultra-thin polystyrene films. *Israel Journal of Chemistry*, 35(1) :21–26, 1995.

[30] DS Fryer, PF Nealey, and JJ de Pablo. Thermal probe measurements of the glass transition temperature for ultrathin polymer films as a function of thickness. *Macromolecules*, 33(17) :6439–6447, 2000.

[31] D Long and F Lequeux. Heterogeneous dynamics at the glass transition in van der waals liquids, in the bulk and in thin films. *EPJE*, 4(3) :371–387, 2001.

[32] J Berriot, H Montes, F Lequeux, D Long, and P Sotta. Evidence for the shift of the glass transition near the particles in silica-filled elastomers. *Macromolecules*, 35(26) :9756–9762, 2002.

[33] H Montes, F Lequeux, and J Berriot. Influence of the glass transition temperature gradient on the nonlinear viscoelastic behavior in reinforced elastomers. *Macromolecules*, 36(21) :8107–8118, 2003.

[34] H Montes, T Chaussee, A Papon, F Lequeux, and L Guy. Particles in model filled rubber : Dispersion and mechanical properties. *European Physical Journal E*, 31(3) :263–268, 2010.

[35] A Serghei and F Kremer. Unexpected preparative effects on the properties of thin polymer films. *Characterization of Polymer Surfaces and Thin FIlms*, 132 :33–40, 2006.

[36] A Serghei, H Huth, C Schick, and F Kremer. Glassy dynamics in thin polymer layers having a free upper interface. *Macromolecules*, 41(10) :3636–3639, 2008.

[37] M Tress, M Erber, EU Mapesa, H Huth, J Muller, A Serghei, C Schick, KJ Eichhorn, B Volt, and F Kremer. Glassy dynamics and glass transition in nanometric thin layers of polystyrene. *Macromolecules*, 43(23) :9937–9944, 2010.

[38] M Erber, M Tress, EU Mapesa, A Serghei, KJ Eichhorn, B Voit, and F Kremer. Glassy dynamics and glass transition in thin polymer layers of PMMA deposited on different substrates. *Macromolecules*, 43(18) :7729–7733, 2010.

[39] GB McKenna. Ten (or more) years of dynamics in confinement : Perspectives for 2010. *The European Physical Journal Special Topics*, 189(1) :285–302, 2010.

[40] CG Robertson and M Rackaitis. Further consideration of viscoelastic two glass transition behavior of nanoparticle-filled polymers. *Macromolecules*, 44(5) :1177–1181, 2011.

[41] CG Robertson, CJ Lin, M Rackaitis, and CM Roland. Influence of particle size and polymer-filler coupling on viscoelastic glass transition of particle-reinforced polymers. *Macromolecules*, 41(7) :2727–2731, 2008.

[42] P Akcora, SK Kumar, VG Sakai, Y Li, BC Benicewicz, and LS Schadler. Segmental dynamics in PMMA-grafted nanoparticle composites. *Macromolecules*, 43(19) :8275–8281, 2010.

[43] P Akcora, SK Kumar, J Moll, S Lewis, LS Schadler, Y Li, BC Benicewicz, A Sandy, S Narayanan, J Ilavsky, P Thiyagarajan, RH Colby, and JF Douglas. "Gel-like" mechanical reinforcement in polymer nanocomposite melts. *Macromolecules*, 43(2) :1003–1010, 2010.

[44] W Stöber, A Fink, and E Bohn. Controlled growth of monodisperse silica spheres in micron range. *Journal of colloid and interface science*, 26(1) :62, 1968.

[45] HB Sunkara, JM Jethmalani, and WT Ford. Composite of colloidal crystals of silica in poly(methyl methacrylate). *Chemistry of materials*, 6(4) :362–364, 1994.

[46] JM Jethmalani and WT Ford. Diffraction of visible light by ordered monodisperse silica-poly(methyl acrylate) composite films. *Chemistry of materials*, 8(8) :2138–2146, 1996.

[47] JM Jethmalani, HB Sunkara, WT Ford, SL Willoughby, and BJ Ackerson. Optical diffraction from silica-poly(methyl methacrylate) composite films. *Langmuir*, 13(10) :2633–2639, 1997.

[48] JM Jethmalani, WT Ford, and G Beaucage. Crystal structures of monodisperse colloidal silica in poly(methyl acrylate) films. *Langmuir*, 13(13) :3338–3344, 1997.

[49] J Berriot, H Montes, F Martin, M Mauger, W Pyckhout-Hintzen, G Meier, and H Frielinghaus. Reinforcement of model filled elastomers : synthesis and characterization of the dispersion state by SANS measurements. *Polymer*, 44(17) :4909–4919, 2003.

[50] JK Percus and GJ Yevick. Analysis of classical statistical mechanics by means of collective coordinates. *Physical Review*, 110(1) :1, 1958.

[51] DJ Kinning and EL Thomas. Hard-sphere interactions between spherical domains in diblock copolymers. *Macromolecules*, 17(9) :1712–1718, 1984.

[52] J Berriot, F Lequeux, H Montes, and H Pernot. Reinforcement of model filled elastomers : experimental and theoretical approach of swelling properties. *Polymer*, 43(23) :6131–6138, 2002.

[53] J Berriot, F Lequeux, L Monnerie, H Montes, D Long, and P Sotta. Filler-elastomer interaction in model filled rubbers, a 1H NMR study. *Journal of Non-Crystalline Solids*, 307-310 :719–724, 2002.

[54] J Berriot, F Martin, H Montes, L Monnerie, and P Sotta. Reinforcement of model filled elastomers : characterization of the crosslinking density at the filler-elastomer interface by 1H NMR measurements. *Polymer*, 44(5) :1437–1447, 2003.

[55] J Berriot, H Montes, F Lequeux, D Long, and P Sotta. Gradient of glass transition temperature in filled elastomers. *Europhysics Letters*, 64(1) :50–56, 2003.

[56] DS Fryer, RD Peters, EJ Kim, JE Tomaszewski, JJ de Pablo, PF Nealey, CC White, and WL Wu. Dependence of the glass transition temperature of polymer films on interfacial energy and thickness. *Macromolecules*, 34(16) :5627–5634, 2001.

[57] K Saalwächter, M Kluppel, H Luo, and H Schneider. Chain order in filled SBR elastomers : a proton multiple-quantum NMR study. *Applied Magnetic Resonance*, 27(3-4) :401–417, 2004.

[58] K Saalwächter. Artifacts in transverse proton NMR relaxation studies of elastomers. *Macromolecules*, 38(4) :1508–1512, 2005.

[59] A Maus, C Hertlein, and K Saalwächter. A robust proton NMR method to investigate Hard/Soft ratios, crystallinity, and component mobility in polymers. *Macromolecular Chemistry and Physics*, 207 :1150–1158, 2006.

[60] M Mauri, Y Thomann, H Schneider, and K Saalwächter. Spin-diffusion NMR at low field for the study of multiphase solids. *Solid State Nuclear Magnetic Resonance*, 34(1-2) :125–141, 2008.

[61] K Saalwächter. Detection of heterogeneities in dry and swollen polymer networks by proton Low-Field NMR spectroscopy. *Journal of the American Chemical Society*, 125(48) :14684–14685, 2003.

[62] K Saalwächter, B Herrero, and MA Lopez-Manchado. Chain order and Cross-Link density of elastomers as investigated by proton Multiple-Quantum NMR. *Macromolecules*, 38(23) :9650–9660, 2005.

[63] K Saalwächter. Proton multiple-quantum NMR for the study of chain dynamics and structural constraints in polymeric soft materials. *Progress in Nuclear Magnetic Resonance Spectroscopy*, 51(1) :1–35, 2007.

[64] JL Valentin, P Posadas, A Fernandez-Torres, MA Malmierca, L Gonzalez, W Chasse, and K Saalwächter. Inhomogeneities and chain dynamics in diene rubbers vulcanized with different cure systems. *Macromolecules*, 43(9) :4210–4222, 2010.

[65] J Berriot, H Montes, F Martin, M Mauger, W Pyckhout-Hintzen, G Meier, and H Frielinghaus. Reinforcement of model filled elastomers : synthesis and characterization of the dispersion state by SANS measurements. *Polymer*, 44(17) :4909–4919, 2003.

[66] TC Farrar and ED Becker. *Pulse and Fourier transform NMR : Introduction to theory and methods*. New-York, academic press edition, 1971.

[67] J Bandrup, EH Immergut, and EA Grulke. *Polymer Handbook*. John Wiley & Sons, New York, 1999.

[68] PW Anderson and PR Weiss. Exchange Narrowing in Paramagnetic Resonance. *Rev. Mod. Phys.*, 25 :269–276, 1953.

[69] R Kimmich. *NMR Tomography, Diffusometry, Relaxometry*. Springer, Berlin, 1997.

[70] M Wind, R Graf, A Heuer, and HW Spiess. Structural Relaxation of Polymers at the Glass Transition : Conformational Memory in Poly(n-alkylmethacrylates). *Phys. Rev. Lett.*, 91 :155702, 2003.

[71] TS Chow. Molecular interpretation of the glass-transition temperature of polymer-diluent systems. *Macromolecules*, 13(2) :362–364, 1980.

[72] A Şerbescu and K Saalwächter. Particle-induced network formation in linear PDMS filled with silica. *Polymer*, 50 :5434–5442, 2009.

[73] C Rotella, S Napolitano, L De Cremer, G Koeckelberghs, and M Wübbenhorst. Distribution of segmental mobility in ultrathin polymer films. *Macromolecules*, 43(20) :8686–8691, 2010.

[74] A Papon, K Saalwächter, K Schäler, L Guy, F Lequeux, and H Montes. Low-Field NMR investigations of nanocomposites : Polymer dynamics and network effects. *Macromolecules*, 44(4) :913–922, 2011.

[75] N Metatla and A Soldera. The Vogel-Fulcher-Tamman equation investigated by atomistic simulation with regard to the Adam-Gibbs model. *Macromolecules*, 40(26) :9680–9685, 2007.

[76] AR Payne. The dynamic properties of carbon black loaded natural rubber vulcanizates. part II. *Journal of Applied Polymer Science*, 6(21) :368–372, 1962.

[77] AR Payne and WF Watson. Carbon black structure in rubber. *Rubber Chemistry and Technology*, 36(432) :147–155, 1963.

[78] JAC Harwood, L Mullins, and AR Payne. Stress softening in natural rubber vulcanizates. part II. stress softening effects in pure gum and filler loaded rubbers. *Journal of Applied Polymer Science*, 9(9) :3011–3021, 1965.

[79] A Lion. A constitutive model for carbon black filled rubber : Experimental investigations and mathematical representation. *Continum Mechanics and thermodynamics*, 8(3) :153–169, 1996.

[80] A Lion, C Kardelky, and P Haupt. On the frequency and amplitude dependence of the Payne effect : Theory and experiments. *Rubber Chemistry and Technology*, 76(2) :533–547, 2003.

[81] P Hofer and A Lion. Modelling of frequency- and amplitude-dependent material properties of filler-reinforced rubber. *Journal of the Mechanics and Physics of Solids*, 57(3) :500–520, 2009.

[82] M Rendek and A Lion. Modelling and finite element simulation of Filler-Reinforced elastomers under dynamic deformations. *Kautschuk Gummi Kunststoffe*, 62(9) :463–470, 2009.

[83] M Rendek and A Lion. Strain induced transient effects of filler reinforced elastomers with respect to the Payne-effect : experiments and constitutive modelling. *Zamm-Zeitschrift Für Angewandte Mathematik Und Mechanik*, 90(5) :436–458, 2010.

[84] CM Roland. Dynamic mechanical-behavior of filled rubbers at small strains. *Journal of rheology*, 34(1) :25–34, 1990.

[85] KS Cho, K Hyun, KH Ahn, and SJ Lee. A geometrical interpretation of large amplitude oscillatory shear response. *Journal of rheology*, 49(3) :747–758, 2005.

[86] S Kallus, N Willenbacher, S Kirsch, D Distler, T Neidhofer, M Wilhelm, and HW Spiess. Characterization of polymer dispersions by fourier transform rheology. *Rheologica Acta*, 40(6) :552–559, 2001.

[87] JL Leblanc. Fourier transform rheometry on gum elastomers. *Journal of Applied Polymer Science*, 89(4) :1101–1115, 2003.

[88] JL Leblanc. Fourier transform rheometry on carbon black filled polybutadiene compounds. *Journal of Applied Polymer Science*, 100(6) :5102–5118, 2006.

[89] M Wilhelm, D Maring, and HW Spiess. Fourier-transform rheology. *Rheologica Acta*, 37(4) :399–405, 1998.

[90] M Wilhelm, P Reinheimer, and M Ortseifer. High sensitivity fourier-transform rheology. *Rheologica Acta*, 38(4) :349–356, 1999.

[91] M Wilhelm, P Reinheimer, M Ortseifer, T Neidhofer, and HW Spiess. The crossover between linear and non-linear mechanical behaviour in polymer solutions as detected by fourier-transform rheology. *Rheologica Acta*, 39(3) :241–246, 2000.

[92] M Wilhelm. Fourier-Transform rheology. *Macromolecular materials and engineering*, 287(2) :83–105, 2002.

[93] K Hyun and M Wilhelm. Establishing a new mechanical nonlinear coefficient q from FT-Rheology : first investigation of entangled linear and comb polymer model systems. *Macromolecules*, 42(1) :411–422, 2009.

[94] RH Ewoldt, C Clasen, AE Hosoi, and GH McKinley. Rheological fingerprinting of gastropod pedal mucus and synthetic complex fluids for biomimicking adhesive locomotion. *Soft Matter*, 3(5) :634–643, 2007.

[95] RH Ewoldt, AE Hosoi, and GH McKinley. New measures for characterizing nonlinear viscoelasticity in large amplitude oscillatory shear. *Journal of Rheology*, 52(6) :1427–1458, 2008.

[96] H Kang, Q Wen, PA Janmey, JX Tang, E Conti, and FC MacKintosh. Nonlinear elasticity of stiff filament networks. *The Journal of Physical Chemistry B*, 113(12) :3799–3805, 2009.

[97] Y Fan and H Liao. Experimental studies on the relaxation behavior of commercial polymer melts. *Journal of Applied Polymer Science*, 110(3) :1520–1530, 2008.

[98] J Wang, L Benyahia, C Chassenieux, JF Tassin, and T Nicolai. Shear-induced gelation of associative polyelectrolytes. *Polymer*, 51(9) :1964–1971, 2010.

[99] L Ma, J Xu, PA Coulombe, and D Wirtz. Keratin filament suspensions show unique micromechanical properties. *J. Biol. Chem.*, 274(27) :19145–19151, 1999.

[100] J Xu, Y Tseng, and D Wirtz. Strain hardening of actin filament networks. *J. Biol. Chem.*, 275(46) :35886–35892, 2000.

[101] C Semmrich, RJ Larsen, and AR Bausch. Nonlinear mechanics of entangled f-actin solutions. *Soft Matter*, 4(8) :1675–1680, 2008.

[102] G Heinrich and TA Vilgis. Contribution of entanglements to the mechanical properties of carbon black-filled polymer networks. *Macromolecules*, 26(5) :1109–1119, 1993.

[103] CO Klein, HW Spiess, A Calin, C Balan, and M Wilhelm. Separation of the nonlinear oscillatory response into a superposition of linear, strain hardening, strain softening, and wall slip response. *Macromolecules*, 40(12) :4250–4259, 2007.

[104] W Yu, P Wang, and CX Zhou. General stress decomposition in nonlinear oscillatory shear flow. *Journal of Rheology*, 53(1) :215–238, 2009.

[105] S Merabia, P Sotta, and DR Long. A microscopic model for the reinforcement and the nonlinear behavior of filled elastomers and thermoplastic elastomers (Payne and Mullins effects). *Macromolecules*, 41(21) :8252–8266, 2008.

[106] S Merabia, P Sotta, and DR Long. Unique plastic and recovery behavior of nanofilled elastomers and thermoplastic elastomers (Payne and Mullins effects). *Journal of Polymer Science Part B - Polymer Physics*, 48(13) :1495–1508, 2010.

[107] S Merabia, P Sotta, and D Long. Heterogeneous nature of the dynamics and glass transition in thin polymer films. *EPJE*, 15(2) :189–210, 2004.

[108] SH Wu. Control of intrinsic brittleness and toughness of polymers and blends by chemical structure - a review. *Polymer International*, 29(3) :229–247, 1992.

[109] WE Wallace, JH vanZanten, and WL Wu. Influence of an impenatrable interface on a polymer glass transition temperature. *Physical Review E*, 52(4) :R3329–R3332, 1995.

[110] JH vanZanten, WE Wallace, and WL Wu. Effect of strongly favorable substrate interactions on the thermal properties of ultrathin polymer films. *Physical Review E*, 53(3) :R2053–R2056, 1996.

[111] Y Grohens, M Brogly, C Labbe, MO David, and J Schultz. Glass transition of stereoregular poly(methyl methacrylate) at interfaces. *Langmuir*, 14(11) :2929–2932, 1998.

[112] AR Payne. Dynamic properties of heat-treated butyl vulcanizates. *Journal of Applied Polymer Science*, 7(3) :873–885, 1963.

[113] JD Ferry. *Viscoelastic Properties of Polymers*. John Wiley and Sons, 1980.

[114] S Merabia and D Long. Heterogeneous dynamics, ageing, and rejuvenating in van der waals liquids. *Journal of Chemical Physics*, 125(23) :234801, 2006.

[115] D Long and P Sotta. Numerical simulation for the mesoscale deformation of disordered reinforced elastomers. *Modeling of Soft Matter*, 141 :205–233, 2005.

[116] D Long and P Sotta. Nonlinear and plastic behavior of soft thermoplastic and filled elastomers studied by dissipative particle dynamics. *Macromolecules*, 39(18) :6282–6297, 2006.

[117] D Long and P Sotta. Stress relaxation of large amplitudes and long timescales in soft thermoplastic and filled elastomers. *Rheologica Acta*, 46(8) :1029–1044, 2007.

[118] JE Mark. *Physical Properties of Polymers Handbook*. American Institute of Physics, 1996.

[119] SS Sternstein and AJ Zhu. Reinforcement mechanism of nanofilled polymer melts as elucidated by nonlinear viscoelastic behavior. *Macromolecules*, 35(19) :7262–7273, 2002.

[120] SK Kumar, S Shenogin, and RH Colby. Dynamics of miscible polymer blends. *Macromolecules*, 40(16) :5759–5766, 2007.

Des élastomères renforcés modèles sont étudiés afin de mettre en relation leur structure microscopique avec leur comportement mécanique macroscopique.
Tout d'abord, la dynamique des chaînes de polymères est étudiée par RMN. Nous mettons en évidence l'existence d'un gradient de température de transition vitreuse autour des charges solides. Nous interprétons ainsi le comportement de plusieurs échantillons à différentes températures avec simplement deux paramètres : l'épaisseur due aux greffons et la taille caractéristique du gradient. Ce modèle de gradient reste valable lors de l'ajout de solvant et permet également d'interpréter les résultats de calorimétrie des échantillons.
Par ailleurs, les propriétés mécaniques des échantillons sont mesurées en cisaillement sinusoïdal. En plus de l'effet Payne classiquement observé pour les élastomères renforcés, une non harmonicité des signaux est détectée. Leur analyse montre la présence d'un raidissement et d'une rhéofluidification à l'intérieur de chaque cycle de sollicitation. Par comparaison avec des simulations obtenues par le modèle de renforcement par ponts vitreux, nous pouvons attribuer ce comportement à la cinétique de destruction – reformation des ponts vitreux au cours des sollicitations.
Enfin, l'arrangement des particules dans chaque échantillon est déterminé grâce à des simulations Monte-Carlo inverses à partir de résultats de diffusion de neutrons. En faisant le lien avec les mesures de dynamique, nous montrons qu'en plus de la couche de polymère vitreux autour des particules, il existe une fraction de polymère plus faiblement ralenti qui joue un rôle non négligeable dans l'effet Payne.

Mots-clés : élastomères renforcés, transition vitreuse, effet Payne, RMN 1H, SANS, LAOS.

Model filled elastomers are studied in order to relate their microscopic structure to their macroscopic mechanical behavior.
First, the polymer dynamics is studied by NMR and we highlight the existence of a gradient glass transition temperature around the solid fillers. We interpret the behavior of several samples at different temperatures with only two parameters: the thickness due to the grafters and the characteristic size of the gradient. This gradient model is still valid in the presence of solvent, as well as for the interpretation of calorimetric measurements.
Moreover, the mechanical properties of the samples are measured in oscillatory shear. In addition to the Payne effect typically observed for reinforced elastomers, a non-harmonic signal is detected. The signal analysis shows the presence of strain-hardening and shear-thinning within each cycle of solicitation. By comparison to the glassy bridge reinforcement model, we can attribute this behavior to the kinetics of destruction-rebirth of the glassy bridges during the solicitation.
Finally, the arrangement of particles in each sample is determined by reverse Monte Carlo simulations based on neutron scattering measurements. Relating this to the polymer dynamics measurements, we show that there is not only a glassy polymer layer around the particles, but also a polymer fraction that is only slightly slowed-down but that contributes significantly to the non linear mechanical behavior of the samples.

Keywords: filled elastomer, glass transition, Payne effect, 1H NMR, SANS, LAOS.